



universität  
wien

# DISSERTATION

Titel der Dissertation

## **On the nature of fossil galaxy groups**

An optical study with SDSS, WHT, and VLT data

Verfasser

**Mag. Paul Eigenthaler**

angestrebter akademischer Grad

**Doktor der Naturwissenschaften (Dr. rer. nat.)**

Wien, im Februar 2011

Studienkennzahl lt. Studienblatt: **A 091 413**

Dissertationsgebiet lt. Studienblatt: **Astronomie**

Betreuer: **Ao. Univ. Prof. Dr. Werner W. Zeilinger**



*Geht man durch den Wald und schaut dabei hartnäckig auf den Boden,  
so entdeckt man sicherlich wunderliche, herrliche Dinge.  
Sieht man dann plötzlich nach oben in die Höhe, so steht man überwältigt  
vor der Offenbarung einer anderen, gleichfalls wunderbaren Welt.  
Die Bedeutung von Sonnen, Monden, Sternbildern, Nebelflecken, Galaxien  
und der ganze Weltraum außerhalb der Erdzone haben sich im letzten Jahrhundert in das  
menschliche Bewusstsein und auch in mein Werk mehr und mehr eingenistet.*

*Max Ernst*

---





# Acknowledgments

Thanks,

**Claudia Mendes de Oliveira** and **Habib Khosroshahi** for our discussions on fossils. It was a pleasure to talk to you and benefit from your experience. Habib, I will never forget your words: “Paul, finish your PhD, you still have 40 years to understand the universe.”

**Werner Zeilinger** for supervising my work, **Bodo Ziegler** for fruitful discussions and **Philippe Prugniel** for the productive time in Lyon.

**Mina** for your help on ULYSS and explaining all the IDL stuff to me.

**Basti, Florent, Hannes, Harsha, Hossein, Ingo, Julia, Mykola, Pedro** for our time in the IK and trying to stay sane together.

**Verena** and **Nigel** for proofreading my thesis. Nigel, it’s actually cool to have a personal language editor.

**Laura** and **Kathi** for all the IK bureaucracy. It must have been hell over the years. Well, we live in Austria, that’s life.

**Florent** and **Roli** for the cool L<sup>A</sup>T<sub>E</sub>X layout. By the way Florent, orange is beautiful.

**Ulli** for our discussions on painting and art.

**Gela, Adam, Sylvia, Hadsch, Claudia, Denise** for everyday university life. Gela, I can’t believe we started astronomy in 2000, yet we are still good looking.

**Humidity** for dropping at 7 p.m. on December 20<sup>th</sup> 2008 on the island of La Palma.

**WHT Telescope Operators** for the support during the nights. I hope that hotel near the ORM won’t be built, although a disco with skybeamer would be nice.

**Mama** and **Papa** for your mental and financial support.

**Astrid** for the nightlife in good old StP.

**Stefan** and **Anita** for being part of my life.

**Valerie** for your smile.

**Tamara** for our true friendship.

**Hannes** for the *legen...* wait for it ...*dary* time in our special office and in the real world of awesomeness.



# Preface

Since, in my experience, master or PhD theses are primarily, not to mention only, read by astronomy students preparing their own manuscripts or students looking for information in a specific field, my intention when planning and preparing the manuscript was to focus on a didactic style, explaining preparations and the execution of observations, be it in visitor or service mode, in detail, since this information is usually hidden somewhere in technical user manuals or marginally mentioned in thick textbooks.

The present thesis is based on service-mode observations obtained with the ESO 8.2m Very Large Telescope (VLT) UT3 Melipal at the Cerro Paranal in Chile (run 383.A-0123) as well as visitor-mode observations with the 4.2m William Herschel Telescope (WHT) on the Canary Island of La Palma (programmes 58-WHT29/08B and 5-WHT1/09A) and archive data from the Sloan Digital Sky Survey.

The work has been funded by the University of Vienna with a *Forschungsstipendium der Universität Wien* (project number F133-N) from January to December 2007 and was supported in the frame of the Initiativkolleg (IK) *The Cosmic Matter Circuit* (I033-N) from January 2008 to December 2010.

Vienna, January 2011





# Contents

<b>Acknowledgments</b>	<b>i</b>
<b>Preface</b>	<b>iii</b>
<b>Abstract</b>	<b>vii</b>
<b>Zusammenfassung</b>	<b>ix</b>
<b>1 Introduction</b>	<b>1</b>
1 Galaxy groups . . . . .	1
2 Fossil groups . . . . .	4
3 Observational results on fossils . . . . .	6
4 Results from cosmological simulations . . . . .	12
5 Characteristics of elliptical galaxy formation . . . . .	15
6 Outline . . . . .	20
<b>2 New fossil candidates in the SDSS</b>	<b>21</b>
1 The SDSS Sky Server . . . . .	21
2 What to look for? . . . . .	23
3 The query . . . . .	23
4 New fossil candidates . . . . .	28
5 Comparison with Santos et al. (2007) . . . . .	34
6 SDSS properties of the WHT and VLT targets . . . . .	35
<b>3 WHT ISIS Observations</b>	<b>43</b>
1 The ISIS spectrograph . . . . .	43
2 Approved nights at the WHT . . . . .	45
3 Preparing observations . . . . .	46
4 Nights at the WHT . . . . .	48
5 Data reduction . . . . .	52
6 Lick Indices . . . . .	58
7 Full spectrum fitting with ULYSS . . . . .	73
8 Kinematics . . . . .	86

## CONTENTS

---

<b>4</b>	<b>VIMOS Observations</b>	<b>89</b>
1	The multi-object spectrograph . . . . .	89
2	Applying for observing time - Phase 1 . . . . .	90
3	Preparing observations - Phase 2 . . . . .	92
4	MOS observations . . . . .	97
5	MOS data . . . . .	97
6	Measuring radial velocities . . . . .	100
7	RX J1548.9+0851 group membership definition . . . . .	102
8	Completeness . . . . .	111
9	The luminosity function . . . . .	116
10	Surface Photometry . . . . .	117
11	SSP equivalent ages and metallicities of group members . . . . .	122
12	Group dynamics and mass-to-light ratio . . . . .	133
<b>5</b>	<b>Discussion</b>	<b>137</b>
1	New fossil candidates in the SDSS . . . . .	137
2	Characteristics of the central ellipticals observed at the WHT . . . . .	139
3	The galaxy population of the fossil candidate RX J1548.9+0851 . . . . .	144
4	Summary, conclusions and outlook . . . . .	150
<b>A</b>	<b>Publications</b>	<b>151</b>
<b>B</b>	<b>Night conditions</b>	<b>163</b>
	<b>References</b>	<b>169</b>
	<b>List of Figures</b>	<b>175</b>
	<b>List of Tables</b>	<b>177</b>
	<b>Curriculum Vitae</b>	<b>179</b>

# Abstract

Poor groups of galaxies are known to be the sites where galaxy-galaxy interactions and galaxy mergers dominate. Numerical simulations as well as optical and X-ray observations over the last few years have shown that this galactic cannibalism can lead to what is called a *fossil* group. Dynamical friction as the driving process leads to the coalescence of individual galaxies in ordinary poor groups, leaving behind nothing more than a central, massive elliptical galaxy, supposed to contain the merger history of the whole group. Recent studies suggest that fossil groups are very abundant and could be the progenitors of the brightest cluster galaxies (BCGs) in the centers of rich galaxy clusters. However, because of their unremarkable appearance in the optical, only a few fossils have been identified up to now, leaving their process of formation and evolution unclear.

Complementary to previous research, the SDSS and RASS surveys have been cross-correlated to identify new fossil structures based on the optical selection criteria for fossils as defined in the literature. This query resulted in 34 newly detected and previously unidentified fossil group candidates. Observations with ISIS at the 4.2m William Herschel Telescope on La Palma have been carried out to study the stellar populations and kinematics of the central ellipticals of six fossil candidates. Ages and metallicities have been determined by analysing Lick indices and fitting single stellar population (SSP) models to the observed galaxy spectra resulting in age, metallicity, and line strength gradients for these galaxies. Complementary, multi-object spectroscopy with ESO VLT VIMOS has been carried out for the fossil candidate RX J1548.9+0851 to determine group memberships, study the optical luminosity function down to  $M_R = -18$ , investigate SSP ages and metallicities of member galaxies, and study the luminosity-weighted dynamics of the system to shed new light on the formation and evolution of fossils.

Amongst others, results have revealed negative metallicity and abundance gradients for all fossil central ellipticals observed at the WHT. The galaxies fall on the Faber-Jackson relation and fundamental plane of early-type galaxies suggesting a similar formation scenario compared to ordinary ellipticals. Group members of the fossil candidate RX J1548.9+0851 show a clear correlation between SSP ages, radial velocities, and the galaxy location within the group. The sample of old member galaxies is distributed along an elongated structure within the system, correlated with the orientation of the major axis of the central elliptical. As they lie at the center of the radial velocity distribution, this suggests that these galaxies formed first, building up a virialized subsample tracing the dark matter halo of the aggregate. The morphology of the central elliptical reveals pronounced symmetric shells along the galaxy major axis indicative of a recent minor merger.



# Zusammenfassung

Galaxienwechselwirkungen und die Verschmelzung von Galaxien treten vorwiegend in losen Galaxiengruppen auf. Numerische Simulationen sowie die Beobachtungen im optischen und im Röntgenbereich der letzten Jahre haben gezeigt, dass dieser galaktische Kannibalismus zur Entstehung sogenannter fossiler Gruppen führen kann. Die dynamische Reibung als wesentlicher physikalischer Prozess fördert die Verschmelzung einzelner Galaxien in gewöhnlichen losen Galaxiengruppen, wobei eine zentrale, massereiche elliptische Galaxie das Endprodukt darstellt. Die Untersuchungen der letzten Jahre legen nahe, dass fossile Galaxiengruppen sehr häufig sind und als die Vorläufer der hellsten elliptischen Galaxien im Zentrum massereicher Haufen gelten könnten. Durch ihre unspektakuläre Erscheinung im Optischen konnten bis heute jedoch nur wenige fossile Gruppen identifiziert werden, weswegen erst wenig über ihre Entstehung und Entwicklung bekannt ist.

In dieser Arbeit wurden ergänzend zu früheren Studien, die SDSS und RASS Durchmusterungen systematisch durchsucht, um neue fossile Galaxiengruppen, basierend auf deren optischen Auswahlkriterien, zu finden. Diese Suche resultierte in 34 neuen, zuvor noch nicht klassifizierten Kandidaten. Es wurden Beobachtungen mit dem Spektrographen ISIS am 4.2 m William Herschel Telescope (WHT) auf La Palma durchgeführt, um die stellaren Populationen und kinematischen Eigenschaften der zentralen elliptischen Galaxien von 6 fossilen Kandidaten zu untersuchen. Alter und Metallizität wurden mittels der Analyse von *Lick/IDS indices* und dem Fitten von *single stellar population* (SSP) Modellen an die beobachteten Galaxienspektren bestimmt. Dies lieferte Alters- und Metallizitätsgradienten, sowie die räumliche Variation der Absorptionslinienstärken in diesen Galaxien. Zusätzlich konnte mit dem *multi-object* Spektrographen VIMOS am ESO VLT die Galaxienpopulation des fossilen Kandidaten RX J1548.9+0851 untersucht werden, um Gruppenmitgliedschaften, die optische Leuchtkraftfunktion, Alter und Metallizität von Gruppenmitgliedern, sowie die Dynamik des Systems zu analysieren.

Die beobachteten zentralen elliptischen Galaxien am WHT zeigen unter anderem negative Metallizitätsgradienten. Des Weiteren liegen diese Objekte auf der Faber-Jackson Relation und auf der Fundamentalebene von Galaxien frühen morphologischen Typs, was ein Entstehungsszenario ähnlich dem von gewöhnlichen elliptischen Galaxien nahelegt. Gruppenmitglieder des fossilen Kandidaten RX J1548.9+0851 zeigen eine klare Korrelation zwischen SSP Alter, Radialgeschwindigkeiten, sowie der Lage der Galaxien innerhalb der Gruppe. Die ältesten Mitglieder der Gruppe sind entlang einer filamentartigen Struktur, welche mit der Orientierung der Hauptachse der zentralen elliptischen Galaxie korreliert, verteilt. Da diese Objekte auch den Kern der beobachteten Radialgeschwindigkeitsverteilung bilden, ist es naheliegend, dass diese Galaxien zuerst entstanden sind und ein virialisiertes subsample darstellen, welches die Orientierung des Dunkle-Materie-Halos der Gruppe skizziert. Die zentrale elliptische Galaxie zeigt außerdem ausgeprägte symmetrische Schalen entlang der Hauptachse der Galaxie, ein Indiz für einen kürzlichen minor merger.



# Chapter 1

## Introduction

When taking a look at the renowned *Hubble Atlas of Galaxies* published by Alan Sandage in 1961, one is confronted with the great variety and beauty of galaxies in our universe. One obvious question arising when facing this large diversity in morphological appearance is evident – what caused these differences? Are they due to unequal galaxy environments, different physical conditions, or do they mark way stations in an evolutionary sequence?

These are fundamental questions in extragalactic astronomy and have been studied since Hubble's pioneering work on the classification of galaxies. Today we know that morphology is strongly affected by environment. While ellipticals are predominantly found in galaxy clusters, i.e. high-density environments, spirals are commonly found in the less-massive galaxy groups or in the field, i.e. low-density environments. This morphology-density relation was first discovered by Dressler (1980). It has also been suggested that ellipticals could be formed by the collision and subsequent merger of two disk galaxies (Toomre & Toomre 1972). This hypothesis is now widely accepted but has been strongly debated in the past.

Following these fundamental questions and findings, the present work focuses on what is believed to be the remainder of continuous galaxy mergers within a group of galaxies, so-called *fossil groups*, or for short *fossils*.

### 1 Galaxy groups

Redshift surveys have shown that most galaxies in the nearby universe are not randomly distributed in space but rather found in aggregates, so called galaxy groups, populated by typically up to 50 members (Geller & Huchra 1983; Tully & Fisher 1988). In contrast, massive clusters can contain more than 1000 individual galaxies. Due to this low number of members in groups and the consequential challenge to distinguish between true physical, bound systems and chance superpositions along the line of sight, detailed studies of galaxy groups have only been carried out during the last few decades. Nowadays, mainly because of the use of eight meter class

telescopes and beyond, the possibility for studying galaxy groups has increased dramatically with the detection of less luminous group members, dwarf galaxies, which by far dominate in numbers, becoming feasible. Because of the investigation of these objects at the faint end of the galaxy luminosity function, better statistical statements on the overall physical properties of the aggregates can be given. Besides the optical, groups and clusters are also prominent in X-rays originating from the hot gaseous haloes associated with their potential wells. Basically galaxy groups can be divided into three major classes that differ mainly in their optical and physical characteristics: poor groups, compact groups, and fossil groups.



**Figure 1.1:** Poor, compact and fossil groups of galaxies. The examples shown are the M81 group, Seyfert’s Sextet, and the fossil RX J1416.4+2315. The fossil is shown in false colours where orange reveals the central elliptical in the optical while blue displays the surrounding X-ray halo. Credits: R. Zmaritsch & A. Gross; J. English; Khosroshahi et al. (2006a).

Poor or loose groups, with a space density of  $\sim 10^{-5} \text{ Mpc}^{-3}$  (Nolthenius & White 1987) resemble simple multiplets of galaxies, represent the most common class and are simply referred to as galaxy groups. They are comprised of approximately 50 members, including numerous dwarf galaxies and take up typical diameters of  $\sim 1.5 \text{ Mpc}$ . A prototypical example of a loose group is found in our immediate neighbourhood, the Local Group. Consisting of three bright spirals (Milky Way, M31, M33) and  $\sim 40$  dwarf galaxies, it presents the characteristic environment of a poor group of galaxies.

Compact groups with a space density of  $\sim 1-2 \times 10^{-6} \text{ Mpc}^{-3}$  (Hickson 1982) are less abundant and typically made up of only 4 to 8 bright galaxies. These strongly interact with each other due to their mutual gravitational attraction, causing tidal forces to form tails around close members. Using the original selection criteria of Hickson (1982), McConnachie et al. (2009) discovered 2297 compact groups from the SDSS DR6 down to a limiting magnitude of  $r' = 18$ .

Fossil groups are characterised through a dominating central bright elliptical galaxy comparable to cD galaxies in clusters, surrounded by a diffuse and extended X-ray halo together with a significant fainter galaxy population. Recent studies have estimated space densities of fossil systems in the local universe of  $\sim 1-4 \times 10^{-6} \text{ Mpc}^{-3}$ , comparable to HCGs. Figure 1.1 shows prototypical examples of all three classes.



## 1 Physical characteristics of galaxy groups

Besides the fact that the vast majority of galaxies in the universe appear to be located in groups (only 30% of all galaxies in the nearby universe are isolated; see Tully (1987)), these systems offer moreover ideal laboratories to study galaxy evolution and galaxy interactions in low density environments. Since the masses of groups are comparatively small ( $M \sim 10^{13} M_{\odot}$ ) with respect to clusters ( $M \sim 10^{14} M_{\odot}$ ), the virial theorem<sup>1</sup>

$$M = \frac{3\pi R\sigma^2}{2G} \quad (1.1)$$

relating group mass  $M$ , a characteristic group radius  $R$ , and group velocity dispersion  $\sigma$ , implies they also have lower values for the group velocity dispersions. Thus, member galaxies experience longer interaction timescales favoring galaxy mergers and the subsequent coalescence of individual objects. These effects are only secondary in clusters, where galaxy harassment, i.e. continuous high speed galaxy encounters, or ram pressure stripping alter the shape of individual galaxies instead. Considering this fact, the presented variety of galaxy groups clearly suggests that these classes are merely way stations in an evolutionary sequence. Indeed, Rood & Struble (1994) stated that in Hickson's original sample of HCGs, 70% are located within loose groups, suggesting that these denser subaggregates form within the loose surrounding configuration.

Numerical simulations have shown that this galactic cannibalism in groups can proceed as long as a single, massive elliptical galaxy remains as the final product of multiple mergers (Barnes 1989) on a timescale of a few gigayears (see Figure 1.2). The physical origin behind the merging of galaxies is explained by dynamical friction of the group member galaxies with the group dark matter halo and is not similarly effective for all types of galaxies. According to the description of dynamical friction by Chandrasekhar (1943)<sup>2</sup>, the friction force is strongly mass dependent leading to longer merging timescales for the less massive dwarf galaxies (equation 1.2)<sup>3</sup> which, as a consequence, should have survived this galactic cannibalism up to now.

$$t_{\text{fric}} \approx \frac{10^{10}}{\ln \Lambda} \left( \frac{r}{60 \text{kpc}} \right)^2 \left( \frac{v_c}{220 \text{km/s}} \right) \left( \frac{2 \cdot 10^{10} M_{\odot}}{M} \right) \text{yr} \quad (1.2)$$

In addition, the hot X-ray gas, as found in  $\sim 50\%$  of all known galaxy groups (not correlated with individual group members but rather diffusely distributed following the global gravitational group potential, Mulchaey 2000) is also expected to be observed in this state of hierarchical galaxy evolution since gas temperatures and electron densities of a typical intragroup medium with  $T_g \sim 10^7$  K and  $n_e \sim 10^{-3} \text{ cm}^{-3}$  suggest gas cooling timescales

$$\tau_{\text{cool}} \propto n_e^{-1} T_g^{1/2} \quad (1.3)$$

exceeding the age of the universe. In terms of group kinematics, relaxation time scales

$$\tau_{\text{rlx}} \approx 0.1 \frac{N}{\ln N} \cdot \tau_{\text{dyn}} \quad \tau_{\text{dyn}} \equiv \frac{R_{\text{typ}}}{v_{\text{typ}}} \quad (1.4)$$

<sup>1</sup> Assuming isotropic velocities. Velocity dispersion  $\sigma$  and radius  $R$  refer to observed quantities.

<sup>2</sup> See Binney & Tremaine (1987) – Section 7.1 for a detailed description.

<sup>3</sup> Taken from Binney & Tremaine (1987) p.429. For  $r$ ,  $v_c$ , and  $M$ , characteristic values representing a group environment have to be considered.

in the order of 4 to 5 Gyrs are estimated with typical group parameters (e.g.  $N = 40$ ,  $R = 1$  Mpc,  $v = 250 \text{ km s}^{-1}$ ) indicating that these evolved aggregates should be relaxed systems exhibiting gaussian velocity distributions.

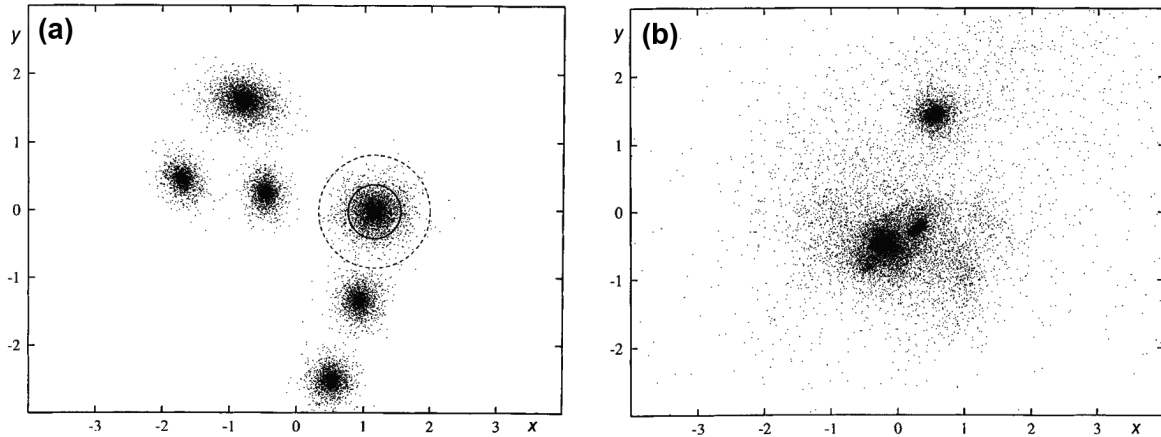


**Figure 1.2:** Numerical simulation of a compact galaxy group. Panel a): Group model, initial conditions. Each point cloud resembles one galaxy. In total, 32768 luminous particles are displayed. Panel b): Most of the initial group member galaxies have merged into one single massive object on a timescale of 2.64 Gyr. Taken from Barnes (1989).

## 2 Fossil groups

Based on these theoretical predictions, one claims that *fossil groups* represented by a central bright, massive elliptical galaxy surrounded by a diffuse and extended X-ray halo and a fainter galaxy population, are the remnants of what was initially a poor group of galaxies. This once poor group of galaxies has been transformed into an old, relaxed, *fossil* stage of galaxy evolution with compact groups acting as likely way station in this evolution. If this scenario is correct then the relative space densities of these three different types of systems give information on their transformation rates.

### 1 Observational definition of a fossil

If fossil groups are treated as a special and distinct class of galaxy groups, well defined observational classification criteria have to be chosen such that a clear distinction between this special class of systems and other galaxy aggregates can be made. The definition of a fossil system as proposed by Jones et al. (2003) was the first real attempt to attribute exact observational characteristics to this class. According to their influential paper, a fossil system is a spatially extended X-ray source with an X-ray luminosity from diffuse, hot gas of  $L_{X,\text{bol}} \geq 10^{42} h_{50}^{-2} \text{ ergs s}^{-1}$ . The optical counterpart is a bound system of galaxies with  $\Delta m_{1,2} \geq 2.0 \text{ mag}$ , where  $\Delta m_{1,2}$  is the absolute total magnitude difference in the  $R$  band between the two brightest galaxies in the system within half the projected virial radius. No upper limit is given for the X-ray luminosity or temperature. The ideas behind this classification scheme are simple. The lower limit in X-ray luminosity excludes normal bright elliptical galaxies exhibiting a hot coronal gas

component. The magnitude gap of  $\Delta m_{1,2} \geq 2.0$  mag for the two brightest galaxies of the group ensures that one single elliptical galaxy dominates the system. Studies of luminosity functions of galaxy groups have shown that this threshold acts as a good criterion to distinguish between poor groups and fossil aggregates since observations have shown that such a high magnitude gap is extremely unlikely to occur in ordinary groups or clusters (Beers et al. 1995). Following these overall characteristics, the detection of new fossils can only succeed if optical and X-ray data from different sky surveys are cross-correlated.

## 2 Fossils in the literature

The first fossil group identified, RX J1340.6+4018, was published in Nature (Ponman et al. 1994). Since then, only a few other objects have been assigned to this class, mainly because of their unremarkable appearance in the optical and the low sensitivity of X-ray detectors, a drawback especially relevant when searching for fossils at higher redshifts.

**Table 1.1:** Most prominent fossils as summarized by Mendes de Oliveira et al. (2006).

Name	$\alpha_{2000}$	$\delta_{2000}$	$z$	$L_{X,bol}^a$	Reference
NGC 1132	02 52 51.8	−01 16 29	0.023	1.9	Yoshioka et al. (2004)
RX J0454.8-1806	04 54 52.2	−18 06 56	0.031	1.9	Yoshioka et al. (2004)
ESO 306- G 017	05 40 06.7	−40 50 11	0.036	129	Sun et al. (2004)
RX J1119.7+2126	11 19 43.7	+21 26 50	0.061	1.7	Jones et al. (2003)
RX J1159.8+5531	11 59 51.4	+55 32 01	0.081	22	Vikhlinin et al. (1999)
CL 1205+44	12 05 53.7	+44 29 46	0.59	180	Ulmer et al. (2005)
RX J1256.0+2556	12 56 03.4	+25 56 48	0.232	61.	Jones et al. (2003)
RX J1331.5+1108	13 31 30.2	+11 08 04	0.081	5.9	Jones et al. (2003)
RX J1340.6+4018	13 40 33.4	+40 17 48	0.171	25	Vikhlinin et al. (1999)
RX J1416.4+2315	14 16 26.9	+23 15 32	0.137	220.	Jones et al. (2003)
RX J1552.2+2013	15 52 12.5	+20 13 32	0.136	63	Jones et al. (2003)
NGC 6034	16 03 32.1	+17 11 55	0.034	0.75	Yoshioka et al. (2004)
NGC 6482	17 51 48.8	+23 04 19	0.013	2.17	Khosroshahi et al. (2004)
RX J2114.3-6800	21 14 20.4	−68 00 56	0.130	20	Vikhlinin et al. (1999)
RX J2247.4+0337	22 47 29.1	+03 37 13	0.199	41	Vikhlinin et al. (1999)

<sup>a</sup> Bolometric X-ray luminosity given in  $10^{42} h_{50}^{-2} \text{ ergs s}^{-1}$ . RX denotations refer to ROSAT X-ray sources.

A catalogue of 15 fossils identified by various authors was summarized by Mendes de Oliveira et al. (2006) (see Table 1.1). However, not all listed objects represent what is typically referred to as the remnant of a group-sized halo since more massive systems with velocity dispersions in the range of  $600 \text{ km s}^{-1}$  (more appropriate to galaxy clusters) are also present (Cypriano et al. 2006; Mendes de Oliveira et al. 2006). Santos et al. (2007) have cross-correlated optical and X-ray data from the Sloan Digital Sky Survey (Adelman-McCarthy et al. 2008) and the ROSAT All Sky Survey (Voges et al. 1999) to identify new fossil group candidates. Their findings comprise a list of 34 candidates, ranging up to  $z = 0.489$ . Similar to this work, a list of additional 34<sup>4</sup> fossil group candidates was published within the framework of this thesis (see Eigenthaler & Zeilinger 2009<sup>5</sup> and Table 2.2). Just recently, Schirmer et al. (2010) reported the discovery of a strong lensing fossil projected near the well-studied cluster MS0451-0305J0454-0309.

<sup>4</sup>What a coincidence.

<sup>5</sup>The publication is included in Appendix A.

The majority of these 84 systems ( $\sim 87\%$ ) reside in the northern celestial hemisphere whereas only 11 objects ( $\sim 13\%$ ) have been identified in the southern one. This is not surprising since the SDSS does not cover the southern sky. The nearest fossil was identified with the elliptical NGC 6482 at a redshift of  $z = 0.013$  (Khosroshahi et al. 2004) while the most distant fossil was found at  $z = 0.59$  combining HST, Chandra and XMM-Newton data (Ulmer et al. 2005).

Jones et al. (2003) assume that fossil systems probably constitute 8-20% of all systems with comparable X-ray luminosity ( $\geq 10^{42}$  ergs  $s^{-1}$ ), thus they also very likely act as the site of formation of brightest cluster galaxies (BCGs) before their infall into clusters. Similar optical luminosities of the central ellipticals in fossils compared to that of BCGs support this idea. Therefore fossils play a crucial role in our understanding of galaxy evolution in low-density environments and the physical connection between groups and clusters.

### 3 Observational results on fossils

Since the catalogue of known fossils is scarce, an analysis of the optical and X-ray properties of these systems has only been carried out for some aggregates, leaving the formation process of this special class of objects still unclear. This section highlights some of the observational results that have been obtained over the last few years.

#### 1 Scaling relations in fossil groups

If fossils are indeed a distinct class of objects, it is obvious to compare the optical and X-ray properties of these systems with those of ordinary poor groups and clusters of galaxies to check if any systematic differences between these aggregates are present. The first study facing this comparison was carried out by Khosroshahi et al. (2007), investigating scaling relations of optical and X-ray properties of fossils with respect to non-fossils (see Fig. 1.3). Based upon Chandra X-ray observations as well as optical imaging and spectroscopy this study comprised the information of seven fossil groups showing regular, symmetric X-ray emission, indicating no recent mergers. Scaling relations focusing on the total gravitational mass  $M$ , X-ray temperature  $kT$ , X-ray luminosity  $L_X$ , group velocity dispersion  $\sigma$ , and the optical luminosity  $L_R$  were studied.

By accumulating the luminosity of spectroscopically confirmed members within  $r_{200}$  down to  $M_R \approx -19$  to estimate the optical group luminosity  $L_R$ , fossils turn out to be more X-ray luminous than non-fossils for a given optical group luminosity and lie at the extreme upper envelope of the distribution of groups in general (Fig. 1.3 a). A possible explanation for this difference is that fossils might be underluminous in the optical because of inefficient star formation. However, for a given velocity dispersion, fossils fall on the distribution of ordinary groups and clusters in the  $L_R - \sigma$  relation showing similar optical group luminosities (Fig. 1.3 b).

If the X-ray overluminosity were the only difference between the X-ray properties of fossils and non-fossils, a deviation from the  $L_X - T_X$  relation for ordinary groups and clusters would be expected. Initially, this seemed to be the case in the work of Jones et al. (2003), who investigated two fossils with ROSAT data. However, it turned out that the X-ray temperature was

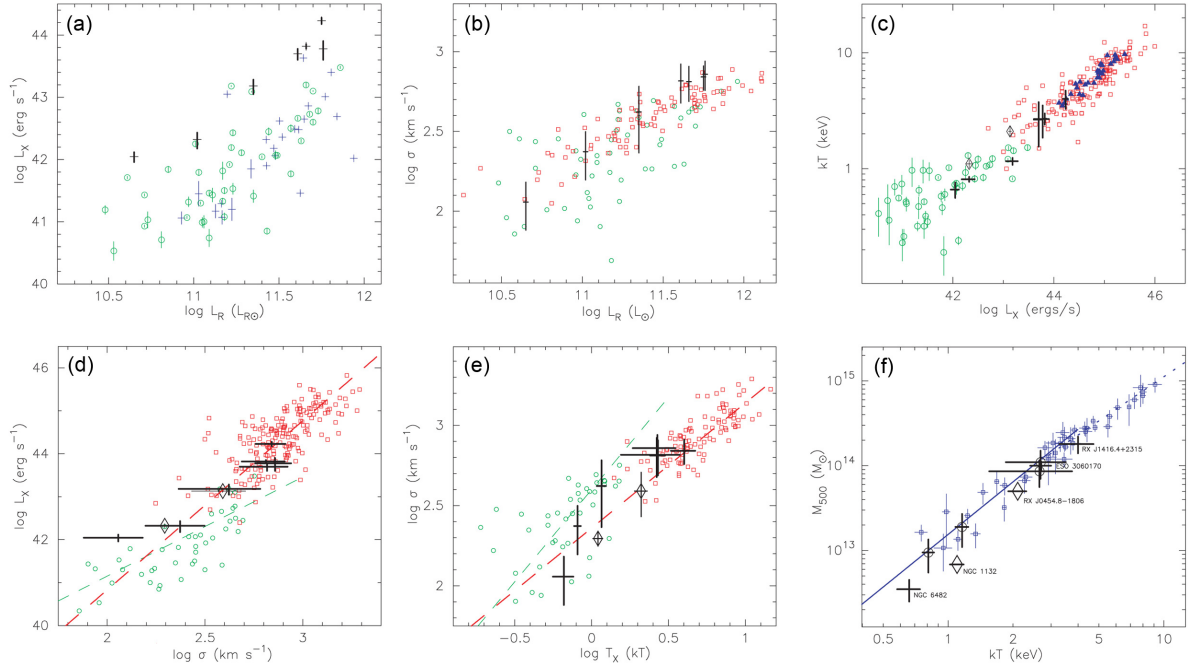


**Figure 1.3:** Scaling relations in fossil groups. Green symbols are non-fossil groups, red ones indicate clusters. Fossils are shown as bold black data points. Adapted from Khosroshahi et al. (2007).

underestimated in this study. The Chandra data from Khosroshahi et al. (2007) show that all studied fossils fall on the  $L_X-T_X$  relation of non-fossil groups and clusters (Fig. 1.3 c). Thus, if fossils are indeed overluminous in  $L_X$ , as argued before, they should also have higher X-ray temperatures compared to non-fossils to remain on the standard group  $L_X-T$  relation.

In the  $L_X-\sigma$  plane, fossils are more X-ray luminous than non-fossil groups for a given group velocity dispersion (Fig. 1.3 d). The relation for fossils flattens at lower velocity dispersions because of the fossil X-ray selection criterion at  $L_X = 10^{42}$  ergs s $^{-1}$ . The  $T_X-\sigma$  plane (Fig. 1.3 e) shows that fossils are hotter compared to non-fossil groups, as expected from the  $L_X-T_X$  and  $L_X-\sigma$  relations, supporting a formation scenario where X-ray temperature and luminosity have been enhanced compared to non-fossils.

Relations involving the mass of groups and clusters are of special interest since the total halo mass is considered to determine the overall physical properties of these systems. Assuming that the X-ray emitting gas is in hydrostatic equilibrium and in spherical symmetry, gas density  $\rho(r)$  and temperature profiles  $T(r)$  allow us to measure the total gravitational mass

$$M_{\text{grav}}(< r) = -\frac{kT(r)r}{G\mu m_p} \left[ \frac{d \ln \rho(r)}{d \ln r} + \frac{d \ln T(r)}{d \ln r} \right] \quad (1.5)$$

where  $G$  is the gravitational constant,  $m_p$  the proton mass, and  $\mu$  the mean particle mass. If radial profiles of gas density and temperature cannot be determined because of low signal-to-noise in X-rays, one can assume an isothermal temperature to derive the mass with equation

1.5. Sanderson et al. (2003) have shown however that this assumption overestimates the total mass. Fig. 1.3f shows the  $M-T_X$  plane for fossils and non-fossils. Open circles indicate fossils with the isothermality assumption. Considering the overestimation of mass in the isothermal case, fossils are hotter than non-fossils for a given mass.

All presented relations suggest an enhancement of  $L_X$  and  $T_X$  for a given optical luminosity or mass compared to ordinary poor groups. This could be explained by differences in the gravitational potential in fossils compared to non-fossils. In fact, there is observational evidence that the potential of fossils is more cuspy leading to higher gas compression and thus to a higher X-ray temperature and luminosity. On the other hand, a cuspy dark matter halo implies an early formation epoch (Navarro et al. 1995), consistent with the fossil group picture.

## 2 Isophotal shapes of the central ellipticals – formation of BGGs and BCGs

Isophotes of elliptical galaxies are not necessarily represented by pure ellipses, but slightly deformed ones. To quantify the extent of this deformation, deviations are Fourier analyzed resulting in the parameter  $a_4$ , indicative of *boxy* ( $a_4 < 0$ ) or *disky* ( $a_4 > 0$ ) isophotes (Jedrzejewski 1987; Bender et al. 1988), see Fig. 1.4a.

These shapes depend on the formation process of the elliptical and hence act as an indicator for the undergone evolution. More precisely, dissipationless merger simulations from Naab & Burkert (2003) have shown that unequal-mass mergers lead to fast rotating, disk-like ellipticals, while equal-mass mergers produce slowly rotating, pressure-supported systems. Major mergers between bulge-dominated systems result in boxy ellipticals, independent of the mass ratio while merger remnants that subsequently accrete gas are always disk-like. More recently, it has been shown that the mergers of spiral galaxies alone cannot reproduce the kinematic and photometric properties of very massive ellipticals (Naab, Khochfar & Burkert 2006) nor can they reproduce the observed correlation between isophotal shapes and the luminosity of ellipticals. Since the space density of fossils is considered to be as large as that of poor and rich clusters combined, fossils could provide suitable environments for the formation of the luminous giant ellipticals as observed in clusters. Following this possible connection, Khosroshahi et al. (2006b) have investigated the central ellipticals in seven fossils. They conclude that the isophotal shapes of the studied central ellipticals in fossils (FCGs) are always disk-like in contrast to brightest group (BGG) and cluster (BCG) galaxies in non-fossil systems (Fig. 1.4b). While BGGs show boxy and disk-like isophotes in similar proportions, BCGs are mostly boxy.

If the central ellipticals in groups have indeed formed via mergers of all other major galaxies, then some of these mergers would have been gas-rich, since groups are known to consist of a large spiral fraction. The disk-like characteristics of FCGs would then be consistent with numerical simulations suggesting that disk-like isophotes result from gas-rich mergers. Thus, BGGs and BCGs in Fig. 1.4b with non-boxy isophotes could likely originate from FCGs that have been integrated into these structures. The difference in the isophotal shapes of FCGs and most luminous BCGs as seen in Fig. 1.4b does not however rule out the possible evolutionary link of infalling pre-processed merged ellipticals from groups in clusters. This could still be the case if these ellipticals have later undergone gas-free mergers within the cluster environment. About 40% of BCGs exhibit at least one secondary nucleus, strongly supporting this idea.

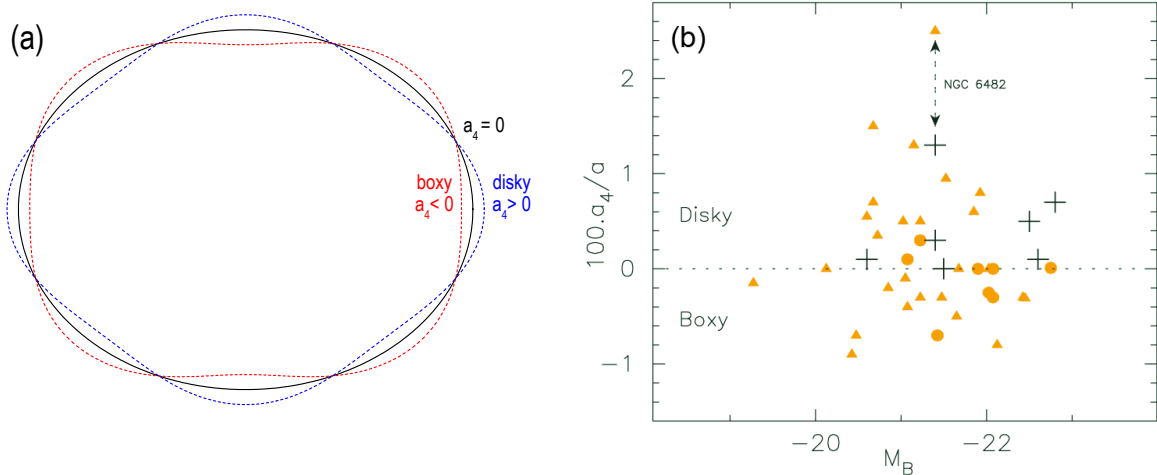


**Figure 1.4:** Panel a): Boxy and disk isophotes. Deviations from a pure ellipse are quantified via the parameter  $a_4$ . Panel b): Variation of isophotal shapes of early-type brightest group (BGG) and cluster (BCG) galaxies with the optical luminosity of the brightest galaxy. Crosses indicate fossils while triangles and circles show BGGs and BCGs from Ellis & O’Sullivan (2006). All fossils show disk isophotes. Taken from Khosroshahi et al. (2006b).

### 3 The optical luminosity function of fossils

The luminosity function of fossil groups shows a lack of bright galaxies by definition, since fossils are considered to be environments where no bright galaxies are present besides the dominating central elliptical. Thus, the bright end of the luminosity function of these systems is unusual compared to what is normally observed in poor groups, with too few  $L^*$  galaxies present.

Concerning the faint end ( $M_R \geq -18$ ) of the galaxy luminosity function, little has been known so far, but a scenario seems to be emerging that massive fossils tend to have steep luminosity functions. Existing studies have only investigated the luminosity functions of the fossil systems RX J1552.2+2013, RX J1416.4+2315, and RX J1340.6+4018 down to  $M_{i'} = -17.5$ ,  $M_{g'} = -16.6$ , and  $M_{i'} = -16.5$  respectively. These aggregates are rather classified as fossil clusters instead of groups due to their relatively large velocity dispersions:  $623 \text{ km s}^{-1}$ ,  $584 \text{ km s}^{-1}$ , and  $565 \text{ km s}^{-1}$  (Mendes de Oliveira et al. 2006; Cypriano et al. 2006; Mendes de Oliveira et al. 2009). Interestingly, besides the expected magnitude gap around  $L^*$  galaxies, also a dip in the luminosity function of RX J1552.2+2013 at the transition to dwarf galaxies  $M_R = -18$  has been found. Such dips have been observed in several systems, mostly dense, dynamically well-evolved aggregates such as X-ray emitting cD clusters (Valotto et al. 2004) or compact groups of galaxies (Hunsberger et al. 1996), suggesting that there may be more than one mechanism driving the depletion of galaxies in these different environments.

Assuming the merger scenario hypothesis from hierarchical galaxy evolution models, the lack of  $L^*$  galaxies is explained by dynamical friction, resulting in a deceleration of the orbital velocity of a galaxy which loses its kinetic energy to the surrounding dark matter particles and subsequent merger. The same physical processes cannot be efficient enough to reproduce the comparatively small number of low-mass galaxies around  $M_R = -18$ . One explanation

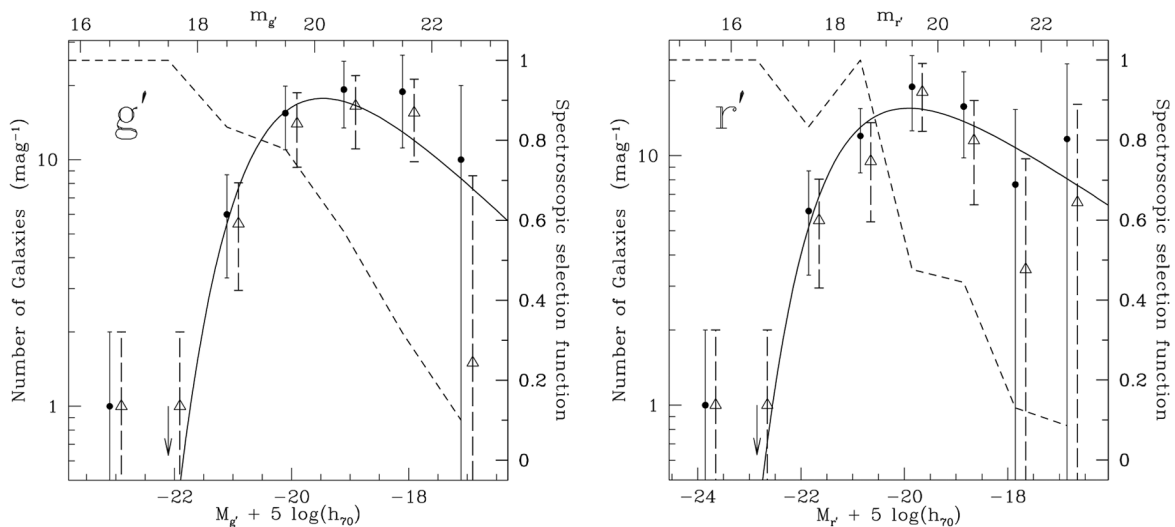


**Figure 1.5:** Luminosity function of the fossil cluster RX J1552.2+2013 in the SDSS  $g'$  and  $r'$  bands. Solid circles show spectroscopically confirmed members while triangles indicate photometrically determined ones. The continuous line shows the best Schechter fit to the spectroscopic sample excluding the brightest galaxy. A dip in the LF can be found around  $M_{r'} = -18$ . Taken from Mendes de Oliveira et al. (2006).

for these missing galaxies could be a succession of tidal encounters (Gnedin 2003). If this scenario is correct, one would not expect such a dip in the luminosity functions for less rich galaxy aggregates than the observed fossil clusters, since the galaxy density and thus the tidal stripping efficiency is much lower in these systems.

#### 4 Dynamics and mass-to-light ratios of fossils

The symmetric and regular X-ray emission together with the lack of  $L^*$  galaxies and the large early-type fraction observed in fossils suggest that these systems are old, evolved systems. Thus, from a dynamical point of view, fossils should present relaxed, virialized galaxy aggregates. The dynamical properties of fossils have only been investigated for the already mentioned fossil clusters RX J1552.2+2013, RX J1416.4+2315, and RX J1340.6+4018.

In these studies, the radial velocity distributions have been used to determine group velocity dispersions and the dynamical mass of the systems. It is interesting to separate morphological types in such an analysis to see if any systematic differences in the velocity distributions of these subsamples are present, especially since galaxy morphology is often also strongly correlated with the spatial location of galaxies in groups. In fact, by excluding four emission-line galaxies in RX J1552.2+2013, Mendes de Oliveira et al. (2006) derive a much smaller velocity dispersion of the system (see Fig. 1.6 a). This is not surprising, however, since such objects are believed to have just been recently accreted by the cluster and thus not yet virialized (Sodré et al. 1989; Biviano et al. 1997). Fig. 1.6 a shows that except one galaxy, all emission-line objects occupy the edges of the velocity distribution.



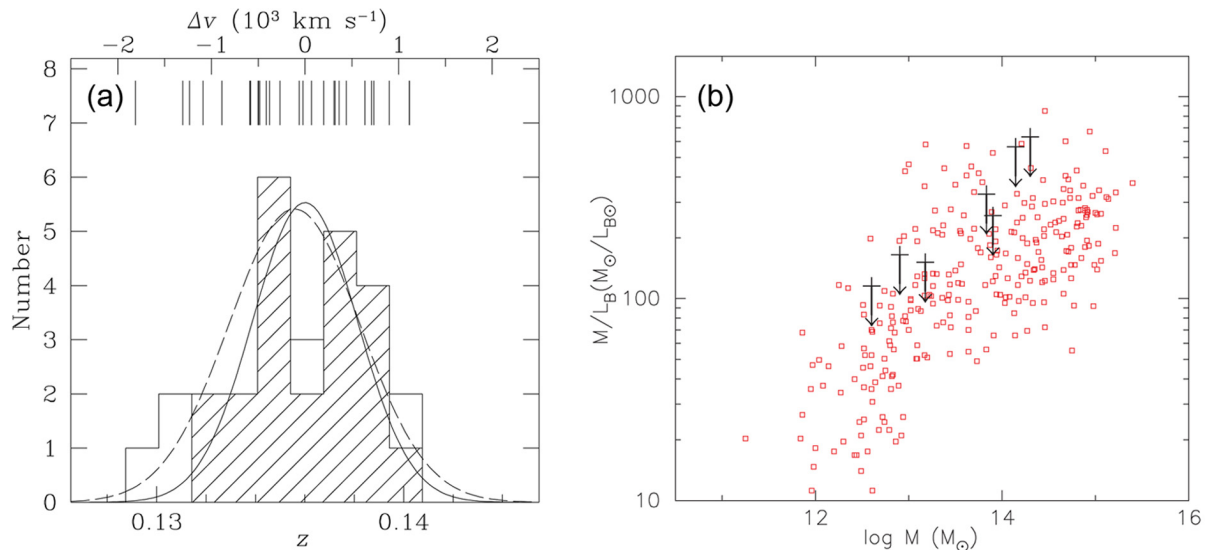


**Figure 1.6:** Panel a): Velocity distribution of member galaxies in RX J1552.2+201. The hatched histogram presents members without emission lines. Taken from Mendes de Oliveira et al. (2006). Panel b):  $B$ -band mass-to-light ratios of fossils (black crosses) and non-fossils (red squares) as a function of group and cluster mass. Fossils show comparatively high mass-to-light ratios at the upper domain of the distribution. Taken from Khosroshahi et al. (2007).

If high quality X-ray data are not available and hence equation 1.5 not applicable, the galaxy velocity distribution of fossils provides a useful tool to estimate the dynamical mass of these systems. Reliable mass estimates on the other hand allow us to constrain the mass-to-light-ratio in these systems, indicative of the existing dark matter content.

There have been various inconsistent findings for the mass-to-light ratio in fossils. While Vikhlinin et al. (1999) determined high values for fossils ( $M/L_R = 250 - 450 M_\odot/L_\odot$ ), Khosroshahi et al. (2004) derived  $M/L_R = 71 M_\odot/L_\odot$  for NGC6482. For the fossil ESO 3060170, Sun et al. (2004) have also reported an ordinary value ( $M/L_R = 150 M_\odot/L_\odot$ ). The mass-to-light ratios from two systems of Yoshioka et al. (2004) are very high, up to  $M/L_B = 1000 M_\odot/L_\odot$ , in contrast. This is not surprising, however, since only 10–20% of the luminosity of the central elliptical had been estimated for the luminosity of the remaining galaxy population in this work. More recent studies have shown that the luminosity of the surrounding galaxy population amounts to at least as much as the central elliptical.

Fig. 1.6 b shows the mass-to-light ratios of the seven fossils from Khosroshahi et al. (2007). Crosses assume that all members in fossils are early types ( $B-R = 1.5$ )<sup>6</sup>. Arrows indicate the shift to be considered if all galaxies except the central elliptical are late types ( $B-R = 0.8$ ). Fossils show comparatively high mass-to-light ratios at the upper domain of the distribution. In general, there are relatively large uncertainties in the determination of mass-to-light ratios of groups and clusters because of the difficulties in obtaining proper values for the total masses and total optical luminosity of these systems.

<sup>6</sup>Since this work focused on  $R$ -band luminosities, an assumption for the corresponding  $B$ -band values had to be made to compare with the mass-to-light ratios of groups and clusters from Girardi et al. (2002) in the  $B$ -band.

## 4 Results from cosmological simulations

Besides the observational effort to understand the formation and evolution of fossil groups, several simulations have been carried out over the last few years to address the same questions from a theoretical point of view.

To trace the evolution of present day fossils back to their formation epoch, Dariush et al. (2007) made use of the Millennium and Millennium gas simulations (Springel et al. 2005; Hartley et al. 2008). The dark-matter Millennium simulation is based on a 10 billion particle  $\Lambda$ CDM cosmological model following the hierarchical structure formation via the merger of small and dense haloes, covering a volume of  $500 h^{-1}$  Mpc a side. The corresponding Millennium gas simulation is a suite of hydrodynamical models implemented for the same volume. In these simulations, Dariush et al. (2007) selected fossil dark matter haloes with  $M_{\text{DM}} = 10^{13} h^{-1} M_{\odot}$  at  $z = 0$  according to the observational criteria defined by Jones et al. (2003) and traced these haloes backwards in time. Fig. 1.7 a relates gas temperature, dark-matter halo mass and bolometric X-ray luminosity for all haloes in the Millennium gas simulation while Fig. 1.7 b links X-ray luminosity and the  $R$  band magnitude gap for these haloes, separating fossil from non-fossil systems. As can be seen from the diagram, fossils do not form a distinct population but are merely the extreme examples of a smooth distribution. Jones et al. (2003) argued that fossils constitute of 8–20% of all systems with comparable X-ray luminosity. The histogram in Fig. 1.7 b shows the fraction of fossils in each bin of  $L_X$ . Integrating this fraction over all X-ray luminosities above  $L_X = 0.2 \cdot 10^{42} h^{-2}$  ergs  $s^{-1}$ , Dariush et al. (2007) find  $\sim 7\%$  of haloes to be

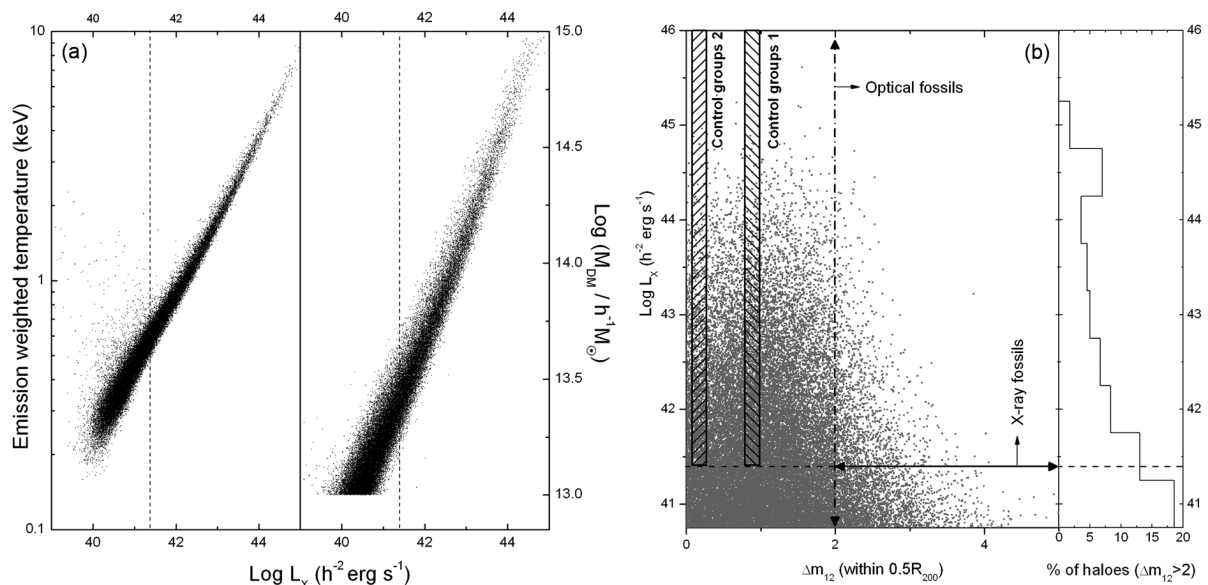


**Figure 1.7:** Fossils in the Millennium and Millennium gas simulations. Panel a): X-ray gas temperature and dark matter halo mass vs. bolometric X-ray luminosity for all haloes in the Millennium gas simulation. The vertical line sets the X-ray limit for fossils  $L_{X,\text{bol}} = 0.25 \times 10^{42} h^{-2}$  erg  $s^{-1}$  corresponding to a temperature of  $T \sim 0.5$  keV. Panel b): X-ray luminosity vs. magnitude gap for all dark matter haloes with gas properties. Horizontal and vertical lines set the thresholds that define fossil groups. The histogram shows the fraction of fossils in each bin of X-ray luminosity. Taken from Dariush et al. (2007).

fossils, in agreement with the work of Jones et al. (2003). Space densities of fossils in the Millennium simulation are also consistent with those estimated by Vikhlinin et al. (1999) and Jones et al. (2003). Fig. 1.8 a shows the history of mass assembly of fossil dark matter haloes in the Millennium simulation from a redshift of  $z = 0.8$  to the present day. The average fraction of halo mass to final halo mass is presented for all fossil haloes as well as two control samples with similar X-ray luminosities (see Fig. 1.7 a). At any given redshift, fossils have assembled a higher fraction of the final halo mass compared to the control samples. In fact, at a redshift of  $z = 0.24$ , corresponding to an expansion factor of 0.8, fossils have already assembled  $\sim 90\%$  of their final mass while the corresponding value for non-fossils goes down to  $\sim 77\%$ . In contrast to fossils, control groups assemble their halo mass even at the present day. This suggests that fossils indeed formed early with most of their halo mass in place at higher redshifts so that bright galaxies had enough time to merge into the central elliptical.

Using self consistent N-body/hydrodynamical simulations based on  $\Lambda$ CDM cosmology, D’Onghia et al. (2005) found a similar result, a clear correlation between the  $\Delta m_{1,2} \geq 2.0$  magnitude gap and the formation time of groups. The earlier a galaxy group is assembled, the larger the magnitude gap at  $z = 0$  (Fig. 1.8 d). Thus, D’Onghia et al. (2005) suggested that fossils have already assembled half of their final dark matter mass at  $z \gtrsim 1$  and subsequently typically grow by minor mergers only. This early mass assembly of fossils leaves sufficient time for  $L^*$  galaxies to be first tidally stripped and finally merge into the central elliptical by dynamical friction, resulting in the exceptional magnitude gap at  $z = 0$  while in non-fossils the final dark matter halo mass is assembled quite recently so that the two largest galaxies in a group do not have time to merge. In fact, the last major merger in one simulated fossil of D’Onghia et al. (2005)

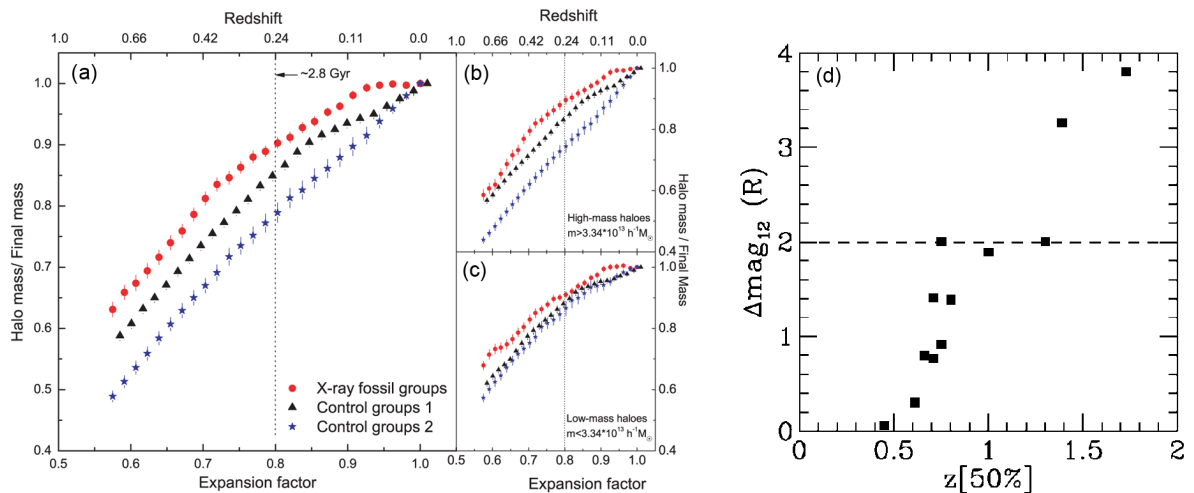


**Figure 1.8:** Panel a): The mass build up of fossil and non-fossil dark matter haloes as a function of redshift and expansion factor in the Millennium run. Panels b) and c): Fossils are separated into low- and high-mass haloes at the median present-day halo mass. All panels indicate the earlier formation of fossils in comparison to non-fossils. All masses are normalized to the mass at  $z = 0$ . Taken from Dariush et al. (2007). Panel d): Correlation between the magnitude gap and the formation time of groups, defined as the redshift where 50% of the system’s final mass has been assembled. The earlier a galaxy group is assembled, the larger the magnitude gap at  $z = 0$ . Taken from D’Onghia et al. (2005).

occurs at  $z = 1.4$ . Finally, these authors state that fossils exist at all only because the infall of  $L^*$  galaxies takes place along filaments with small impact parameters. Fossils should also reside in fairly isolated environments during a time typically longer than the galaxy crossing time in the considered group (Sarazin 1986) preventing the late infall of galaxies which could refill the observed magnitude gap.

Sales et al. (2007) used the Millennium simulation to investigate correlations between the central *primary* galaxies and the surrounding galaxy populations. This study does not restrict itself to fossils only, but studies all primaries where the surrounding satellites are at least 2 magnitudes fainter, not necessarily involving a group sized dark matter halo. They find that red satellites are clearly much more concentrated towards the central galaxy than blue ones (see Fig. 1.9 a). They argue that this is presumably due to the gas loss of satellites once they are accreted. The earlier a satellite was accreted, the older, i.e. redder, its stellar population will be. The simulation also revealed a systematic anisotropy in the spatial distribution of satellites around primaries (Fig. 1.9 b). It has been established that dark matter haloes are triaxial objects, preferentially exhibiting prolate shapes whose angular momentum is perpendicular to the major-axis of the halo (e.g. Hopkins et al. 2005). Simulated satellites show an *anti-Holmberg* effect, being aligned along the plane perpendicular to the angular momentum axis of the halo. Thus, based on this simulation and assuming that the major axis of a primary is aligned with the major axis of the dark matter halo, an alignment of satellites with the major axis of the central galaxy in fossils would be expected.

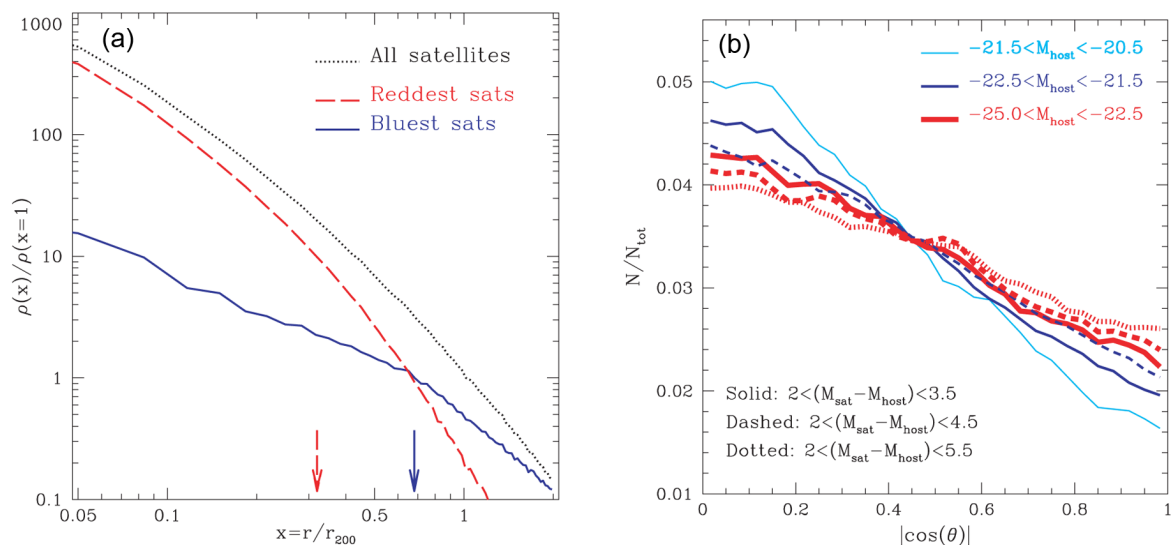


**Figure 1.9:** Panel a): Number density profiles of red and blue satellites around bright, *primary* galaxies in the Millennium simulation. Red satellites are much more concentrated than blue ones. Arrows indicate the radius enclosing half of the satellites in each subsample. Panel b): Anisotropy of the satellite spatial distribution. The fraction of galaxies at different polar angles  $|\cos(\Theta)|$ , measured from the angular momentum axis of the host halo, is shown. An isotropic spatial distribution of satellites would appear as horizontal line. Satellites show an *anti-Holmberg* effect, i.e. they tend to populate the plane perpendicular to the angular momentum axis of the host halo. Taken from Sales et al. (2007).

## 5 Characteristics of elliptical galaxy formation

When studying the origin and evolution of fossils, the structural properties and stellar populations of the central ellipticals offer valuable information for this challenging task since the whole merger history of the progenitor group is expected to be contained in this central remnant. If the central ellipticals in fossils have undergone a systematically different evolution compared to non-fossil ellipticals such as BCGs in clusters, then this difference should also be reflected in the overall characteristics of these galaxies. It is now widely known that the structural parameters of ellipticals, i.e. the luminosity  $L$ , effective radius  $r_e$ , effective surface brightness  $\mu_e$ , colour, line strength indices, and central velocity dispersion  $\sigma_0$  are not randomly distributed in the parameter space, but follow certain relations, crucial to constrain theories on elliptical galaxy formation. Thus, any theoretical formation scenario for ellipticals has to reproduce these parameter correlations to understand the origin and evolution of these galaxies.

### 1 The fundamental plane

Observations have shown that ellipticals fall on a so-called *fundamental plane* (FP), a tight correlation between effective radius  $r_e$ , central velocity dispersion  $\sigma_0$ , and the average effective surface brightness within  $r_e$ ,  $\langle I_e \rangle$

$$r_e \propto \sigma_0^A \langle I_e \rangle^B \quad (1.6)$$

with varying values of  $A$  and  $B$  by different authors (Bernardi et al. 2003b). Since this fundamental plane spans about three orders of magnitude in luminosity, exhibiting very low residual scatter and little variation with environment, it suggests a uniform formation process of ellipticals. A similar relation to the observed one can indeed be reconstructed by means of the virial theorem which implies values of  $A = 2$  and  $B = -1$  and a constant mass-to-light ratio along the plane. However, observed values of  $A = 1.49$  and  $B = -0.75$  from a sample of 9000 SDSS early-type galaxies by Bernardi et al. (2003b) indicate a tilted plane that deviates from the virial prediction. The observed inclination can still be interpreted by the theorem if the mass-to-light ratio scales systematically with mass ( $M/L \propto M^\gamma$ ) along the plane. This dependence has been interpreted as differences in the stellar populations or the dark matter content.

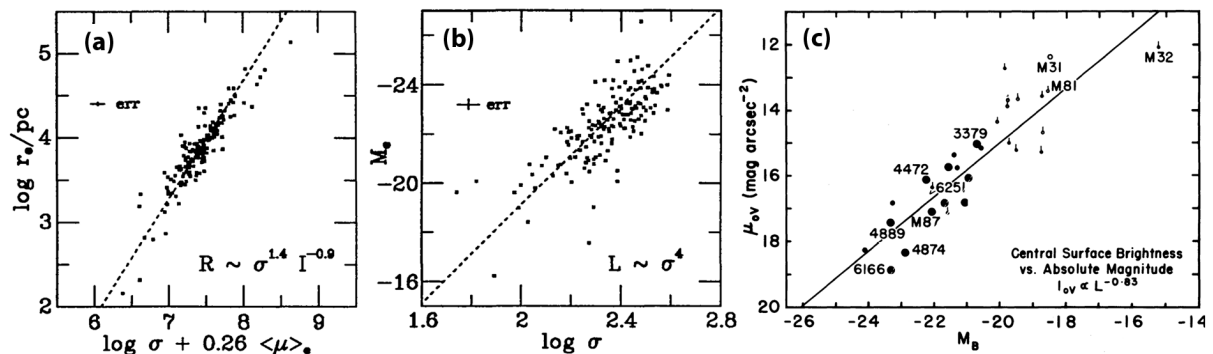


**Figure 1.10:** The fundamental plane of elliptical galaxies and its projections. Panel a): The plane seen edge on. Panel b): Projection onto the  $L - \sigma$  plane resulting in the Faber-Jackson relation  $L \propto \sigma^4$ . Both taken from Kormendy & Djorgovski (1989). Panel c): Projection onto the  $L - \mu_e$  plane resulting in the Kormendy relation. Adapted from Kormendy (1985).

Before the discovery of the FP, corresponding relations involving only two of the three plane parameters had been observed. In fact, the projection of the FP onto the  $L - \sigma$  plane results in the Faber & Jackson (1976) relation  $L \propto \sigma^4$  or  $M \propto -0.1 \log \sigma + \text{const.}$ , while its projection onto the  $L - \mu_e$  plane produces the Kormendy (1977) relation, i.e. the decrease of effective surface brightness with increasing luminosity. Figure 1.10 illustrates the FP and its projections.

## 2 The colour-magnitude, colour- $\sigma$ and $\text{Mg}_2$ - $\sigma$ relations

Besides the fundamental plane, ellipticals also follow a tight colour-magnitude relation (CMR) which was first recognized by Baum (1959) and later confirmed by Sandage & Visvanathan (1978a,b), who claimed that the tightness of the relation implies very uniform stellar populations of these galaxies. The relation is often interpreted as a sequence of increasing metallicity with increasing luminosity (Kodama, Bower & Bell 1999). Considering the CMR and Faber-Jackson relations, it is not surprising that ellipticals also fall on a colour- $\sigma$  relation. Its small intrinsic scatter in colour was interpreted as an age dispersion by Bower, Lucey & Ellis (1992) and was used to set tight age constraints on the corresponding galaxy formation epochs. The slopes of both relations, on the other hand, can set constraints on the amount of merging that led to the galaxies observed today since merging increases luminosity and  $\sigma$ , but leaves colour unchanged, hence broadening and flattening the observed relations. Another widely studied relation involves the absorption index  $\text{Mg}_2$  which was found to increase with increasing velocity dispersion, highlighting that more massive ellipticals have more heavy elements. A disadvantage in all of these relations is the lack of knowledge on what drives them; age or metallicity.

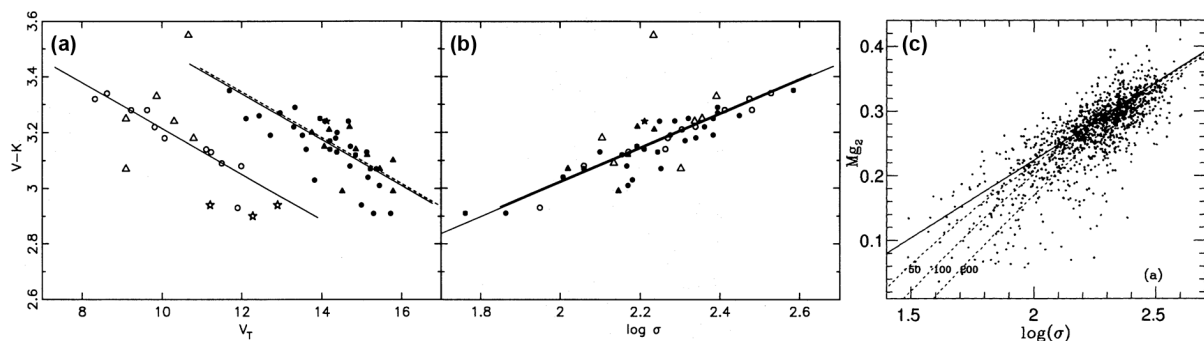


**Figure 1.11:** The colour-magnitude, colour- $\sigma$  and  $\text{Mg}_2$ - $\sigma$  relations. Panels a) and b): Brighter ellipticals are redder and exhibit a higher central velocity dispersion. Open symbols indicate early-type galaxies in the Virgo cluster, filled ones are early-type galaxies in the Coma cluster. Adapted from Bower, Lucey & Ellis (1992). Panel c): Ellipticals with a higher central velocity dispersion show a stronger  $\text{Mg}_2$  index. Taken from Chiappini et al. (2002).

## 3 The age-metallicity degeneracy

A reliable determination of ages and metallicities in ellipticals is difficult however, since both quantities alter the overall spectra and colours of these galaxies in a similar way. In particular, an age change of +30% has nearly the same effect on isochrones and spectra as a metallicity change of +20% (see Fig. 1.12), or in other words an age change of +30% is canceled by a simultaneous metallicity change of -20%. This is widely known as the age-metallicity degeneracy, or 3/2 degeneracy (Worthey 1999).

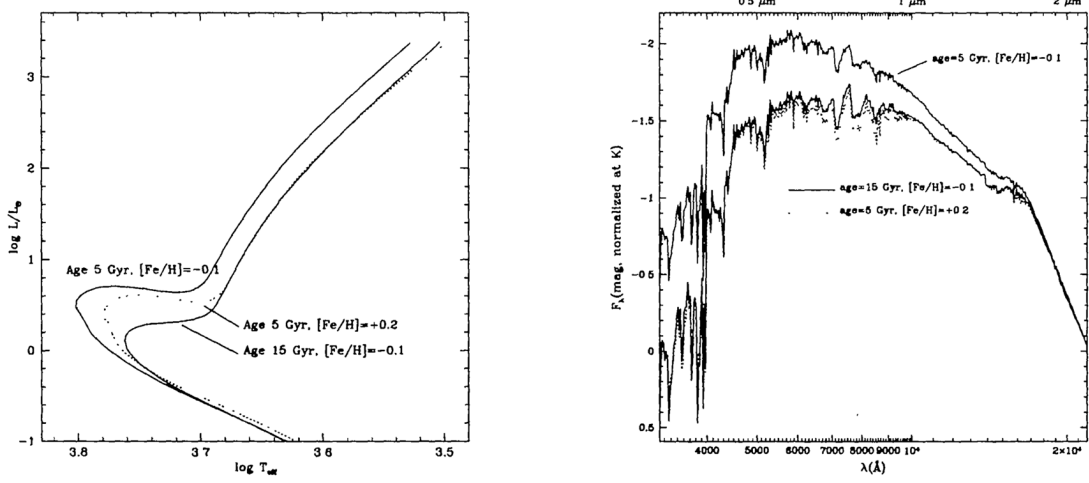


**Figure 1.12:** The age-metallicity degeneracy. Isochrones of 3 times the age or twice the metallicity have nearly identical spectra, making it impossible to measure both quantities from overall galaxy spectra or colours alone. Taken from Worthey (1999).

However, it was early realized that individual spectral features are more sensitive to age than to metallicity, indicating a possible method to break the degeneracy if such features are properly calibrated. For that purpose, Burstein et al. (1984) defined a set of 11 spectral indices comprised of molecular band and atomic line features observed with the image dissector scanner (IDS) at Lick observatory. Since then, additional indices have been added to this Lick/IDS system (Worthey et al. 1994; Worthey & Ottaviani 1997) resulting in a total of 25 features. Based on this set of well-defined spectral indices, it was possible to construct empirical polynomial fitting functions for these features as a function of stellar temperature, gravity, and metallicity (Gorgas et al. 1993). Thus, it became feasible to predict absorption-line strengths for whole single stellar populations (SSPs) of a given age and metallicity (Worthey et al. 1994) that can be compared with the observed values. Based on these models, a plot of an age sensitive Balmer index versus a metal sensitive iron line yields a two-dimensional theoretical grid, allowing to determine SSP equivalent ages and metallicities of the investigated old stellar population (Fig. 1.13).

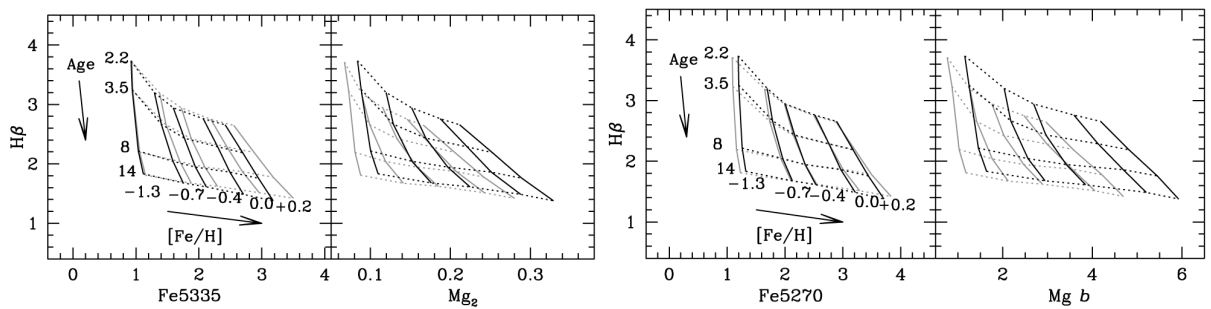


**Figure 1.13:** SSP model grids for Lick/IDS indices. While the Balmer index  $H\beta$  is basically age sensitive, iron line indices such as  $\text{Fe}5270$  or  $\text{Fe}5335$  are good metallicity indicators. Grey lines represent solar-scaled models while black ones indicate  $\alpha$ -enhanced ones. In contrast to  $H\beta$ ,  $\text{Fe}5270$  and  $\text{Fe}5335$ ,  $\text{Mg}_2$  and  $\text{Mg } b$  are strongly dependent on  $\alpha$ -enhancement, as expected. Taken from Schiavon (2007).

It is known, however, that nonsolar abundance ratios, i.e. the enhancement of  $\alpha$ -elements such as Mg relative to Fe, can severely alter these models. In fact, Trager (1997) showed that metallicities obtained from Mg were indeed higher than those derived from Fe. Current models implement  $\alpha$ -enhancement to correct for these inconsistencies. Instead of measuring only specific features in the spectrum of an old stellar population, full spectrum fitting techniques comparing synthetic SSP models with an observed galaxy spectrum pixel by pixel provide another approach to disentangle the degeneracy. In the present work, in addition to the measurement of Lick indices for a sample of fossil central ellipticals, the full spectrum fitting package ULYSS has been used (see chapter 3 for a detailed description).

#### 4 Metallicity, abundance, and age gradients in ellipticals

In addition to the global stellar population characteristics of ellipticals, the structure within these galaxies can provide further constraints on their formation process. For example, in the classical monolithic formation scenario, ellipticals form in a dissipative collapse (Larson 1974) where stars preserve their orbits and do not mix. In this picture, the metal-enriched gas ejected by the stars flows to the galaxy centre, leading to a higher central metallicity compared to the galaxy outskirts, thus predicting negative radial metallicity gradients. Indeed, such negative metallicity gradients are a common feature in ellipticals (Davies et al. 1993). Focusing on the competing hierarchical clustering scenario where bigger galaxies arise from the merger of smaller dark matter halos, it was suggested that metallicity gradients are flattened and erased due to the mixing of the stellar populations during the merger (White 1980). Mihos & Hernquist (1994) modelled the merger of disk galaxies and concluded that pure stellar disks do not reproduce the power-law gradients observed in ellipticals unless the effects of a metal-rich starburst population are included. Instead of focusing on gas-rich, *wet* disk mergers, Di Matteo et al. (2009) investigated the shape of resulting metallicity gradients in gas-free or *dry* mergers.

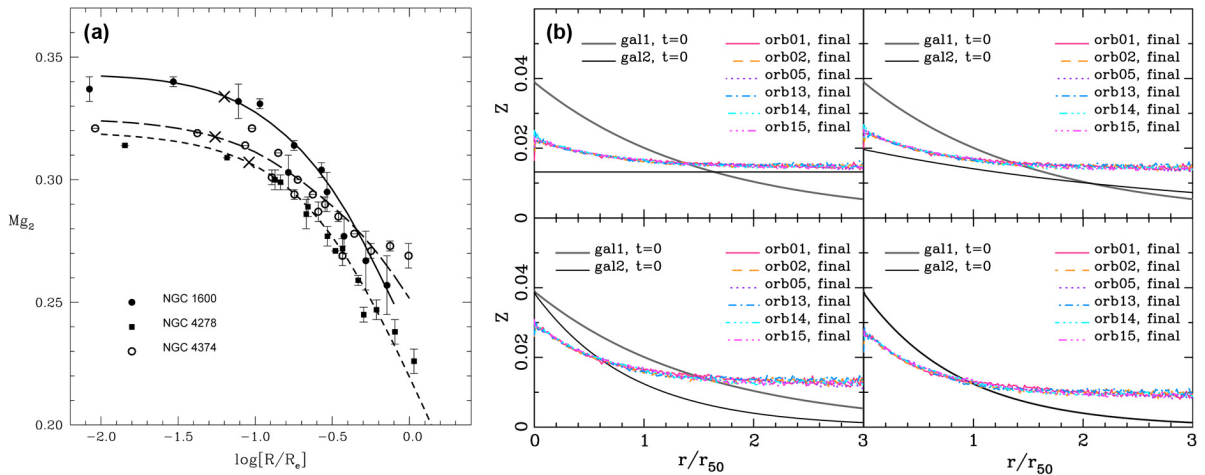


**Figure 1.14:** Metallicity gradients in ellipticals. Panel a):  $Mg_2$  gradients in three ellipticals observed by Davies et al. 1993. Theoretical models from Angeletti & Giannone (2003) (lines) confirm these trends. Taken from Angeletti & Giannone (2003). Panel b): Evolution of metallicity gradients in major dry mergers. The steepness of the metallicity gradient in the merger remnant depends strongly on the gradients of the two progenitor galaxies (black lines). Adapted from Di Matteo et al. (2009).



The simulations revealed that the slope of the resulting gradient depends strongly on those of the progenitor galaxies (see Fig. 1.14 b). In particular, when considering two galaxies with the same profile, the resulting gradient flattens due to the mixing of stars in the systems. However, the initial gradient can also be preserved or even increased by the merger if the slope of the companion galaxy is sufficiently steep. While strongly dependent on the progenitor gradients, the remnant slope is not very sensitive to the orbits of the interacting galaxies.

Observations have also revealed that metallicity gradients are generally steeper in more massive galaxies, but with an increasing dispersion (Ogando et al. 2005). This is in good agreement with the dissipative collapse model since more massive galaxies retain the metal-enriched gas ejected by stars and supernovae much easier than less-massive ones. However, this relation can also be interpreted in the presented picture of dry mergers. As the elliptical increases its mass over time, its gradient continuously decreases if the companion slope is not steep enough until the gradient becomes so shallow that it will finally merge with a sufficiently steep one to eventually increase the final gradient. Since multiple mergers with different gradient slopes should be involved in this scenario, the dispersion of observed metallicity gradients in the most massive ellipticals should be the largest, consistent with what is observed.

Besides metallicity gradients, abundance gradients of  $\alpha$ -elements may also provide useful information regarding the formation of ellipticals. Since the abundance of  $\alpha$ -elements is often interpreted as an indicator of star formation timescale, a positive  $[\alpha/\text{Fe}]$  gradient would suggest an outside-in formation, while a negative one the opposite. The dissipative collapse model implies an inside-out formation where the central galaxy regions form first, thus predicting a negative  $[\alpha/\text{Fe}]$  gradient (Ferreras & Silk 2002). Recent observations have shown that the  $[\alpha/\text{Fe}]$  gradient slope in ellipticals is either negative or positive with a mean value close to zero, indicating no correlation with other galactic properties (Annibali et al. 2007). These results suggest that there is no preferred scenario for the formation of ellipticals, either outside-in or inside-out.

Finally, age gradients can provide further insights on these studies because if ellipticals indeed only formed by dissipative collapse, a uniform old stellar population would be expected. It has also been found that age gradients likely correlate with the central age, implying that a young burst of star formation is confined to the inner galaxy regions, producing a steep positive gradient (Reda et al. 2007). On the other hand, negative age gradients, i.e. older stars inside, younger ones outside, could be interpreted by late gas accretion or the merger of a gas-rich satellite (Kobayashi 2004).

## 6 Outline

As the subtitle of this thesis already suggests, the present work is based on archival data from the SDSS, visitor-mode observations at the WHT, and service-mode observations at the VLT to study fossils in the optical. More precisely, the SDSS has been queried to identify new, previously unpublished fossil candidates to extend the present inventory of fossils. Since the stellar population of the central elliptical in fossils is supposed to contain the merger history of the whole group, long-slit spectroscopy at the WHT has been carried out in visitor-mode for six fossil central ellipticals. Finally, focusing on the surrounding, faint galaxy population of fossils, MOS spectroscopy with VIMOS has been carried out in service-mode at the VLT for one fossil candidate.

The structure of this manuscript has been organized according to these individual studies, each of the three upcoming chapters focusing on one of the presented approaches.

### Chapter 2

highlights the query carried out on the SDSS to identify new fossil candidates. The applied SQL code and all selection criteria considered in the search are explained. SDSS archive data are used to study the surface brightness profiles of the six fossil central ellipticals observed with the WHT and the properties of their surrounding galaxy populations.

### Chapter 3

focuses on the spectroscopic observations of the six fossil central ellipticals at the William Herschel Telescope. The detailed preparation of an observing run in visitor mode as well as the subsequent reduction of the obtained datasets is presented. Furthermore, the derivation of SSP ages and metallicities by means of Lick indices and a full spectrum fitting technique within the software package ULYSS is discussed. In addition, kinematics of the studied ellipticals are analyzed. The resulting SSP ages and metallicities are presented at the end of the chapter for the galaxies as a whole and spatially resolved along the spectrograph slit.

### Chapter 4

outlines the service mode observations of the fossil candidate RX J1548.9+0851 at the VLT. A detailed guide, from the acceptance of an ESO proposal (Phase 1) to the preparation of all necessary observing blocks for both pre-imaging and multi-object spectroscopy (Phase 2), is presented. The resulting VIMOS pipeline products and the measurement of galaxy radial velocities to determine group memberships are explained. Further data analysis focuses on the luminosity function of the system, SSP ages and metallicities of members, their spatial distribution, and group dynamics. In addition, the photometric fine structure of the central elliptical is analyzed.

### Chapter 5

summarizes and discusses all results.

### Appendices A + B

present publications related to this work and illustrate the night conditions of both visitor and service mode observations.

# Chapter 2

## New fossil candidates in the SDSS

To extend the sample of known fossils, a query in the SDSS DR5 was carried out. The wealth of information in the database can be queried by means of **Structured Query Language**, a well-known computer language designed for managing data in relational database management systems which allows us to undertake complex scans involving several variables. This chapter highlights the structure of the performed query and focuses on all the constraints considered to shortlist the enormous number of objects in the database to the presented list of new fossil candidates. Optical and X-ray properties of the resulting sample are summarized and the differences to the query carried out by Santos et al. (2007) are discussed. Finally, SDSS data of the fossil candidates selected for the follow-up observations at the WHT and the VLT from both Santos et al. (2007) and the present work are presented in more detail. The newly found fossil candidates have been published in Eigenthaler & Zeilinger (2009), see Appendix A.

### 1 The SDSS Sky Server

The data collected and processed by the SDSS are organized in data releases and stored systematically in the SDSS Sky Server <sup>1</sup>, easily accessible for anyone interested in astronomy. Several tools to view and download the datasets of interest are provided for that purpose.

#### 1 Tables and functions

All data in the sky server are arranged in *Tables* of columns and rows, which can moreover be subdivided into special subsets called *Views*. To get an overview on all available SDSS tables as well as their individual data entries, SDSS provides a Schema Browser<sup>2</sup>. It lists a total number of 95 tables containing amongst others the name of the data entry, data type and unit, as well as a short description of each data entry. When preparing an SQL query on the SDSS it is therefore necessary to check in which table and under which name the intended information is

---

<sup>1</sup><http://cas.sdss.org/dr7/>

<sup>2</sup><http://cas.sdss.org/dr7/en/help/browser/browser.asp>

stored to properly access the corresponding data. For the present work, the `photoobj`, `specobj`, `rosat`, and `photoz` tables have been queried<sup>3</sup> (see Table 2.1).

**Table 2.1:** SDSS tables queried in the present work.

table	description
<code>photoobj</code>	contains all photometric attributes of photometric targets.
<code>specobj</code>	contains all spectroscopic attributes of spectroscopic targets.
<code>rosat</code>	contains ROSAT data entries of all ROSAT sources that are correlated with SDSS objects.
<code>photoz</code>	contains photometric redshifts as well as absolute magnitudes and K corrections for all objects in the <code>photoobj</code> table.

In addition to tables, SDSS also provides a list of numerous functions executing a predefined sequence of commands for a special scientific problem. Their names are prefixed by `f` to be easily identified. The schema browser lists a total number of 224 SDSS functions. In the present work, only one function, `fGetNearbyObjEq` has been used (see Sect. 3).

## 2 How to query?

To access the intended datasets, search tools of different handling difficulty are provided for querying the SkyServer<sup>4</sup>. Basic radial or rectangular search tools allow to query for objects within user-defined magnitude limits around specified equatorial coordinates. More advanced to these tools, the SkyServer *Search Form* allows to specify colours, restrict to objects with spectroscopic data, and distinguish between stars, galaxies or quasars. All these routines follow a rather simple approach and don't permit more complex queries involving multiple tables or functions. This is only achieved by programming the appropriate SQL code for each scientific problem. Though there are a thousand ways to program various SQL queries, the logical structure is always the same and restricted to only a few keywords. Listing 2.1 illustrates the basic structure of an SQL query. In principle one simply has to specify the intended data entries, their associated tables or views, and the logical conditions to constrain the available information.

**Listing 2.1:** The typical structure of an SQL query in the SDSS.

```

1 SELECT p.objid           specify data entries
2 FROM photoobj p         from the corresponding tables and views
3
4 WHERE p.r < 17
5 AND   p.g - p.r > 1
6      :
7      :                   define logical conditions to constrain the dataset
8 AND   p.dec > 20

```

<sup>3</sup>`photoobj` and `specobj` are actually views and thus subsets of the more general `PhotoObjAll` and `SpecObjAll` tables. For simplicity these views are considered as tables here.

<sup>4</sup><http://cas.sdss.org/dr7/en/tools/search/>

## 2 What to look for?

When planning a query in a database covering 357 million unique objects<sup>5</sup>, one has to think of how to constrain this enormous amount of information to yield the actual scientific data suitable for the corresponding problem. In the present work, the search for new fossil candidates is considered. Thus, the query has to be based on the physical characteristics of this rare class of objects. Since the dominating galaxy in a fossil is thought to be a luminous elliptical, the first constraint on all possible sources in the database is to focus only on intrinsically bright ellipticals with measured redshifts. Since a prototypical fossil group is surrounded by an X-ray halo comparable to that of ordinary poor groups, it is also obvious to check whether these ellipticals are associated with an extended X-ray source to further shortlist the sample. Finally, to avoid the contamination by regular groups and clusters, the  $2^{\text{mag}}$  criterion as proposed by Jones et al. (2003) has to be considered. It is evident that such a query will not result in a list of bona fide fossils such as NGC 1132, since only survey data instead of detailed pointed observations are taken into account. For a more specific classification, every object in the resulting sample would have to be observed individually in both the optical and X-rays. Thus, the objects shortlisted in the performed query are considered as new fossil candidates rather than new fossils.

## 3 The query

Taking into account these physical characteristics, the corresponding data entries fulfilling these criteria have to be extracted from the database. Thus, one has to translate these physical constraints into logical SQL conditions. The following paragraphs outline this procedure.

### 1 The central elliptical

Focusing on intrinsically bright ellipticals, a first shortlisting of possible sources was carried out by taking only red ( $g' - r' > 0.8$ ), luminous ( $M_{r'} \leq -21 + 5 \log h$ ) objects, spectroscopically classified as galaxies, into account. The lower limit in absolute  $r'$  band magnitudes is based on the work of Vikhlinin et al. (1999), who stated that fossils host nearly all field E galaxies brighter than  $M_R - 22.5$  ( $h = 0.5$ )<sup>6</sup>. The lower limit in colour was chosen according to the location of the SDSS galaxy red sequence as shown in Fig. 2.1. The diagram demonstrates that these adopted constraints restrict the galaxies in the database to the bright end of the SDSS galaxy red sequence. Only galaxies up to a maximum redshift of  $z = 0.5$  have been considered. This upper limit in redshift space was selected on the basis of the most distant fossil known to date ( $z = 0.59$ ; Ulmer et al. 2005). More distant objects become increasingly difficult to investigate because of their faintness and small angular size. To estimate absolute magnitudes and projected linear extents at different redshifts, luminosity distances  $D_L$  as well as angular diameter distances  $D_A$  have been calculated by means of the *Cosmology Calculator*<sup>7</sup> (Wright 2006) assuming the  $\Lambda$ CDM concordance model ( $\Omega_m = 0.3$ ,  $\Omega_\Lambda = 0.7$ ,  $H_0 = 70 \text{ km s}^{-1}$ ).

<sup>5</sup>SDSS DR7 total imaging catalog.

<sup>6</sup>Assuming  $h = 0.5$ ,  $M_{r'} = -21 + 5 \log h$  corresponds to  $\sim -22.5$ .

<sup>7</sup><http://www.astro.ucla.edu/~wright/CosmoCalc.html>

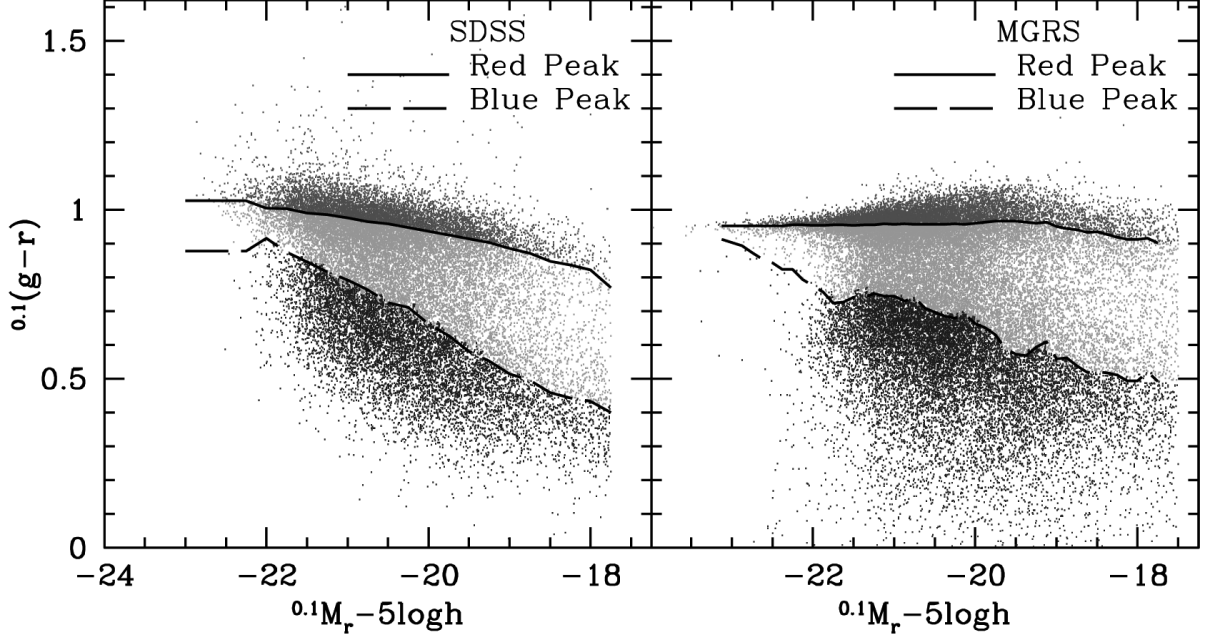


**Figure 2.1:** The bimodality of galaxy colors in the SDSS and in a mock galaxy redshift survey (MGRS) constructed from the Millennium semianalytical galaxy sample. Galaxies are clearly separated into blue and red sequences. The dotted and dashed lines indicate the centers of Gaussians used to describe the color distributions at a given luminosity bin. The query constraints presented in this work restrict the SDSS galaxies to the bright end of the red sequence. Taken from Wang et al. (2008).

Both distances are related via  $D_L(z) = (1+z)^2 D_A(z)$  and compared in Fig. 2.2(a) to illustrate the necessity to distinguish between these individual distance definitions when dealing with redshifts up to  $z = 0.5$ <sup>8</sup>. Fig. 2.2(b) shows the corresponding scale with increasing redshift. To ensure the lower limit in absolute magnitude, corresponding apparent magnitude limits were derived via the luminosity distances  $D_L(z)$  based on the SDSS spectroscopic redshifts of the central ellipticals

$$m < M + 25 + 5 \log \left[ \frac{D_L(z)}{h^{-1} \text{Mpc}} \right] + A + K(z) \quad (2.1)$$

accounting for Galactic extinction  $A$  and  $K$  correction too. Galactic extinction was taken from the `extinction_r` entry in the SDSS `photoobj` table. Concerning  $K$  corrections, the `kcorr_r` entry in the SDSS `photoz` table was not directly used in the query since these values are based on photometric redshifts which can strongly deviate from true redshifts and would mislead to wrong results. Therefore  $K(z)$  was estimated based on SDSS galaxies with  $g' - r' > 0.8$  that differ by at most 0.005 between photometric and spectroscopic redshifts ( $|z - z_{\text{phot}}| \leq 0.005$ ). Using this sample, average  $K$  corrections and one- $\sigma$  confidence intervals were calculated for redshift bins of 0.01 (see Listing 2.2). The final  $K$  values were then fit by a third order polynomial to get a reliable estimate of  $K$  corrections at every individual redshift. Fig. 2.2(c) shows the average  $K$  values for all redshift bins together with the polynomial fit.

<sup>8</sup>At a redshift of  $z = 0.5$ ,  $D_L/D_A$  amounts already to 2.25.

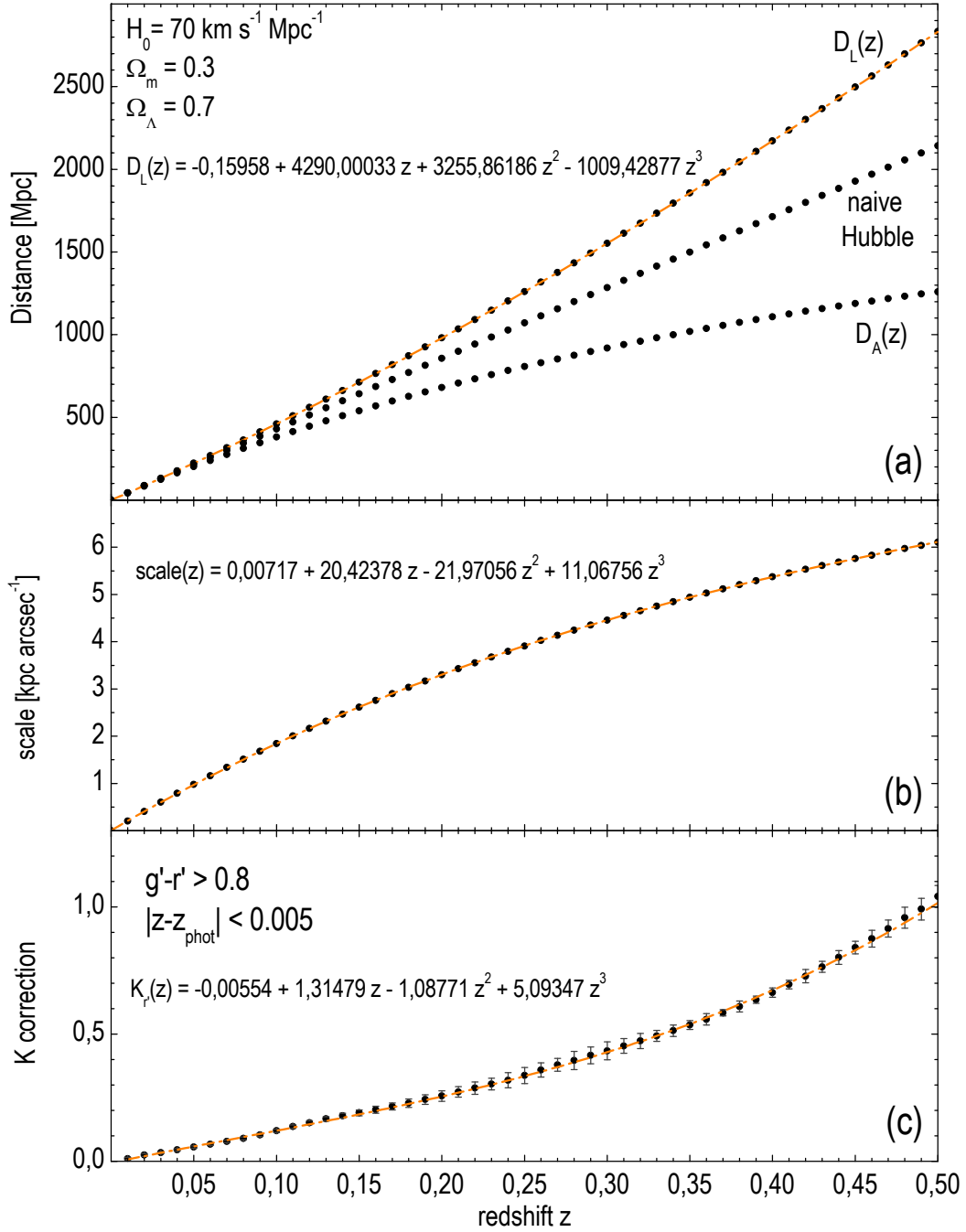


**Figure 2.2:** Cosmological distances, scales and  $K$  corrections with increasing redshift as determined from the SDSS and used for the present work. The dashed lines indicate third order polynomial fits. The divergence of  $D_L(z)$  and  $D_A(z)$  at higher redshifts indicates the necessity to distinguish between these two quantities.

**Listing 2.2:** Evaluating  $K$ -corrections in the SDSS.

```

1 SELECT count(*), AVG(pz.kcorr_r), STDEV(pz.kcorr_r)
2 FROM photoz pz, specobj s, photoobj p
3 WHERE pz.objid = s.bestobjid
4 AND s.bestobjid = p.objid
5 AND s.specclass = 2
6 AND s.z BETWEEN z1 AND z2
7 AND ABS(pz.z - s.z) < 0.005
8 AND p.g-p.r > 0.8

```

**Notes:** Estimating  $K$  corrections based on SDSS galaxies fulfilling  $(|z - z_{\text{phot}}| \leq 0.005)$  for redshift bins of  $\Delta z = z_2 - z_1 = 0.01$ .

**Listing 2.3:** Cross-correlating bright, red galaxies and extended ROSAT X-ray sources within the SDSS DR5.

```

1 SELECT p.objid, p.ra, p.dec, p.r, p.g-p.r, p.extinction_r, s.z, r.delta, r.extent, r.cps, r.cpserr, r.poserr
2 FROM specobj s, photoobj p, rosat r
3 WHERE s.bestobjid = p.objid
4 AND s.specclass = 2
5 AND s.z BETWEEN 0.0 AND 0.50
6 AND p.r <
7 - 21.0
8 + 25 + 5*LOG10 (( -0.15958 + 4290.00033 *s.z + 3255.86186 *s.z*s.z - 1009.42877 *s.z*s.z*s.z)*0.7)
9 - 0.00554 + 1.31479 *s.z - 1.08771 *s.z*s.z + 5.09347 *s.z*s.z*s.z
10 + p.extinction_r
11 AND p.g - p.r > 0.8
12 AND r.delta = 100/(0.00717 + 20.42378 *s.z - 21.97056 *s.z*s.z + 11.06756 *s.z*s.z*s.z) + r.poserr
13 AND r.extent >= 1

```

**Notes:** The query mainly follows equation 2.1 and makes use of the third order polynomials shown in Fig. 2.2



**Listing 2.4:** Validating the  $2^{\text{mag}}$  criterion.

```

1 SELECT count(*) - 1
2 FROM photoObj p, dbo.fGetNearbyObjEq(ra, dec, radius) n
3 WHERE p.objID = n.objID
4 AND p.type = 3
5 AND p.r -  $m_1$  < 2.0

```

**Notes:** For every object in the sample, equatorial coordinates ( $ra$ ,  $dec$ ) in decimal degrees, half the virial  $radius$  in arcminutes and the magnitude of the central galaxy  $m_1$  have to be specified in this query. To avoid counting the central galaxy itself, the resulting number is diminished by 1.

An obvious idea that one might consider is to adopt the absolute magnitude directly from the corresponding SDSS `photoz` entry for every individual galaxy instead of calculating it separately via equation 2.1. Similar to  $K$  corrections, this would lead to systematic errors for a large number of galaxies since the derivation of absolute magnitudes in the SDSS is also based on the inaccurate photometric redshift measurements. In fact, the fraction of galaxies in one redshift bin fulfilling  $|z - z_{\text{phot}}| \leq 0.005$ , compared to all galaxies with spectroscopic redshifts amounts roughly to  $\sim 20\%$ .

## 2 The associated X-ray source

Only galaxies with an entry in the SDSS ROSAT table were considered for the further shortlisting. Since the query aims to identify the spatially extended X-ray halo surrounding the central elliptical, the associated X-ray component had to be extended with a ROSAT extent parameter of at least one arcsecond. This value does not reflect the true extent of the X-ray source but gives merely the excess of the source over the ROSAT point-spread-function (PSF). The ROSAT PSF is highly dependent on the location of the source on the detector. While the FWHM of the PSF is minimal at the detector center, it strongly increases towards the detector edges. Therefore objects with a low extent parameter also represent possible fossil candidates due to the uncertainty of the source location on the detector. Also considering the ROSAT position error, the distance of the source to the central elliptical had to be less than 100 kpc<sup>9</sup>.

Listing 2.3 presents the final SQL code executed in the SDSS DR5 to cross-correlate bright, red galaxies with extended ROSAT X-ray sources. The query mainly follows equation 2.1 and makes use of the third order polynomials shown in Fig. 2.2.

## 3 The $2^{\text{mag}}$ criterion

To complete the shortlisting, the  $2^{\text{mag}}$  criterion, forcing all systems to have no galaxies with  $\Delta m_{1,2} \geq 2.0$  mag in the SDSS  $r'$  band within one-half virial radius, was applied. In contrast to the work of Santos et al. (2007), who use a constant value of  $0.5h^{-1}$  Mpc for half the virial radius, the description of Evrard et al. (1996)

$$r_{\text{vir}} = 1.945 \cdot \left( \frac{T}{10\text{keV}} \right)^{1/2} (1+z)^{-3/2} \cdot h^{-1}\text{Mpc} \quad (2.2)$$

<sup>9</sup>derived for individual redshifts by means of the spatial scale given in Fig. 2.2(b)

as used by Jones et al. (2003) was applied here<sup>10</sup>. Since the gas temperature of the fossil candidates is not known, a lower limit of 0.7 keV was assumed for all aggregates. This value was based on the relation between X-ray gas temperatures and bolometric X-ray luminosities from the Millennium gas simulation as shown in Fig. 1.7. Considering this relation, a value of 0.7 keV corresponds to about  $L_{X,\text{bol}} = 10^{42} h^{-2} \text{ erg s}^{-1}$ , the X-ray limit of fossils as proposed by Jones et al. (2003). This value seems reasonable since the lowest X-ray gas temperature of the 15 fossil aggregates listed by Mendes de Oliveira et al. (2006) shows a similar value (NGC 6482; Khosroshahi et al. 2004).

The  $2^{\text{mag}}$  criterion was incorporated by means of the SDSS SQL function `fGetNearbyObjEq`. This function lists all objects within a given radius in arcminutes around an equatorial point. A query was defined to count all surrounding galaxies within one-half virial radius brighter than  $m_1 - 2^{\text{mag}}$  in a single aggregate (see Listing 2.4). If the result of this query yielded a value of zero, the corresponding system was considered as a fossil candidate. This procedure was carried out for all objects in the remaining sample.

## 4 Morphology

The leftover systems were checked for morphology. Five central galaxies were identified as spirals while three objects have been found in the vicinity of bright stars ruling out the possibility to properly quantify these objects. These systems have been excluded from the sample leaving a final list of 34 previously nondetected fossil candidates.

## 4 New fossil candidates

Table 2.2 lists equatorial coordinates as well as SDSS and ROSAT identifications of the final sample while Table 2.3 presents basic data on the central ellipticals and the associated ROSAT X-ray component. Absolute magnitudes were calculated via

$$M = m - 25 - 5 \log \left[ \frac{D_L(z)}{h^{-1} \text{Mpc}} \right] - A - K(z) + 5 \log h \quad (2.3)$$

To quantify the prominence of the associated X-ray source, the ratio of ROSAT extent and  $\Delta$  parameters was calculated for all fossil candidates. A higher value of this characteristic number indicates a more extended X-ray source closer to the central elliptical compared to lower values. X-ray luminosities were derived from the corresponding ROSAT count rates by converting these data to X-ray fluxes in the energy range 0.5–2 keV via the tool PIMMS (Mukai, 1993) assuming a Raymond-Smith model with 2 keV and a metallicity of  $Z = 0.4 Z_{\odot}$ <sup>11</sup>. Extinction-free fluxes were determined by considering HI column densities of the Leiden/Argentine/Bonn (LAB) Survey of Galactic HI (Kalberla et al., 2005). These fluxes were subsequently converted to luminosities by means of

<sup>10</sup>Radii in kpc were converted to arcmin with the angular scale presented in Fig. 2.2(b)

<sup>11</sup>This assumption is not consistent with the lower limit of 0.7 keV used to detect the listed fossils. However, since the X-ray luminosity does not strongly depend on the estimated gas temperature and to compare the present data with the work of Santos et al. (2007), a value of 2 keV was chosen.

$$L_X[\text{ergs s}^{-1}] = 4r^2\pi \cdot f_X[\text{ergs s}^{-1}\text{cm}^{-2}] \quad (2.4)$$

with  $r$  denoting the luminosity distance in cm. Figure 2.3 shows SDSS images of the whole sample. The frames display a field of view of  $4 \times 4$  arcmin and are listed with increasing redshift. The dominance of the central elliptical is evident in all systems as expected from the  $2^{\text{mag}}$  criterion. The charts also illustrate the difficulty of observing fossils at higher redshifts due to the small angular extents and faint magnitudes present.

**Table 2.2:** Fossil candidates – ROSAT and SDSS identifications.

ID	ROSAT source	SDSS $\alpha_{2000}^a$	SDSS $\delta_{2000}^b$	SDSS objid
01.....	RXJ0159.8–0850	01 59 49.3	–08 49 58.8	587727884161581256
02.....	RXJ0725.7+3741	07 25 41.3	+37 40 27.7	587737826206482926
03.....	RXJ0730.3+3728	07 30 20.4	+37 27 40.8	587725775602450780
04.....	RXJ0801.0+3603	08 00 56.8	+36 03 23.6	587728905564258619
05.....	RXJ0825.9+0415	08 25 57.8	+04 14 48.3	587732702851170810
06.....	RXJ0826.9+3108	08 26 57.6	+31 08 04.9	587732469849325635
07.....	RXJ0909.9+3106	09 09 53.3	+31 06 03.2	588016878295318532
08.....	RXJ1005.8+1058	10 05 50.7	+10 58 11.7	587734949665243313
09.....	RXJ1006.1+0710	10 06 08.3	+07 10 29.5	587732579379904650
10.....	RXJ1030.5+1416	10 30 34.8	+14 15 41.8	587735349637349534
11.....	RXJ1041.8+5303	10 41 47.6	+53 03 41.4	587733081343656013
12.....	RXJ1055.1+4246	10 55 06.6	+42 45 24.4	588017626148634721
13.....	RXJ1056.1+0252	10 56 06.6	+02 52 13.5	587726033315299465
14.....	RXJ1107.4+1245	11 07 24.2	+12 44 20.0	588017567629509093
15.....	RXJ1115.9+0130	11 15 51.9	+01 29 55.1	587728307491897590
16.....	RXJ1128.6+3530	11 28 34.4	+35 30 14.0	587739305286238362
17.....	RXJ1152.6+0328	11 52 37.6	+03 28 21.8	587726033858330762
18.....	RXJ1211.1+3520	12 11 08.3	+35 19 58.8	587739304216232052
19.....	RXJ1327.1+0212	13 27 01.0	+02 12 19.5	587726015078465728
20.....	RXJ1349.9+4217	13 49 51.1	+42 16 47.8	588017604154687567
21.....	RXJ1352.0+6105	13 51 58.3	+61 04 19.0	588011219135889619
22.....	RXJ1353.4+4424	13 53 20.3	+44 24 19.8	588298662507184284
23.....	RXJ1402.8+3431	14 02 46.6	+34 31 08.0	587739131880603717
24.....	RXJ1431.3–0054	14 31 21.2	–00 53 44.3	588848898855469518
25.....	RXJ1450.2+4134	14 50 08.3	+41 33 59.8	588017116130246662
26.....	RXJ1453.6+0359	14 53 38.5	+03 59 33.4	587726101487747355
27.....	RXJ1501.3+5455	15 01 18.0	+54 55 18.3	588011101565354082
28.....	RXJ1520.9+4840	15 20 52.3	+48 39 38.6	587735666921898155
29.....	RXJ1539.8+4143	15 39 51.4	+41 43 25.4	587733397568356378
30.....	RXJ1540.4+3622	15 40 23.0	+36 21 56.6	587736751928770630
31.....	RXJ1624.7+3727	16 24 43.4	+37 26 42.4	587735666392105305
32.....	RXJ1653.1+3909	16 53 07.8	+39 08 53.1	588007005270966692
33.....	RXJ1717.1+2931	17 17 06.9	+29 31 21.1	587729408084935169
34.....	RXJ2139.5–0722	21 39 28.5	–07 21 46.6	587726878878728621

<sup>a</sup> Right ascension is given in hours, minutes, and seconds.

<sup>b</sup> Declination is given in degrees, arcminutes, and arcseconds.

**Table 2.3:** Fossil candidates –  
Properties of the central elliptical and the associated X-ray component.

ID	redshift <sup>a</sup>	$D_L^b$ [Mpc]	$\frac{1}{2}r_{\text{vir}}^c$ [arcmin]	[kpc]	central elliptical galaxy			ROSAT X-ray properties			
					$i'^a$ [mag]	$g' - i'^a$ [mag]	$M_{i'} - 5 \log h^b$ [mag]	$\Delta^d$ [arcsec]	extent <sup>d</sup> [arcsec]	extent/ $\Delta^d$	$L_x$ (0.5–2keV) <sup>e</sup> [ergs s <sup>-1</sup> ]
01	0.405	2205	0.680	221	17.29	2.00	-24.05	12.8	44	3.44	8.42E+44
02	0.425	2335	0.647	216	17.34	2.58	-24.28	42.8	56	1.31	1.84E+44
03	0.200	981	1.411	280	17.58	1.69	-21.86	21.8	40	1.83	6.29E+43
04	0.287	1477	0.970	252	16.13	2.23	-24.30	35.5	47	1.33	3.85E+44
05	0.225	1119	1.249	271	15.81	2.01	-23.93	21.4	21	0.98	1.51E+44
06	0.209	1032	1.346	276	15.26	1.92	-24.31	52.1	76	1.46	1.25E+44
07	0.272	1388	1.026	256	16.57	1.20	-23.49	9.2	22	2.39	6.65E+44
08	0.162	776	1.755	293	15.15	1.68	-23.74	7.4	85	11.45	4.58E+43
09	0.202	994	1.394	279	17.25	1.35	-22.08	48.9	22	0.45	1.89E+43
10	0.317	1657	0.875	243	16.23	2.31	-24.45	26.1	61	2.34	2.07E+44
11	0.187	907	1.517	284	16.52	1.71	-22.66	28.2	13	0.46	1.97E+43
12	0.371	1991	0.744	229	18.57	1.48	-22.38	7.2	17	2.36	1.00E+44
13	0.236	1181	1.189	267	17.60	1.28	-22.14	6.1	19	3.12	1.03E+45
14	0.420	2300	0.655	217	17.93	2.46	-23.47	15.8	9	0.57	1.19E+44
15	0.352	1870	0.786	234	17.19	2.03	-23.78	22.5	57	2.54	7.30E+44
16	0.402	2186	0.685	221	17.59	2.52	-23.74	15.6	12	0.77	3.02E+44
17	0.081	366	3.600	327	14.25	1.38	-22.91	27.4	71	2.59	1.08E+43
18	0.136	643	2.097	303	15.14	1.58	-23.27	35.8	52	1.45	4.11E+43
19	0.260	1318	1.075	260	16.26	2.16	-23.86	40.5	58	1.43	2.30E+44
20	0.289	1487	0.964	251	17.67	1.92	-22.65	8.2	19	2.30	1.08E+44
21	0.323	1694	0.858	241	17.32	2.34	-23.37	23.2	6	0.26	3.61E+43
22	0.152	724	1.873	297	17.03	1.37	-21.60	24.1	9	0.37	1.23E+43

Table 2.3 – continued.

ID	redshift <sup>a</sup>	$D_L^b$ [Mpc]	$\frac{1}{2}r_{\text{vir}}^c$		central elliptical galaxy			ROSAT X-ray properties			
			[arcmin]	[kpc]	$i^a$ [mag]	$g' - i^a$ [mag]	$M_V - 5 \log h^b$ [mag]	$\Delta^d$ [arcsec]	extent <sup>d</sup> [arcsec]	extent/ $\Delta^d$	$L_X$ (0.5-2keV) <sup>e</sup> [ergs s <sup>-1</sup> ]
23	0.175	846	1.619	289	17.14	1.31	-21.84	6.7	10	1.49	1.28E+43
24	0.403	2190	0.684	221	17.49	2.70	-23.90	43.1	52	1.21	2.27E+44
25	0.157	748	1.818	296	14.89	1.65	-23.87	35.9	54	1.50	2.24E+43
26	0.370	1983	0.746	229	16.82	2.35	-24.30	36.1	42	1.16	2.33E+44
27	0.339	1786	0.818	237	17.24	1.83	-23.52	7.3	15	2.05	1.54E+44
28	0.074	334	3.933	330	13.35	1.37	-23.60	31.4	71	2.26	4.35E+43
29	0.119	557	2.404	310	14.83	1.55	-23.30	10.3	12	1.17	7.06E+42
30	0.231	1155	1.213	269	16.53	1.76	-23.22	27.7	11	0.40	2.63E+43
31	0.199	976	1.417	280	16.89	1.79	-22.54	12.1	13	1.08	2.97E+43
32	0.147	696	1.945	299	15.70	1.64	-22.90	33.0	19	0.58	1.40E+43
33	0.278	1423	1.003	254	16.95	1.68	-23.26	4.2	30	7.08	6.92E+44
34	0.410	2234	0.672	220	17.58	2.50	-23.86	26.3	20	0.76	1.53E+44

<sup>a</sup> Redshifts and magnitudes are taken from the SDSS DR 6.<sup>b</sup> Calculated with the relation from Fig.2.2(a) and equation 2.3.<sup>c</sup> Half the virial radius given in arcminutes. The virial radius was estimated via  $r_{\text{vir}} = 1.945 \cdot \left(\frac{T}{10\text{keV}}\right)^{1/2} (1+z)^{-3/2} \cdot h^{-1}\text{Mpc}$  as used in Jones et al. (2003). For the X-ray temperature a lower limit of 0.7 keV was assumed.<sup>d</sup> ROSAT  $\Delta$  and extent parameters.  $\Delta$  gives the distance of the X-ray source to the central elliptical. Extent gives the excess of the detected X-ray source over the ROSAT PSF. The ratio extent/ $\Delta$  indicates the prominence of the X-ray source with larger values being more extended sources close to the central elliptical.<sup>e</sup> ROSAT X-ray luminosities. ROSAT countrates have been converted to X-ray fluxes via the tool PIMMS (Mukai 1993) assuming a Raymond-Smith model with 2keV and a metallicity of  $Z = 0.4Z_{\odot}$ . HI column densities of the Leiden/Argentine/Bonn (LAB) Survey of Galactic HI (Kalberla et al. 2005) were taken into account to determine extinction-free fluxes.

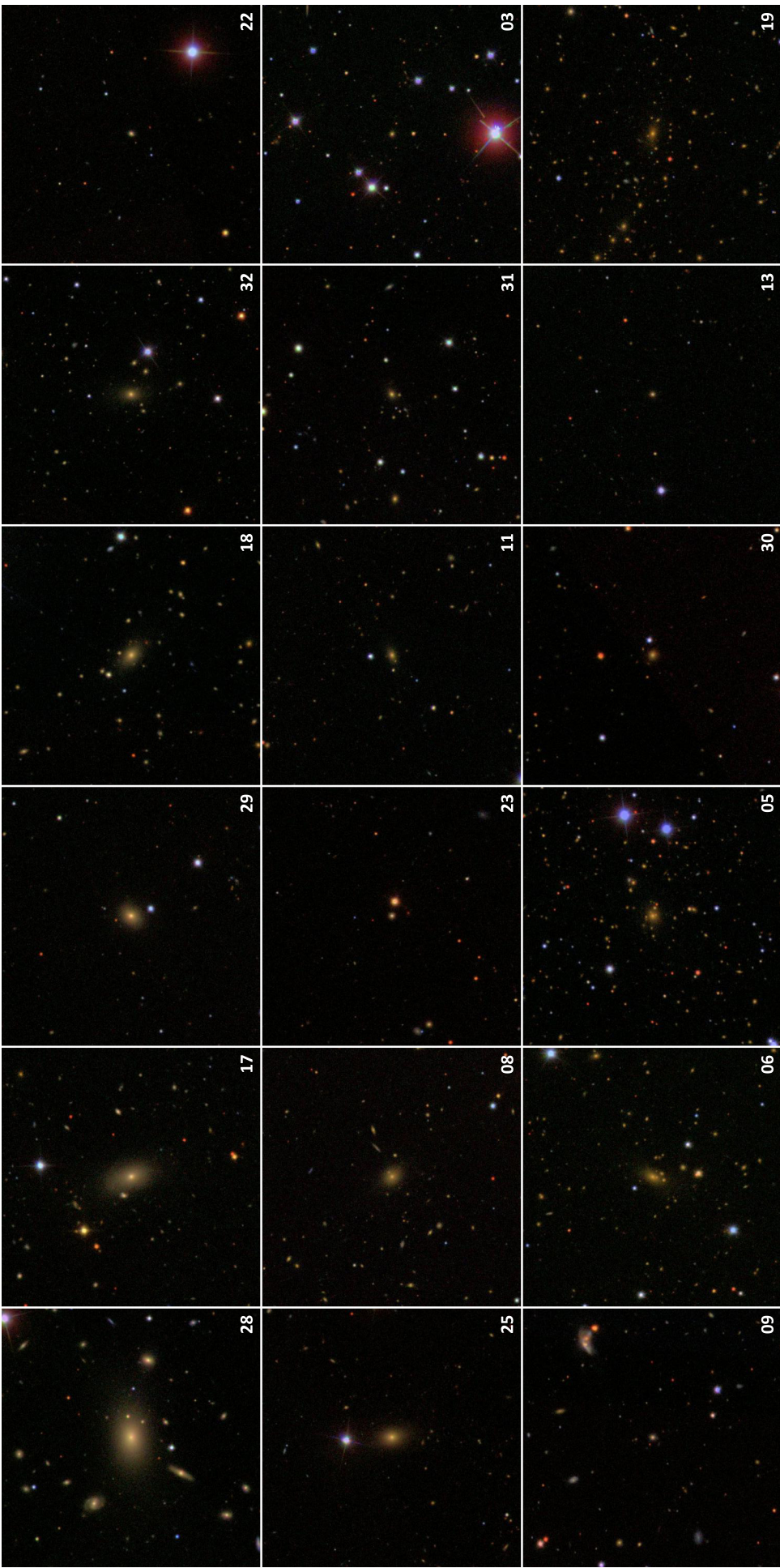


**Figure 2.3:** Fossil candidates listed with increasing redshift. The field of view is  $4 \times 4$  arcmin.

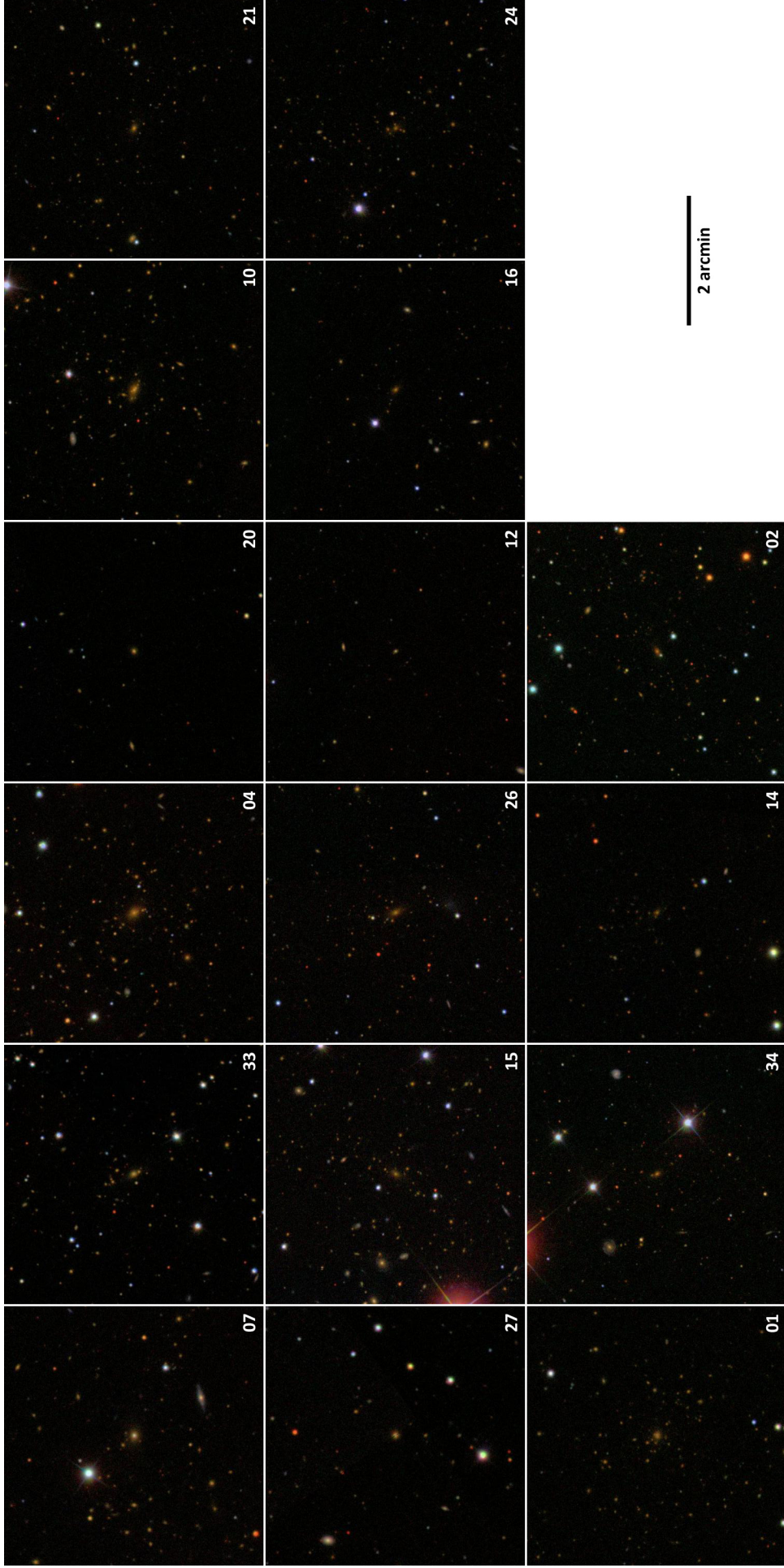
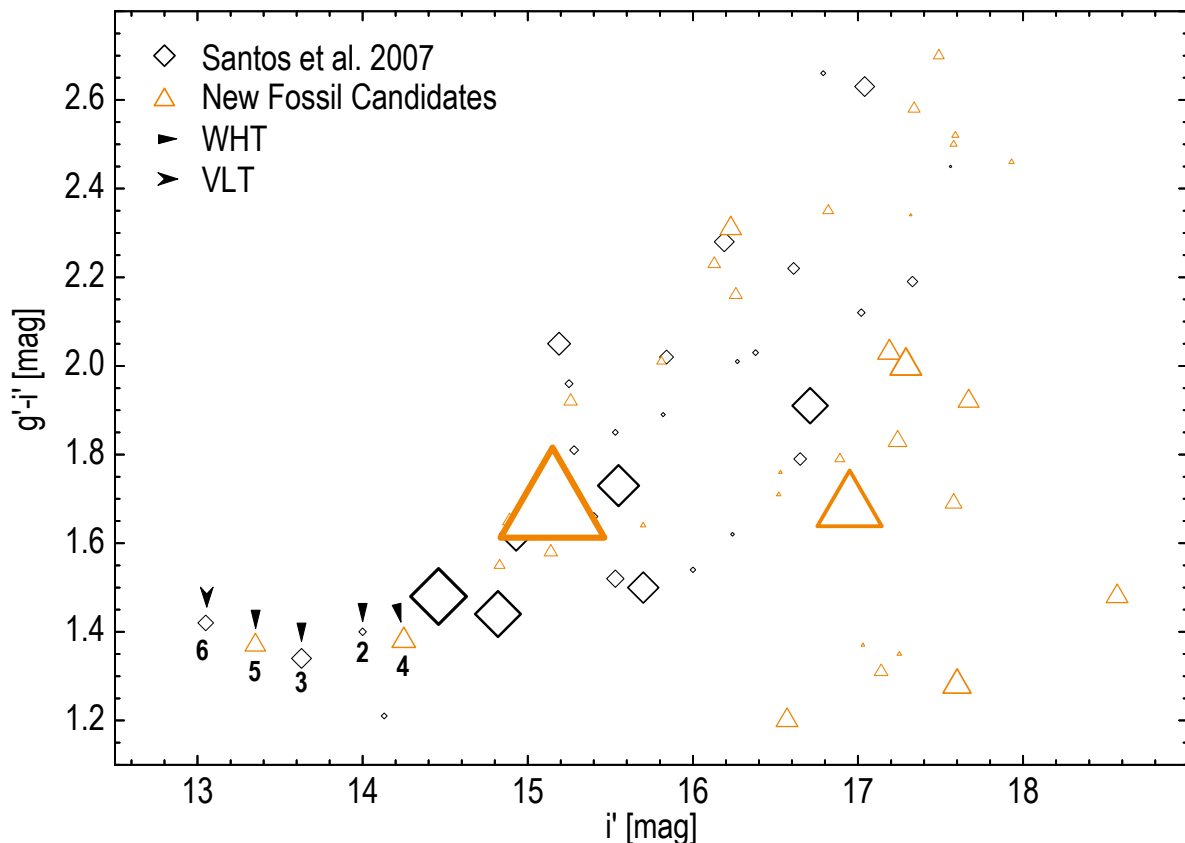


Figure 2.3 – continued.

## 5 Comparison with Santos et al. (2007)

Since Santos et al. (2007) also queried the SDSS for fossils, but with a different SQL code, one obvious thing is to compare the results of both algorithms. The present query re-identifies 12 systems from the work of Santos et al. (2007) corresponding to  $\sim 35\%$  of their sample. However, many objects could not be reidentified since the procedure used here excludes all galaxies within half the virial radius violating the  $2^{\text{mag}}$  criterion, regardless if it is a background galaxy or not, thus eliminating possible fossil candidates that would pass the  $2^{\text{mag}}$  criterion if group memberships were known. This indicates that there might be much more fossil candidates in the present query when accounting also for group memberships via photometric redshifts. In fact, 14 systems from Santos et al. (2007) host 1 galaxy violating the  $2^{\text{mag}}$  criterion in this work. Fig. 2.4 shows a CMD of the central ellipticals from both samples. Arrows point to the galaxies which have been selected for observations at the William Herschel Telescope (WHT) and Very Large Telescope (VLT). From both samples, these galaxies were the most suitable targets for follow-up observations based on their brightness and observability. Chapters 3 and 4 outline the performed observations and the data analysis of these systems in detail.



**Figure 2.4:** CMD of the central ellipticals for all fossil candidates identified in the SDSS. Diamonds show the objects published by Santos et al. (2007) while triangles present the aggregates found in this work. The arrows point to the objects that have been observed with the WHT and the VLT. Numbers refer to the ID of Table 3.3 (see Chapter 3). The size of the symbols scales with the extent/ $\Delta$  ratio presented in Table 2.2 to illustrate the prominence of the associated X-ray source.



## 6 SDSS properties of the WHT and VLT targets

To get a first impression on the systems selected for follow-up observations at the WHT and VLT, surface-brightness profiles of the central ellipticals have been analyzed with the publicly available SDSS data. Figures 2.6–2.10 present the results of the isophote analysis. A deVaucouleurs  $r^{1/4}$  law

$$I(r) = I_e \exp \left[ -7.67 \left( \left( \frac{r}{r_e} \right)^{1/4} - 1 \right) \right] \quad (2.5)$$

$$\mu(r) = \mu_e + 8.328 \left( \left( \frac{r}{r_e} \right)^{1/4} - 1 \right) \quad (2.6)$$

was fit to all galaxies in SDSS  $g'$ ,  $r'$ , and  $i'$  bands. Following equation 2.6, the model displays a linear relation when plotting  $\mu(r)$  against  $r^{1/4}$ . This is the case for nearly all investigated ellipticals, hence exhibiting pure deVaucouleurs profiles. Only RX J1152.6+0328 shows slight deviations from the model. Besides position angle (PA) and ellipticity profiles, the fourier coefficient  $a_4$ , indicating the deviation from purely elliptical isophotes ( $a_4 < 0$ : boxy –  $a_4 > 0$ : disk), is also presented. Model parameters  $\mu_e$  and  $r_e$  were derived from the linear least squares fit via equation 2.6.

In addition, a list of all SDSS targets within one-half virial radius, photometrically classified as galaxies, was extracted for every system. Photometric and spectroscopic redshifts, when available, were used to estimate group memberships and construct luminosity functions. Listings 2.12 and 2.13 show the corresponding SQL queries to acquire these data.

**Listing 2.5:** Obtaining photometric redshifts for the faint galaxy population.

```
1 SELECT photoz.objID, photoz.z, photoz.zerr
2 FROM photoz, dbo.fGetNearbyObjEq(ra, dec, radius) n
3 WHERE photoz.objID = n.objID
```

**Listing 2.6:** Obtaining spectroscopic redshifts for the faint galaxy population.

```
1 SELECT s.bestobjid, s.specclass, s.z, s.zerr
2 FROM specObj s, dbo.fGetNearbyObjEq(ra, dec, radius) n
3 WHERE s.bestobjID = n.objID
```

The next two pages illustrate the surrounding faint galaxy populations of the investigated systems. Upper panels show SDSS redshifts, middle ones the corresponding colour-magnitude-diagrams, and lower panels display luminosity functions in bins of one magnitude. Triangles refer to photometric redshifts while diamonds represent spectroscopic ones. Group membership was defined such that redshifts had to fulfill  $|z_{\text{phot}} - z_1| < 0.1$ <sup>12</sup> or  $|z - z_1| < 0.005$ <sup>13</sup>. Galaxies within these limits are shown in colour. A red sequence is clearly visible in all CMDs and indicated by a straight line. The corresponding equation is shown in the lower left corners. Histograms of the luminosity functions are plotted logarithmically and display the same color coding. Vertical lines indicate an absolute magnitude of  $M_{i'} = -18 + 5 \log h$ . RX J1520.9+4840 is the only system to show a dip at  $M_{i'} = -18 + 5 \log h$  as observed by Mendes de Oliveira et al. (2006).

<sup>12</sup>This threshold is based on the SDSS photometric redshift uncertainty (Csabai et al., 2003).

<sup>13</sup>Corresponding to  $1500 \text{ km s}^{-1}$ .

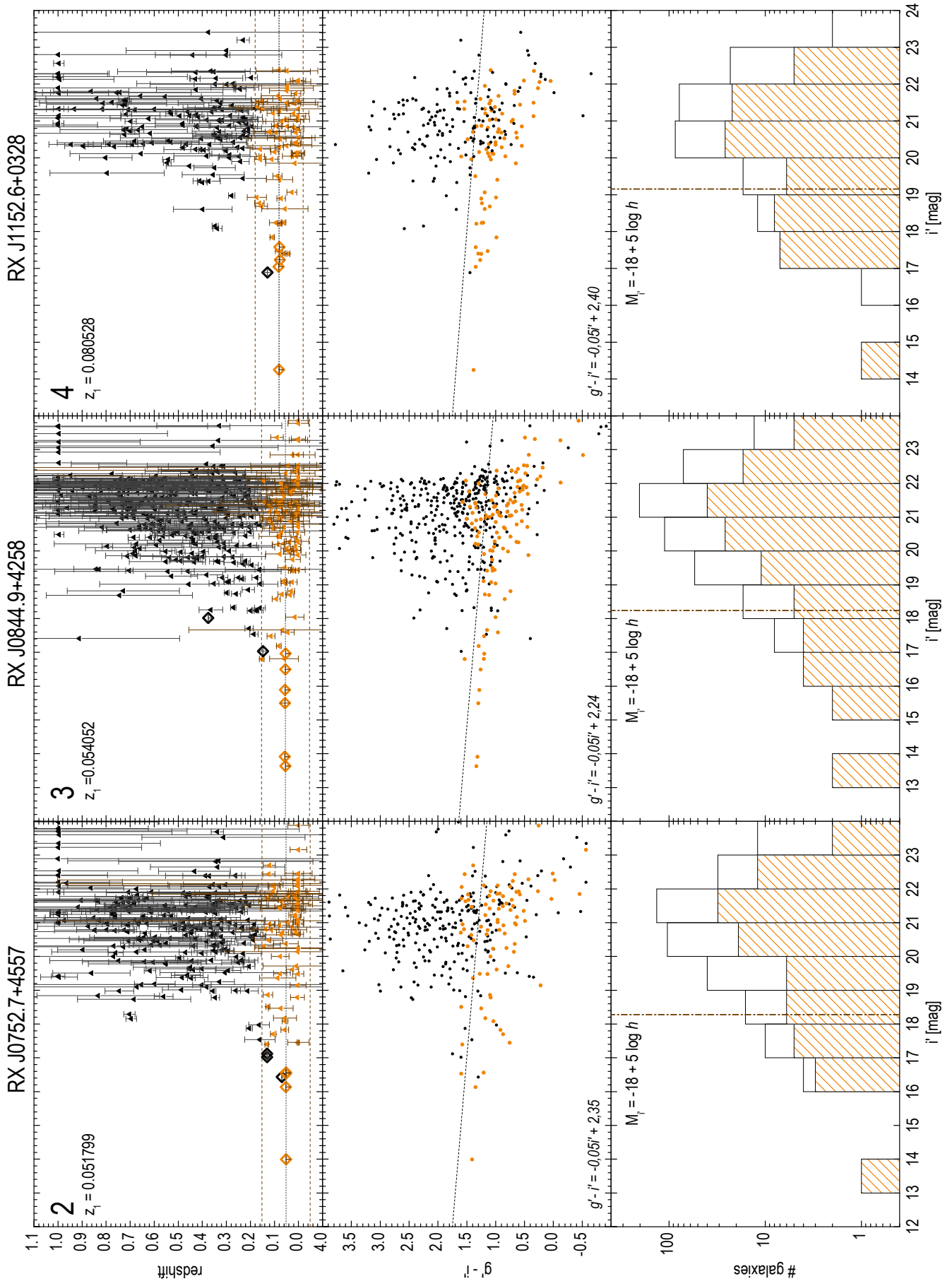


Figure 2.5: The faint galaxy populations of the WHT and VLT targets.

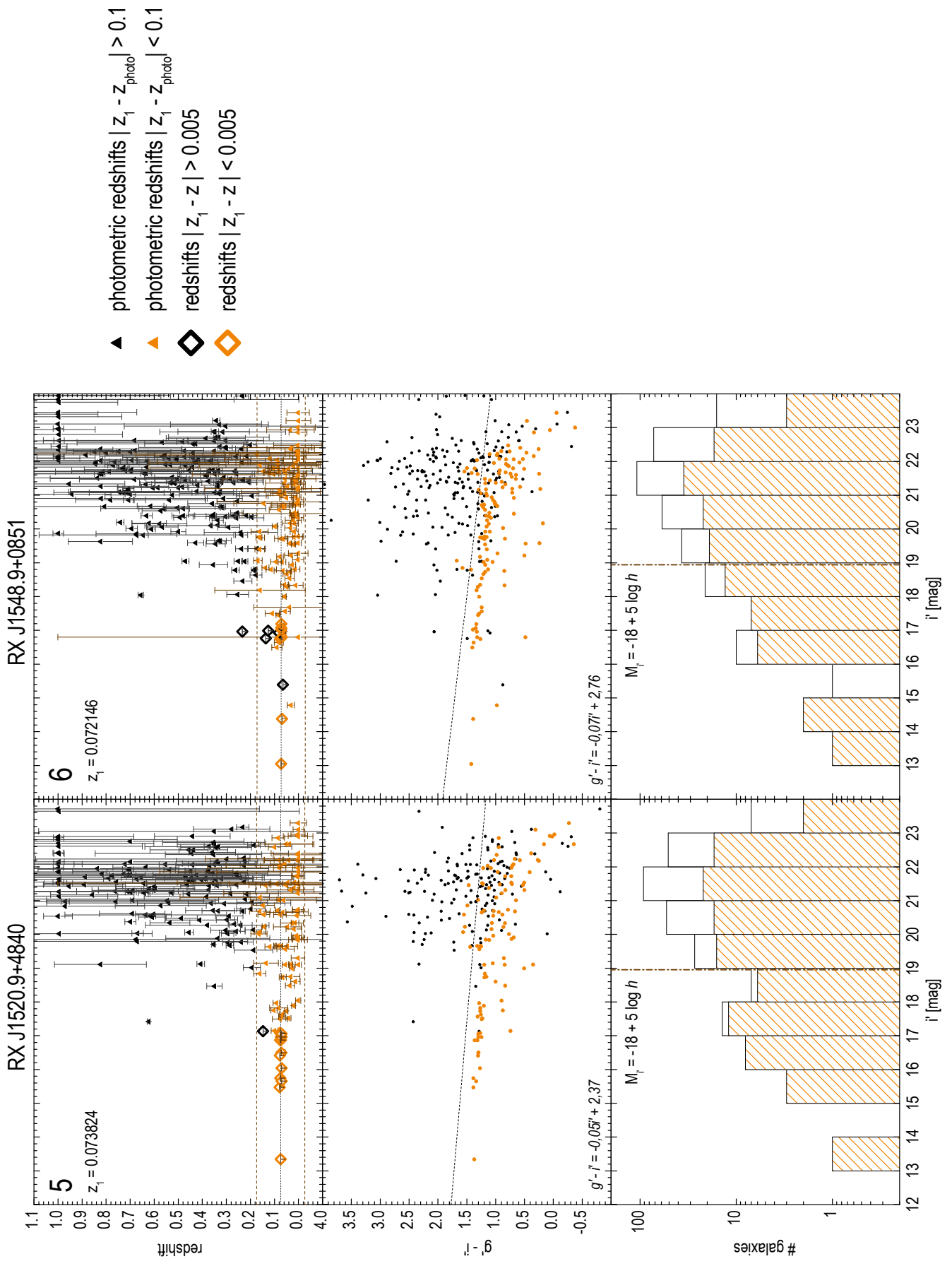
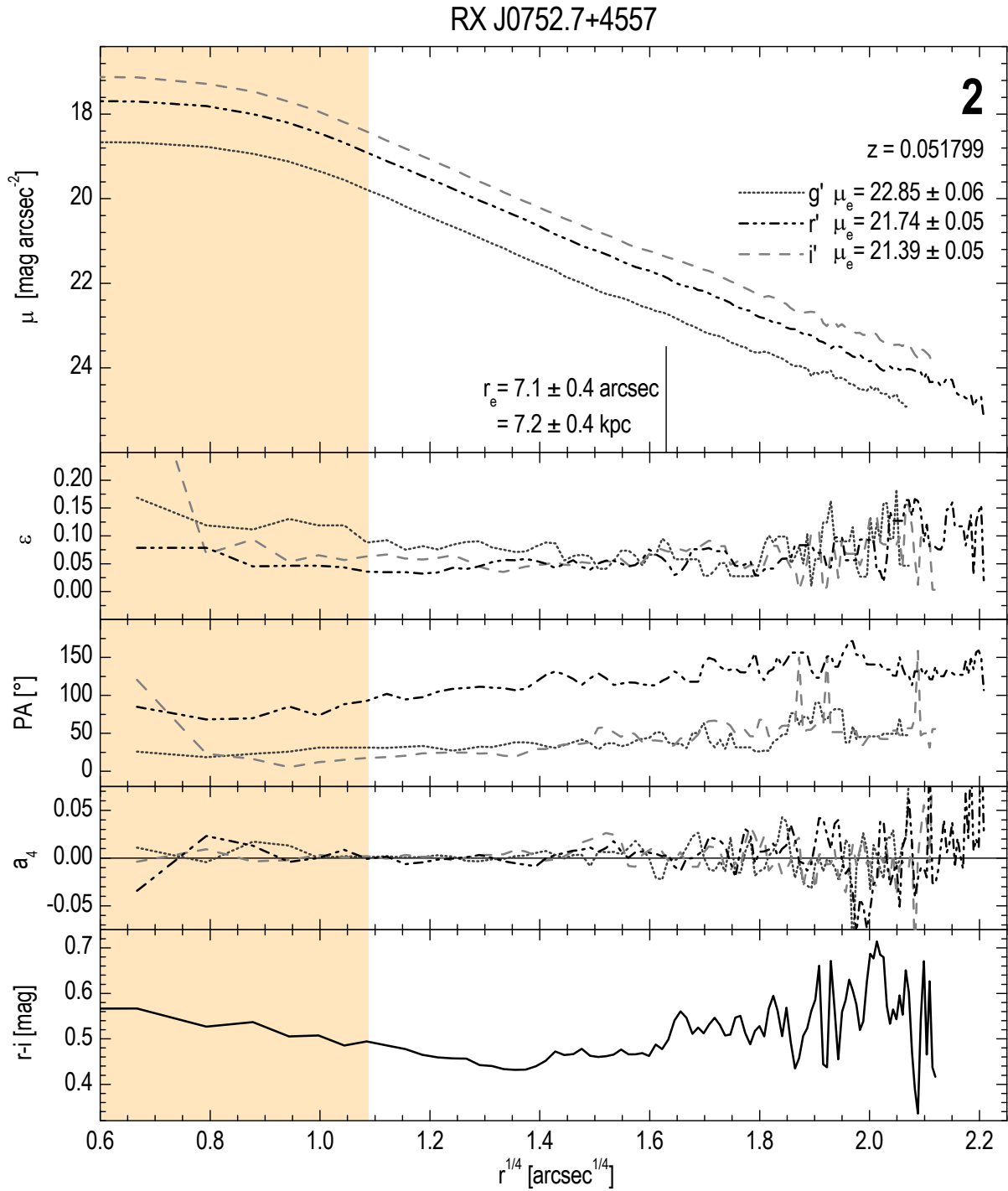
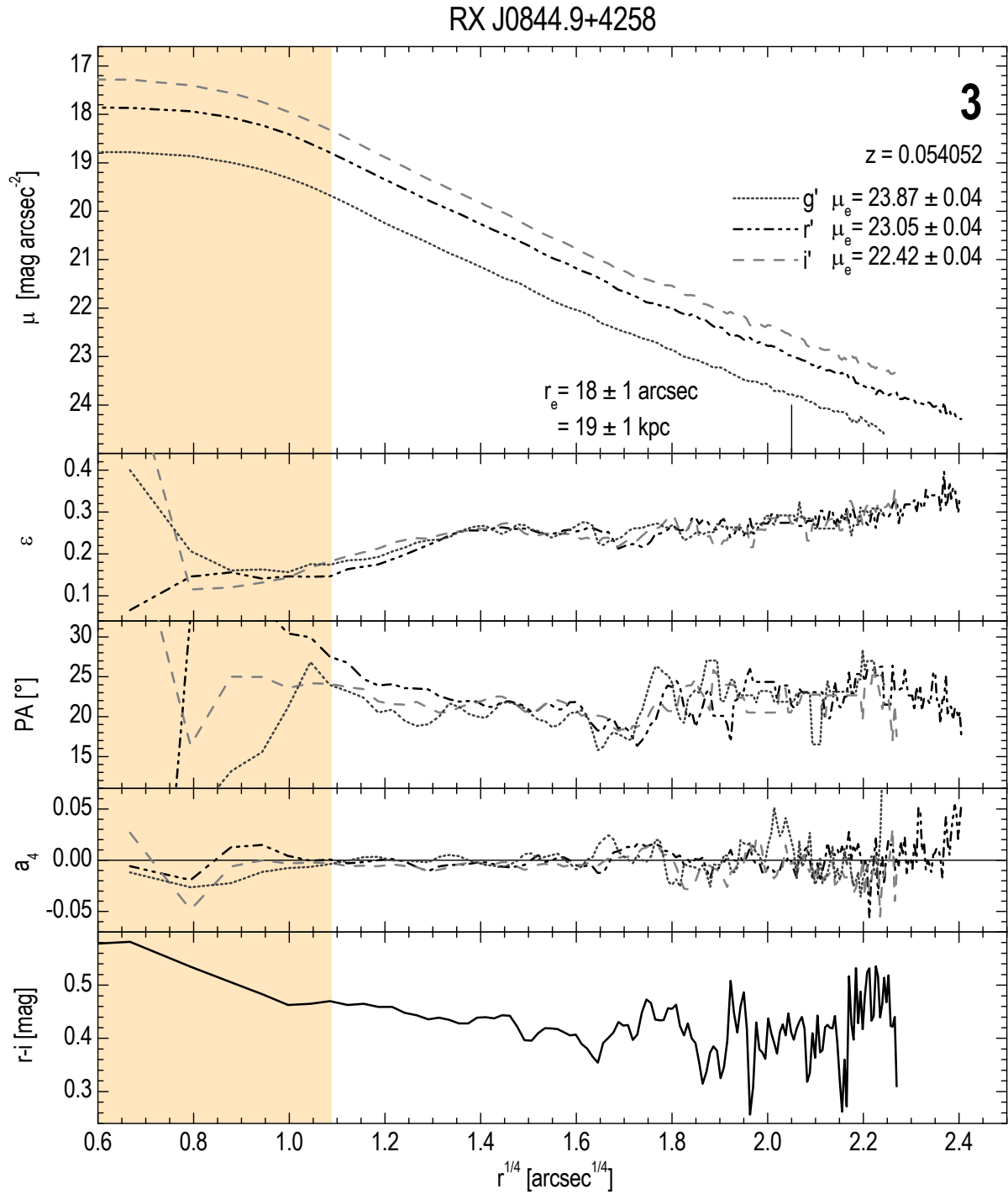


Figure 2.5 — continued.



**Figure 2.6:** Surface photometry of RX J0752.7+4557 in  $g'$ ,  $r'$ , and  $i'$ . The shaded area is seeing dominated. The vertical line indicates the average effective radius determined from all three bands.



**Figure 2.7:** Surface photometry of RX J0844.9+4258. Same as Fig. 2.6.

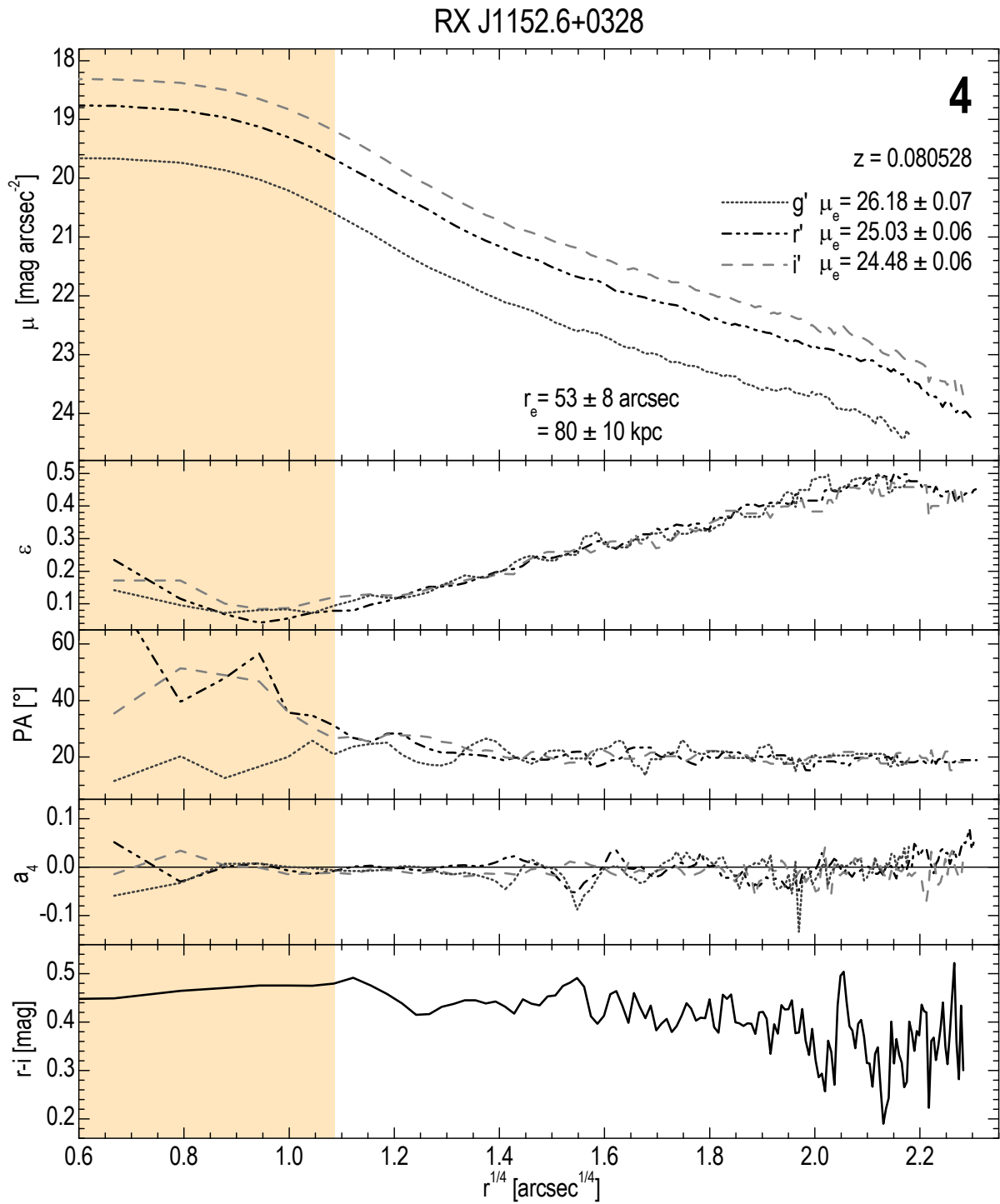


**Figure 2.8:** Surface photometry of RX J1152.6+0328. Same as Fig. 2.6.

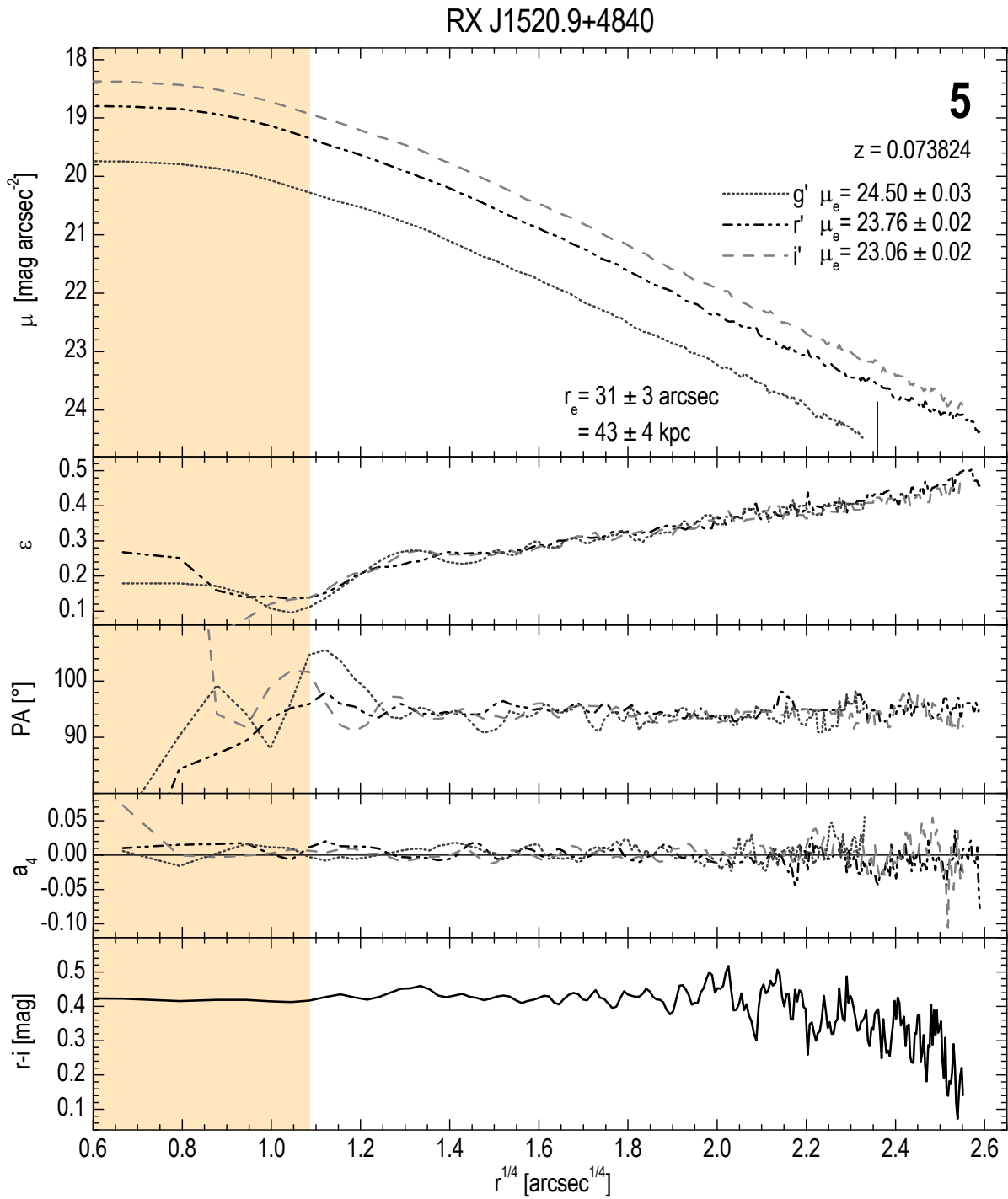


**Figure 2.9:** Surface photometry of RX J1520.9+4840. Same as Fig. 2.6.

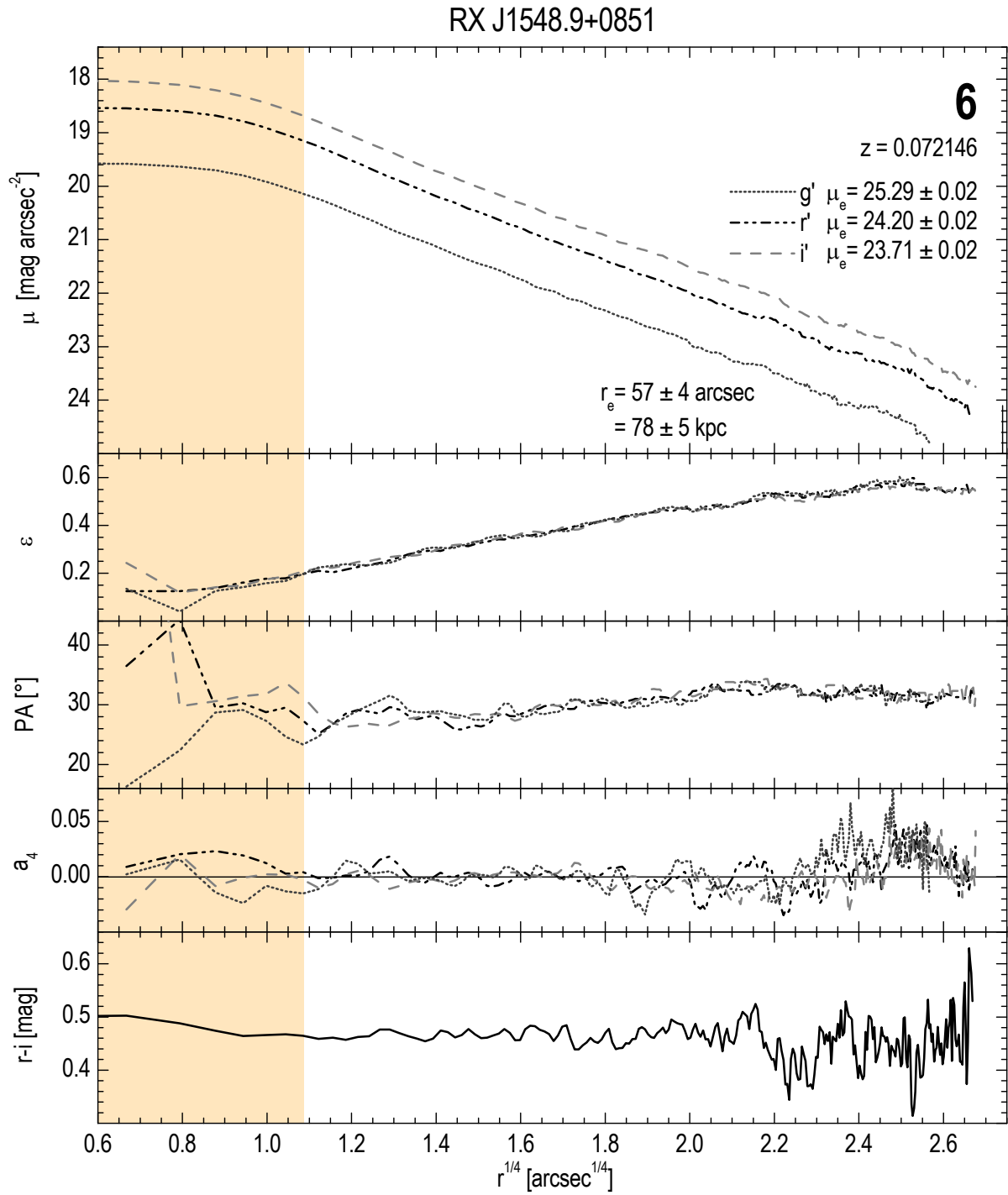


**Figure 2.10:** Surface photometry of RX J1548.9+0851. Same as Fig. 2.6.



# Chapter 3

## WHT ISIS Observations

In order to measure age and metallicity gradients in a sample of fossil group central ellipticals, observing time with ISIS (Intermediate Dispersion Spectrograph and Imaging System) at the William Herschel Telescope (WHT) was requested in visitor mode. The telescope is located within the Observatorio del Roque de los Muchachos (ORM), 2396 meters above sea level on the canary island of La Palma operated by the Instituto de Astrofísica de Canarias (IAC). The WHT itself is part of the Isaac Newton Group of Telescopes (ING)<sup>1</sup> operated by the United Kingdom, the Netherlands, and Spain. With a primary mirror of 4.2 m, the WHT is the largest optical telescope in Europe with a single mirror design<sup>2</sup> and was the third largest single mirror telescope in the world at its first light in 1987. Observing time on the WHT is scheduled on a semester basis and is allocated by national time allocation committees (TACs) of the three operating countries. Proposals by PIs and COIs from different countries are also accepted by all national TACs. Being one of the largest optical telescopes in Europe, there is high competition when obtaining observing time at the WHT. The telescope is heavily oversubscribed with approximately three times more applications than can be scheduled.

This chapter focuses on the observations that have been carried out at the WHT, including the preparations for observing time, the observations themselves, as well as the reduction and final analysis of the obtained data products, so that the reader gets an overview on how to structure and plan observations in visitor mode at an international observatory.

### 1 The ISIS spectrograph

ISIS is a high-efficiency, long-slit spectrograph mounted at the cassegrain focus of the WHT providing spectral resolutions from  $8\text{-}120 \text{ \AA mm}^{-1}$  in first order. It is suitable for long-slit spec-

<sup>1</sup>also operating the 2.5 m Isaac Newton Telescope (INT) and the 1.0 m Jacobus Kapteyn Telescope (JKT).

<sup>2</sup>In fact, only the Gran Telescopio de Canarias (GTC), located at the same site, is larger but is constructed in segmented mirror design.

troscopy up to 4 arcmin slit length. Through the use of dichroic filters, the instrument allows simultaneous observations in both a blue and a red arm, each designed for the corresponding wavelength ranges. In addition to long-slit spectroscopy, the instrument can also be converted into a spectropolarimeter applicable for measuring linear and circular polarization. Figure 3.1 shows the size of the instrument with respect to the WHT 4.2 m primary mirror.



**Figure 3.1:** Left panel: The William Herschel Telescope (WHT) located on the Roque de los Muchachos on the edge of the Caldera de Taburiente National Park, 2396 meters above sea level. Photo Courtesy of the Isaac Newton Group of Telescopes, La Palma. Right panel: ISIS mounted at the cassegrain focus of the WHT. Private photograph.

## 1 Blue and red arm characteristics

The detector for the ISIS blue arm consists of a thinned, blue-sensitive EEV12 CCD, providing an array of  $4096 \times 2048$  pixels with  $13.5 \mu\text{m}$  pixel size. The CCD is arranged so that the long axis is placed along the dispersion direction maximizing the spectral coverage of the instrument. The camera optics vignette the outer regions of the chip so that only the central 3500 pixels are unobstructed while  $\sim 300$  pixels have considerable lower response on each side of the detector. The spatial scale of the blue arm is  $0.2 \text{ arcsec pixel}^{-1}$  yielding a maximum unvignetted slit-length of 3.7 arcmin. The detector for the ISIS red arm is a red-sensitive RED+ CCD also providing an array of  $4096 \times 2048$  pixels with  $15 \mu\text{m}$  pixel size. Similar to the blue arm, the long axis is oriented along the dispersion direction. The vignetting of the camera optics leaves only the central 2475 pixels unobstructed. Since the spectrum is slightly shifted in the dispersion axis, the central wavelength does not exactly correspond to the center of the CCD but is shifted by approximately 300 pixels. With the pixel size of 15 microns, the spatial scale of the red arm corresponds to  $0.22 \text{ arcsec pixel}^{-1}$  yielding the same unvignetted slit-length as in the blue arm.

The spectrograph setup is designed such that a slit-width matching the typical seeing of the site ( $\sim 1 \text{ arcsec}$ ) corresponds to approximately 4 pixels FWHM on the CCD for all gratings. Since sampling theory states that a spectral line is resolved if it consists of 2 dispersion elements at its FWHM, this configuration is oversampling the best possible spectral resolution. To increase the signal per dispersion element and decrease the readout noise one can rebin the CCDs at readout

by combining two pixels to one dispersion element without degrading spectral resolution. It is also possible to bin in the spatial direction along the slit since perfect seeing conditions would be necessary to fully benefit from the given spatial scale.

## 2 Dichroic filters

When observing with ISIS, the observer is not forced to use both arms of the spectrograph. If only interested in a smaller wavelength interval, a plane mirror can be inserted into the light path to reflect all of the light into the blue arm. Removing the mirror will cause the light to pass directly into the red arm. To allow observations in both the red and blue arms simultaneously, a dichroic filter is used instead of the mirror. The dichroic reflects blue light while being transparent for red radiation, splitting the incident beam into the corresponding arms. The observer can select one of five different dichroics for ISIS, each labelled according to the wavelength of its *cross-over point*, i.e. the wavelength threshold at which the light is separated into the two arms. As a consequence of splitting the light there is a strong drop-off in the dichroic response near the cross-over point which has to be taken into account when preparing the observations. The default ISIS dichroic is the 5300 while 5400, 5700, 6100, and 7500 dichroics are also available<sup>3</sup>.

## 2 Approved nights at the WHT

As already mentioned, observing time at the WHT is allocated and scheduled on a semester basis (see Figure 3.2) by the national time allocation committees (TACs). For the present work, two proposals have been submitted to the spanish TAC, the Comisión de Asignación de Tiempos (CAT)<sup>4</sup> for semesters 2008B and 2009A. Since applications for observing time at the WHT refer to visitor mode observations, only full nights can be requested. However, a service programme is also managed by the ING for short observations of up to 8 hours. It is intended for astronomers who want to try new ideas or complement an existing visitor mode programme. It has the advantage that instead of only two deadlines for application submission per year, monthly deadlines are scheduled.

		Semester A - 1.2. - 31.7.							Semester B - 1.8. - 31.1.																	
		January	February	March	April	May	June	July	August	September	October	November	December													
$\alpha$		6	7	8	9	10	11	12	13	14	15	16	17	18	19	20	21	22	23	0	1	2	3	4	5	6

**Figure 3.2:** Observing semesters at the WHT. Numbers indicate the optimal right ascension of targets for a given month. The small markers show the deadline for the corresponding semester.

Both proposals for visitor mode observations at the WHT were granted one night, respectively. Table 3.1 gives an overview on the allocated nights. Detailed graphs on the weather conditions for both nights are given in Appendix B.

<sup>3</sup>Response curves for all dichroics can be found at [http://www.ing.iac.es/Astronomy/instruments/isis/isis\\_dich.html](http://www.ing.iac.es/Astronomy/instruments/isis/isis_dich.html)

<sup>4</sup><http://cat.iac.es/>

**Table 3.1:** Nights at the WHT in the framework of this thesis.

semester	date	programme	instrument	nights	seeing <sup>a</sup>	moon
2008B	20.12.2008	58-WHT29/08B	ISIS	1	1.3	grey <sup>b</sup>
2009A	28.04.2009	5-WHT1/09A	ISIS	1	0.7	dark

<sup>a</sup> given in arcsec – estimated with the available RoboDIMM<sup>5</sup> data provided by the ING.

<sup>b</sup> last quarter, 34% illumination of lunar disc

### 3 Preparing observations

When planning observations at an observatory in visitor mode, a detailed preparation of the allocated nights is self-evident. Besides the specification of the technical setup<sup>6</sup>, all the necessary information on the scientific targets and standard stars (finding charts, coordinates, visibility, magnitudes, S/N estimates, ... ) should be well-prepared and always at hand to avoid delay during the night. It is also useful to outline a timetable for each night arranging time slots for scientific exposures, night calibrations, and so on. With such a plan, one always knows what to do next without losing important minutes and is able to check whether they are behind schedule. This section gives an overview on the preparation for both nights at the WHT.

#### 1 Observational setup

To cover the relevant Lick-IDS indices  $H\beta$ ,  $H\gamma$ ,  $Mg_1$ ,  $Mg_2$ ,  $Mgb$ ,  $MgFe$ ,  $Fe5270$  and  $Fe5335$  together with the prominent emission lines from  $[OII]$  to  $H\alpha/[NII]$ , the wavelength region  $\lambda\lambda 4000 - 6800 \text{ \AA}$  shifted to the corresponding galaxy redshifts was considered. Since the cross-over point of the ISIS default dichroic 5300 falls exactly in the range where most of the prominent Lick indices are situated, the 6100 dichroic was requested instead. To select the appropriate grating for each arm, the unvignetted spectral range<sup>7</sup> (USP) was considered. With the R300B grating ( $0.86 \text{ \AA pixel}^{-1}$ ) in the blue arm, an USP of  $3024 \text{ \AA}$  is achieved. For comparison, the blue range of interest covers at most  $1912 \text{ \AA}$  (63%), allowing full coverage of all relevant features. The central wavelength for the blue arm was set to  $\lambda_{cen} = 4800 \text{ \AA}$ . The setup for red arm observations was chosen such that the  $[NII]$ ,  $H\alpha$ ,  $[NII]$  emission-line triplet could be resolved if present. Thus, the R1200R grating ( $0.26 \text{ \AA pixel}^{-1}$ ) was considered for that purpose yielding an USP of  $631 \text{ \AA}$ . If no emission lines were expected around  $H\alpha$ <sup>8</sup>, the R316R grating ( $0.93 \text{ \AA pixel}^{-1}$ ) was used instead to cover a broader wavelength range ( $2302 \text{ \AA USP}$ ). For R1200R and R316R the central wavelength was set to  $\lambda_{cen} = 6900 \text{ \AA}$  and  $\lambda_{cen} = 7000 \text{ \AA}$ , respectively. Once a setup is fixed, it cannot be changed during the night since new calibration frames would have to be considered, not to mention the tedious procedure of changing a grating in the spectrograph by hand. A slit width of 1 arcsec was used for all targets except for spectrophotometric standards. For these stars the maximum slit width of 6 arcsec was considered to make sure that the whole standard star flux was measured.

<sup>5</sup> Robotic Differential Image Motion Monitor – <http://catserver.ing.iac.es/robodimm/>

<sup>6</sup> The setup defined in the proposal is not compulsory and can still be changed after acceptance.

<sup>7</sup> The central 3500 pixels in the blue and central 2475 pixels in the red arm (see Sect. 1).

<sup>8</sup> Since all observed ellipticals show 1-D spectra in SDSS except NGC 1132, these datasets were considered first to check whether emission lines around  $H\alpha$  are present.

## 2 S/N estimates

To get an idea on the incident flux and resulting S/N of the investigated ellipticals, the WHT exposure time calculator SIGNAL<sup>9</sup> was used. Assuming dark sky conditions, (21.5 mag arcsec<sup>-2</sup>), a slit-width of 1 arcsec, airmass of 1, and a target surface brightness of 20 mag arcsec<sup>-2</sup>, a S/N pixel<sup>-1</sup> of  $\sim 13$  is achieved within two and a half hours (9000 s) exposure for grating R300B in the blue arm. The same assumptions yield a S/N pixel<sup>-1</sup> of  $\sim 7$  for R1200R and  $\sim 17$  for R316R in the red arm. With these requirements in exposure time, three objects were scheduled for one night. The S/N is strongly dependent on the spectral resolution, the target flux, and the sky brightness whereas airmass and the exposure time itself are only secondary factors.

## 3 Standard stars

For the purpose of flux-calibrating the observed long-slit spectra, ING spectrophotometric standard stars were selected by means of the ING landscape tool<sup>10</sup>. The program lists adequate spectrophotometric standard stars sorted by UT and airmass for every specified night. Since the airmass of a standard star should always match the one of the scientific target, only a standard star fulfilling  $|X_{\text{standard}} - X_{\text{elliptical}}| \leq 0.1$  was selected for the corresponding galaxy. In addition to spectrophotometric standards, Lick IDS standard stars have been observed to transform the observed data into the Lick IDS system. The purpose in doing so is to compare the observed absorption line strength index data with Simple Stellar Population (SSP) models that have been developed for this system. Standards were selected from the list of field stars from the homepage of Dr. Guy Worthey<sup>11</sup>. To match the stellar population of the observed galaxies, G and K giants with appropriate coordinates and magnitudes<sup>12</sup> were selected.

**Table 3.2:** Standard stars observed at the WHT.

No. <sup>a</sup>	name	$\alpha_{\text{B1950}}$	$\delta_{\text{B1950}}$	spectral type	$V$	night
S1.....	Feige 24	02 32 30.9	+03 30 52	DAM1V	12.40	20.12.2008
S2.....	G191-B2B	05 01 31.5	+52 45 52	DA0	11.78	20.12.2008
S3.....	He 3	06 44 14.9	+37 35 03	DA	12.08	20.12.2008
S4.....	HD 84937	09 46 12.1	+13 59 18	sdF5	8.28	28.04.2009
S5.....	Feige 92	14 09 41.4	+50 21 08	Bp	11.50	28.04.2009
S6.....	PG 1545+035	15 45 53.9	+03 32 03	sdOB	14.34 <sup>b</sup>	28.04.2009
L1.....	HD 221148	23 26 57.0	-04 48 19	K3 III	6.25	20.12.2008
L2.....	HD 2665	00 27 58.3	+56 47 23	G5 IV	7.7	20.12.2008
L3.....	HD 4744	00 47 09.8	+30 10 43	G8 IV	7.62	20.12.2008
L4.....	HD 7010	01 08 28.4	+60 14 27	K0	8.0	20.12.2008
L5.....	HD 72324	08 30 02.9	+24 15 23	G9 III	6.36	28.04.2009
L6.....	HD 73665	08 37 14.0	+20 11 08	K0 III	6.39	28.04.2009
L7.....	HD 73710	08 37 30.0	+19 50 53	K0 III	6.44	28.04.2009

<sup>a</sup> S indicates spectrophotometric standards while L presents Lick IDS standards

<sup>b</sup>  $m_{\lambda 5556}$  magnitude since no value for  $V$  is given in the literature

<sup>9</sup><http://catserver.ing.iac.es/signal/>

<sup>10</sup><http://catserver.ing.iac.es/landscape/>

<sup>11</sup><http://astro.wsu.edu/worthey/html/system.html>

<sup>12</sup>The list comprises very bright stars up to  $V \sim 0^{\text{mag}}$ . Because of a minimum ISIS exposure time of 1 second and to avoid pixel saturation, fainter stars around  $V \sim 7^{\text{mag}}$  have been selected.

## 4 Nights at the WHT

Once the schedules for the ongoing observing semester are published online<sup>13</sup>, a support astronomer (SA), various telescope operators (TO)<sup>14</sup> and duty engineers (DE) are assigned to each individual programme. The SA is present on only the first night of each run to provide an introduction to the telescope and instrumentation. It is thus intended to meet with the SA in the telescope control room at 3 p.m. on the first day to set-up the spectrograph and get accustomed to operating the device. While the SA and DE leave the telescope at  $\sim 11$  p.m., the TO is present for the whole night. The duty of the visiting astronomer is to operate the instrument while the TO is responsible for the movement of the telescope, pointing targets, and the alignment of the spectrograph slit as requested by the visiting astronomer. Figure 3.3 shows the WHT control room and the working area of the visiting astronomer.

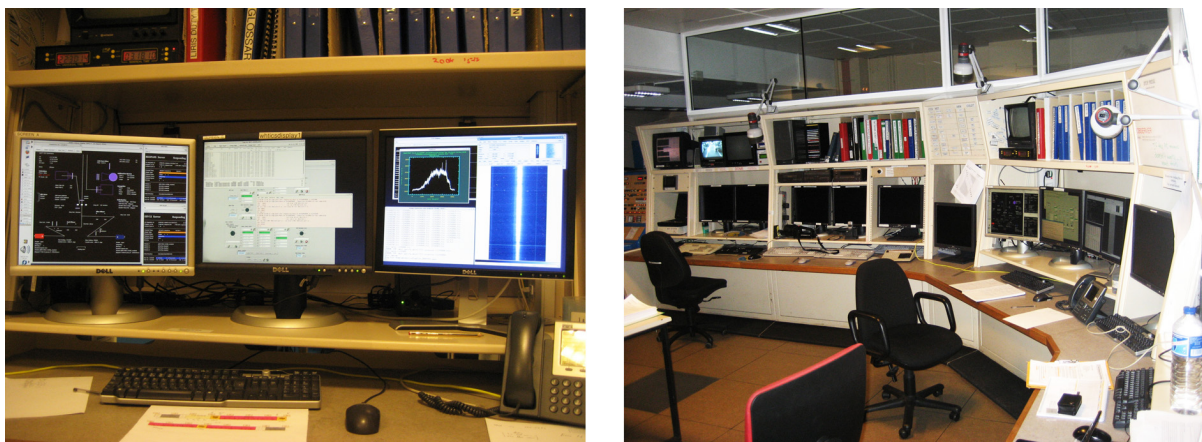


**Figure 3.3:** Left panel: workstations for the visiting astronomer. Right panel: the WHT control room. Most of the monitors are handled by the telescope operator. Private photographs.

### 1 Observing with ISIS

As shown in Figure 3.3, only three monitors are of interest for the visiting observer. The left monitor covers the so-called *mimic* display as well as two detector information panels, one for the blue and one for the red arm. The *mimic* display gives a schematic overview on the trace of the light path within ISIS and monitors all of the ISIS instrument components (slit, dichroic, calibration lamps, ... ) and their status specified by the observer. The detector information panels show most importantly the elapsed time of a running exposure as well as some CCD characteristics (temperature, readout speed, binning, ... ). The central monitor displays a pink xterm window from which the observations are carried out on the command-line. To run an exposure of 2700 seconds in both the red and blue arms with an output fits file title *galaxy*, following command is used:

```
run red 2700 "galaxy" & ; run blue 2700 "galaxy" &
```

Use of the ampersands allows simultaneous observations in both arms. For a detailed list of all observing commands the *ISIS Users' Manual Quick Reference Guide* is recommended. In

<sup>13</sup><http://catsserver.ing.iac.es/schedules/>

<sup>14</sup>usually only one

addition to the unix terminal, an observing log is also shown on the central display. It lists all of the saved frames with the associated title, coordinates, UT, airmass, exposure time, slit-width and grating and is thus extremely helpful in keeping track of the executed exposures. The right monitor displays a regular IRAF session and allows immediate examination of the observed frames.

## 2 Afternoon settings and calibrations

Before the actual observations can start, the user specific CCD settings such as binning, slow or fast readout, and windowing of the CCD have to be defined. Since the readout noise is slightly lower and CCDs are operated with a higher gain, the slow readout mode has been adopted for all observations. Because of the wide spatial coverage of more than 4 arcminutes needless for most scientific targets, the ISIS standard window [585:1550,1:4200] has been adopted to reduce the CCD readout time<sup>15</sup>. No binning was set in both the spatial and dispersion directions.

Once these settings have been defined, the bias, flat, and arc calibration frames can be taken. No dark frames have been observed since at the operating temperature of the CCDs ( $\sim 160$  K), the dark current is below  $1 \text{ e}^- \text{ pixel}^{-1} \text{ hour}^{-1}$ . Ten exposures were taken in a row for all calibration frames in the afternoon and at dawn, using the commands:

```
multbias red 10 "bias" & ; multbias blue 10 "bias" &
multflat red 10 1.3 "flat" & ; multflat blue 10 1.5 "flat" &
multarc red 10 2 "arc" & ; multarc blue 10 40 "arc" &
```

The integration time was adjusted to avoid saturation of flat and arc frames. In fact, with the low-resolution grating R316R in the red arm, a neutral density filter had to be used for that purpose since exposures shorter than 1 second are not allowed<sup>16</sup>. Generally, counts should not exceed  $\sim 40000$  ADUs because of detector nonlinearity. Arcs and flats are generated by means of comparison lamps which are turned on with the commands `complamps w` for a tungsten continuum source and `complamps cuar+cune` for copper-neon and copper-argon arc lamps. To drive the light from the lamps into the red and blue arms, a mirror has to be inserted in the light beam with the command `agcomp`. To remove the mirror and turn the lamps off, the commands `agslit` and `complamps off` are used. After the calibration frames had been taken in the afternoon, the telescope had to be focused. This was done during twilight by measuring the FWHM of standard star spectra around  $V = 8^{\text{mag}}$  at different telescope foci. The focus yielding the minimum FWHM was adopted for the upcoming night.

## 3 Targets and time schedule

Table 3.3 lists all elliptical galaxies observed at the WHT while Table 3.4 presents the corresponding observing log. The galaxies were chosen from the lists of Mendes de Oliveira et al. (2006), Santos et al. (2007), and the new fossil group candidates presented in chapter 3. Since these lists do not cover a lot of objects, the inevitable constraints in target visibility and target brightness reduce the candidates of interest to an already humble catalog leaving not much freedom in the shortlisting.

<sup>15</sup>For targets RX J0752.7+4557 and RX J0844.9+4258, this window was disabled to cover nearby bright galaxies.

<sup>16</sup>This threshold is set by the CCD shutter mechanics.

**Table 3.3:** Central fossil group ellipticals observed with ISIS.

ID	galaxy <sup>a</sup>	$\alpha_{2000}$	$\delta_{2000}$	$z$	$cz$	$D_L$	$r'$
1 . . . . .	NGC 1132 <sup>b</sup>	02 52 51.8	-01 16 28.8	0.023133	6935 km s <sup>-1</sup>	101 Mpc	12.16 <sup>b</sup>
2 . . . . .	RX J0752.7+4557 <sup>c</sup>	07 52 44.2	+45 56 57.4	0.051799	15529 km s <sup>-1</sup>	231 Mpc	14.46
3 . . . . .	RX J0844.9+4258 <sup>c</sup>	08 44 56.6	+42 58 35.7	0.054052	16204 km s <sup>-1</sup>	241 Mpc	14.08
4 . . . . .	RX J1152.6+0328 <sup>d</sup>	11 52 37.6	+03 28 21.8	0.080528	24142 km s <sup>-1</sup>	366 Mpc	14.69
5 . . . . .	RX J1520.9+4840 <sup>d</sup>	15 20 52.3	+48 39 38.6	0.073824	22132 km s <sup>-1</sup>	334 Mpc	13.81
6 . . . . .	RX J1548.9+0851 <sup>c</sup>	15 48 55.9	+08 50 44.4	0.072146	21629 km s <sup>-1</sup>	326 Mpc	13.50

<sup>a</sup> RX denotations refer to the corresponding ROSAT X-ray sources.

<sup>b</sup> from the list of Mendes de Oliveira et al. (2006); the  $R$  band magnitude is given instead of  $r'$ .

<sup>c</sup> from the list of Santos et al. (2007)

<sup>d</sup> from the new fossil group candidates (see Sect. 3)

**Table 3.4:** Observing log of spectroscopic observations.

ID	date	exposure	gratings	resolution <sup>a</sup>		PA <sup>b</sup>	spectral range
				blue	red		
1 . . . . .	20.12.2008	4 × 2700 s	R300B; R1200R	0.86	0.26	140°	3800–6250 Å ; 6600–7200 Å
2 . . . . .	20.12.2008	3 × 3000 s	R300B; R1200R	0.86	0.26	76°	3800–6250 Å ; 6600–7200 Å
3 . . . . .	20.12.2008	3 × 3000 s	R300B; R1200R	0.86	0.26	36°	3800–6250 Å ; 6600–7200 Å
4 . . . . .	28.04.2009	3 × 2700 s	R300B; R316R	0.86	0.93	23°	3800–6250 Å ; 6300–8500 Å
5 . . . . .	28.04.2009	3 × 2600 s	R300B; R316R	0.86	0.93	94°	3800–6250 Å ; 6300–8500 Å
6 . . . . .	28.04.2009	3 × 2600 s	R300B; R316R	0.86	0.93	33°	3800–6250 Å ; 6300–8500 Å

<sup>a</sup> in Å pix<sup>-1</sup>

<sup>b</sup> slit position angle (see Fig. 3.6)

The ellipticals have been selected according to their brightness, building up the bright end of the galaxy distribution as shown in Fig. 2.4.

Figure 3.4 illustrates the timetables for both nights. Time slots for Lick standards, spectrophotometric standards, arc comparison spectra, and the scientific targets are shown with the exposure time and average airmass of each individual slot<sup>17</sup>. The total integration time of the scientific targets was split into 3 or 4 single exposures of  $\sim 45$  minutes each (see Table 3.3) to correct for cosmic rays. Time refers to UT. The relatively large timeslots for spectrophotometric standards include the time for taking arcs, movement of the telescope, and locating targets (see Sect. 4). The box-sizes relate to the corresponding time intervals.

## 4 Observing process

As shown in Fig. 3.4, standard stars were observed first. The positioning of the telescope was checked by means of the ISIS TV camera displaying the current field-of-view of the telescope. Once Lick standards were located, various short exposures of different integration times of the order of a few seconds were taken to get a reasonable S/N without saturating the CCDs<sup>18</sup>.

<sup>17</sup>Detailed graphs of altitude and airmass are shown in Appendix B for all galaxies.

<sup>18</sup>The exposure times predicted by the exposure time calculator are merely guidelines and can differ due to the actual weather conditions or not exact positioning of the slit.



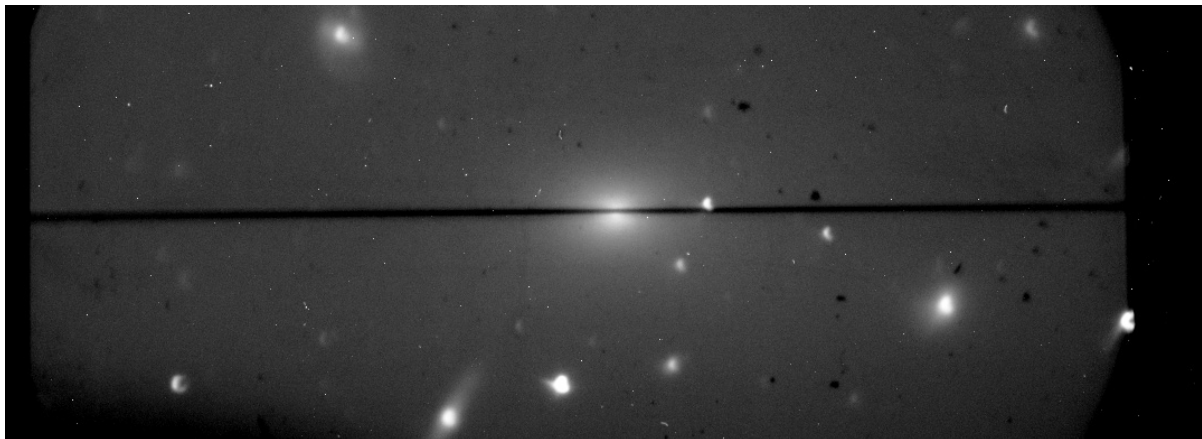
20.12.2008													
L1 - L4	S1	1-1	1-2	1-3	1-4	S2	2-1	2-2	2-3	S3	3-1	3-2	3-3
65min	25m	45min	45min	45min	45min	30m	50min	50min	50min	35m	50min	50min	50min
...	1.21	1.22	1.16	1.16	1.22	1.10	1.20	1.10	1.06	1.05	1.03	1.05	1.12
	20:05	20:30	21:20	22:10	23:00	23:45	00:15	01:10	02:05	02:55	03:30	04:25	05:20

28.04.2009													
S4	L5 - L7	4-1	4-2	4-3	S5	5-1	5-2	5-3	S6	6-1	6-2	6-3	
15m	40min	45min	45min	45min	25min	45min	45min	45min	25min	45min	45min	45min	
1.04	...	1.12	1.12	1.15	1.08	1.09	1.07	1.06	1.11	1.11	1.15	1.27	
	21:00	21:40	22:25	23:10	23:55	00:20	01:05	01:50	02:35	03:00	03:45	04:30	

**Figure 3.4:** Timetables for both nights at the WHT. Time slots for Lick standards, spectrophotometric standards, arc comparison spectra, and the scientific targets are shown. Times refer to UT.

For the fainter spectrophotometric standards integration times hadn't to be adjusted since no saturation was expected. After every movement of the telescope between individual targets, arc calibration frames were taken during the night since the heavy weight of the ISIS spectrograph could cause a slight shift in the observed wavelength region on the detector. Once the galaxies were located, the slit was aligned to the major axis of each galaxy. For that purpose the correct slit position angles were calculated for every galaxy in advance. Only for targets RX J0752.7+4557 and RX J0844.9+4258 the slit was aligned so that nearby bright galaxies were also covered by the slit (see Fig. 3.6).



**Figure 3.5:** TV slit view of RX J1520.9+4840 in 400s exposure. The black line is the spectrograph slit. Based on such previews, the slit was aligned for all targets.

Figure 3.5 shows a cutout of the ISIS TV slit view of RX J1520.9+4840. The horizontal black line is the spectrograph slit positioned along the major axis of the elliptical. Figure 3.6 shows the orientation of the spectrograph slit for all targets. Since extended sources such as galaxies take a much longer exposure time to reach an adequate S/N compared to stars, observations were unproblematic and did not necessitate any interference. Moreover, these sources are so faint that no concerns in saturating the CCDs are given. Thus, the only action that had to be carried out in-between the individual galaxy time slots was to take arc comparison spectra.

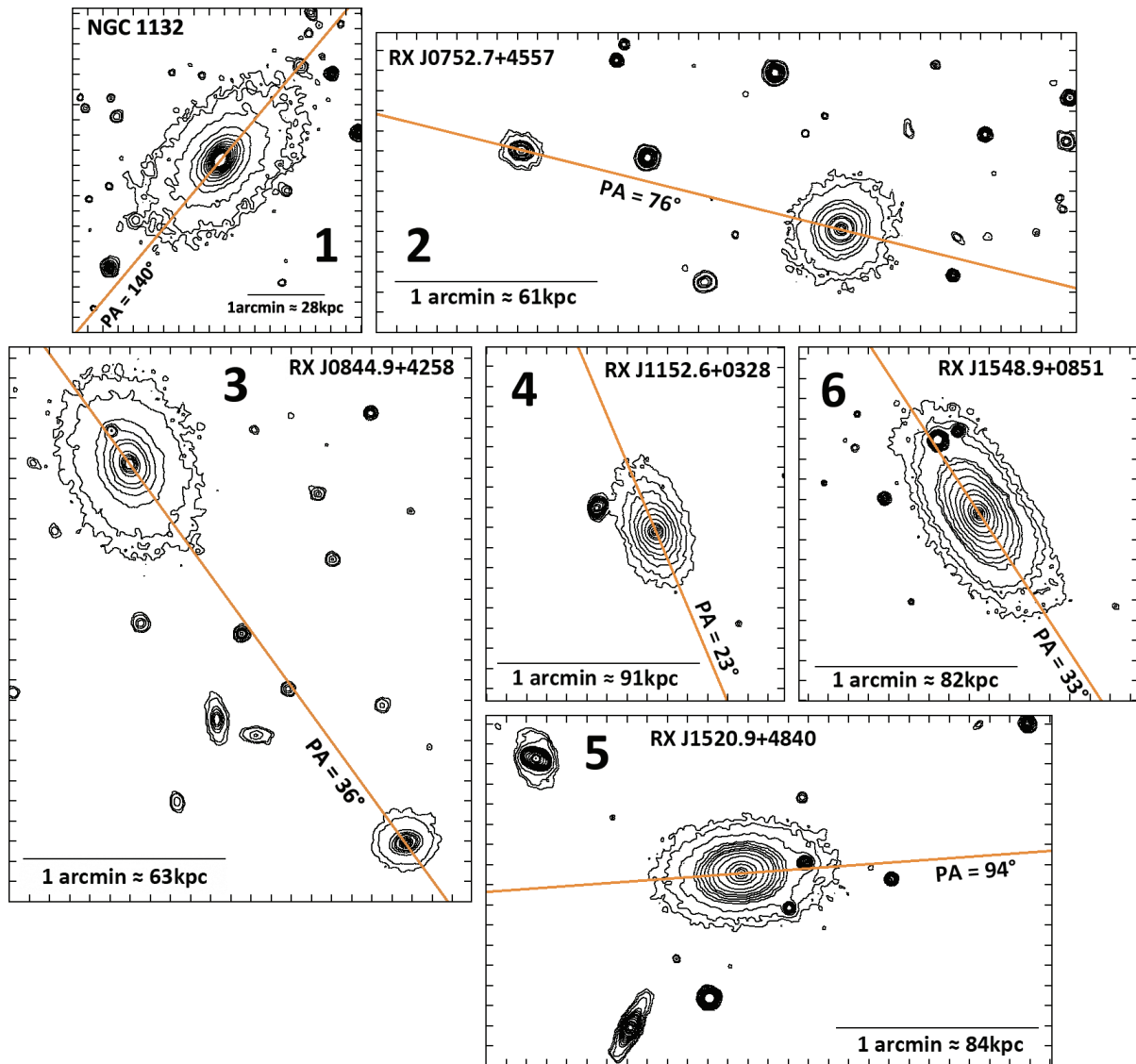


**Figure 3.6:** Orientation of the spectrograph slit for all targets observed at the WHT. Spatial scales and slit position angles are also shown. Isophotes are based on SDSS  $r'$  band images except for NGC 1132 (DSS image). In all charts, north is up, east to the left.

## 5 Data reduction

The fits files obtained with ISIS are stored with a running number in the order of observation. Before starting the actual data reduction steps, the files were renamed according to the type of observation (bias, flat, arc, science), target name, and spectrograph arm (blue, red) to avoid any mix-up. Additional information such as UT, airmass, or exposure time listed in the observing log were also considered for that purpose, unambiguously identifying each frame.

The reduction of long-slit spectra can be split into two parts. First, general CCD reduction steps such as bias subtraction, trimming, and flat-fielding are applied to remove the *instrument signature* on the obtained CCD frames. Once these general reduction steps have been carried out, the actual spectral reduction, i.e. extracting the spectrum, subtracting sky lines, flux-calibration, and wavelength calibration can be performed<sup>19</sup>. A detailed description of each reduction step is given in the next paragraphs.

## 1 CCD reduction

To apply the basic CCD reductions to the observed frames, the IRAF task `ccdproc` within the `ccdred` package was used. Since the tasks within the package rely on the header information of the images to be processed, the first step was to make sure that the individual image types used by `ccdred` (*zero*, *flat*, *object*, *comp*) were recognized correctly. Only arc comparison spectra were not recognized and had to be edited by `hedit file IMAGETYP comp`<sup>20</sup>.

### Bias subtraction and trimming

First, bias subtraction and trimming was carried out for all calibration and science exposures by means of the corresponding `ccdproc` parameters. Flat-field exposures were used to determine the bias- and trim-sections in the raw images. To remove any frame-to-frame variations in the average zero level, a constant bias value was estimated in the overscan region of the blue arm while a linear fit to the overscan region was adopted in the red. Remaining bias patterns were removed with the obtained bias exposures. For that purpose, master bias frames were created by average combining all individual bias frames of each night with `zerocombine`.

### Flat-fielding and fixing bad pixels

The bias-corrected flat-field frames were averaged to master flats with `flatcombine`. Since these flats are dominated by the large-scale spectral continuum shape of the tungsten lamps and the flat-fielding procedure intends to correct the multiplicative small-scale pixel to pixel gain variations across the CCD chip, these overall lamp characteristics had to be removed first. This was achieved with the `response` task, allowing us to interactively fit a function along the dispersion direction to normalize the lamp continuum. For both the red and blue arms a cubic spline was considered for that purpose. The order of the splines was chosen so that all the bumps and wiggles originating from the tungsten lamps were fit properly. The normalized master flats were then used to flat-field all galaxy and standard star science frames.

Remaining bad columns or lines in the flat-fielded science frames were removed with the `fixpix` task by creating a bad pixel mask<sup>21</sup> for both the red and blue arms. The routine replaces bad pixels by interpolating over the nearby pixel regions.

<sup>19</sup>For a detailed overview on CCD and spectral reduction, the *User's Guide to CCD Reductions with IRAF* and *User's Guide to Reducing Slit Spectra with IRAF* by Phil Massey are strongly recommended (<http://iraf.noao.edu/docs/spectra.html>)

<sup>20</sup>The task `ccdlist` allows to check if all frames are properly identified.

<sup>21</sup>The mask is defined with a simple table of the form  $x_{\text{begin}} x_{\text{end}} y_{\text{begin}} y_{\text{end}}$  specifying the image coordinates of the bad pixels.

## 2 Spectral reduction

With the detector signature removed from the data, the actual spectral reduction can be tackled. The package `twospec.longslit` was used for that purpose<sup>22</sup>.

### Removing geometric distortions and wavelength calibration

The first step in the spectral reduction was to remove all geometric distortions introduced by the camera optics or by any misalignment of the spectrograph gratings or slit. For that purpose the tasks `identify`, `reidentify`, `fitcoords` and `transform` have been used.

To correct for any tilt in the galaxy spectra, the peak of the spatial profile was identified every 250 columns along the dispersion direction. This trace was then fit by a 6<sup>th</sup> order Chebyshev polynomial and removed by applying the corresponding coordinate transformation. The result was checked by overplotting the spatial profile from different columns. To ensure the position of the spatial peak was located at the same pixel coordinate in all frames, the spectra were aligned manually along the spatial axis via `imshift`.

The detector pixel scale was then transformed into Ångstroms by means of the corresponding CuNe and CuAr arc comparison spectra taken during the nights. To achieve an optimal dispersion solution, the ISIS CuNe and CuAr line tables were added to the IRAF linelist defaults. First, a few features were identified by hand in the arc spectra. The remaining line positions were then recognized automatically and fit by a 3<sup>rd</sup> order cubic spline to set the dispersion solution. The procedure was iterated as long as a reliable RMS of the order of a few pixel percent was achieved.

This solution was then used to reidentify the corresponding features every 10 lines along the spatial direction to generate a wavelength coordinate map for all CCD frames. The procedure revealed shifts of the arc lines in the dispersion direction of the order of  $\sim 1-2$  pixel from frame to frame. The deviations along the slit were found to be negligible without any systematic trend.

Thus the created coordinate maps were fit by 6<sup>th</sup> order Chebyshev polynomials to transform the untilted and spatially aligned spectra to the two-dimensional wavelength scale resulting in orthogonal spatial and dispersion axes parallel to the image axes. The wavelength scale was verified with the position of the brightest sky lines.

### Image combination and cosmic ray removal

Once the individual wavelength scales had been assigned to each frame accounting for the small shifts in the dispersion direction, the spectra were average combined with `lscombine`. To filter out cosmic rays, the rejection parameter `minmax` was used. This proved to be very effective with almost all cosmic ray events removed. Any remaining signature was cleaned by hand within `splot`.

<sup>22</sup>To avoid any confusion: in all frames mentioned here, the dispersion axis runs along lines, the spatial axis along columns, hence `DISPAXIS=1`.

### Sky subtraction

The subtraction of the night sky background and emission lines was carried out with the `background` task by specifying two or three background windows on either side of the combined galaxy spectra. A 6<sup>th</sup> order Chebyshev polynomial was then fit to these background regions in all columns along the dispersion direction and subtracted from the data. For the fainter night sky emission lines, this procedure yielded an excellent result. Only the strongest lines, [O I]  $\lambda 5577 \text{ \AA}$  and the sodium doublet at  $\lambda \lambda 5890/6 \text{ \AA}$  in the blue and the bright OH lines in the red showed minor residual patterns.

### Extraction of standard star spectra

Standard star spectra were extracted by means of the `apall` task in the `twodspec.apextract` package. The extraction aperture and background windows were selected interactively. The sky background and trace of the spatial profile were fit by a 6<sup>th</sup> order Chebyshev polynomial. To minimize light loss due to differential atmospheric refraction, all stars have been observed with the slit oriented along the parallactic angle. However, because of the large slit width used for spectrophotometric standards and airmasses below 1.2, this atmospheric effect did not pose a severe problem. To retrieve the maximum signal-to-noise without biasing the resulting fluxes, the optimal extraction algorithm described by Horne (1986) has been applied.

### Flux calibration and telluric absorption lines

These extracted spectra were finally used to flux-calibrate the combined galaxy frames. Due to the long overall exposure times of the observed ellipticals, effective airmasses have been calculated for each individual target. For that purpose, the formula given by Stetson (1989)  $X_{\text{eff}} = 1/6 [X_{\text{start}} + 4 X_{\text{middle}} + X_{\text{end}}]$  has been used. Absolute flux tables (AB magnitudes) of the observed standard stars were taken from the La Palma Technical Notes 65 and 100<sup>23</sup>. To account for atmospheric extinction, the data from La Palma Technical Note 31 was applied. The task `standard` was used to integrate the standard star spectra over the bandpasses defined in the fluxtables, divide them by the exposure time, and compare these normalized count rates with the absolute flux values<sup>24</sup>. The output was then fit interactively with `sensfunc` to create sensitivity functions for both nights and both blue and red arms. These sensitivity functions were finally applied to the corresponding galaxy spectra with the task `calibrate`, removing both atmospheric extinction and the sensitivity characteristics of the CCD.

In addition to the contamination by night sky emission lines, the spectra in the red arm are also affected by absorption features originating in the Earth's atmosphere, so-called telluric lines. The strongest telluric features occur in the A band  $\lambda \lambda 7600 - 7630 \text{ \AA}$ , in the B band  $\lambda \lambda 6860 - 6890 \text{ \AA}$ , and also between  $\lambda \lambda 7170 - 7350 \text{ \AA}$ . Since a proper correction for these telluric features is challenging and most of the observed spectra do not show any presence of the nebular lines of interest ([N II], H $\alpha$ , and [S II]), no correction for telluric line removal was applied.

Figures 3.7 and 3.8 show the final reduced spectra in the blue and red arm of the central pixel of each galaxy in arbitrary flux units.

<sup>23</sup>[http://www.ing.iac.es/Astronomy/observing/manuals/man\\_tn.html](http://www.ing.iac.es/Astronomy/observing/manuals/man_tn.html)

<sup>24</sup>For that purpose AB magnitudes were converted into fluxes  $f_\nu$  [ergs s<sup>-1</sup> cm<sup>-2</sup> Hz<sup>-1</sup>] via  $AB_\nu = -2.5 \log f_\nu - 48.60$ .

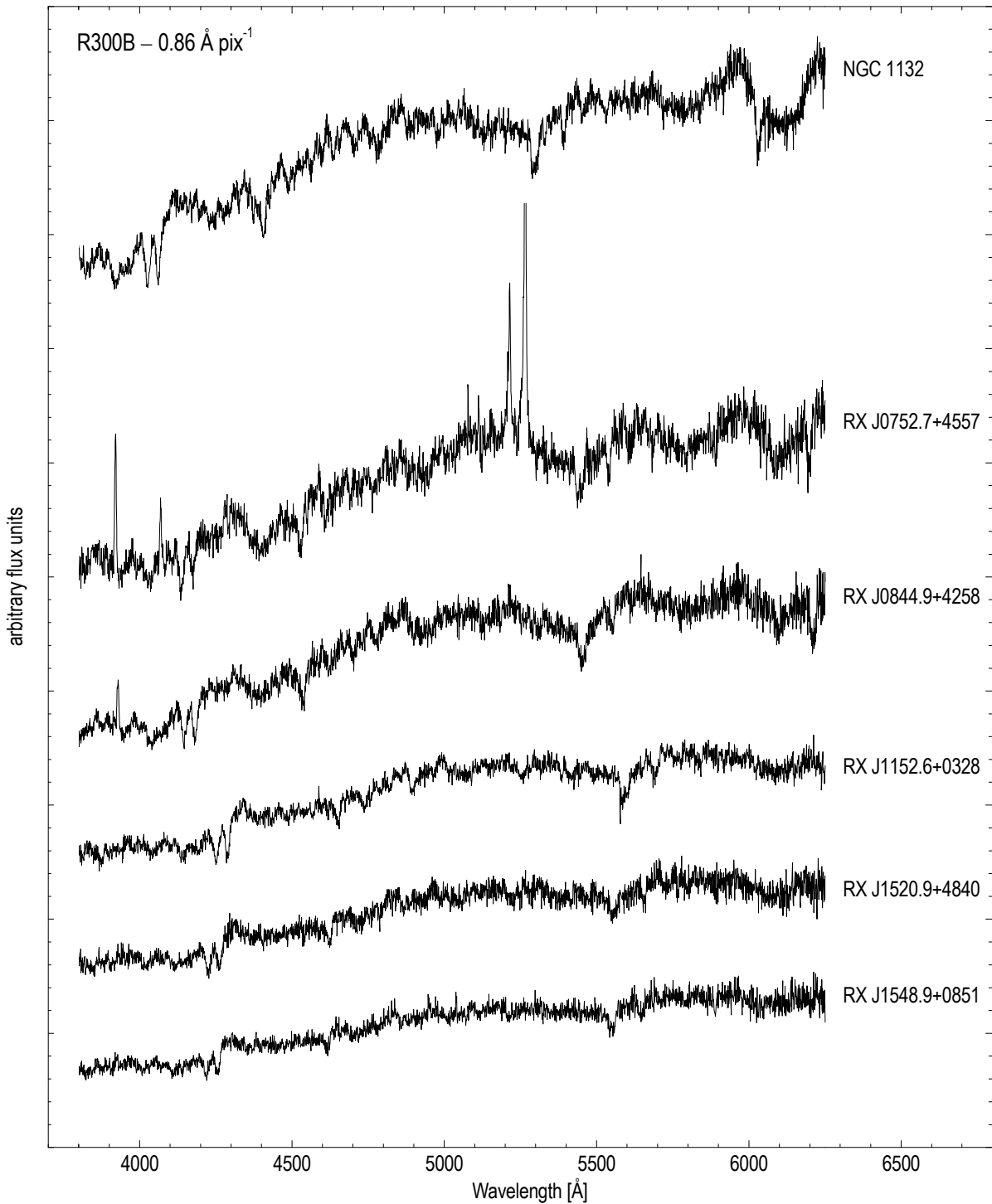


**Figure 3.7:** The reduced long-slit spectra in the ISIS blue arm of the central row of all six ellipticals observed at the WHT. The displayed spectral range is  $\lambda\lambda 3800\text{--}6250\text{ \AA}$ , the spectral resolution  $0.86\text{ \AA pix}^{-1}$ .

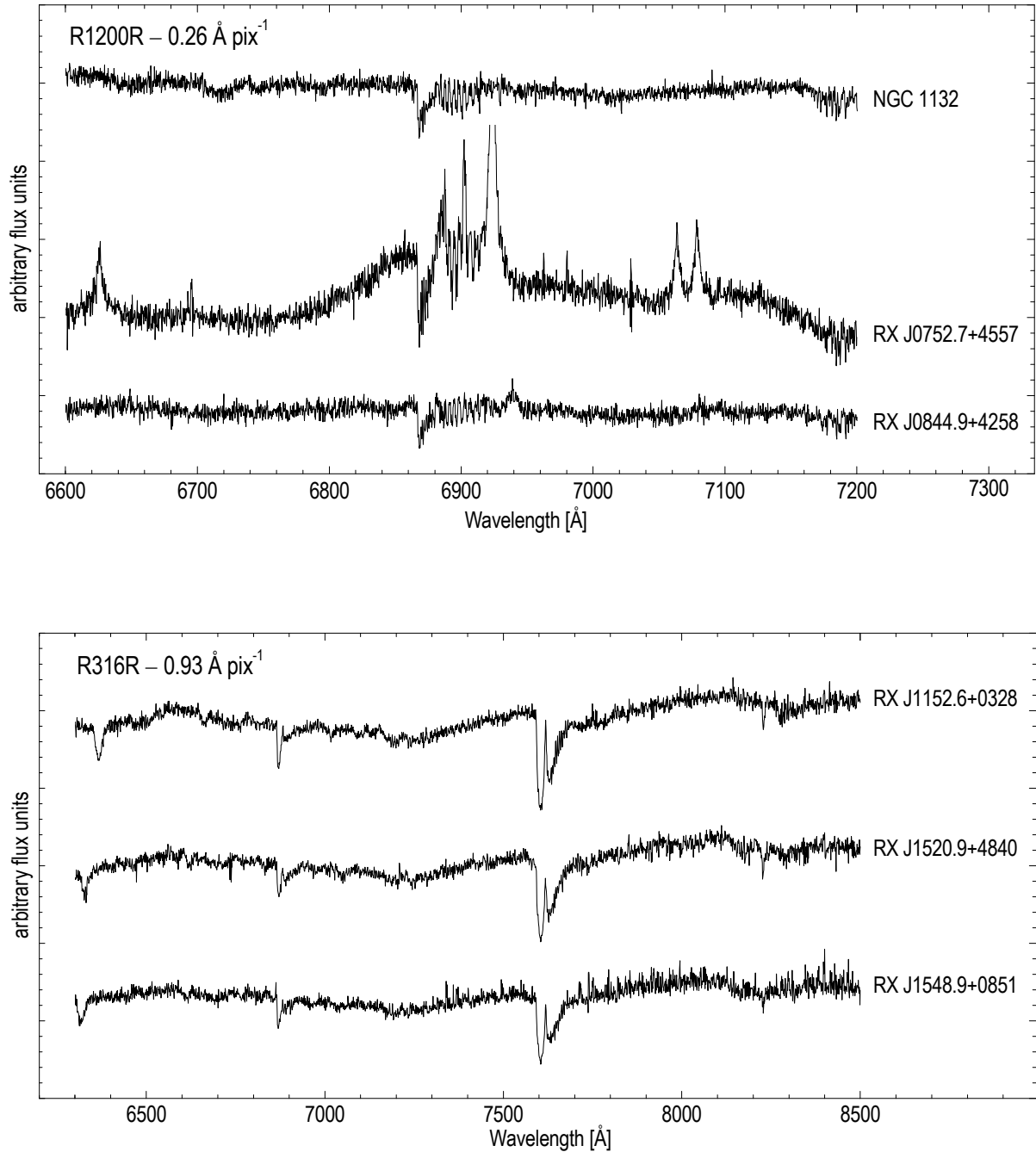


**Figure 3.8:** The reduced long-slit spectra in the ISIS red arm of the central row of all six ellipticals observed at the WHT. The displayed spectral range is  $\lambda\lambda 6600\text{--}7200\text{ \AA}$  in the upper panel and  $\lambda\lambda 6300\text{--}8500\text{ \AA}$  in the lower. The corresponding spectral resolutions are  $0.26\text{ \AA pix}^{-1}$  and  $0.93\text{ \AA pix}^{-1}$ . The spectra are dominated by the telluric absorption bands at  $\lambda\lambda 7600\text{--}7630\text{ \AA}$  and  $\lambda\lambda 6860\text{--}6890\text{ \AA}$ .

## 6 Lick Indices

In order to measure ages, metallicities and line strength gradients of the six observed fossil group central ellipticals, Lick/IDS indices as defined in Worthey et al. (1994) and Worthey & Ottaviani (1997) have been analyzed. The system covers a total of 25 indices (consisting of a central index band and blue and red continuum bands) measuring different blends of atomic absorption lines as well as six molecular bands (see Table 3.5). Atomic features are expressed in Å of equivalent widths while molecular bands are given in magnitudes

$$EW = \int_{\lambda_1}^{\lambda_2} \left(1 - \frac{F_{I\lambda}}{F_{C\lambda}}\right) d\lambda \quad \text{Mag} = -2.5 \log \left[ \left(\frac{1}{\lambda_2 - \lambda_1}\right) \int_{\lambda_1}^{\lambda_2} \frac{F_{I\lambda}}{F_{C\lambda}} d\lambda \right] \quad (3.1)$$

where  $F_{I\lambda}$  and  $F_{C\lambda}$  are the fluxes per unit wavelength in the index passband and continuum, respectively. Since the indices have been defined at moderate spectral resolution ( $\sim 9$  Å) one has to transform the galaxy spectra of interest to this low resolution first. For that purpose the Lick standard stars listed in Table 3.2 have been observed. Figures 3.9–3.14 highlight the redshifted index bands for all six ellipticals in the central pixel spectra smoothed to the LICK/IDS resolution. Other prominent lines are also marked. The strong bumps around the NaD feature in NGC 1132 are likely caused by the strong fall-off of the sensitivity function of the dichroic in that wavelength region.

**Table 3.5:** Lick/IDS indices.

name	index band		blue continuum		red continuum		unit <sup>a</sup>
H $\delta_A$ .....	4083.500	4122.250	4041.600	4079.750	4128.500	4161.000	Å
H $\delta_F$ .....	4091.000	4112.250	4057.250	4088.500	4114.750	4137.250	Å
CN <sub>1</sub> .....	4142.125	4177.125	4080.125	4117.625	4244.125	4284.125	mag
CN <sub>2</sub> .....	4142.125	4177.125	4083.875	4096.375	4244.125	4284.125	mag
Ca4227 .....	4222.250	4234.750	4211.000	4219.750	4241.000	4251.000	Å
G4300 .....	4281.375	4316.375	4266.375	4282.625	4318.875	4335.125	Å
H $\gamma_A$ .....	4319.750	4363.500	4283.500	4319.750	4367.250	4419.750	Å
H $\gamma_F$ .....	4331.250	4352.250	4283.500	4319.750	4354.750	4384.750	Å
Fe4383 .....	4369.125	4420.375	4359.125	4370.375	4442.875	4455.375	Å
Ca4455 .....	4452.125	4474.625	4445.875	4454.625	4477.125	4492.125	Å
Fe4531 .....	4514.250	4559.250	4504.250	4514.250	4560.500	4579.250	Å
Fe4668 .....	4634.000	4720.250	4611.500	4630.250	4742.750	4756.500	Å
H $\beta$ .....	4847.875	4876.625	4827.875	4847.875	4876.625	4891.625	Å
Fe5015 .....	4977.750	5054.000	4946.500	4977.750	5054.000	5065.250	Å
Mg <sub>1</sub> .....	5069.125	5134.125	4895.125	4957.625	5301.125	5366.125	mag
Mg <sub>2</sub> .....	5154.125	5196.625	4895.125	4957.625	5301.125	5366.125	mag
Mg <i>b</i> .....	5160.125	5192.625	5142.625	5161.375	5191.375	5206.375	Å
Fe5270 .....	5245.650	5285.650	5233.150	5248.150	5285.650	5318.150	Å
Fe5335 .....	5312.125	5352.125	5304.625	5315.875	5353.375	5363.375	Å
Fe5406 .....	5387.500	5415.000	5376.250	5387.500	5415.000	5425.000	Å
Fe5709 .....	5696.625	5720.375	5672.875	5696.625	5722.875	5736.625	Å
Fe5782 .....	5776.625	5796.625	5765.375	5775.375	5797.875	5811.625	Å
NaD .....	5876.875	5909.375	5860.625	5875.625	5922.125	5948.125	Å
TiO <sub>1</sub> .....	5936.625	5994.125	5816.625	5849.125	6038.625	6103.625	mag
TiO <sub>2</sub> .....	6189.625	6272.125	6066.625	6141.625	6372.625	6415.125	mag

<sup>a</sup> Atomic features are expressed in Å of equivalent widths, molecular bands in magnitudes.



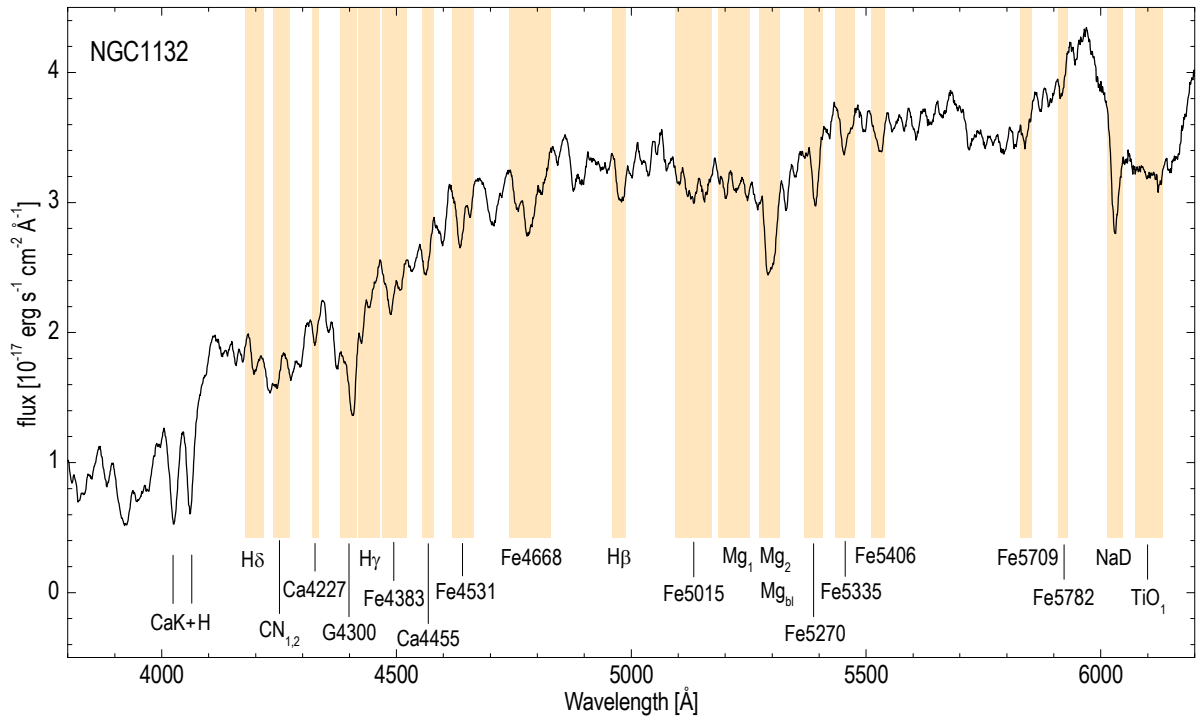


**Figure 3.9:** NGC 1132 – spectrum of the central pixel in the ISIS blue arm smoothed to the Lick/IDS resolution ( $\sim 9 \text{ \AA}$ ). Spectral lines and Lick/IDS index passbands are highlighted.

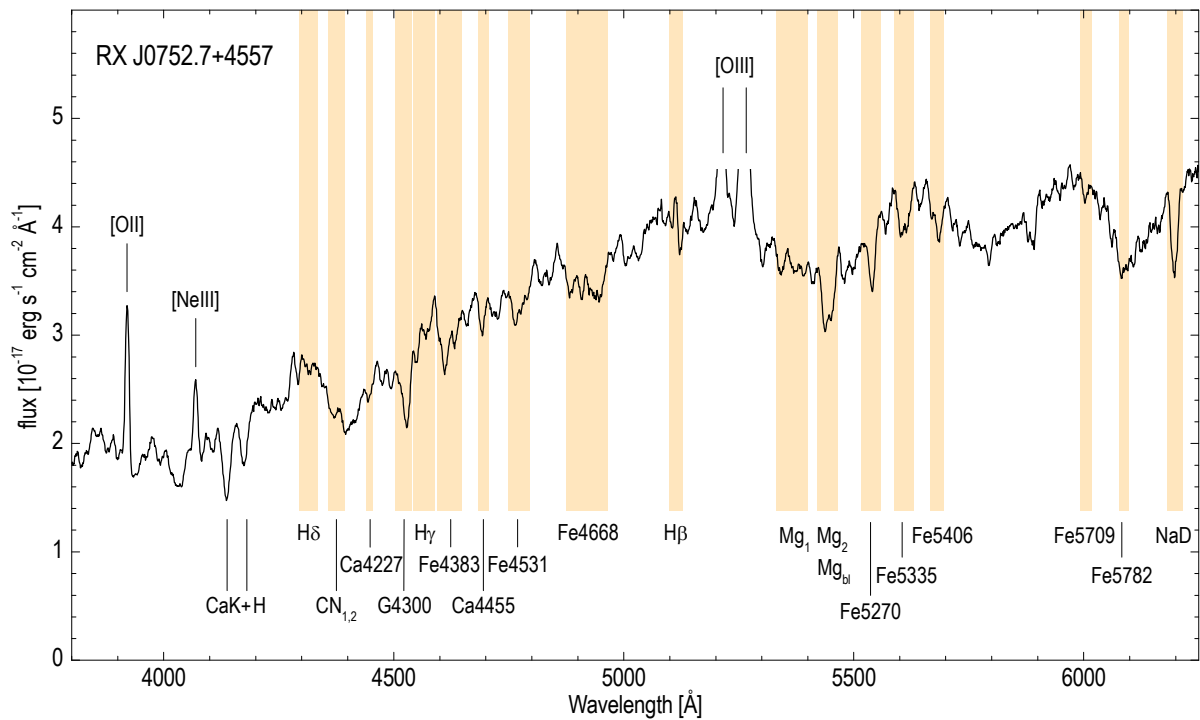


**Figure 3.10:** RX J0752.7+4557 – spectrum of the central pixel in the ISIS blue arm smoothed to the Lick/IDS resolution ( $\sim 9 \text{ \AA}$ ). Spectral lines and Lick/IDS index passbands are highlighted.

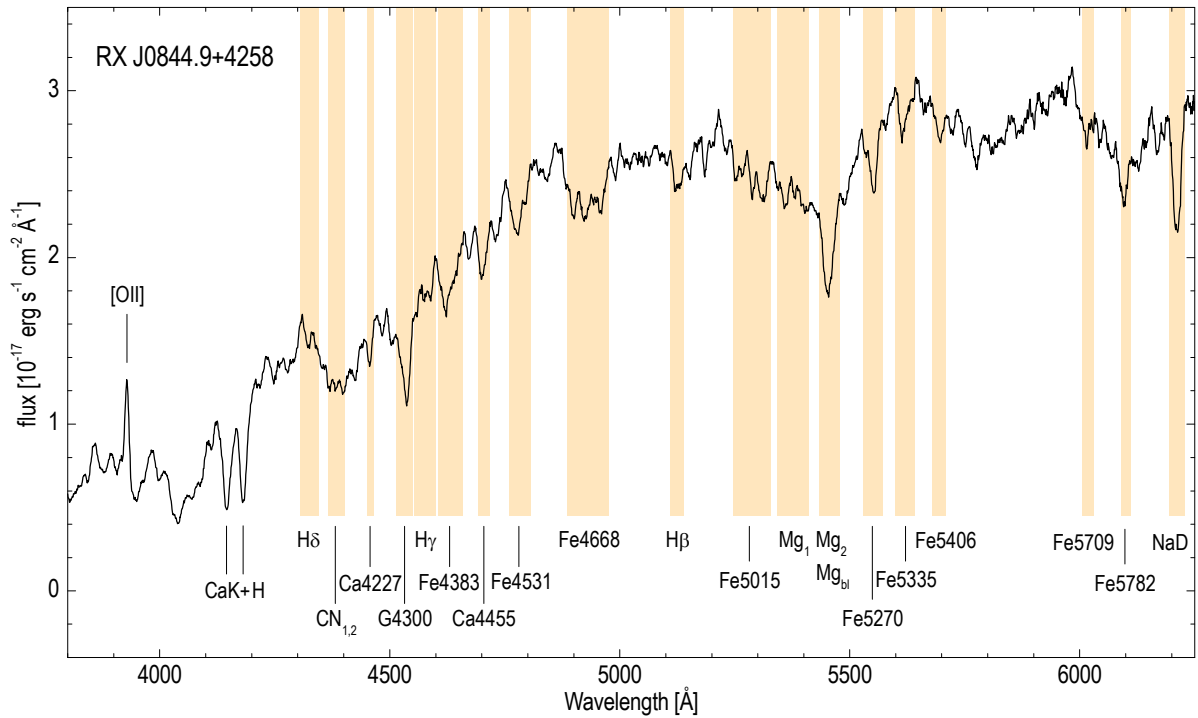


**Figure 3.11:** RX J0844.9+4258 – spectrum of the central pixel in the ISIS blue arm smoothed to the Lick/IDS resolution ( $\sim 9 \text{ \AA}$ ). Spectral lines and Lick/IDS index passbands are highlighted.

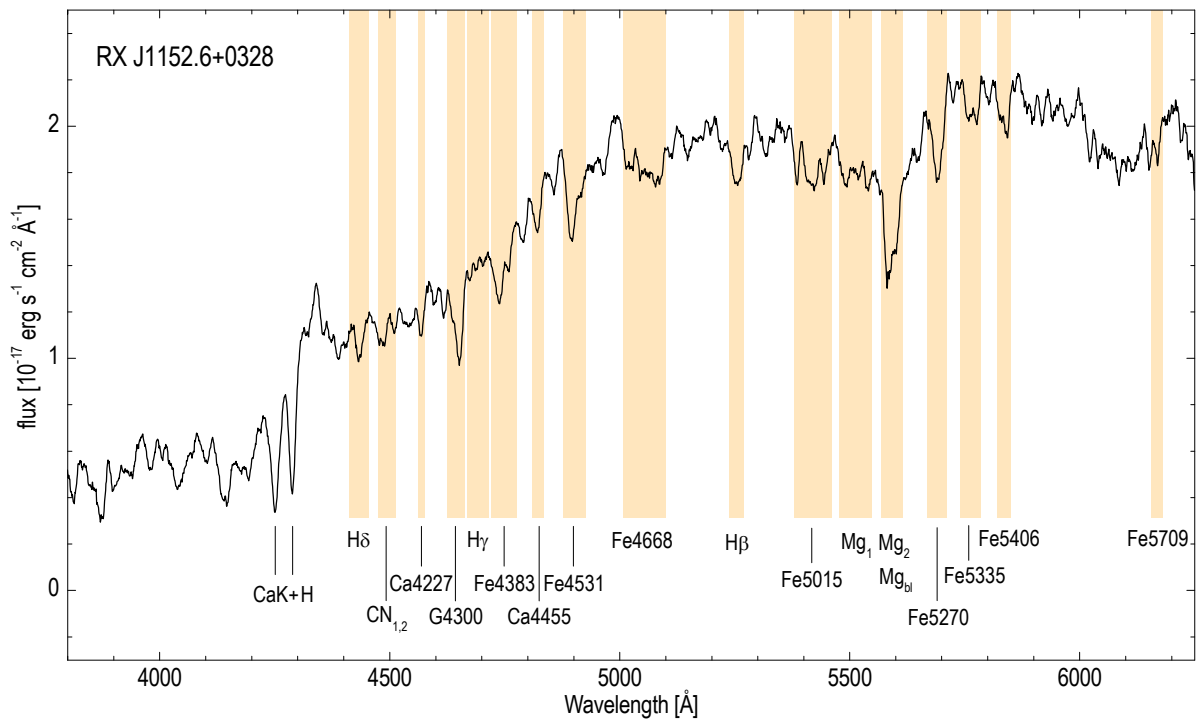


**Figure 3.12:** RX J1152.6+0328 – spectrum of the central pixel in the ISIS blue arm smoothed to the Lick/IDS resolution ( $\sim 9 \text{ \AA}$ ). Spectral lines and Lick/IDS index passbands are highlighted.

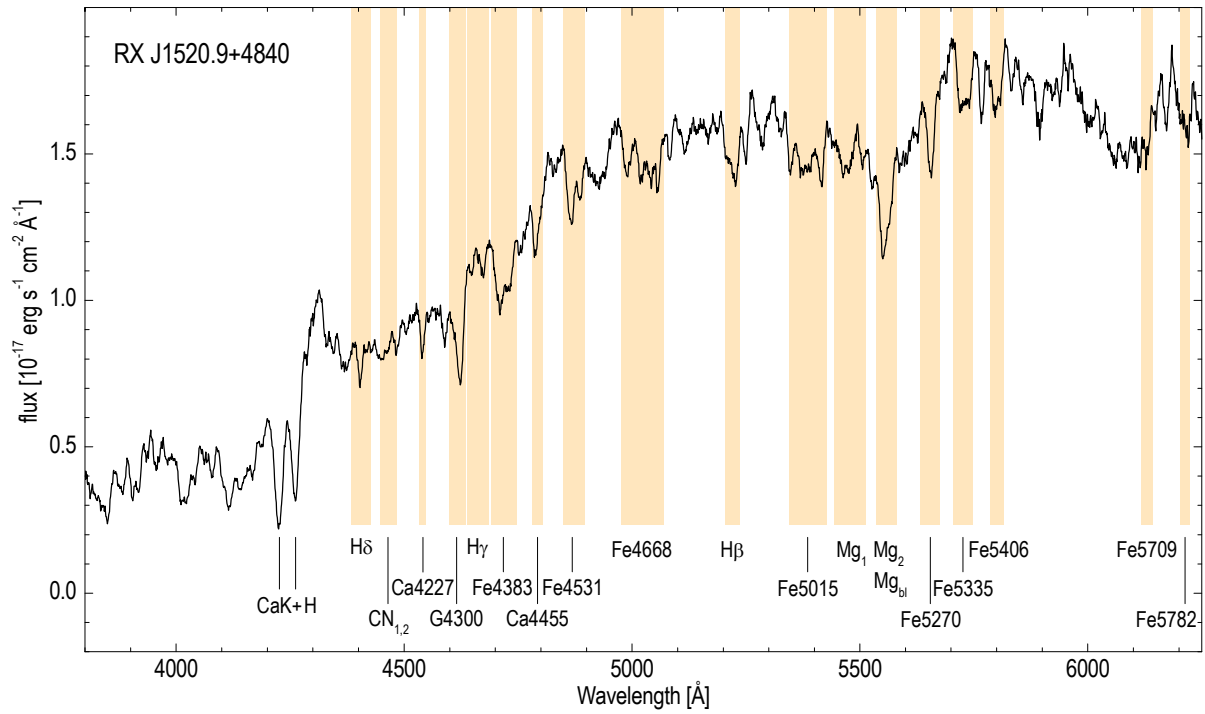


**Figure 3.13:** RX J1520.9+4840 – spectrum of the central pixel in the ISIS blue arm smoothed to the Lick/IDS resolution ( $\sim 9 \text{ \AA}$ ). Spectral lines and Lick/IDS index passbands are highlighted.

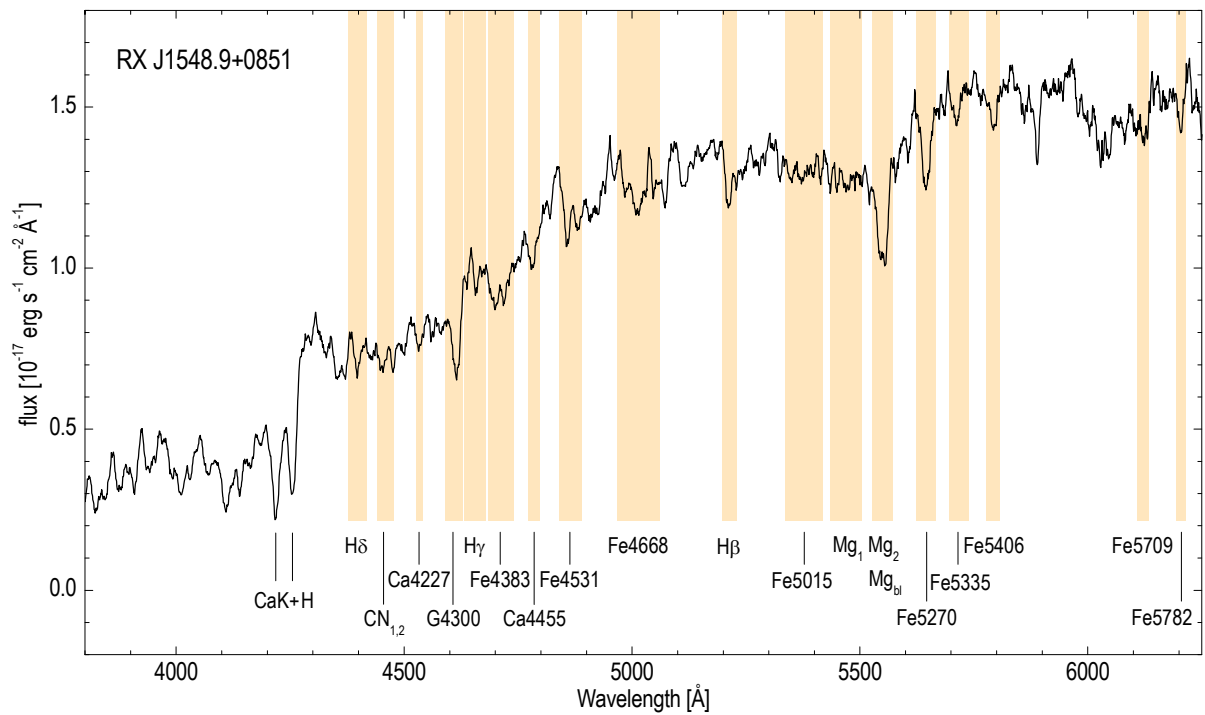


**Figure 3.14:** RX J1548.9+0851 – spectrum of the central pixel in the ISIS blue arm smoothed to the Lick/IDS resolution ( $\sim 9 \text{ \AA}$ ). Spectral lines and Lick/IDS index passbands are highlighted.

## 1 Measuring Lick indices with `indexf`

To measure Lick indices for the presented sample of ellipticals, the open-source program `indexf`<sup>25</sup> (Cardiel 2007) has been used. The software allows us to compute the indices presented in Table 3.5 according to equations 3.1.

With the exception of Fe5782, NaD and TiO for individual galaxies, all features of interest are located in the blue arm. Thus, only blue-arm spectra were taken into account for the Lick index measurements. Since the investigation of spatial variations of age and metallicity along the galaxy major axis is the primary goal, the spectra were binned along the spatial direction to achieve a higher S/N. Because the seeing was estimated to 1.3 and 0.7 arcsec for the two nights at the WHT (see Table 3.1), these values set a reasonable lower limit for any binning along the spatial direction and correspond to about 7 and 4 pixels, respectively. To achieve a reasonable S/N along the whole slit, more rows were binned in the galaxy outskirts than in the central parts.

The signal-to-noise ratio was estimated for all binned spectra in a small, featureless region ( $35 \text{ \AA} \simeq 70 \text{ pixel}$ ) at rest-frame wavelength of  $\sim 5140 \text{ \AA}$  by means of the IRAF `splot` task. It is essential that the continuum of the chosen region isn't contaminated by any emission or absorption lines since `splot` would treat these features as noise.

Since the spectral resolution of the Lick/IDS system amounts to only  $\sim 9 \text{ \AA}$ , the observed spectra had to be degraded in resolution first. For that purpose, the widths of emission lines in the arc comparison spectra were measured yielding a FWHM of  $\sim 3.6 \text{ \AA}$  at  $\sim 4800 \text{ \AA}$  in all spectra. To obtain a resolution comparable to the Lick/IDS system, the spectra have been convolved with a Gaussian kernel<sup>26</sup> of dispersion

$$\sigma_{\text{smooth}} = \sqrt{\frac{(\text{FWHM}_{\text{Lick}})^2 - (\text{FWHM}_{\text{obs.}})^2}{8 \ln 2}} \quad (3.2)$$

For the present values of  $\text{FWHM}_{\text{Lick}} = 9 \text{ \AA}$  and  $\text{FWHM}_{\text{obs.}} = 3.6 \text{ \AA}$ , and the dispersion of  $0.86 \text{ \AA pix}^{-1}$ ,  $\sigma_{\text{smooth}}$  was set to 4.1 pixel. The broadened spectra were then analysed with `indexf`. The program is operated on the command line and input parameters are specified in pairs of `keyword=keyvalue`. For example, the Mg<sub>2</sub> index was measured by typing

```
indexf if=galaxy.fits,0,0 index=Mg2 rv=23456,30 minmaxsn=34,34 nsimulsn=200 > Mg2.txt
```

where *galaxy.fits* is the spectrum to be measured, `index` the corresponding index, `rv` the radial velocity of the galaxy and associated error. In order to estimate errors of the measured indices, `indexf` offers the possibility to either provide an error spectrum or alternatively a range of S/N ratios for each utilized spectrum. In the latter case, a certain number of Monte Carlo simulations can be specified by the user via `nsimulsn=` to estimate the index errors according to the given S/N range set by `minmaxsn=`. In the present work, the fixed S/N estimated at rest-frame wavelength of  $\sim 5140 \text{ \AA}$  and 200 Monte Carlo simulations were considered. Final index strengths and errors were then computed as the mean of the 200 Monte Carlo simulations.

<sup>25</sup>version 3.0 – 24.08.2005

<http://www.ucm.es/info/Astrof/software/indexf/indexf.html>

<sup>26</sup>see IRAF task `gauss`

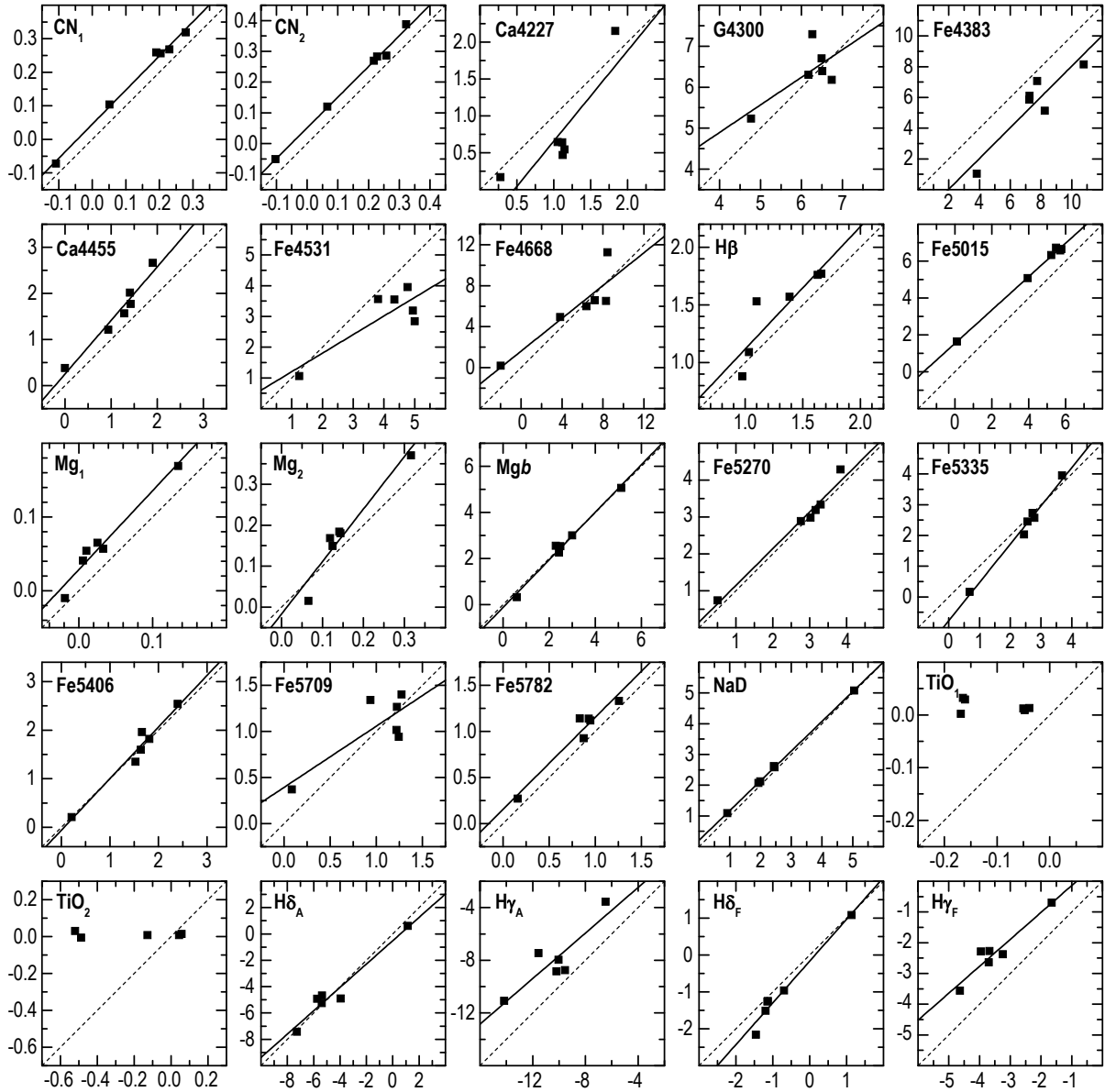


**Figure 3.15:** Comparison between the measured indices and the original Lick data from Worthey & Ottaviani (1997) for the observed Lick standards. Horizontal data present the measured indices from this work while vertical data are those from the literature. Dashed lines indicate unity and solid ones present linear least squares fits to the data.

## 2 Index corrections

Figure 3.15 shows the comparison between the measured indices and the original Lick data from Worthey & Ottaviani (1997) for the observed Lick standards. While some indices show only small differences compared to the original Lick data (e.g. Fe5270), others exhibit clear deviations (e.g. TiO1). This can be explained by the fact that indices at the very edge of the detector like TiO1 and TiO2 are severely noise-dominated because of the strong sensitivity cut-off of the CCD chip or simply because the index itself is not very strong and thus difficult to measure. To quantify the deviations to the Lick system, linear relations of the form

$$\text{index}_{\text{measured}} = \beta + \alpha \cdot \text{index}_{\text{Lick}} \quad (3.3)$$

have been fit to the data, indicated as solid lines in Fig. 3.15.

When analysing absorption line strengths in elliptical galaxies, one also has to consider the stellar velocity dispersion of the investigated galaxy which can severely alter the observed index. In general, line strengths decrease continuously with increasing velocity dispersion because of the Doppler broadening of the investigated spectral line. Thus, in order to get reasonable line strengths related to the element abundances only, one has to correct for this broadening.

Figure 3.16 shows the dependence of index strengths as a function of increasing velocity dispersion for the observed Lick standards. Index values at different dispersions were obtained by measuring all indices consecutively in the Lick standard star spectra broadened to 50–400 km s<sup>-1</sup> in steps of 50 km s<sup>-1</sup> according to equation 3.2. The presented index strengths have been normalized to the corresponding values at zero velocity dispersion.

Assuming that  $(\text{index}_{i,j,\sigma})$  and  $(\text{index}_{i,j,0})$  are the absorption line strengths of index  $i$  and standard star  $j$  measured at velocity dispersion  $\sigma$  and 0, then

$$\mathcal{R}_{i,\sigma} = \frac{1}{n} \sum_{j=1}^n \left( \frac{\text{index}_{i,j,\sigma}}{\text{index}_{i,j,0}} \right) \quad (3.4)$$

is the average correction factor estimated from all observed standard stars for index  $i$ . Thus, an index in a galaxy with velocity dispersion  $\sigma$  can be corrected by means of

$$\text{index}_{i,0} = \text{index}_{i,\sigma} \cdot \mathcal{R}_{i,\sigma}^{-1} \quad (3.5)$$

The graphs in Fig. 3.16 represent the correction factors  $\mathcal{R}_{i,j,\sigma}$  for the individual standard stars  $j$  with increasing velocity dispersion. Not all indices show the same dependency. While iron lines show a rather steep decline in index strengths, Balmer lines such as H $\beta$  or H $\gamma$ , or the molecular index Mg<sub>2</sub> show comparatively small dependence. The individual data were averaged according to equation 3.4 (excluding obvious outliers) and fit by third order polynomials to estimate the final correction factors  $\mathcal{R}_{i,\sigma}$  at any given dispersion.

Ultimately, all indices measured in the six observed ellipticals were corrected for velocity dispersion first following equation 3.5 and subsequently transformed to the published Lick data according to relation 3.3.

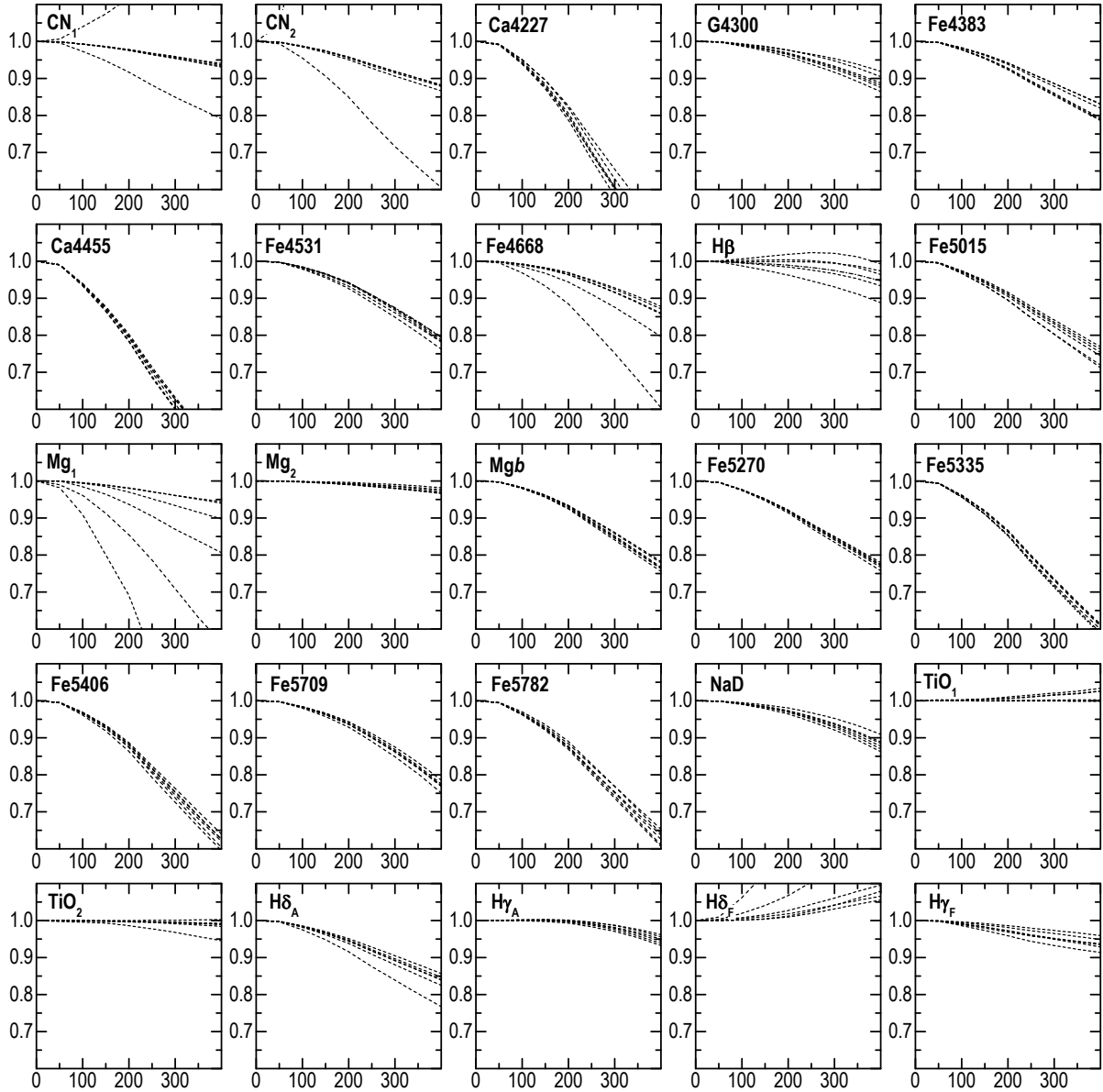


**Figure 3.16:** Index strengths as a function of increasing velocity dispersion normalised to zero dispersion for the observed Lick standards. The graphs are based on index measurements at 50–400 km s<sup>-1</sup> dispersion in steps of 50 km s<sup>-1</sup>. Indices decline with increasing dispersion because of line broadening. Values correspond to correction factors  $\mathcal{R}_{i,j,\sigma}$ , see text.

### 3 Results

According to Schiavon (2007), the best way to estimate the age and metallicity of a stellar population by means of the integrated absorption line-strengths is to compare the observed strengths with SSP models involving an iron index, preferably Fe5270 or Fe5335, and  $H\beta$ .

Figure 3.17 shows the corresponding SSP models for Fe5270, Fe5335 and  $H\beta$  from Schiavon (2007). The models are based on solar scaled abundances. Dashed lines indicate constant ages from 2.5 to 15.8 Gyr and metallicities from -1.3 to 0.2 dex. The triangles refer to the observed ellipticals. As expected, all galaxies exhibit old ( $> 10$  Gyr) stellar populations. According to the measured  $H\beta$  index, galaxies 2 and 3 show comparatively old ages and have been shifted to the bottom of the diagram for better visualization. Since these galaxies exhibit emission lines in their spectra, the age estimated from the measured  $H\beta$  index is questionable anyway. However, metallicities lie in the same range in both diagrams, yet showing clear differences for individual galaxies. This is not surprising since the overall metallicity of a galaxy is derived from individual absorption features only. A more precise method, accounting for every pixel in the observed spectrum is highlighted in the upcoming section.

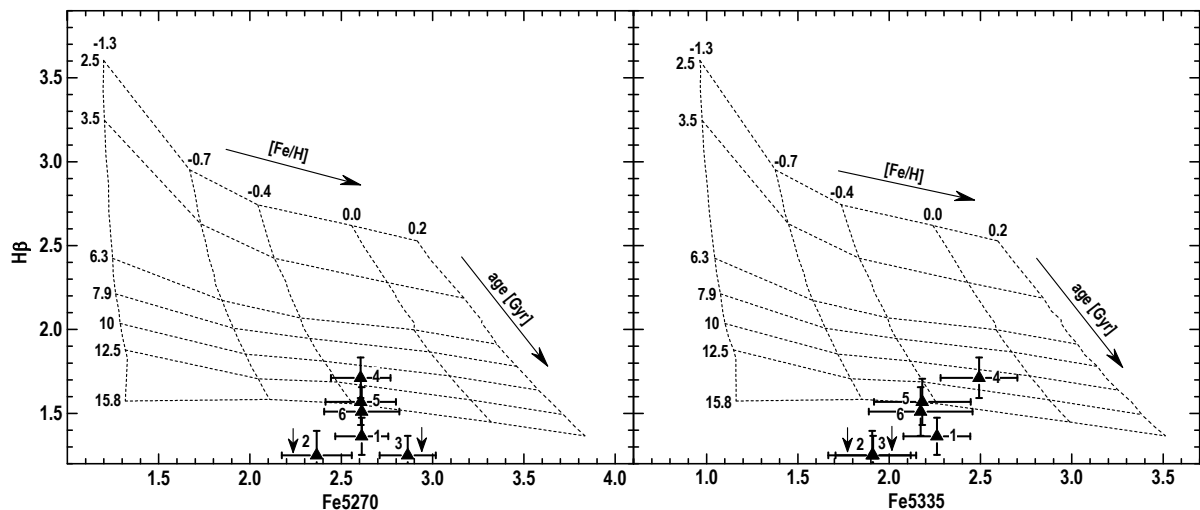


**Figure 3.17:** SSP models for the Lick indices Fe5270, Fe5335, and  $H\beta$  taken from Schiavon (2007). The WHT ellipticals are shown as triangles.

Figures 3.18–3.23 show the radial line-strength gradients derived from all measured indices in the six observed ellipticals. Every index and corresponding error bar is the result and average of 200 Monte Carlo simulations. To correct the indices for velocity dispersion, the accordant data obtained from the full spectrum fitting technique in the upcoming section have been considered. In all panels, the galaxy center is indicated as vertical dashed line. The distance from the galaxy center is given in arcsec. Negative line-strength gradients are clearly visible in the most prominent absorption features such as  $Mg_2$  or various iron lines (Fe5270, Fe4383, ...) indicating negative metallicity gradients. No gradients have been measured for  $TiO_1$  and  $TiO_2$  following their location at the very edge of the detector and hence impossible transformation to the Lick/IDS system.



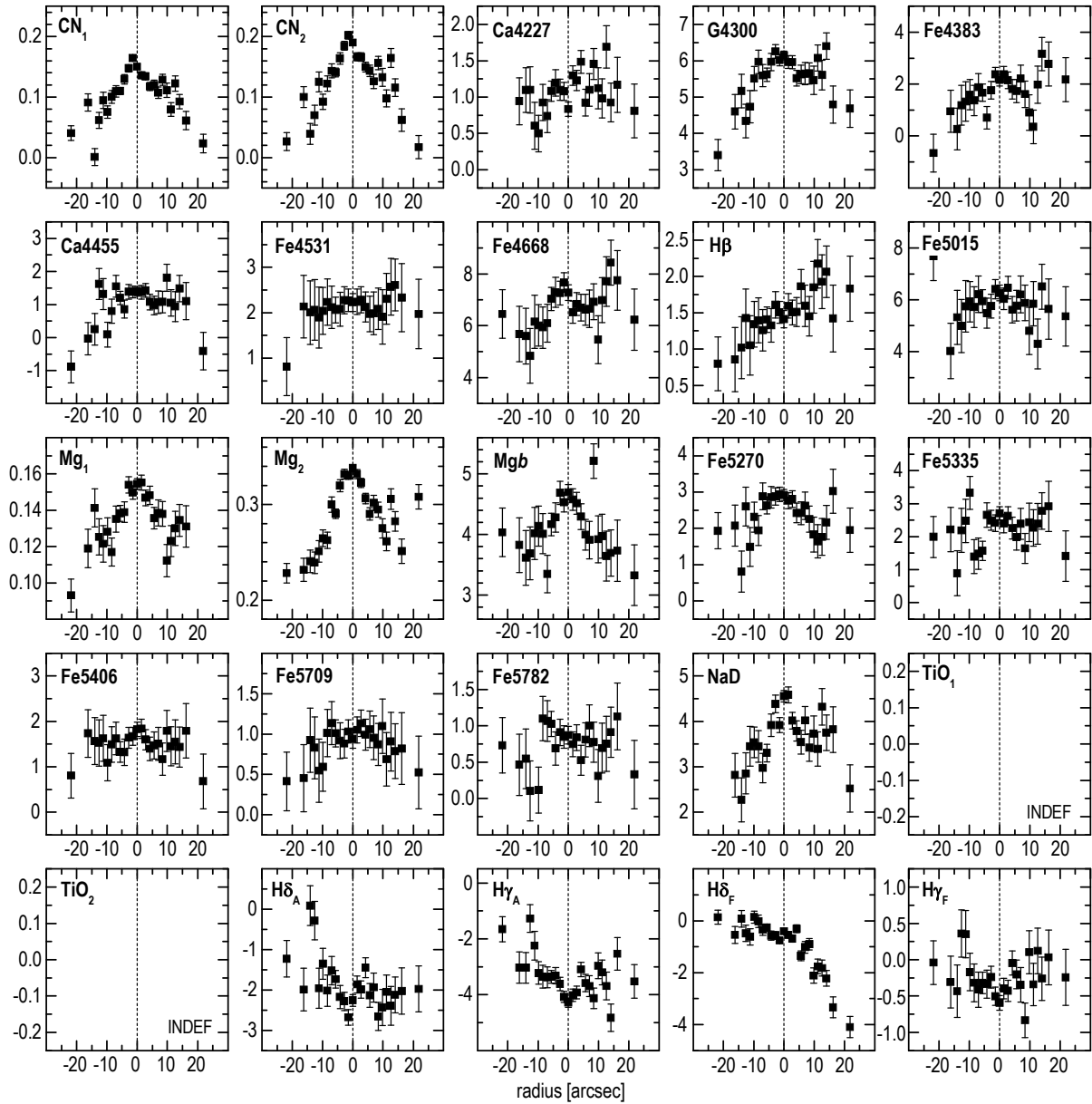


Figure 3.18: 1 – NGC 1132. Line strength gradients.

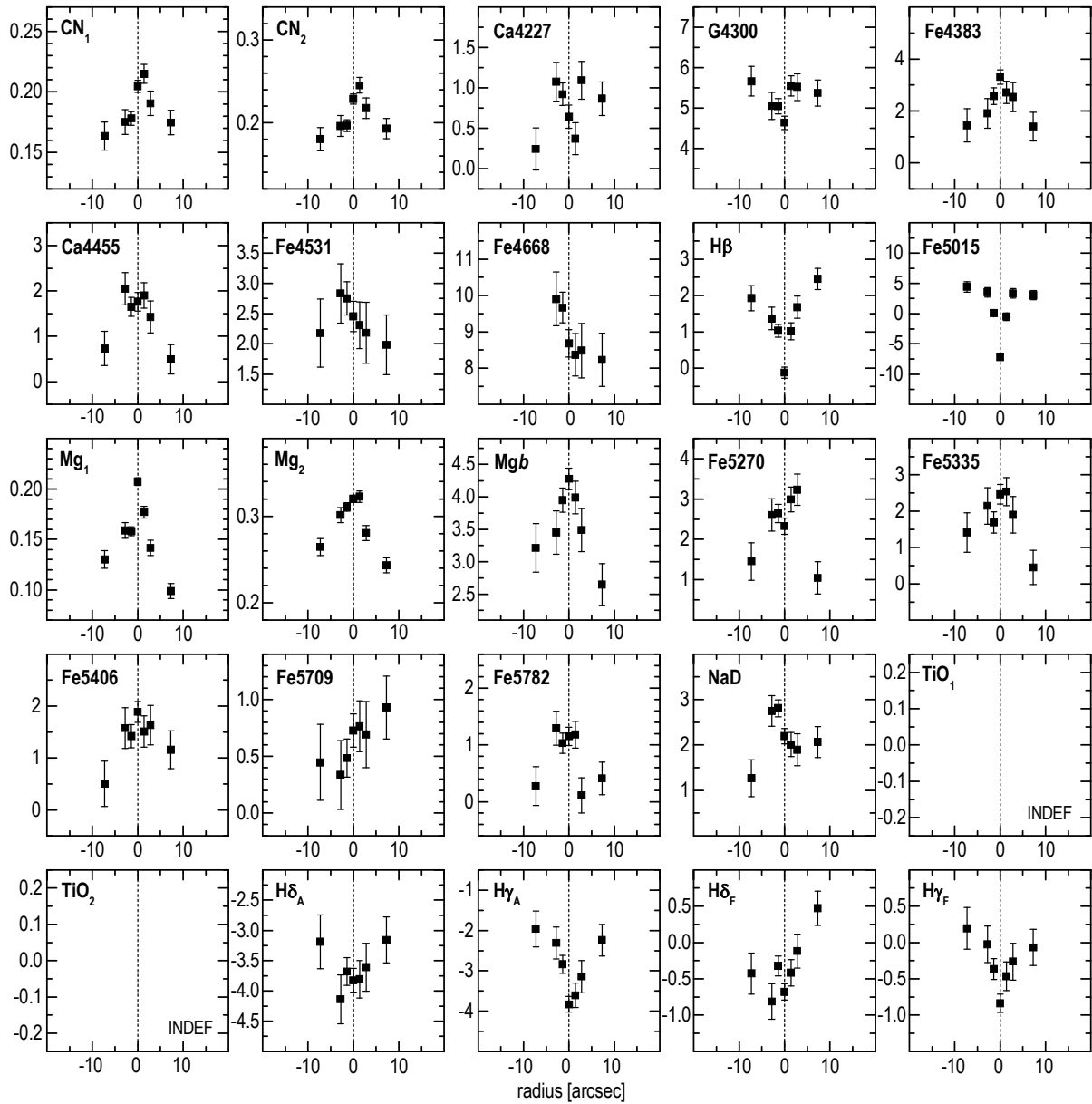
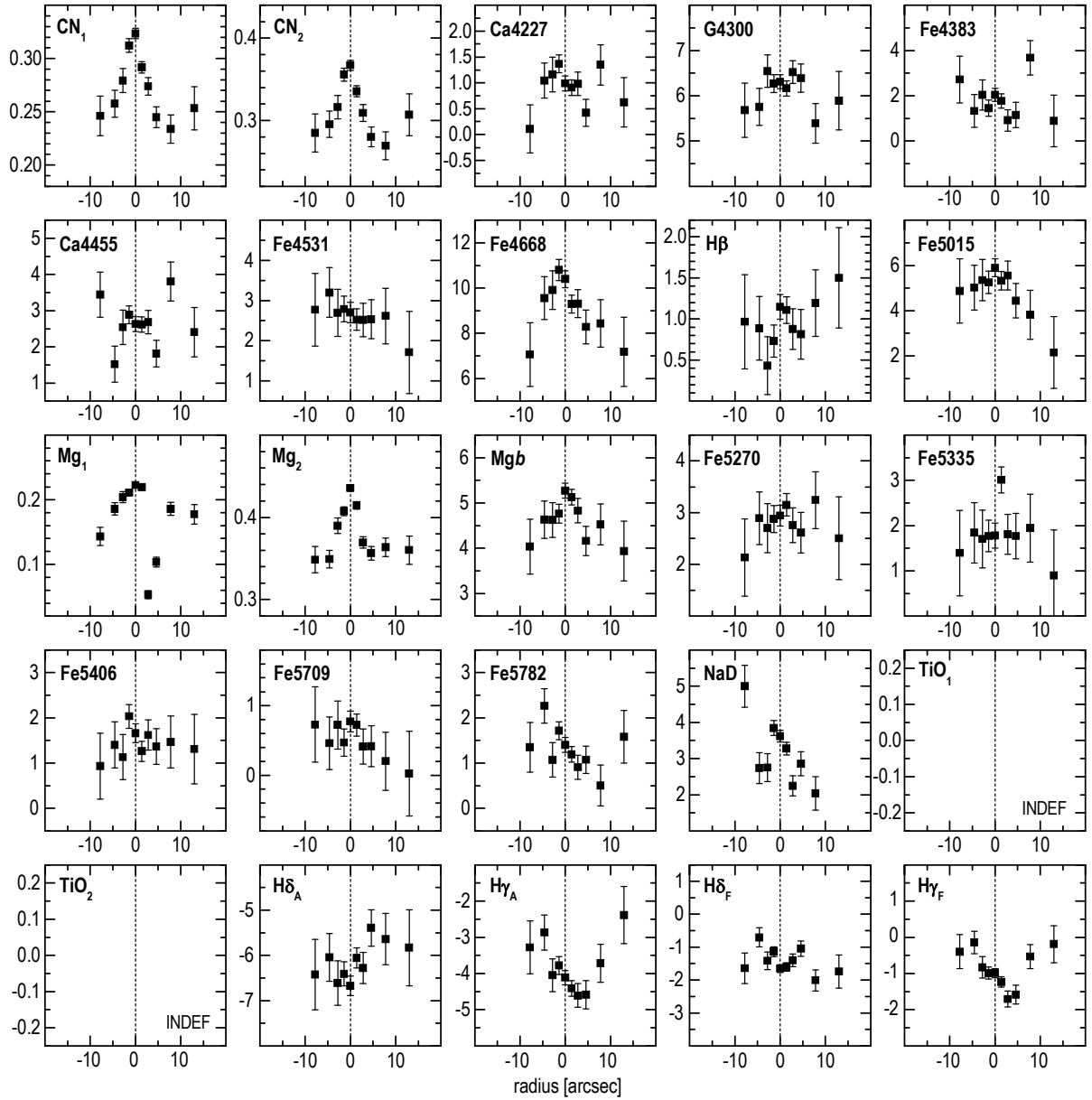
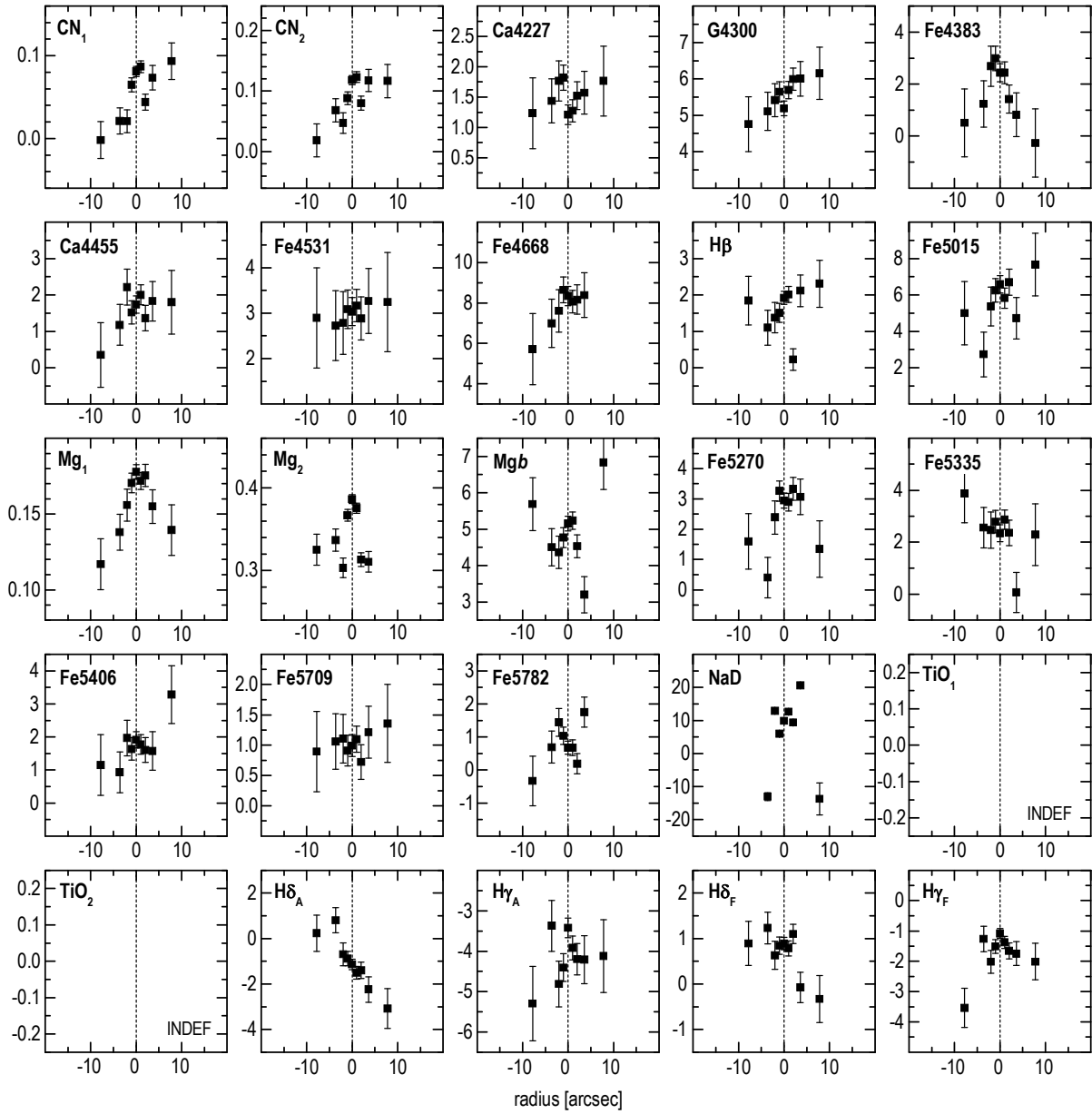


Figure 3.19: 2 – RX J0752.7+4557. Same as Fig. 3.18. Effective radius  $r_e = 7.1$  arcsec.



**Figure 3.20:** 3 – RX J0844.9+4258. Same as Fig. 3.18. Effective radius  $r_e = 18$  arcsec.



**Figure 3.21:** 4– RX J1152.6+0328. Same as Fig. 3.18. Effective radius  $r_e = 53$  arcsec.

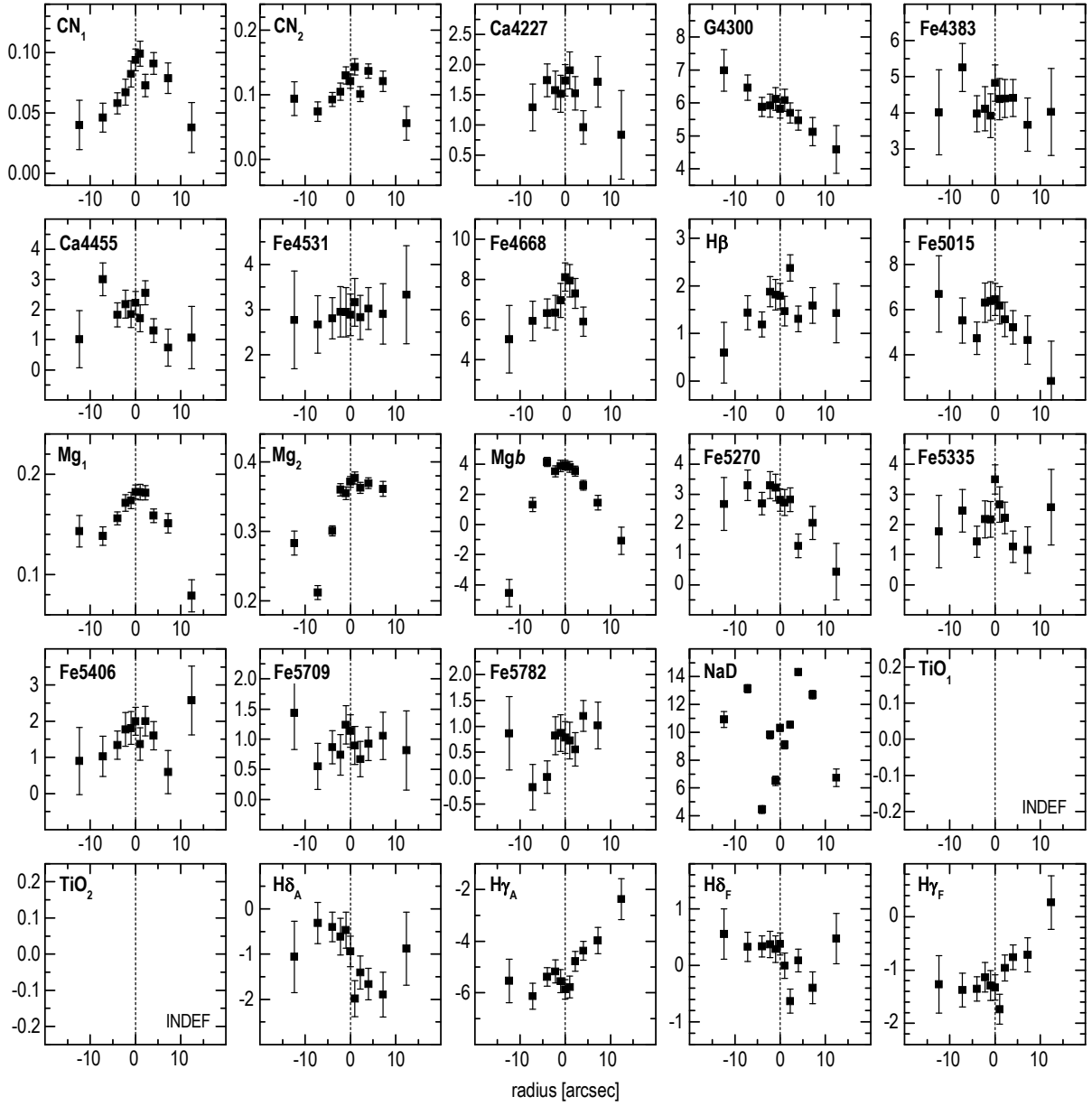


**Figure 3.22:** 5 – RX J1520.9+4840. Same as Fig. 3.18. Effective radius  $r_e = 31$  arcsec.

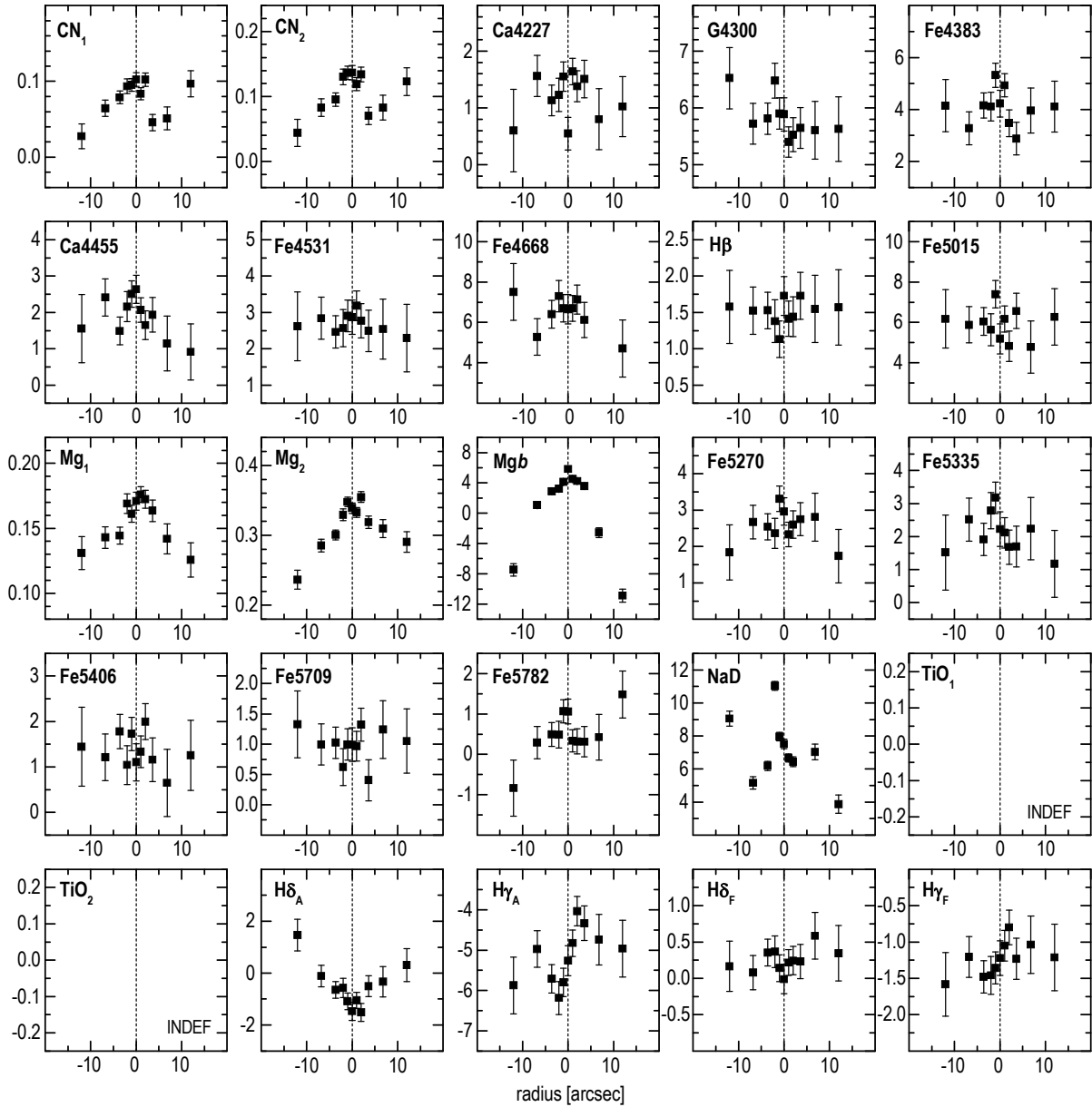


Figure 3.23: 6 – RX J1548.9+0851. Same as Fig. 3.18. Effective radius  $r_e = 57$  arcsec.

## 7 Full spectrum fitting with ULySS

When focusing only on specific features in the spectrum of an old stellar population, one obviously misses the wealth of information embedded in all the remaining pixels along the dispersion direction. To account for this additional information besides the strongest absorption features, full spectrum fitting techniques have been developed. In this approach synthetic single stellar population (SSP) models based on a library of stars with different atmospheric parameters are fit directly to the observed spectrum yielding SSP equivalent ages and metallicities of the stellar population of the investigated galaxy.

Following this idea, the open-source package ULySS<sup>27</sup> (University of Lyon Spectroscopic Analysis Software) written in IDL (Koleva et al. 2009) has been used in this work to fit synthetic SSP models to the observed galaxies and compare the results with those derived from Lick indices. ULySS makes use of the Pegase HR models from Le Borgne et al. (2004) based on the Elodie 3.1<sup>28</sup> library of stellar spectra (Prugniel & Soubiran 2001; Prugniel et al. 2007). Since the synthesis of a stellar population requires a stellar spectrum at any point in the parameter space ( $T_{\text{eff}}$ ,  $\log g$  and  $[\text{Fe}/\text{H}]$ ), the library involves an interpolator for that purpose. All Pegase HR models are computed assuming a Salpeter IMF and Padova 1994 evolutionary tracks providing synthetic SSPs with ages between 1–20000 Myr and metallicities between  $-2.3 - 0.69$  dex.

Galaxy spectra analyzed with ULySS do not necessarily have to be flux-calibrated since a multiplicative polynomial is used to adjust the overall spectrum shape to the SSP model. If the spectra are flux-calibrated, the shape of the polynomial allows us to evaluate the accuracy of the calibration and also reveals the systematic reddening caused by dust in the galaxy, if present. The order of the multiplicative polynomial  $P_n$  can be freely chosen by the user but shouldn't be taken too low resulting mostly in a severe mismatch of the investigated spectrum and the SSP model. Balancing between a minimum order to achieve reasonable, stable values and a maximum order to avoid long, unnecessary computing time, an order of 40 was chosen for all galaxies in this thesis except where otherwise stated. Figure 3.24 presents the variation of fit results with increasing order  $n$ , specifically the deviations to the adopted values at  $n = 40$ . Shaded areas correspond to deviations of 0.1 dex. The plot shows that for orders  $40 \leq n \leq 80$  values stay roughly<sup>29</sup> constant and start to diverge again for higher  $n$ , especially in age.

A simple ULySS SSP fit is carried out with the commands

```
IDL> cmp=uly_ssp()
IDL> ulyss, spectrum, cmp, MD=40, SG=0.07216, LMIN=[3800], LMAX=[5800], SNR=61, /CLEAN,
/PLOT, FILE_OUT='output'
```

where `uly_ssp()` defines the Pegase HR model, `MD` sets the polynomial degree, `SG` the redshift of the spectrum, `LMIN` and `LMAX` the wavelength range to be fit, and `SNR` the signal-to-noise of the data. The parameters `/CLEAN`, `/PLOT`, and `FILE_OUT` allow us to clip outliers in the fit, plot the fit, and save the results to an output file respectively.

<sup>27</sup><http://ulyss.univ-lyon1.fr/>

<sup>28</sup>[http://www.obs.u-bordeaux1.fr/m2a/soubiran/elodie\\\_library.html](http://www.obs.u-bordeaux1.fr/m2a/soubiran/elodie\_library.html)

<sup>29</sup>The spread of age and  $[\text{Fe}/\text{H}]$  between  $40 \leq n \leq 80$  is of the same order as the average error of all fit results with fixed  $n$  of the VIMOS sample and can thus be considered stable in that range.

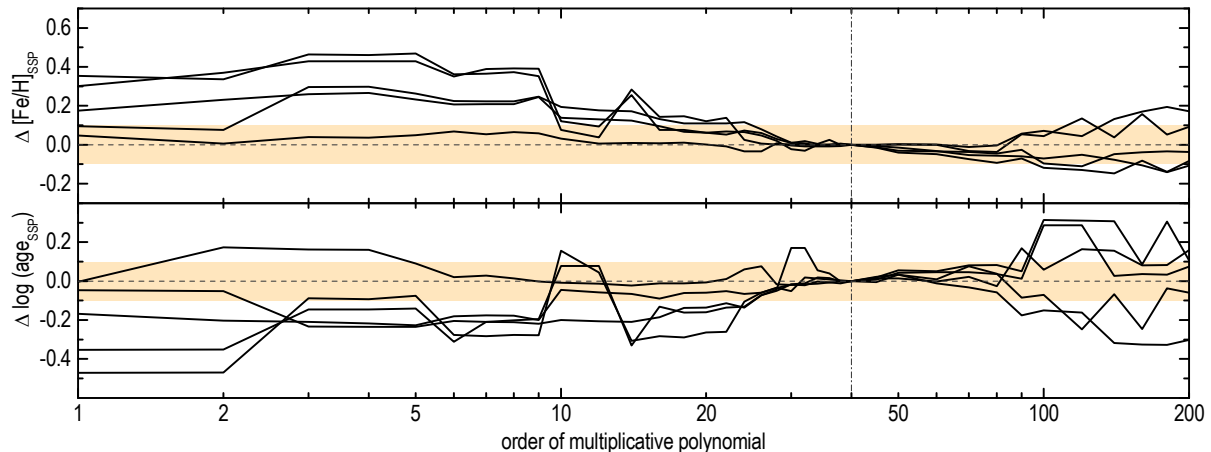


**Figure 3.24:** Variation of SSP age and metallicity with increasing order  $n$  of the multiplicative polynomial. The six galaxies with the highest SNR from the VIMOS sample (see Chapter 4) are shown. The deviations to the adopted values at  $n = 40$  are displayed. Deviations corresponding to 0.1 dex are shaded.

Besides SSP ages and metallicities, ULySS also provides the user with the amount of broadening applied to the SSP model to match a galaxy spectrum. These data are output as velocity dispersions in  $\text{km s}^{-1}$ . However, to get physically meaningful values, one has to correct the results for the instrumental dispersion of the used spectrograph.

Since SSP fitting is a complex problem involving degeneracies and multiple minima in the parameter space, ULySS provides Monte Carlo simulations,  $\chi^2$  maps and convergence maps to validate the fitting results.

Monte Carlo simulations repeat a fit several times with random Gaussian noise applied to the spectrum in each step. The distribution of the resulting scatter plot can then be used to measure average values of the intended parameters as well as their dispersion. The dimension of the added noise is based on user-defined noise estimates, either a signal-to-noise ratio or an error spectrum. The number of simulations is defined by the keyword `NSIMUL=` and set to 200 for all galaxies in this work while the noise is specified by `SNR=`.

Local minima in the parameter space can also be visualized by convergence maps which show the convergence paths from a grid of guesses to the individual solutions. Thus, ideally a convergence map should look like a star where all convergence paths lead to one center showing that the solution is independent of the guesses. In general this is not necessarily the case.

Finally,  $\chi^2$  maps directly reveal the structure of the parameter space. A fit is repeated on a user-defined grid of nodes where the corresponding  $\chi^2$  is computed for every node. Minima then appear as  $\chi^2$  valleys in the parameter plane.

## 1 Fitting the WHT ellipticals

The fitting of the WHT ellipticals was split into two parts. First, all six galaxies were fit in 1-D by summing up all signal along the slit to determine SSP equivalent ages and metallicities.



ties of the galaxies as a whole. Secondly, the galaxies were chopped into the same bins along the spatial axis as used for the Lick index analysis to measure any spatial variation of the stellar population parameters, if present. The individual binned spectra were then fit separately with ULySS. To estimate the reliability of the fits with Monte Carlo simulations, the same S/N as determined for the Lick index measurements was applied. Again only blue arm spectra were considered because of the lack of prominent absorption features in the red channel.

Figure 3.25 presents Monte-Carlo simulations and convergence maps of the 1-D fits. The given ages and metallicities are the averages of the scatter plots while the adopted error bars relate to the associated standard deviations. Outliers clearly detached from the general distribution have been excluded for these measurements. The convergence maps confirm the independence of the obtained results from the initial guesses. Figure 3.26 shows all six ellipticals overplotted in the age-metallicity plane. While the galaxies spread from 8 to 17 Gyr in age, metallicities show consistent values around -0.15 dex. Table 3.6 summarizes the results of the 1-D fits and the corresponding input parameters. The listed velocity dispersions have been corrected for the ISIS instrumental dispersion<sup>30</sup>.

Figures 3.27–3.32 show the fit results of the ellipticals in all bins along the spectrograph slit. The vertical dashed lines mark the galaxy center while the horizontal dashed lines indicate the results from the 1-D fits. The width of the boxes visualizes the applied binning along the slit while their height illustrates the error bars of the measurements. The corresponding Monte-Carlo simulations and associated S/N ratios are also presented. Boxes and simulations are serially numbered with increasing distance from the galaxy center. Any outliers clearly detached from the general point distributions have been excluded for age and metallicity measurements.

Almost all simulations follow a similar trend, being much more elongated in age than in metallicity. The effect of the estimated noise is also evident. While the central bins show well-defined distributions, the outer ones yield much more diffuse results. In addition, there is a clear tendency that the fits in the outer bins tend to converge to the model limit at 19.99 Gyr. These data points were all neglected for the age and metallicity measurements. Table 3.7 summarizes the results of all six ellipticals in all bins along the spectrograph slit.

**Table 3.6:** ULySS 1-D fit results of the WHT ellipticals.

object	MD <sup>a</sup>	LMIN–LMAX <sup>b</sup>	SNR <sup>c</sup>	age <sub>SSP</sub> [Gyr]	[Fe/H] <sub>SSP</sub>	$\sigma$ [km s <sup>-1</sup> ] <sup>d</sup>
1.....	50	3800–6100 Å	63	13.9 ± 1.0	-0.20 ± 0.02	237
2.....	40	3800–5800 Å	47	8.0 ± 1.0	-0.14 ± 0.07	232
3.....	60	3800–5800 Å	60	16.8 ± 1.3	-0.13 ± 0.02	286
4.....	40	3800–5800 Å	55	13.3 ± 1.1	-0.17 ± 0.03	258
5.....	40	3800–5800 Å	49	11.4 ± 0.8	-0.15 ± 0.03	313
6.....	40	3800–5800 Å	47	10.7 ± 0.9	-0.15 ± 0.04	330

<sup>a</sup> Order of polynomial degree.

<sup>b</sup> Wavelength region used for the ULySS fit.

<sup>c</sup> SNR determined at 5140 Å rest-frame wavelength.

<sup>d</sup> Corrected for instrumental and model dispersions, see equations 3.7.

<sup>30</sup>The ISIS instrumental dispersion was determined by fitting Gaussians to the arc lamp spectral lines.

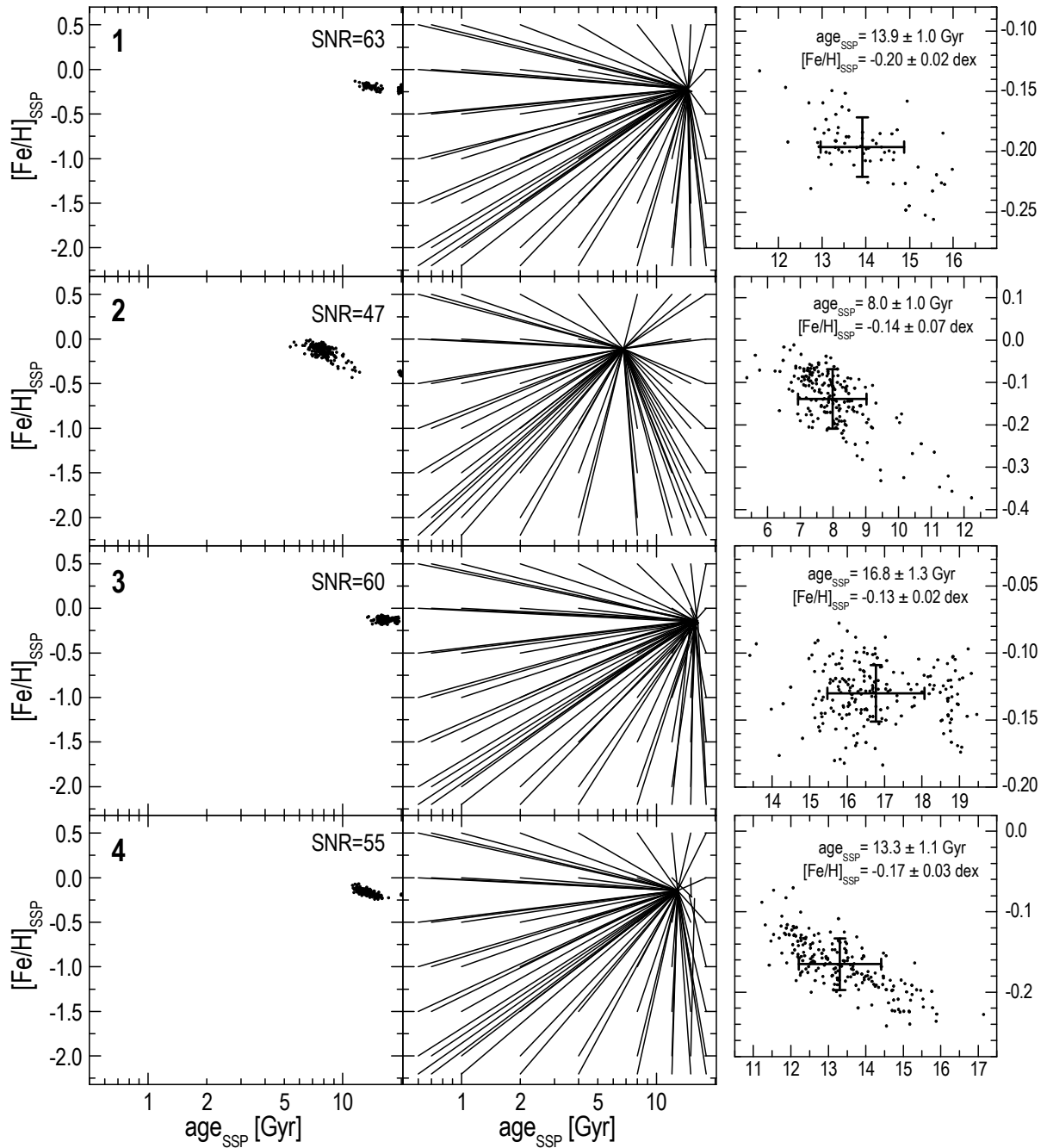


**Figure 3.25:** ULYSS 1-D fit results for all six WHT ellipticals. The scatter plots are the output of 200 Monte-Carlo simulations. Left panels show the full parameter space of the Pegase HR model. Middle panels display the corresponding convergence maps. Right panels show the enhanced cutout of the age-metallicity distributions. The given values and error bars relate to averages and standard deviations of the scatter plots excluding outliers.

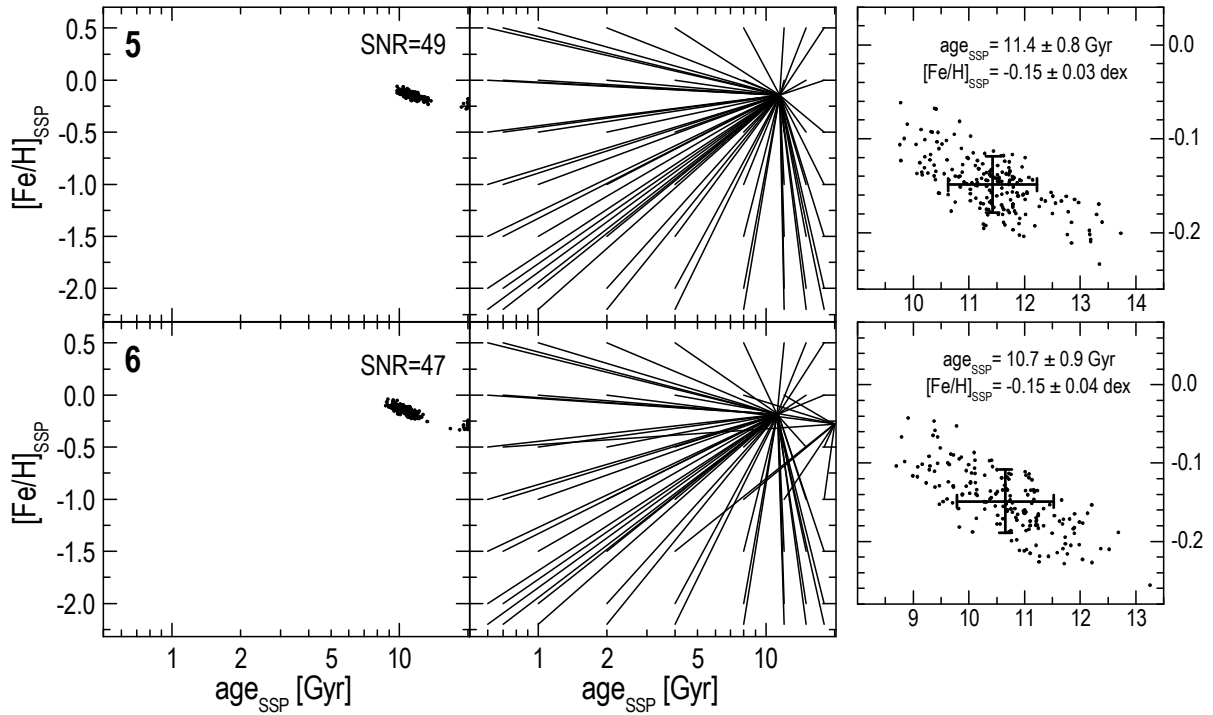
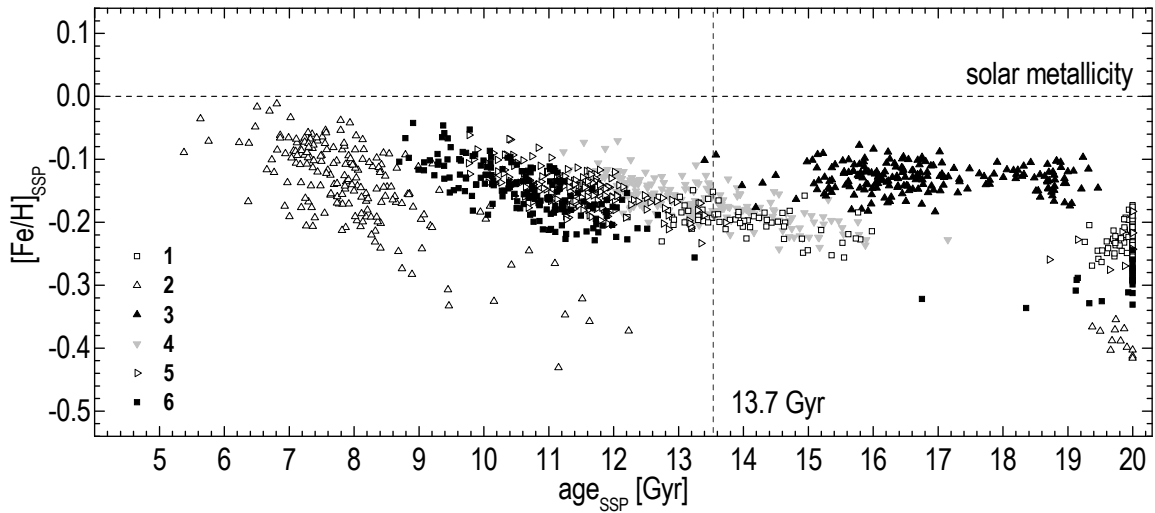
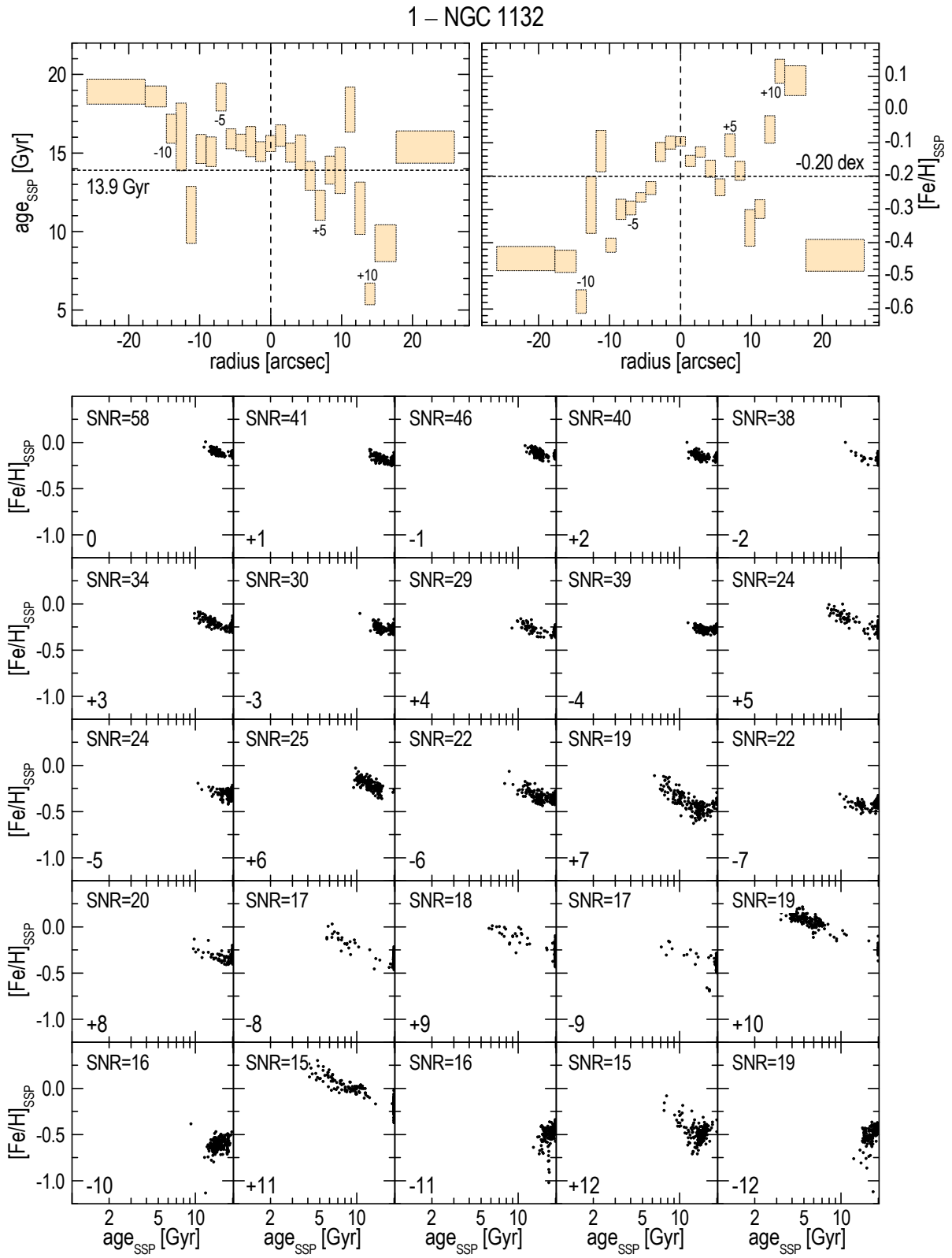


Figure 3.25 – continued.



**Figure 3.26:** Distribution of the WHT ellipticals in the age-metallicity plane. The horizontal line indicates solar metallicity while the vertical one represents the age of the universe. All galaxies have similar metallicities around  $[\text{Fe}/\text{H}]_{\text{SSP}} = -0.15$  dex while ages spread from 8 to 17 Gyr. The outliers at the model limit have been excluded for age and metallicity determinations.



**Figure 3.27:** Spatial variation of SSP equivalent age and metallicity in NGC 1132 as determined with ULySS. See text for explanations.

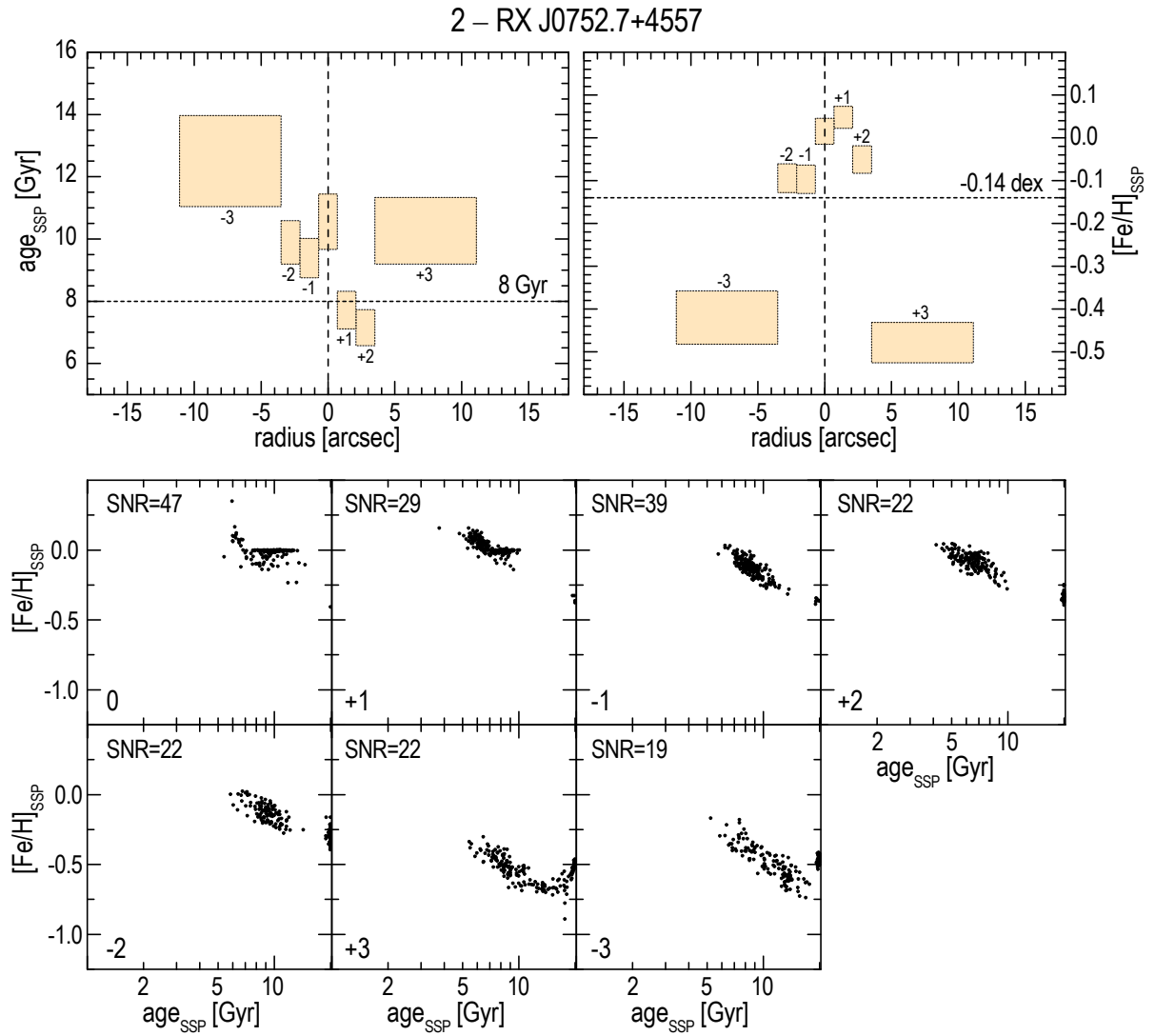


**Figure 3.28:** Spatial variation of SSP equivalent age and metallicity in RX J0752.7+4557 as determined with ULySS. See text for explanations. Effective radius  $r_e = 7.1$  arcsec.

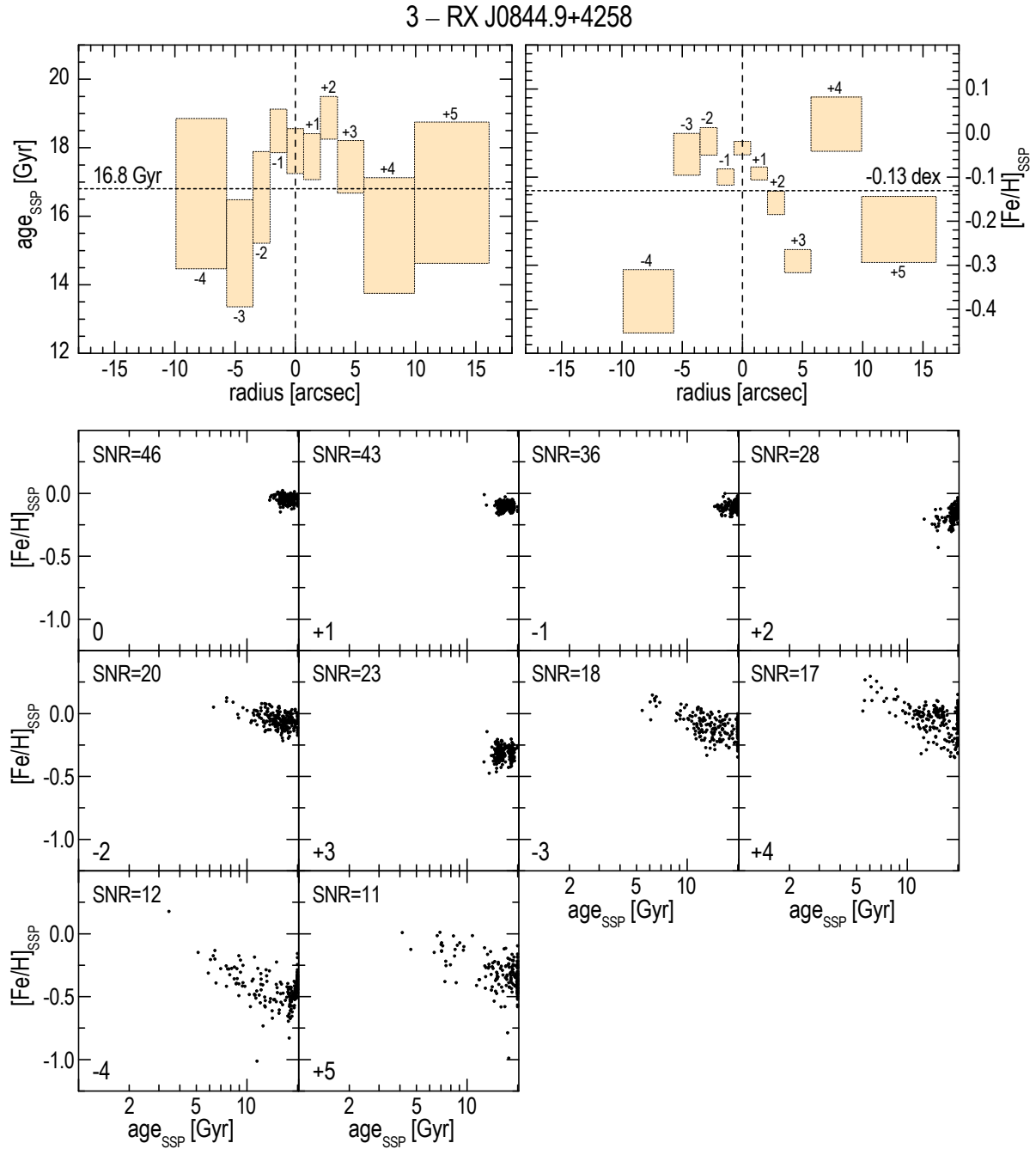


**Figure 3.29:** Spatial variation of SSP equivalent age and metallicity in RX J0844.9+4258 as determined with ULySS. See text for explanations. Effective radius  $r_e = 18$  arcsec.

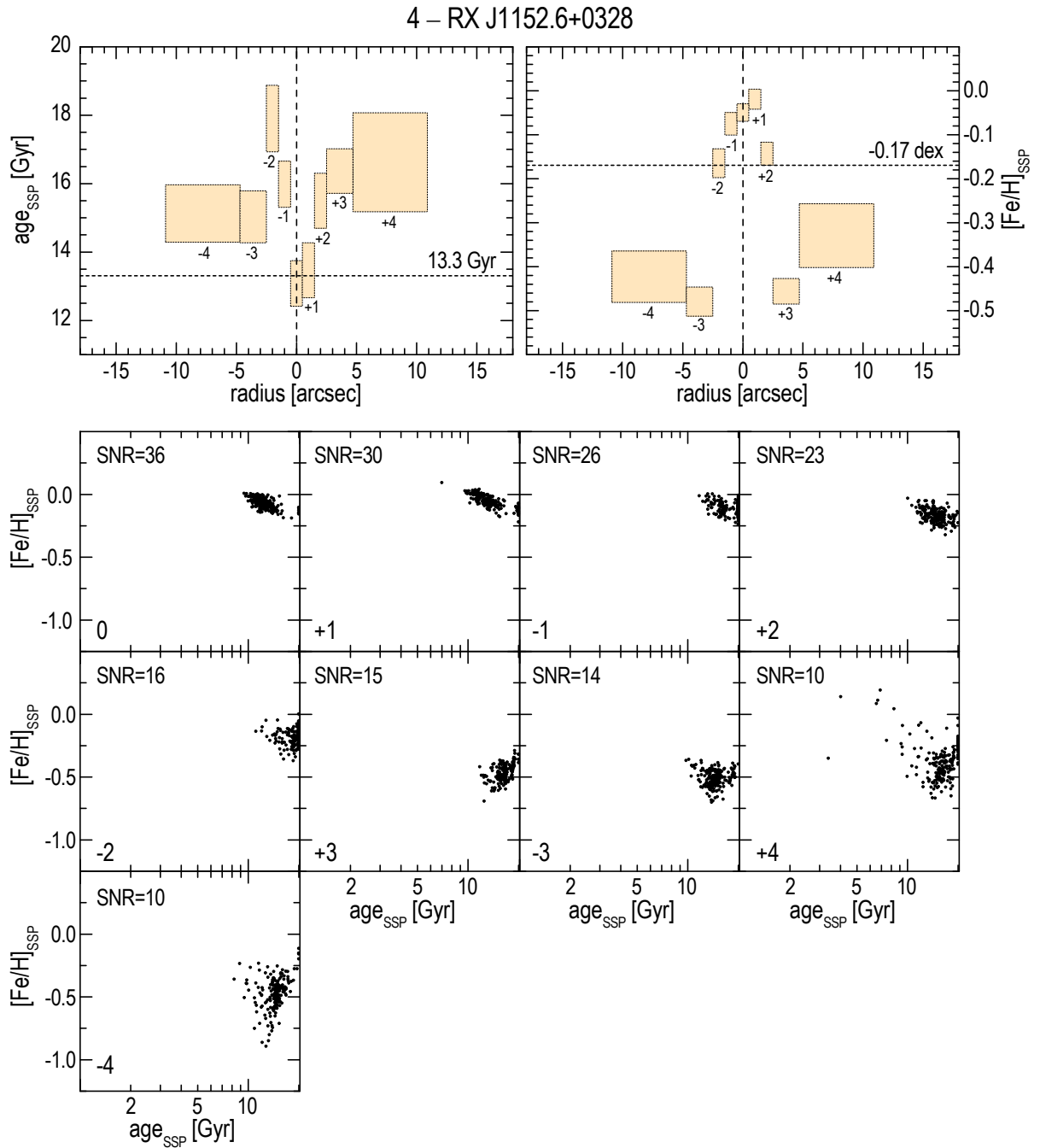


**Figure 3.30:** Spatial variation of SSP equivalent age and metallicity in RX J1152.6+0328 as determined with ULySS. See text for explanations. Effective radius  $r_e = 53$  arcsec.

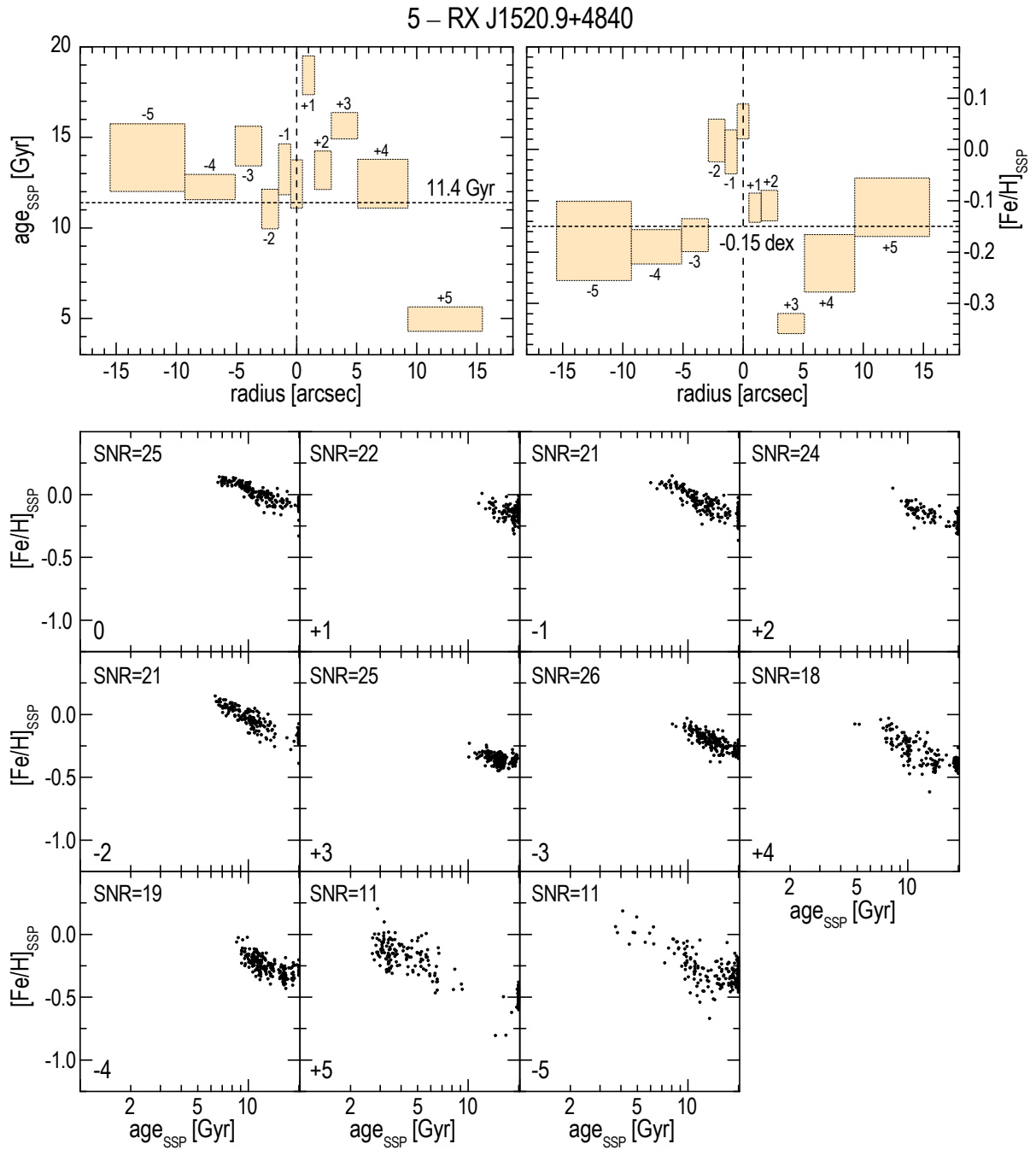


**Figure 3.31:** Spatial variation of SSP equivalent age and metallicity in RX J1520.9+4840 as determined with ULySS. See text for explanations. Effective radius  $r_e = 31$  arcsec.



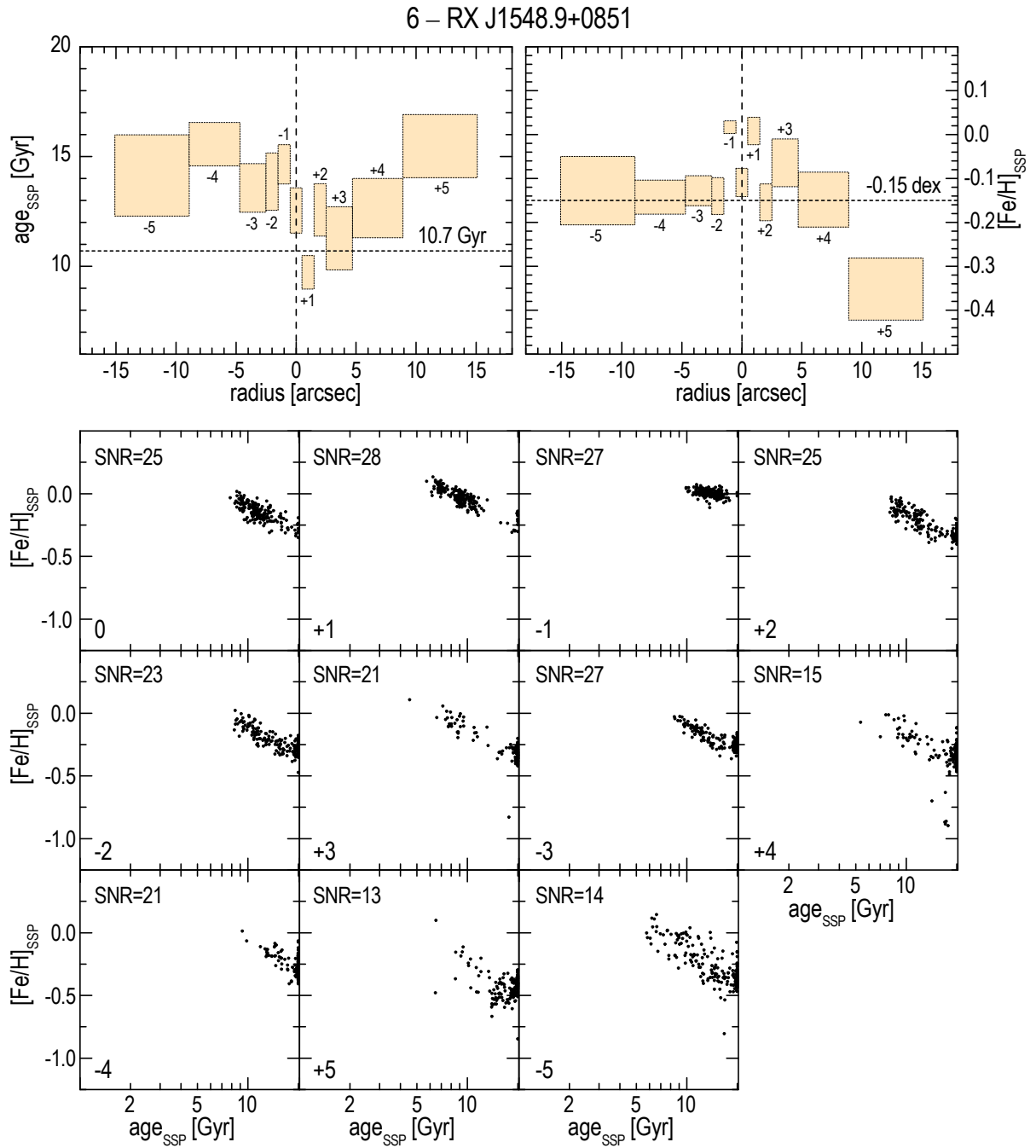


**Figure 3.32:** Spatial variation of SSP equivalent age and metallicity in RX J1548.9+0851 as determined with ULYSS. See text for explanations. Effective radius  $r_e = 57$  arcsec.

**Table 3.7:** ULySS fit results of the WHT ellipticals in all bins along the spectrograph slit.

object	MD <sup>a</sup>	LMIN–LMAX <sup>b</sup>	SNR <sup>c</sup>	age <sub>SSP</sub> [Gyr]	[Fe/H] <sub>SSP</sub>	$\sigma$ [km s <sup>-1</sup> ] <sup>d</sup>
1–NGC1132						
+0 .....	50	3800–6100 Å	58	15.1 ± 1.0	-0.11 ± 0.03	247
+1 .....	50	3800–6100 Å	41	15.4 ± 1.4	-0.17 ± 0.03	237
-1 .....	50	3800–6100 Å	46	14.5 ± 1.2	-0.12 ± 0.04	242
+2 .....	50	3800–6100 Å	40	14.4 ± 1.2	-0.14 ± 0.03	240
-2 .....	50	3800–6100 Å	38	14.8 ± 1.9	-0.16 ± 0.06	237
+3 .....	50	3800–6100 Å	34	13.9 ± 2.2	-0.20 ± 0.05	226
-3 .....	50	3800–6100 Å	30	15.1 ± 1.1	-0.26 ± 0.04	227
+4 .....	50	3800–6100 Å	29	12.6 ± 1.8	-0.26 ± 0.05	222
-4 .....	50	3800–6100 Å	39	15.3 ± 1.3	-0.28 ± 0.03	222
+5 .....	50	3800–6100 Å	24	10.7 ± 1.9	-0.14 ± 0.07	224
-5 .....	50	3800–6100 Å	24	17.7 ± 1.8	-0.32 ± 0.04	220
+6 .....	50	3800–6100 Å	25	13.0 ± 1.8	-0.21 ± 0.06	227
-6 .....	50	3800–6100 Å	22	14.1 ± 1.9	-0.33 ± 0.06	221
+7 .....	50	3800–6100 Å	19	12.4 ± 2.9	-0.4 ± 0.1	219
-7 .....	50	3800–6100 Å	22	14.4 ± 1.8	-0.43 ± 0.04	221
+8 .....	50	3800–6100 Å	20	16.3 ± 2.9	-0.33 ± 0.06	219
-8 .....	50	3800–6100 Å	17	9.2 ± 3.6	-0.2 ± 0.1	218
+9 .....	50	3800–6100 Å	18	9.8 ± 3.3	-0.10 ± 0.08	225
-9 .....	50	3800–6100 Å	17	13.9 ± 4.3	-0.4 ± 0.2	223
+10 .....	50	3800–6100 Å	19	5.4 ± 1.4	0.08 ± 0.07	193
-10 .....	50	3800–6100 Å	16	15.6 ± 1.8	-0.61 ± 0.07	188
+11 .....	50	3800–6100 Å	15	8.1 ± 2.3	0.04 ± 0.09	242
-11 .....	50	3800–6100 Å	16	17.9 ± 1.3	-0.49 ± 0.07	200
+12 .....	50	3800–6100 Å	15	14.4 ± 2.0	-0.5 ± 0.1	226
-12 .....	50	3800–6100 Å	19	18.1 ± 1.6	-0.49 ± 0.07	255
2–RX J0752.7+4557						
+0 .....	40	3800–5800 Å	47	9.7 ± 1.8	-0.01 ± 0.06	298
+1 .....	40	3800–5800 Å	29	7.1 ± 1.2	0.02 ± 0.05	236
-1 .....	40	3800–5800 Å	39	8.8 ± 1.3	-0.13 ± 0.07	228
+2 .....	40	3800–5800 Å	22	6.6 ± 1.2	-0.08 ± 0.06	212
-2 .....	40	3800–5800 Å	22	9.2 ± 1.4	-0.13 ± 0.07	223
+3 .....	40	3800–5800 Å	22	9.2 ± 2.1	-0.53 ± 0.09	154
-3 .....	40	3800–5800 Å	19	11.0 ± 2.9	-0.5 ± 0.1	170
3–RX J0844.9+4258						
+0 .....	60	3800–5800 Å	46	17.3 ± 1.3	-0.05 ± 0.03	297
+1 .....	60	3800–5800 Å	43	17.1 ± 1.3	-0.11 ± 0.03	287
-1 .....	60	3800–5800 Å	36	17.9 ± 1.3	-0.12 ± 0.04	285
+2 .....	60	3800–5800 Å	28	18.3 ± 1.2	-0.18 ± 0.05	286
-2 .....	60	3800–5800 Å	20	15.2 ± 2.7	-0.05 ± 0.06	303
+3 .....	60	3800–5800 Å	23	16.7 ± 1.5	-0.32 ± 0.05	254
-3 .....	60	3800–5800 Å	18	13.4 ± 3.1	-0.10 ± 0.09	269
+4 .....	60	3800–5800 Å	17	13.8 ± 3.4	0.0 ± 0.1	299
-4 .....	60	3800–5800 Å	12	14.5 ± 4.4	-0.5 ± 0.1	223
+5 .....	60	3800–5800 Å	11	14.6 ± 4.1	-0.3 ± 0.1	211

<sup>a</sup> Order of polynomial degree.<sup>b</sup> Wavelength region used for the ULySS fit.<sup>c</sup> SNR determined at 5140 Å rest-frame wavelength.<sup>d</sup> Corrected for instrumental and model dispersions, see equations 3.7.

Table 3.7 – continued.

object	MD <sup>a</sup>	LMIN–LMAX <sup>b</sup>	SNR <sup>c</sup>	age <sub>SSP</sub> [Gyr]	[Fe/H] <sub>SSP</sub>	$\sigma$ [km s <sup>-1</sup> ] <sup>d</sup>
4–RX J1152.6+0328						
+0 .....	40	3800–5800 Å	36	12.4 ± 1.3	-0.07 ± 0.04	262
+1 .....	40	3800–5800 Å	30	12.7 ± 1.6	-0.04 ± 0.04	246
-1 .....	40	3800–5800 Å	26	15.3 ± 1.3	-0.10 ± 0.05	249
+2 .....	40	3800–5800 Å	23	14.7 ± 1.6	-0.17 ± 0.05	234
-2 .....	40	3800–5800 Å	16	16.9 ± 2.0	-0.20 ± 0.06	240
+3 .....	40	3800–5800 Å	15	15.7 ± 1.3	-0.48 ± 0.06	240
-3 .....	40	3800–5800 Å	14	14.3 ± 1.5	-0.51 ± 0.07	223
+4 .....	40	3800–5800 Å	10	15.2 ± 2.9	-0.4 ± 0.1	266
-4 .....	40	3800–5800 Å	10	14.3 ± 1.7	-0.5 ± 0.1	261
5–RX J1520.9+4840						
+0 .....	40	3800–5800 Å	25	11.1 ± 2.7	0.02 ± 0.07	300
+1 .....	40	3800–5800 Å	22	17.4 ± 2.1	-0.14 ± 0.06	313
-1 .....	40	3800–5800 Å	21	11.8 ± 2.8	-0.05 ± 0.08	297
+2 .....	40	3800–5800 Å	24	12.1 ± 2.1	-0.14 ± 0.06	308
-2 .....	40	3800–5800 Å	21	10.0 ± 2.2	-0.02 ± 0.08	309
+3 .....	40	3800–5800 Å	25	14.9 ± 1.5	-0.36 ± 0.04	307
-3 .....	40	3800–5800 Å	26	13.4 ± 2.2	-0.20 ± 0.06	325
+4 .....	40	3800–5800 Å	18	11.1 ± 2.7	-0.3 ± 0.1	343
-4 .....	40	3800–5800 Å	19	11.6 ± 1.4	-0.22 ± 0.07	334
+5 .....	40	3800–5800 Å	11	4.3 ± 1.4	-0.17 ± 0.11	351
-5 .....	40	3800–5800 Å	11	12.0 ± 3.7	-0.26 ± 0.15	319
6–RX J1548.9+0851						
+0 .....	40	3800–5800 Å	25	11.5 ± 2.1	-0.14 ± 0.06	315
+1 .....	40	3800–5800 Å	28	9.0 ± 1.5	-0.02 ± 0.06	302
-1 .....	40	3800–5800 Å	27	13.7 ± 1.8	0.00 ± 0.03	318
+2 .....	40	3800–5800 Å	25	11.4 ± 2.4	-0.20 ± 0.08	310
-2 .....	40	3800–5800 Å	23	12.6 ± 2.6	-0.18 ± 0.08	301
+3 .....	40	3800–5800 Å	21	9.8 ± 2.9	-0.1 ± 0.1	318
-3 .....	40	3800–5800 Å	27	12.5 ± 2.2	-0.16 ± 0.07	324
+4 .....	40	3800–5800 Å	15	11.3 ± 2.7	-0.2 ± 0.1	352
-4 .....	40	3800–5800 Å	21	14.6 ± 2.0	-0.18 ± 0.08	345
+5 .....	40	3800–5800 Å	13	14.0 ± 2.9	-0.4 ± 0.1	309
-5 .....	40	3800–5800 Å	14	12.3 ± 3.7	-0.2 ± 0.2	413

<sup>a</sup> Order of polynomial degree.<sup>b</sup> Wavelength region used for the ULySS fit.<sup>c</sup> SNR determined at 5140 Å rest-frame wavelength.<sup>d</sup> Corrected for instrumental and model dispersions, see equations 3.7.

## 8 Kinematics

When using ULySS one has to specify the redshift of the investigated galaxy so that the SSP model spectrum at rest-frame wavelengths is shifted to the corresponding wavelengths at the galaxy redshift. Since ULySS measures the shift in wavelength between the observed spectrum and this redshifted SSP model, as well as the broadening of the SSP model applied to match the observed spectrum, the program also allows us to measure the kinematics, i.e. radial velocity and velocity dispersion profiles along the spectrograph slit of the investigated galaxies.

To construct these kinematic profiles, the average values of the redshift offset  $\Delta cz$  and the dispersion of the SSP model  $\sigma_{\text{ulyss}}$  in the 200 Monte-Carlo simulations have been used for the six ellipticals. The same spatial binning as defined for the age- and metallicity profiles has been considered. For every bin, the shifts  $\Delta cz$  and the corresponding errors were transformed to the analogous shifts  $\Delta v_r$  in radial velocity<sup>31</sup>. Finally, radial velocities were computed relative to those in the central bin of each galaxy to construct radial velocity curves.

To determine the corresponding profiles for the velocity dispersion, the dispersion  $\sigma_{\text{ulyss}}$  resulting from the fit had to first be converted to a physically meaningful value  $\sigma_{\text{phys}}$  related to the random distribution of stars. ULySS determines the broadening relative to the SSP model dispersion  $\sigma_{\text{model}}$ , amounting to  $\sigma_{\text{model}} = 13 \text{ km s}^{-1}$  for the Pegase HR models. In addition, the instrumental dispersion  $\sigma_{\text{instr}}$  of the spectrograph itself has also to be taken into account when computing the physical dispersions. To estimate the instrumental dispersion of the ISIS spectrograph, the arc lamp comparison spectra taken during the night in the same setup as the galaxies have been considered. In particular, the emission lines in these spectra have been fit by Gaussians yielding the FWHMs of these features. Equation 3.6 shows the relation between the FWHM and  $\sigma$  for a Gaussian and has been used to compute the corresponding instrumental dispersions. For the final value of  $\sigma_{\text{instr}} = 95 \text{ km s}^{-1}$  the average of several lines was used.

$$\text{FWHM} = 2\sqrt{2 \ln 2} \cdot \sigma \approx 2.35482 \cdot \sigma \quad (3.6)$$

Equations 3.7 show the relations between the different dispersions and have been used to calculate the final value of  $\sigma_{\text{phys}}$ . Besides SSP ages and metallicities, Tables 3.6 and 3.7 also include these  $\sigma_{\text{phys}}$  values.

$$\begin{aligned} \sigma_{\text{ulyss}}^2 &= \sigma_{\text{obs}}^2 - \sigma_{\text{model}}^2 \\ \sigma_{\text{obs}}^2 &= \sigma_{\text{phys}}^2 + \sigma_{\text{instr}}^2 \\ \sigma_{\text{phys}}^2 &= \sigma_{\text{ulyss}}^2 + \sigma_{\text{model}}^2 - \sigma_{\text{instr}}^2 \end{aligned} \quad (3.7)$$

Figure 3.33 shows the resulting radial velocity and velocity dispersion profiles of the six WHT ellipticals. Vertical lines indicate the center of the galaxies while horizontal ones represent the radial velocity at the central bin and amount to zero since velocities relative to this bin have been computed. NGC 1132 (panel 1) as the brightest of the investigated objects shows the typical kinematic profiles as one would expect, a symmetric flat radial velocity curve and a central enhancement of the line-of-sight velocity dispersion. The fainter objects in the sample follow these trends more or less. No counter-rotating cores, indicative of a recent merger are visible in the profiles.

<sup>31</sup>The relativistic Doppler effect was considered in this work, see equation 4.1 in chapter 4.

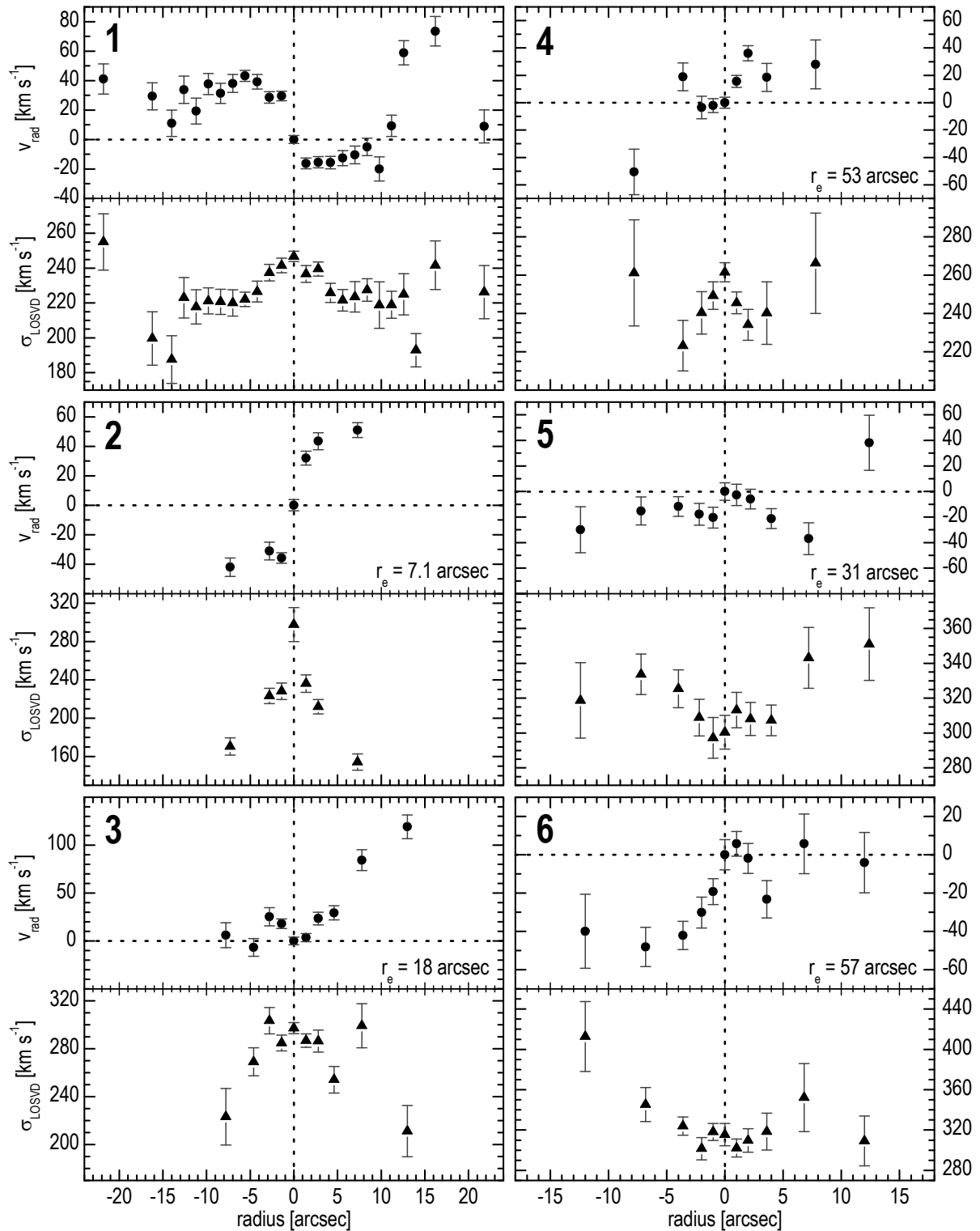


**Figure 3.33:** Kinematics of the WHT ellipticals. Circles show radial velocities while triangles present the line-of-sight-velocity-dispersion (LOSVD). Radial velocities are normalized to the central velocity, indicated as horizontal dashed lines. Vertical lines mark the galaxy center. The binning along the slit is the same as in Figs. 3.27–3.32.



# Chapter 4

## VIMOS Observations

In order to determine group memberships for the faint galaxy populations of our fossil groups, observations with VIMOS, the multi-object spectrograph on the ESO VLT have been carried out. The observations were taken in service mode, i.e. ESO astronomers at the VLT arrange the observations within the ongoing observation period based on the constraint set given by the principal investigator (PI) of the project. All observations have to be prepared in so-called *observing blocks* (OBs), individual time slots that contain all the information necessary to arrange and conduct a single observation. OBs are limited to one hour in total execution time (including instrument overheads). The philosophy behind this data-flow system is simple. If longer OBs would be allowed, the scheduling of individual observations is more complicated and the observing conditions are more likely to lie outside the constraint set specified by the PI. As a result and in contrast to visiting a telescope for a certain number of nights, observations on one target are not necessarily carried out in a single night but can be arranged all over the observing period. Therefore, service mode observations can be incomplete. If the constraint set, the weather conditions, or the ranking of the project do not permit the observations, OBs won't be carried out at all.

This chapter highlights the process of observing with VIMOS from the application for observing time to the final analysis of the obtained datasets. The aim is to give the reader a short, but comprehensive overview on the different steps that are necessary to receive the final data products holding the key to the actual scientific output. The chapter is organized in the chronological way the user will encounter when applying for observing time at ESO.

### 1 The multi-object spectrograph

VIMOS (VIvisible Multi-Object Spectrograph) is a wide field imager and multi-object spectrograph mounted on the Nasmyth focus B of UT3 Melipal. It operates in the optical, covering a wavelength range from 3600 to 10000 Å. The instrument is made up of four individual quad-

rants, each with a field of view of  $7 \times 8$  arcmin separated by a gap of 2 arcmin (see Fig. 4.2). The CCD size is  $4 \times 2048 \times 4096$  pixels (the 4096 pixels are used along the dispersion direction to maximize the spectral coverage) with a pixel size of  $15 \mu\text{m}$ . The spatial scale of the detector is  $0.205 \text{ arcsec pixel}^{-1}$ . The spectrograph provides 6 grisms yielding spectral resolutions from  $R = 180$  to 2500 (with a 1 arcsec slit). The instrument can be operated in three different modes: **Imaging (IMG)**, **Multi-Object Spectroscopy (MOS)**, and by means of an **Integral Field Unit (IFU)**. MOS is carried out through the use of slit masks (one for each quadrant) prepared by a laser cutting mask manufacturing unit. Depending on the resolution of the grism, multiple slits can be placed along the dispersion direction. For the present work, the HR blue grism with a spectral resolution of  $0.51 \text{ \AA pixel}^{-1}$  and a wavelength range of 4150 to 6200  $\text{\AA}$  was chosen permitting only one slit along the dispersion. With this setup the maximum number of slits in one quadrant is limited to  $\sim 40$ . Figures 4.1 and 4.2 show the instrument and the schematic field of view. For MOS mode the user has to precisely define the masks for each quadrant setting the exact position of each slit on the detector in advance.

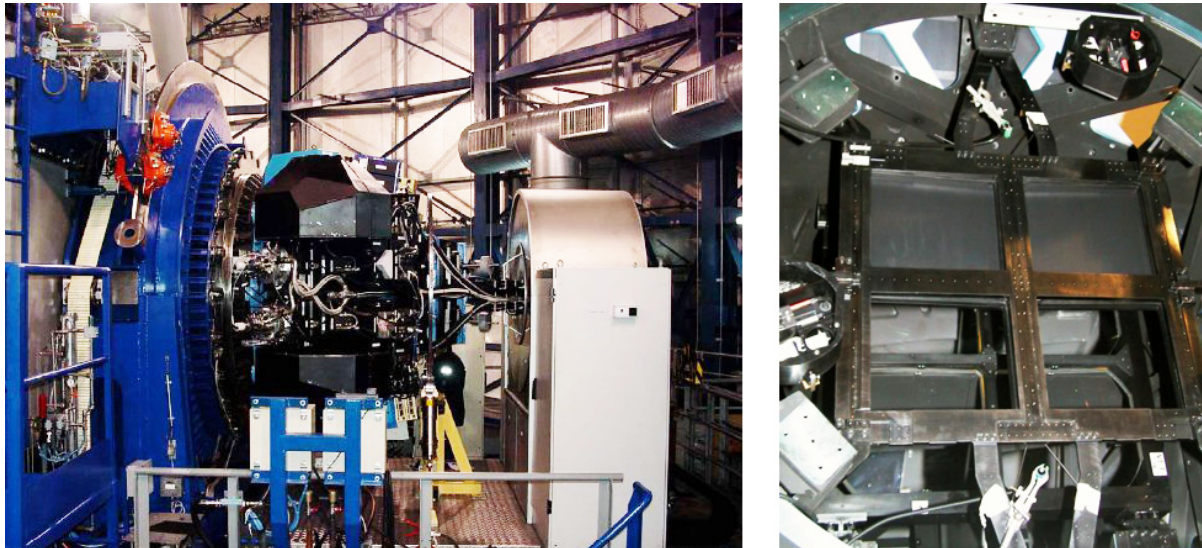


**Figure 4.1:** The VIMOS multi-object spectrograph. Left panel: VIMOS mounted at the Nasmyth focus of UT3 Melipal. Right panel: VIMOS interior. The four quadrants of the detector are clearly visible. Credits: European Southern Observatory (ESO).

ESO provides a special software package developed exactly for this task (see section 2). In order to properly assign the mask slit positions to the scientific targets, a pre-imaging run prior to the actual follow-up spectroscopic observation is mandatory.

## 2 Applying for observing time - Phase 1

Observations at the European Southern Observatory (ESO) are arranged in two periods over the year (see Figure 4.3). Each period is announced early enough on the ESO website<sup>1</sup> in a *Call for Proposals* to inform the scientific community. The observations have to be planned

<sup>1</sup><http://www.eso.org>



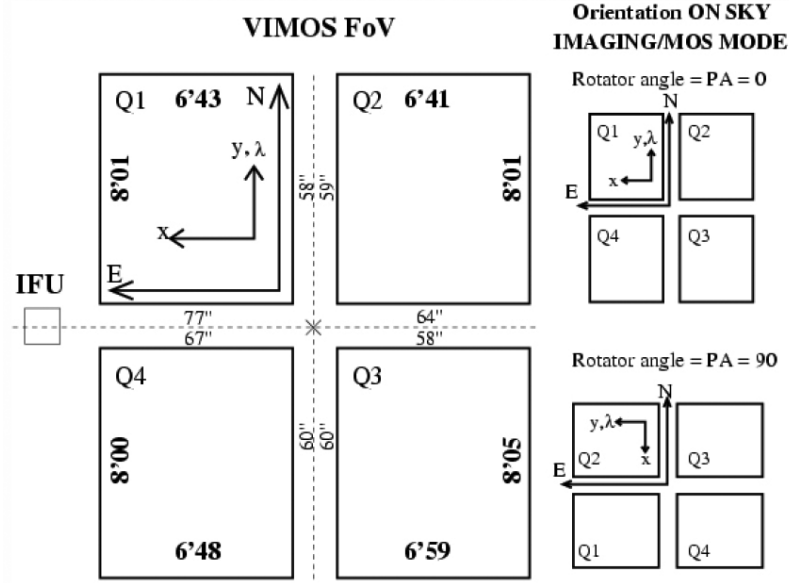


**Figure 4.2:** Orientation of the VIMOS field of view on the sky for position angles  $0^\circ$  and  $90^\circ$ , in IMG and MOS mode. Taken from the VIMOS User Manual.

		Even Period			Odd Period 1.4. - 30.9.									1.10. - 31.3.											
		January	February	March	April	May	June	July	August	September	October	November	December												
$\alpha$	6	7	8	9	10	11	12	13	14	15	16	17	18	19	20	21	22	23	0	1	2	3	4	5	6

**Figure 4.3:** ESO observing periods. Numbers indicate the optimal right ascension of targets for a given month. The small markers show the deadline for the corresponding period.

well in advance, at least 6 months before they are carried out. There are three different types of programmes one can apply for: short, normal and large ones. Short programmes have to stay below 10 hours, while large programmes comprise at least 100 hours of observing time. It should always be kept in mind that the less time applied for, the more chance one has to get the proposal accepted by the **Observing Programme Committee (OPC)** since shorter programmes are easier to schedule within a period. For the present work, a short programme with a total execution time of 7.2 hours for the two fossil aggregates RX J1152.5+0328 and RX J1548.9+0851 was requested. Table 4.1 lists all approved observing runs at ESO in the framework of this thesis. Run 383.A-0123(B) was not fully executed due to the observability limit of the object RX J1152.5+0328 in the course of the period.

## 1 Observational setup

For the purpose of getting reliable redshifts of the fossil group faint galaxy populations and to measure absorption line indices of the brightest group members, the VIMOS HR blue grism was chosen. In order to obtain spectra down to a typical surface brightness level of  $\mu_R \simeq 22$  mag arcsec $^{-2}$  for the faintest objects, dark time was considered essential. Therefore the optimal observing time was defined to be typically one week around new moon. Using the

**Table 4.1:** Accepted ESO runs in the framework of this thesis. Moon and seeing refer to the constraints defined in the proposal.

Period	run ID	instrument	OPC hours	moon	Seeing <sup>a</sup>	status
P83	383.A-0123(A)	VIMOS	0.2	dark	2.00	COMPLETED/PRE <sup>b</sup>
P83	383.A-0123(B)	VIMOS	7.0	dark	1.00	TERMINATED/IA <sup>c</sup>

<sup>a</sup> Seeing in arcsec<sup>b</sup> COMPLETED/PRE: **pre**-imaging run, all OBs completed within allocated time<sup>c</sup> TERMINATED/IA: Terminated, targets **InA**ccessible

VIMOS ETC (**Exposure Time Calculator**)<sup>2</sup> for extended sources (elliptical galaxy template spectrum), assuming dark sky condition (3 days from new moon) with a seeing of one arcsec and a slit width of one arcsec, a S/N  $\sim 15$  (at central wavelength per pixel) with the HR blue grism at 5100 Å for a galaxy with central surface brightness of 20 mag arcsec<sup>-2</sup> (R-band) was estimated to be reached in three hours exposure. For pre-imaging, a S/N  $\sim 23$  (per pixel) for a surface brightness of 22 mag arcsec<sup>-2</sup> (R-band) was reached in 300 s. Based on these integration time requirements the P2PP (see Sect. 3) tutorial account was used to estimate the overall execution time of the proposed observations including VIMOS overheads for pre-imaging and multi-object spectroscopy. Thus, a total of 7.2 hours execution time with VIMOS within an ESO short programme was requested.

### 3 Preparing observations - Phase 2

Once a proposal is accepted, the individual observing blocks have to be defined by the PI so that the scheduling of all observations in service mode is feasible. For this purpose, ESO provides the user with the Phase 2 Preparation tool<sup>3</sup>, short P2PP. The use of this software package is mandatory for the preparation of OBs at ESO. For each individual OB the user has to define acquisition, science, and calibration templates containing all the necessary information for the observation: grisms, order separation filters, target coordinates, integration time, guide stars, observing constraints, etc. . Furthermore, the tool allows us to calculate the total execution time of an OB including all instrument specific overheads. Once all OBs have been prepared, a verification script checks the consistency of the input parameters. If OBs have been verified by this procedure, they can be submitted to the ESO database, where they are finally scheduled for execution.

#### 1 Sample definition and pre-imaging

The first step in preparing MOS observations with VIMOS was to specify a target sample for each fossil aggregate. This was accomplished with the use of the SDSS database. All objects photometrically classified as galaxies within one-half virial radius were queried and taken as basis for the further planning of pre-imaging and spectroscopy. Based on these target samples,

<sup>2</sup><http://www.eso.org/observing/etc/><sup>3</sup><http://www.eso.org/observing/p2pp/>

the positioning of the VIMOS field of view was carried out. Dealing with redshifts of the central ellipticals around  $z \sim 0.07$ , the diameter of the circular target sample distribution ( $\sim 8$  arcmin) matches roughly the spatial extent of one VIMOS quadrant. Thus, a single pointing per fossil aggregate, with the dominating ellipticals centered on Q3 was scheduled (see Fig. 4.4).

When preparing pre-images, the user has to select a suitable guide star for the respective field on the sky. This is easily accomplished with the use of the ESO guidecam tool<sup>4</sup>, designed especially for this task. Guidecam allows a guide star to be selected from catalogues overlaid on the VIMOS field of view indicating also the projected shadow of the telescope guide probe (see Fig. 4.4). The selection of a guide star with guidecam is mandatory for all pre-imaging observations. The user must select a guide star that does not vignette the field of view by the guide probe or one that produces only negligible vignetting by blocking only those regions of the detector that are not of scientific interest. Once a guide star is selected, its coordinates can be entered in the OB. Figure 4.4 shows the VIMOS field of view for the pre-image of the fossil aggregate RX J1548.9+0851 with Q3 centered on the central elliptical.

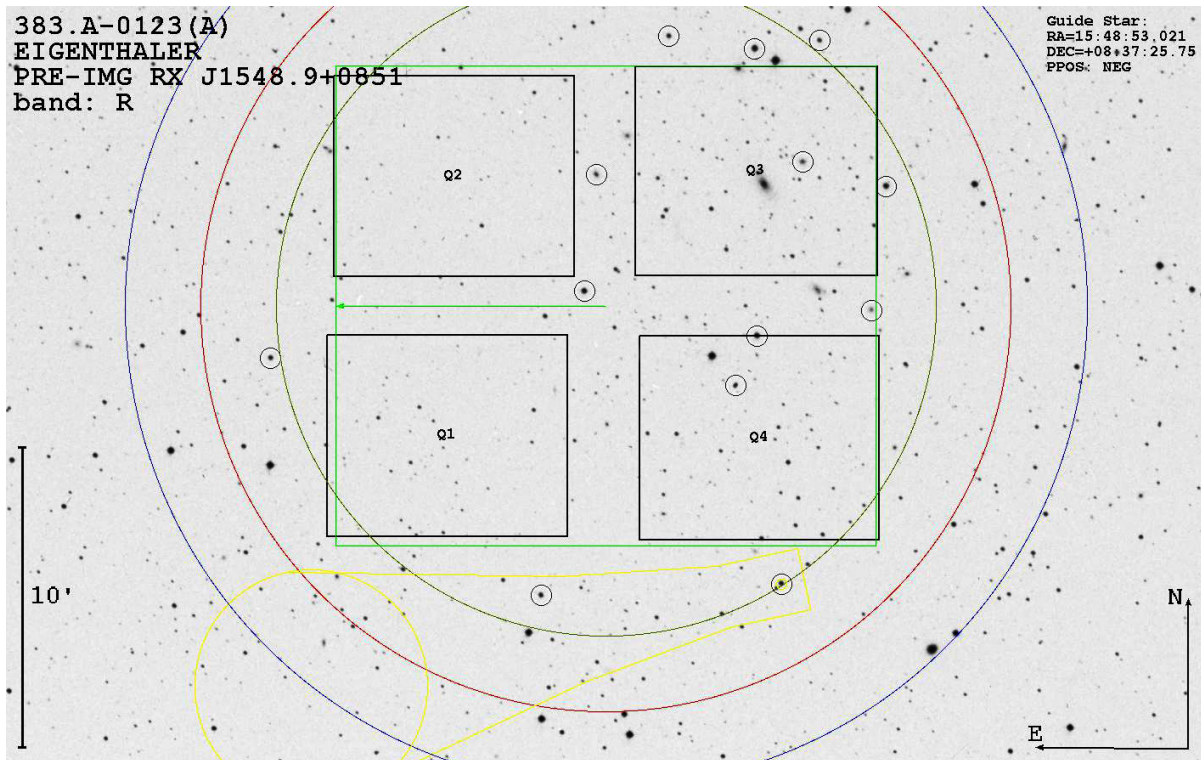


**Figure 4.4:** Selecting a guide star with the guidecam tool. The small circles show available guidestars. The yellow structure indicates the projected shadow of the VIMOS guideprobe. The green area is the VIMOS field of view while the red circle shows the maximum radius for selecting guide stars. The blue circle shows the rotation axis of the guideprobe arm. The guideprobe doesn't vignette any of the four quadrants.

<sup>4</sup><http://www.eso.org/sci/observing/phase2/VIMOS/Guidecam.html>

## 2 Mask preparation

Once the pre-images have been executed and sent to the PI, the slit masks for each of the four quadrants have to be prepared. This is done by means of the ESO **VMMPS (ViMOS Mask Preparation Software)** tool<sup>5</sup>. This software allows slits to be assigned to scientific targets and converts the individual object pixel coordinates on the pre-image into physical millimeter coordinates on the mask. For this procedure it is not allowed to change the VIMOS pre-images processed by the ESO pipeline in even the slightest detail since the transformation recipe for this task is located in the pre-image header.

The first and most important step of the mask preparation is the definition of an input catalog that lists exactly the objects to be observed in each quadrant. There are two different ways to accomplish this task.

Either the user creates a so-called **contributed catalog** containing the equatorial coordinates  $(\alpha, \delta)$  of all the spectroscopic targets as well as a number of bright sources and reference objects. This contributed catalogue is subsequently used for cross-correlation with a **VIMOS pre-image catalog** containing the same bright sources and reference objects as in the contributed catalogue, but given in pixel coordinates instead. The VIMOS pre-image catalog has the only purpose of translating the  $(\alpha, \delta)$  coordinates from the contributed catalog into  $(x, y)$  pixel values. The result of this cross-correlation is a **VIMOS catalog** in  $(x, y)$  pixel coordinates containing the target sample and  $\sim 3$  reference objects necessary to center the masks on the detector.

The second option is to define the VIMOS catalog directly for every quadrant by simply identifying each object on the pre-images and entering the corresponding pixel values into the catalog. In the VIMOS catalogs optional flags can be set for individual objects to define compulsory targets as well as the mandatory reference objects for mask centering, usually three per quadrant. Figure 4.5 shows the **VIMOS catalog** of Q3 for RX J1548.9+0851.

With the final VIMOS catalogs ready for each quadrant, the automatic slit assignment with **VMMPS** can start. Since only one spectrum can be placed in the dispersion direction for the HR blue grism, the software has to find the optimal arrangement of slits on the mask to maximize the number of observable targets within one exposure. For this purpose **VMMPS** solves a complex 2D combinatorial problem with **SPOC (Slit Positioning Optimization Code)**, the heart of **VMMPS**. The product of this slit assignment procedure are **ADP (Aperture Definitions in Pixels)** files for every quadrant that contain the necessary information to convert the pre-image slit positions in pixels to a real millimeter scale usable for the mask manufacturing unit drilling the final slitlets. Figure 4.6 gives a schematic overview of the whole mask preparation procedure.

---

<sup>5</sup><http://www.eso.org/sci/observing/phase2/VIMOS/VMMPS.html>

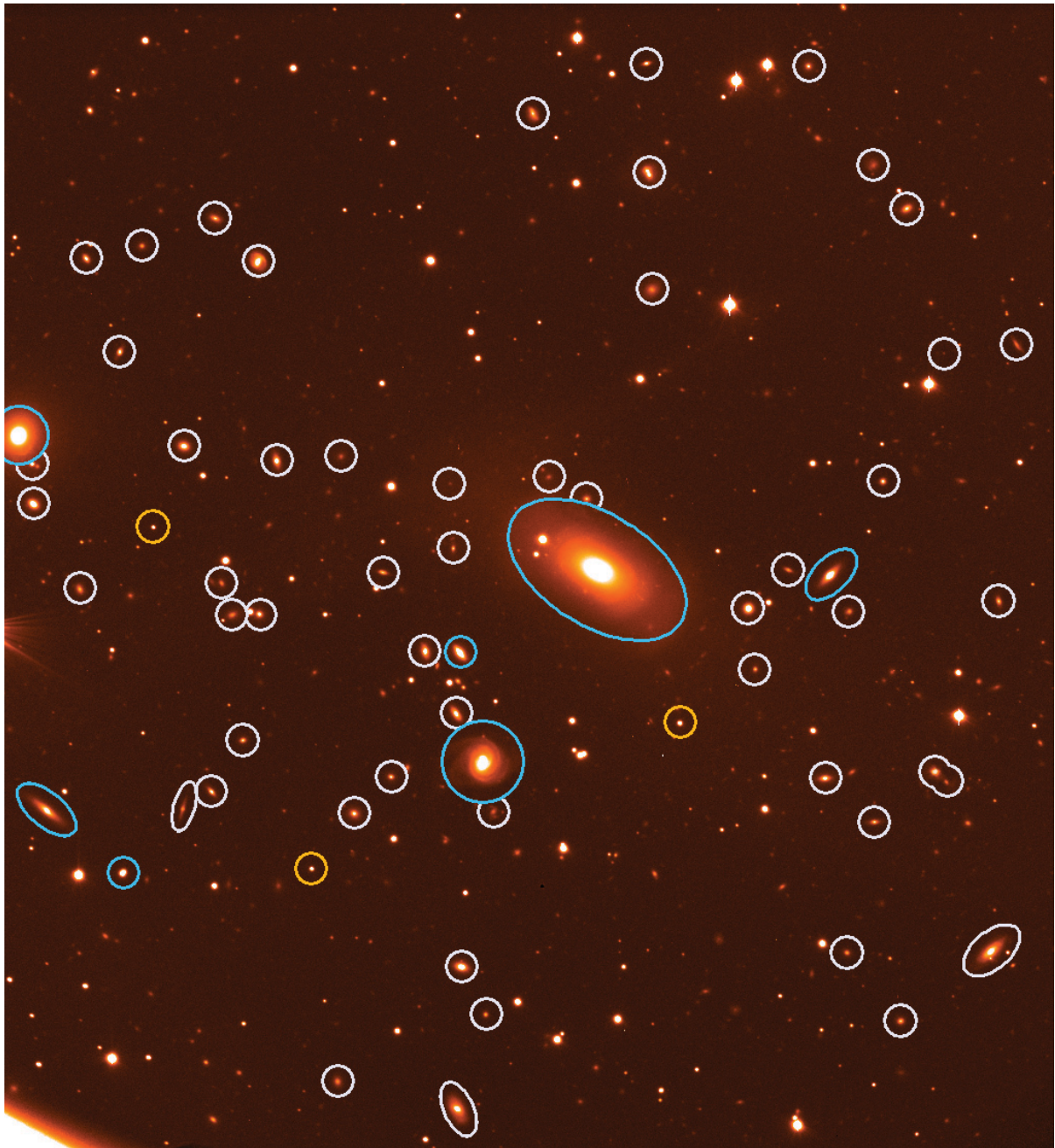


**Figure 4.5:** VIMOS catalog of RX J1548.9+0851 for Q3. Blue circles and ellipses are compulsory objects while yellow ones are the reference objects to center the masks. White circles/ellipses show all other spectroscopic targets. This input catalog provides the basis for the automatic slit assignment by VMPS trying to maximize the number of observable targets within one exposure.

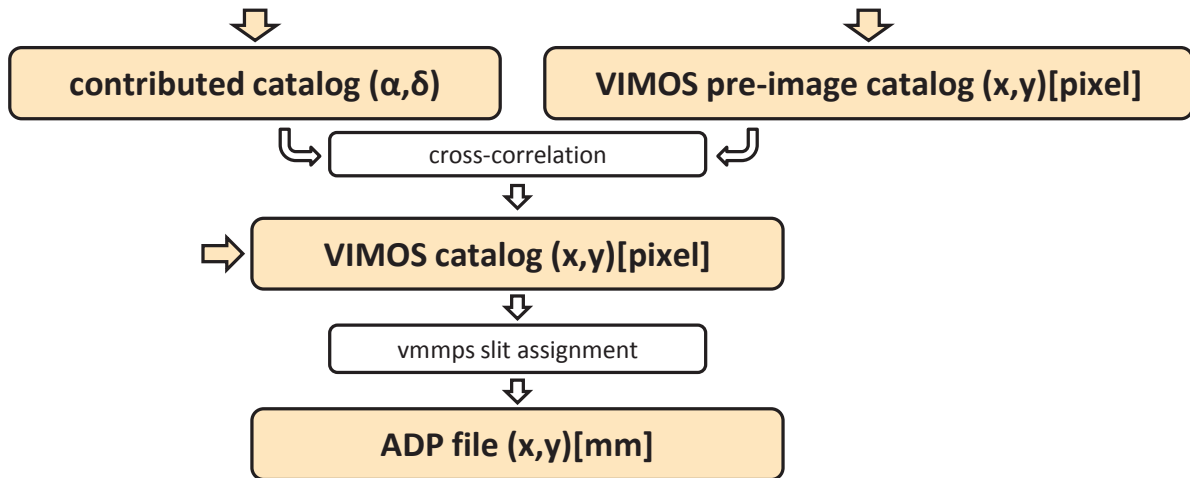


**Figure 4.6:** VIMOS mask preparation.

Since all SDSS objects photometrically classified as galaxies within one-half virial radius of the central ellipticals represent a huge number, a selection for our VIMOS catalogs in Q3 had to be applied. This was simply accomplished by setting a lower magnitude limit of  $i' \sim 20^{\text{mag}}$  for the spectroscopic targets. Obvious stars classified falsely as galaxies as well as objects in the immediate vicinity of the central elliptical hardly seen on the pre-image have not been added to the catalogs. In the remaining quadrants only the brightest galaxies have been selected as spectroscopic targets. In order to cover as many faint galaxies as possible, two masks have been prepared for Q3 for the two fossil aggregates. It is also possible to fine-tune slits after the automatic assignment. This was done for bright objects with large spatial extent, increasing the slit-lengths to a more suitable value. The final ADP files were attached to the acquisition templates of all individual OBs.

Table 4.2 lists all masks prepared with VMMPs for the observed aggregate RX J1548.9+0851. In addition to the acquisition and science templates that were sufficient for the pre-imaging OBs, spectroscopic OBs also require attached night calibration templates for an arc spectrum to properly calibrate wavelengths. It is furthermore mandatory to include finding charts of the slit positions on each quadrant from the VMMPs tool. Once the spectroscopic OBs have been verified by P2PP and sent to the ESO database, the VIMOS phase 2 is finished.

**Table 4.2:** Overview of masks prepared with the VMMPs tool for RX J1548.9+0851.

quadrant	mask	integration time	# VIMOS catalog <sup>a</sup>	# ref, objects	# slits <sup>a</sup>	coverage <sup>b</sup>
Q1	101736	2×4500s	30	3	19	63.33%
Q2	201736	2×4500s	16	3	10	62.50%
Q3	301736	4500s	60	3	28	81.67%
	301746	4500s		3	21	
Q4	401736	2×4500s	30	3	19	63.33%

<sup>a</sup> excluding reference objects

<sup>b</sup> fraction of spectroscopic targets in the VIMOS catalog with assigned slits (excluding reference objects)

## 4 MOS observations

Out of the two fossil aggregates proposed for observations, only RX J1548.9+0851 has been observed. Due to the observability constraint of RX J1152.5+0328, this aggregate would have had to be observed in April to yield optimal observing conditions (see Fig. 4.3) making observations impossible in the course of the period. Table 4.3 lists the observing log for the two OBs assigned to the observed aggregate and presents the observing parameters in the corresponding nights. The observations were carried out in April and May 2009. Since two masks were prepared for Q3, two OBs had to be defined for this system. All OBs were graded *A*, hence they are fully within the specifications set by the PI. A detailed overview on the night conditions of both OBs displaying temperature, pressure, seeing, ... can be found in Appendix B.

**Table 4.3:** Night conditions of the executed spectroscopic OBs.

RX J1548.9+0851								
OB ID	date	UT	exposure time	airmass	seeing [arcsec]	moon <sup>a</sup> %	sky <sup>b</sup>	grade <sup>c</sup>
367273	2009-05-26	03:33 - 05:07	4500s	1.217	0.80	N/A	CLR	A
367282	2009-04-24	05:08 - 06:41	4500s	1.219	0.69	N/A	CLR	A

<sup>a</sup> lunar illumination in %; if below the horizon: N/A

<sup>b</sup> PH-Photometric, CL-CLEAR, TN-Thin cirrus, TK-Thick cirrus

<sup>c</sup> A: fully within specifications B: mostly within specifications C: out of specs - repeat

## 5 MOS data

Once an OB has been successfully completed, the raw data are stored in the ESO archive<sup>6</sup> under the corresponding OB ID and can be downloaded by the PI. In the case of MOS mode, the raw data consists of the science frames for each quadrant, the acquisition images, and the attached night calibration arc spectra. As soon as the whole run is completed, all of the raw data as well as calibration files measured as part of the regular calibration plan (bias, flats, ...) and static calibrations (extinction tables, standard star flux tables, ...) are shipped to the PI on DVDs. A proprietary period of one year applies to the raw science datasets starting with the day of data shipment while the calibration data are publicly available from the beginning.

### 1 The ESO VIMOS MOS reduction pipeline

In addition to the raw science and regular calibration data, ESO also provides the PI with processed science data automatically reduced by means of the corresponding instrument reduction pipeline. Each pipeline is based on well-defined recipes especially designed for a specific task. If a user wants to reduce the raw science data on his own for whatever scientific or personal reason, ESO offers two applications for executing pipeline recipes: *Gasgano*<sup>7</sup> and *EsoRex*<sup>8</sup>.

<sup>6</sup>[http://archive.eso.org/eso/eso\\_archive\\_main.html](http://archive.eso.org/eso/eso_archive_main.html)

<sup>7</sup><http://www.eso.org/gasgano>

<sup>8</sup><http://www.eso.org/cpl/esorex.html>

While *Gasgano* provides a complete graphic interface, *EsoRex* is operated on the command line<sup>9</sup>.

The observed MOS raw science data is reduced automatically by ESO by means of the *vm-mosobsstare* recipe. If the raw data consists of a sequence of exposures with slight offsets in equatorial coordinates (jittered data), the recipe *vmmosobsjitter* is used instead. For a detailed description of *vmmosobsstare*, the *VIMOS Pipeline User Manual* is recommended. Here, just a short description is given.

The recipe *vmmosobsstare* is used to apply basic reduction steps to the raw data and to extract and flux-calibrate the individual object spectra. The recipe does bias subtraction and uses skylines to apply wavelength calibration. Spectral distortions of the instrument are determined with the *vmspcaldisp* recipe to construct an extraction table allowing for the proper extraction of each individual 2-D spectrum. Scientific targets in the slits are detected above a certain background noise level. If more than one object is found in an individual slit, both objects are extracted<sup>10</sup>. A median sky level is estimated for each wavelength and subtracted from the data. The extracted spectra are resampled to a constant wavelength interval ( $0.603 \text{ \AA pix}^{-1}$  for the HR blue grism). A reduced standard star is processed with *vmmosstandard* yielding a spectro-photometric table containing the instrument efficiency and response curves used for flux calibration. The fluxes are valid except for a constant factor, the calibration being relative instead of absolute. Finally, 1-D spectra are extracted by applying the method of Horne (1986) for optimal spectral extraction. The individual *vmmosobsstare* parameters used by the ESO pipeline can be found in the *VIMOS Pipeline User Manual*.

## 2 Processed science products

The *vmmosobsstare* recipe creates 7 processed science products which are the 1-D and 2-D extracted object spectra, the 1-D and 2-D sky models for these objects, and an object and window table to correlate the extracted spectra with a corresponding slit ID and the object ID set in the ADP files. Table 4.4 lists all processed science products obtained by ESO.

All processed science products are easily identified by means of their structured naming scheme. It follows the simple pattern:

$$\text{VI\_}<\text{TYPE}>\_<\text{OB\_ID}>\_<\text{TIMESTAMP}>\_<\text{PARAMS}>.\_<\text{SUFFIX}>$$

where VI stands for VIMOS, <TYPE> is the product code (see Table 4.4), <OB\_ID> the OB identification and <TIMESTAMP> the observation date and time in the form

$$<\text{YEAR}>-<\text{MONTH}>-<\text{DAY}>\text{T}<\text{HOUR}>:<\text{MINUTE}>:<\text{SECOND}>.\_<\text{MILLISEC}>$$

<PARAMS> lists the observation parameters in the form <ORDFLT>\_<GRISM>\_<MASK>\_<QQUAD>\_<GAIN>, representing order sorting filter, grism, mask, quadrant, and gain. <SUFFIX> is the file extension. As an example,

$$\text{VI\_SRFM\_367273\_2009-05-27T03\_48\_55.237\_HRb\_301736\_Q3\_hi.fits}$$

<sup>9</sup>A complete list of VIMOS MOS recipes for the creation of regular calibration products (master bias, master flats, ...) and for reducing the raw science data is given in the *VIMOS Pipeline User Manual*.

<sup>10</sup>A maximum object size parameter can be set above which the recipe tries to unblend multiple objects.



**Table 4.4:** VIMOS MOS science products processed by the standard reduction pipeline.

code	product type	mode	description
SREI	IMG_SCIENCE_REDUCED	IMG	reduced science image
SREM	MOS_SCIENCE_REDUCED	MOS	1-D object spectra
SRFM	MOS_SCIENCE_FLUX_REDUCED	MOS	1-D flux calibrated object spectra <sup>a</sup>
SEXM	MOS_SCIENCE_EXTRACTED	MOS	2-D object spectra
SSKM	MOS_SCIENCE_SKY	MOS	2-D sky spectra (per slit)
SSRM	MOS_SKY_REDUCED	MOS	1-D sky spectra (per object)
SOTM	OBJECT_TABLE	MOS	object identification table for SREM, SRFM, and SSRM <sup>b</sup>
SWTM	WINDOW_TABLE	MOS	object position table for SEXM and SSKM <sup>c</sup>

<sup>a</sup> flux units are given in  $\text{ergs s}^{-1} \text{cm}^{-2} \text{\AA}^{-1}$

<sup>b</sup> correlating 1-D apertures (spectra) with the corresponding slit IDs

<sup>c</sup> listing the exact pixel position of each extracted 2-D spectrum

contains the 1-D flux calibrated spectra of OB 367273 in quadrant 3 observed with mask 301736 with high gain and the HR blue grism without any order sorting filter. The observation was carried out on the 27<sup>th</sup> of May 2009 at 03:48:55 UT.

For the purpose of measuring radial velocities of the faint galaxies surrounding the central elliptical galaxy in RX J1548.9+0851, the 1-D flux-calibrated spectra (SRFM) were used.

### 3 Object identification

The 1-D extracted and flux-calibrated spectra of all objects identified in a quadrant are stored in rows (apertures) in the SREM and SRFM files. The number of objects (apertures) is not necessarily the number of slits assigned to the scientific targets. First, some objects may be too faint to be identified by the recipe. Secondly, there may be multiple objects identified in individual slits. In order to properly assign each aperture to the corresponding object, an object identification table (SOTM) is provided as a fits table. This table relates each aperture<sup>11</sup> with the corresponding slit number. To correlate these slit numbers with the object IDs as listed in the prepared ADP files (see Sect. 2), the SREM and SRFM image headers hold the keywords SLIT: $x$  ID<sup>12</sup> with the object IDs for each individual slit. Knowing the object ID of every aperture, the SRFM 1-D spectra were copied to individual files for easier identification. These spectra were then used for the radial velocity measurements.

### 4 Cleaning spectra

As highlighted in Sect. 5.1, the VIMOS MOS reduction pipeline automatically estimates sky models for all extracted 1-D and 2-D spectra and subtracts these models from the corresponding object spectra. This task is not perfect, however. Especially for fainter objects this procedure is problematic since most of the processed spectra still exhibit a strong contamination by a large number of obvious sky lines. This is not surprising since it is much more difficult to

<sup>11</sup> More precisely it relates the  $Y$  pixel position of each aperture, counting from the image bottom upwards with the first row at  $Y = 0$ , with the corresponding slit number.

<sup>12</sup>  $x$  refers to the slitnumber.

determine the correct sky level when the target flux is close to the background noise. In order to correct for obvious sky lines in the processed SRFM spectra, each file was compared with the associated sky model. If a strong feature was present at a certain wavelength in the sky model and the object spectrum, it was deleted from the object spectrum manually within the IRAF `splot` task. For the brighter objects in the sample hardly any corrections had to be applied. For faint objects the uncertainty remains as to whether some features are due to a falsely estimated sky model or represent intrinsic emission lines from the galaxy. Since these galaxies are only considered for radial velocity measurements (with absorption lines present), no further importance was attached to this problem. In fact, true emission lines from the galaxy itself would also complicate the radial velocity measurements (see below).

## 6 Measuring radial velocities

In order to measure radial velocities and determine group membership of the RX J1548.9+0851 candidate faint galaxy population, the cross-correlation technique as described in detail by Tonry & Davis (1979) was used in the present work. Only a very rough introduction is given here.

### 1 A brief theory of cross-correlation

Let us assume that  $g(n)$  is the spectrum of a galaxy with unknown redshift and  $t(n)$  a template spectrum with zero redshift similar to the spectral type of the investigated galaxy. These spectra are sampled into  $N$  bins with  $n = A \ln \lambda + B$  representing the bin number. Since the spectra are binned linearly with  $\ln \lambda$ , a redshift always corresponds to a uniform linear shift<sup>13</sup> in these spectra. The normalized cross-correlation function is now defined as

$$c(n) \equiv g \times t(n) = \frac{1}{N\sigma_g\sigma_t} \sum_m g(m)t(m-n)$$

with  $\sigma_t$  and  $\sigma_g$  being the rms of the spectra. The  $\times$  denotes the cross-correlation product. If a spectrum is correlated with itself – so-called *autocorrelation*,  $c(n)$  will have a peak at 1 at zero redshift. This is the best possible solution of the cross-correlation procedure. If the template and object are identical except for a shift  $\delta$  in wavelengths, the peak of 1 will appear at  $n = \delta$ . Not surprisingly, when dealing with actual observations, the largest peak of the cross-correlation function will always be only a fraction of 1. If  $g(n)$  is assumed to be of the form  $g(n) \cong \alpha t * b(n - \delta)$ , where  $*$  denotes convolution and  $b(n)$  is a broadening function, one tries to minimize the expression

$$\chi^2 = \sum_n [\alpha t * b(n - \delta) - g(n)]^2$$

to get the optimal match of the object spectrum with the zero-velocity template. The position of the highest peak in the cross-correlation function can then be used to calculate the redshift or radial velocity of the galaxy.

<sup>13</sup> $\lambda = (1+z)\lambda_0 \Rightarrow \ln \lambda = \ln(1+z) + \ln \lambda_0$

## 2 The xcsao task

The aforementioned cross-correlation technique as introduced by Tonry & Davis (1979) has been fully integrated into IRAF by means of the `xcsao` task in the `rvsao` package. The task is straightforward and requires only the object spectrum as well as one or more template spectra to be correlated. The application simply assumes the galaxy to be the convolution of a stellar spectrum with a Gaussian. Peaks in the cross-correlation function are identified and fit by parabolas to obtain their position and widths resulting in the redshift and velocity dispersion of the galaxy.

Stellar spectral templates of zero radial velocity<sup>14</sup> have been taken from the library of stellar spectra by Jacoby et al. (1984). Spectral types similar to the stellar populations of ellipticals, i.e. G and K giants have been selected. Table 4.5 lists the corresponding spectral types of all stellar templates used with `xcsao`.

**Table 4.5:** Stellar spectral templates used for the `xcsao` cross correlation technique. All stars were taken from the library of Jacoby et al. (1984).

JHC84 <sup>a</sup>	name	$\alpha_{J2000}$	$\delta_{J2000}$	Spectral Type	$(B - V)_0$
92 .....	HD 26514	04 12 25.0	+23 34 30	G6 III	0.94
95 .....	HD 245389	05 37 25.1	+32 14 58	G8 III	0.98
97 .....	SAO 55164	01 58 52.8	+37 48 58	K0 III	1.01
101 .....	HD 21110	03 25 23.9	+31 43 52	K4 III	1.45
144 .....	HD 191010	20 06 45.8	+25 41 07	G3 I	0.93
146 .....	HD 186293	19 43 05.3	+09 29 22	K0 I	1.18
149 .....	HD 1400	00 18 28.7	+62 12 12	K5 I	1.56

<sup>a</sup> record number from Jacoby et al. (1984)

In addition to the computed cross-correlation function, `xcsao` lists redshifts in the form  $cz$  for each template with the corresponding errors and a confidence parameter  $R$  (see Fig. 4.7).  $R$  ( $r$  in the literature) indicates the reliability of the chosen peak being the correct one. Kurtz & Mink (1998) have calibrated  $r$  empirically and consider the redshift determination to be reliable above  $r_{\min} = 3.0$ . This value was also adopted in this work. Since seven templates were used, the redshift average was chosen as the final result while the redshift error was taken as the standard deviation<sup>15</sup>. All redshifts measured with `xcsao` have been checked by fitting Gaussians to the strongest absorption features. For objects with  $R \gtrsim 3.0$ , the manually determined redshifts were always within the `xcsao` error bars.

## 3 Computing radial velocities

At the SDSS redshift of the RX J1548.9+0851 central elliptical ( $cz = 21629 \text{ km s}^{-1}$ ), the difference in measuring radial velocities by either the classical or relativistic Doppler effect

<sup>14</sup>These spectra have not been corrected for the radial velocities of the stars since deviations to the rest wavelength are negligible and in the order of only  $0.5 \text{ \AA}$ .

The spectra can be downloaded from `ftp://ftp.stsci.edu/cdbs/grid/jacobi/` in both `.fits` and `.ascii` format.

<sup>15</sup>If 5 of 7 templates yielded the same redshift, the outliers were not taken into account in deriving average and  $\sigma$ .

already amounts to 3.60% ( $\sim 778 \text{ km s}^{-1}$ ). Since the typical redshift uncertainty measured by `xcsao` is much lower for the studied sample ( $\Delta cz \sim 40 \text{ km s}^{-1}$ ), the relativistic Doppler effect

$$v_r = c \cdot \frac{(z+1)^2 - 1}{(z+1)^2 + 1} \quad 1+z = \sqrt{\frac{1+v_r/c}{1-v_r/c}} \quad (4.1)$$

was considered in this work. Similar to redshifts, radial velocity errors are calculated by standard deviations. Table 4.6 lists the velocities of all spectroscopic targets extracted by the ESO `vmmosobsstare` recipe as well as the corresponding cross-correlation parameters  $h$  and  $R$ . The objects are listed with increasing right ascension, i.e. from bottom to top in Figs. 4.8 to 4.11. In total, 84 redshifts out of the 90 extracted spectra were measured, amounting to  $\sim 93\%$ .

## 7 RX J1548.9+0851 group membership definition

In order to distinguish group members from background galaxies, a certain threshold in radial velocity or redshift space with respect to the systemic group velocity has to be defined. There are different ways to define the systemic velocity: either the radial velocity of the brightest, central galaxy assumed to be located at the center of the system potential well, or the median or average of the groups radial velocity distribution. The group membership for galaxy  $i$  is then simply verified if the condition  $|v_i - v_{\text{sys}}| < \Delta v$  is fulfilled.  $\Delta v$  varies amongst different authors. According to Ramella et al. (1994), a  $\Delta v$  of  $1500 \text{ km s}^{-1}$  is considered a good match to the scale of loose groups and is used in this work. Figure 4.12 shows the distribution of radial velocities for all objects in Table 4.6. The group is well-defined in radial-velocity space with a strong peak around  $v_r \sim 20700 \text{ km s}^{-1}$ . Orange histograms show group members fulfilling the aforementioned condition while grey histograms present nonmembers. Assuming the median or average radial velocity of the orange distribution as a system velocity, the membership condition when accounting for error bars holds until  $\Delta v = 1250 \text{ km s}^{-1}$ . The radial velocity of the central elliptical  $v_r = 20854 \text{ km s}^{-1}$  is significantly shifted towards higher velocities with respect to the median and average velocities by  $158$  and  $212 \text{ km s}^{-1}$ , respectively.

### 1 Spatial distribution of the faint galaxy population

Figures 4.8 to 4.11 show the finding charts for all spectroscopic targets in the four VIMOS quadrants as well as all non-observed SDSS objects photometrically classified as galaxies down to  $i' = 21^{\text{mag}}$ . Taking into account a luminosity distance of  $D_L = 326 \text{ Mpc}$  based on the median redshift of the system  $cz_{\text{median}} = 21462 \text{ km s}^{-1}$ , this magnitude limit corresponds to an absolute magnitude limit of  $M_{i'} = -16.7$ <sup>16</sup>. Hardly any objects outside quadrant 3 have been found to be group members indicating that the projected number density of group members drops rapidly with increasing radius. Interestingly, the projected spatial distribution of members in quadrant 3 is correlated with the position angle of the major axis of the central elliptical. While most objects lie near the extrapolated major axis, hardly any are found perpendicular to it. Quadrants are shown as sent to the PI, i.e. the orientation following the VIMOS CCD coordinates  $(x, y)$  (compare with Fig. 4.2 – MOS mode rotator angle  $90^\circ$ ). To avoid any confusion, coordinate axes for both CCD  $(x, y)$  and equatorial  $(N, E)$  coordinates are shown.

<sup>16</sup>following equation 2.3.

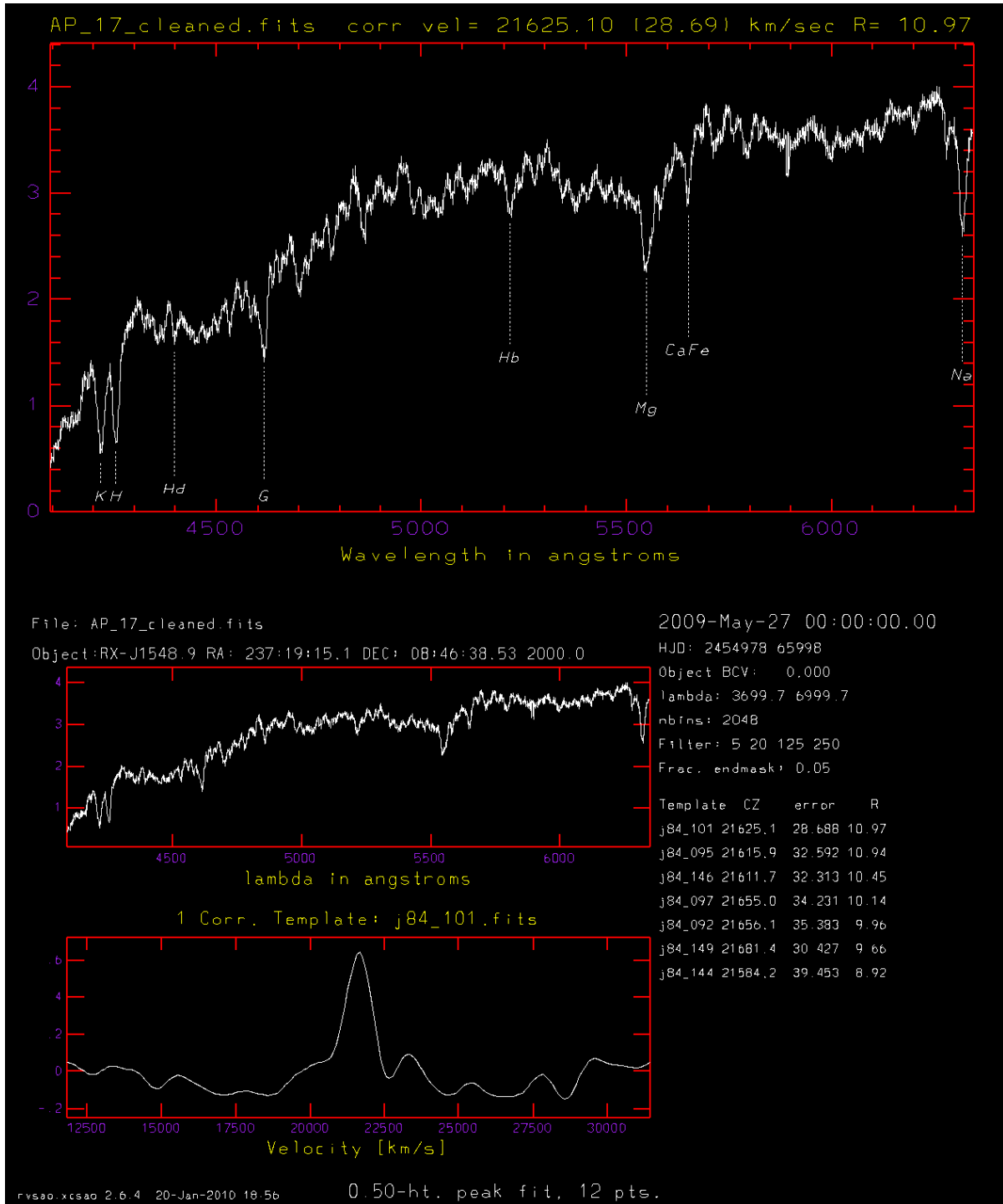


**Figure 4.7:** The xcsao environment. Upper panel: galaxy spectrum of the central elliptical with the strongest absorption lines identified by the routine. Lower panel: galaxy spectrum and the cross-correlation function of the best-fitting template. To the right, the template names, resulting redshifts  $cz$ , redshift errors, as well as the confidence parameter  $R$  is shown for all templates used in the cross-correlation.

**Table 4.6:** Radial velocities of the candidate faint galaxy population.

object	$\alpha_{J2000}$	$\delta_{J2000}$	$h^a$	$R^a$	$v_{\text{rad}}^b$	$v_{\text{rad,error}}^b$
01 .....	15 48 42.24	08 52 26.3	0.38	5.70	19899	26
02 .....	15 48 43.85	08 41 10.6	0.39	6.46	79430	56
03 .....	15 48 43.86	08 48 42.5	0.35	4.25	20960	27
04 .....	15 48 44.04	08 51 27.5	0.43	5.61	75470	39
05 .....	15 48 45.15	08 41 24.1	0.34	4.58	79249	51
06 .....	15 48 45.57	08 39 53.0	0.35	4.84	85439	39
07 .....	15 48 45.70	08 49 03.8	0.32	4.28	21172	33
08 .....	15 48 45.73	08 48 06.7	0.37	5.57	23197	24
09 .....	15 48 45.99	08 43 24.6	0.43	5.64	21183	27
10 .....	15 48 47.84	08 53 51.8	0.18	2.25	-	-
11 .....	15 48 48.30	08 43 41.2	0.28	4.21	91436	47
12 .....	15 48 49.20	08 48 53.0	0.31	4.04	19469	28
13 .....	15 48 49.43	08 52 19.8	0.48	6.09	75538	39
14 .....	15 48 49.51	08 54 21.9	0.45	5.65	21716	42
15 .....	15 48 49.55	08 53 28.0	0.36	4.39	54552	81
16 .....	15 48 50.01	08 53 16.5	0.49	7.59	62003	35
17 .....	15 48 50.37	08 49 12.6	0.44	5.36	21512	23
18 .....	15 48 50.41	08 52 05.1	0.47	5.89	75369	36
19 .....	15 48 50.55	08 48 28.9	0.46	5.73	20599	32
20 .....	15 48 50.73	08 42 48.4	0.41	5.72	20632	36
21 .....	15 48 50.78	08 51 28.6	0.37	5.32	18681	33
22 .....	15 48 51.39	08 53 04.0	0.40	5.05	19889	23
23 .....	15 48 53.30	08 49 40.3	0.57	8.12	22672	28
24 .....	15 48 53.74	08 51 37.7	0.63	9.34	20983	24
25 .....	15 48 53.78	08 51 51.5	0.61	10.07	19572	26
26 .....	15 48 54.75	08 53 08.2	0.47	6.65	21851	74
27 .....	15 48 54.77	08 52 57.5	0.65	10.65	20793	26
28 .....	15 48 54.85	08 49 02.9	0.41	6.30	21776	96
29 .....	15 48 54.93	08 49 43.0	0.65	10.11	20648	30
30 .....	15 48 55.12	08 48 03.5	0.55	8.61	21049	24
31 .....	15 48 55.44	08 54 08.9	0.51	7.99	20303	29
32 .....	15 48 55.82	08 49 10.6	0.65	11.39	20205	27
33 .....	15 48 55.89	08 52 08.4	0.34	4.14	44472	34
34 .....	15 48 55.96	08 50 42.9	0.67	10.15	20854	31
35 .....	15 48 55.97	08 49 27.2	0.49	7.84	20234	26
36 .....	15 48 56.71	08 44 58.3	0.61	10.39	20558	26
37 .....	15 48 56.98	08 44 10.7	0.58	9.87	52731	24
38 .....	15 48 57.78	08 41 49.6	0.29	3.71	29862	35
39 .....	15 48 57.87	08 50 47.3	0.61	10.87	20815	22
40 .....	15 48 58.28	08 51 41.6	0.12	1.47	-	-
41 .....	15 48 58.45	08 51 02.4	0.34	4.90	19489	53
42 .....	15 48 58.80	08 54 27.9	0.71	12.90	19464	30
43 .....	15 48 58.88	08 52 50.6	0.69	11.88	21392	28
44 .....	15 48 59.00	08 52 25.0	0.32	5.02	20981	32
45 .....	15 48 59.20	08 44 30.7	0.48	6.18	52789	28
46 .....	15 48 59.22	08 44 47.0	0.36	5.32	64675	50
47 .....	15 48 59.28	08 53 27.5	0.69	12.90	20696	23
48 .....	15 48 59.56	08 54 33.2	0.64	10.14	19781	28

<sup>a</sup> height  $h$  of the cross-correlation peak and `xsao` confidence parameter  $R$ .<sup>b</sup> Values given in  $\text{km s}^{-1}$ .

Table 4.6 – continued.

object	$\alpha_{J2000}$	$\delta_{J2000}$	$h^a$	$R^a$	$v_{\text{rad}}^b$	$v_{\text{rad,error}}^b$
49 .....	15 49 01.77	08 48 25.3	0.13	2.00	-	-
50 .....	15 49 01.80	08 53 53.0	0.35	4.99	44436	29
51 .....	15 49 02.01	08 47 56.5	0.22	3.20	19606	34
52 .....	15 49 02.63	08 42 40.0	0.22	2.92	20783	42
53 .....	15 49 02.87	08 40 45.0	0.49	7.45	54601	36
54 .....	15 49 04.23	08 52 58.1	0.43	6.29	35489	34
55 .....	15 49 04.31	08 54 06.4	0.62	9.90	20678	25
56 .....	15 49 05.38	08 53 15.1	0.63	10.55	20334	31
57 .....	15 49 05.41	08 40 54.6	0.55	9.95	45469	23
58 .....	15 49 05.65	08 48 40.1	0.66	11.06	21607	26
59 .....	15 49 05.74	08 45 27.5	0.42	5.90	29767	30
60 .....	15 49 06.57	08 42 12.0	0.36	4.65	64034	37
61 .....	15 49 06.61	08 50 22.8	0.49	6.11	61812	49
62 .....	15 49 06.64	08 42 02.3	0.42	5.95	50169	50
63 .....	15 49 06.82	08 48 53.2	0.19	3.24	21043	37
64 .....	15 49 07.05	08 41 37.7	0.22	2.05	20225	37
65 .....	15 49 08.20	08 51 08.8	0.39	5.30	61797	47
66 .....	15 49 09.05	08 39 41.4	0.55	7.80	44953	45
67 .....	15 49 09.47	08 49 19.2	0.60	10.35	19801	28
68 .....	15 49 09.54	08 50 23.6	0.53	8.56	61735	47
69 .....	15 49 23.71	08 39 09.5	0.28	3.67	53057	37
70 .....	15 49 23.93	08 41 01.2	0.36	4.84	61959	31
71 .....	15 49 24.05	08 43 44.7	0.24	3.19	21512	39
72 .....	15 49 25.22	08 47 51.3	0.28	3.58	60144	28
73 .....	15 49 25.98	08 52 18.8	0.44	6.90	79003	44
74 .....	15 49 27.48	08 50 56.4	0.17	1.93	-	-
75 .....	15 49 28.47	08 45 18.9	0.37	4.73	62148	46
76 .....	15 49 28.82	08 54 06.0	0.23	3.17	20756	29
77 .....	15 49 29.13	08 42 41.3	0.22	2.23	-	-
78 .....	15 49 30.07	08 41 27.1	0.43	6.62	52943	34
79 .....	15 49 35.59	08 48 23.9	0.14	1.84	-	-
80 .....	15 49 37.66	08 39 47.8	0.58	9.18	21624	24
81 .....	15 49 40.40	08 43 04.3	0.54	8.36	62071	36
82 .....	15 49 41.04	08 50 21.2	0.34	4.57	16385	26
83 .....	15 49 41.70	08 48 42.1	0.59	8.71	19873	24
84 .....	15 49 43.33	08 53 43.6	0.39	5.30	84485	40
85 .....	15 49 43.47	08 40 03.0	0.42	6.37	74288	57
86 .....	15 49 43.76	08 44 16.8	0.40	5.39	84792	36
87 .....	15 49 44.54	08 45 03.8	0.54	9.04	50622	44
88 .....	15 49 45.14	08 39 26.3	0.31	4.25	87051	39
89 .....	15 49 47.53	08 42 56.7	0.28	3.79	53291	35
90 .....	15 49 47.66	08 51 14.5	0.32	3.31	29497	40

<sup>a</sup> height  $h$  of the cross-correlation peak and `xcsao` confidence parameter  $R$ .<sup>b</sup> Values given in  $\text{km s}^{-1}$ .

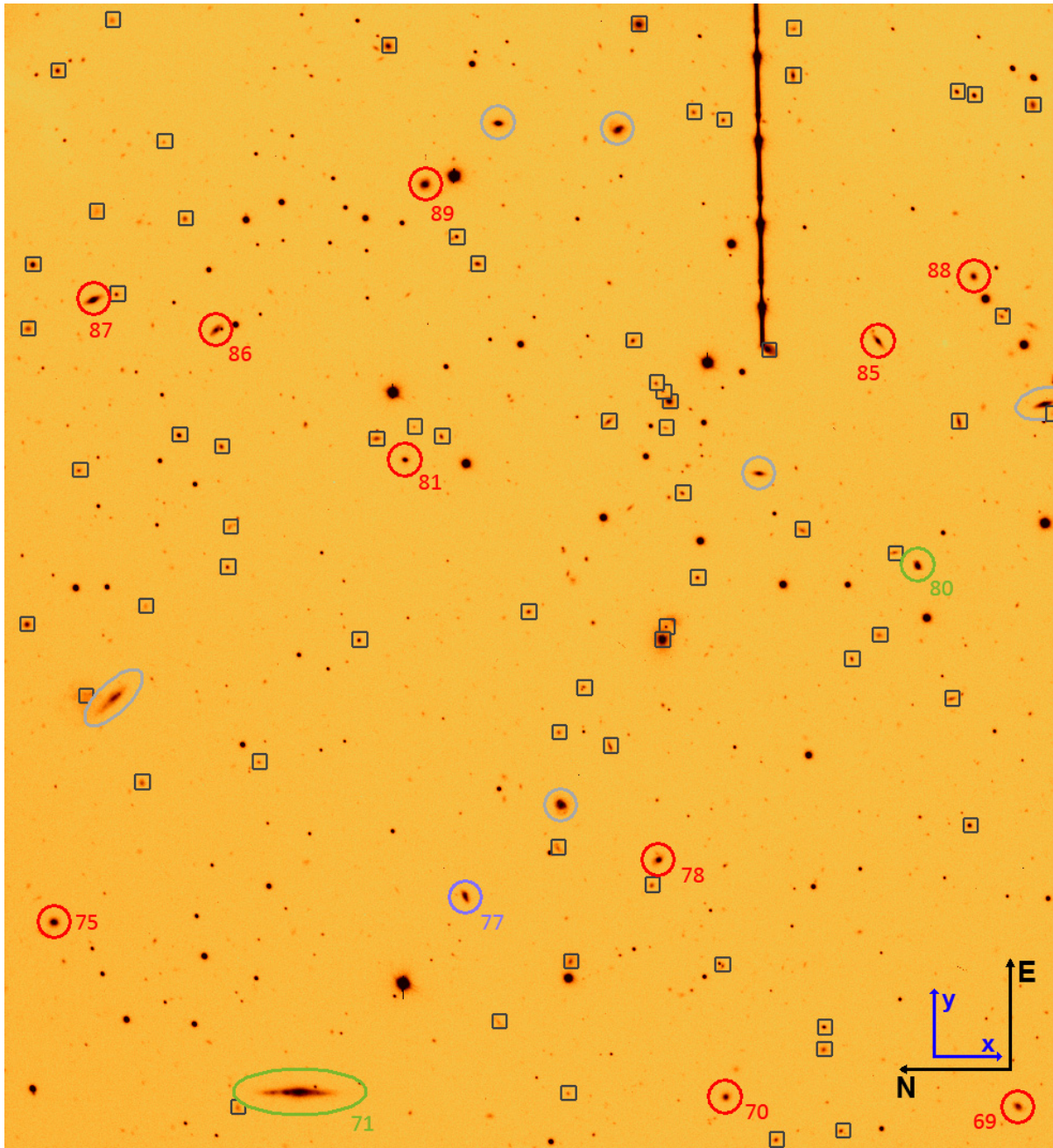


**Figure 4.8:** Spectroscopic targets – quadrant 1. Numbers as given in Table 4.6.

*Color coding*

group members: ○    nonmembers: ○    no consistent velocity within xcsao: ○  
 assigned slits but no extracted spectra:     SDSS galaxies down to  $i' = 21^{\text{mag}}$ :



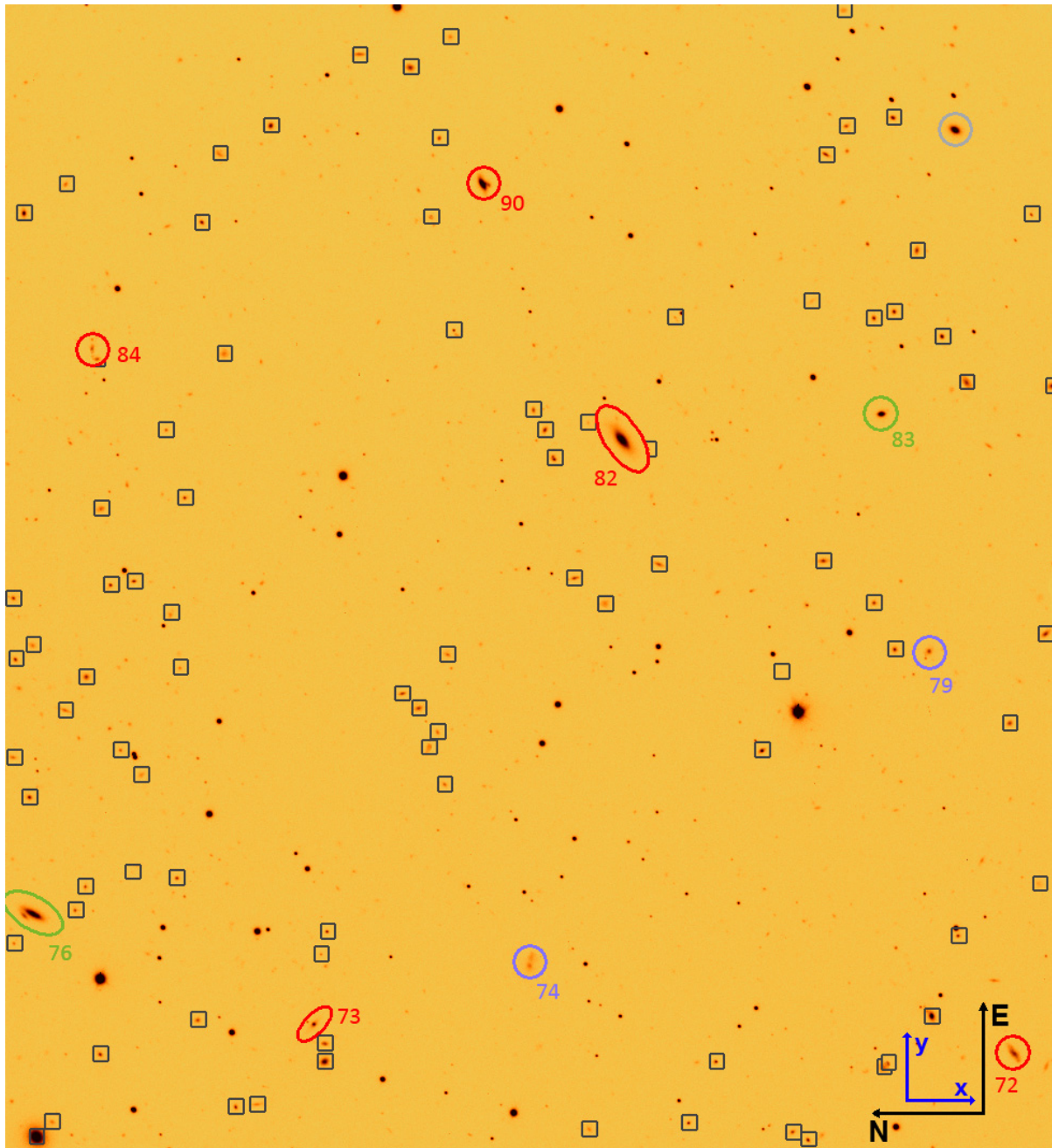


**Figure 4.9:** Spectroscopic targets – quadrant 2. Numbers as given in Table 4.6.

*Color coding*

group members: ○    nonmembers: ○    no consistent velocity within xcsao: ○  
 assigned slits but no extracted spectra:     SDSS galaxies down to  $i' = 21^{\text{mag}}$ :

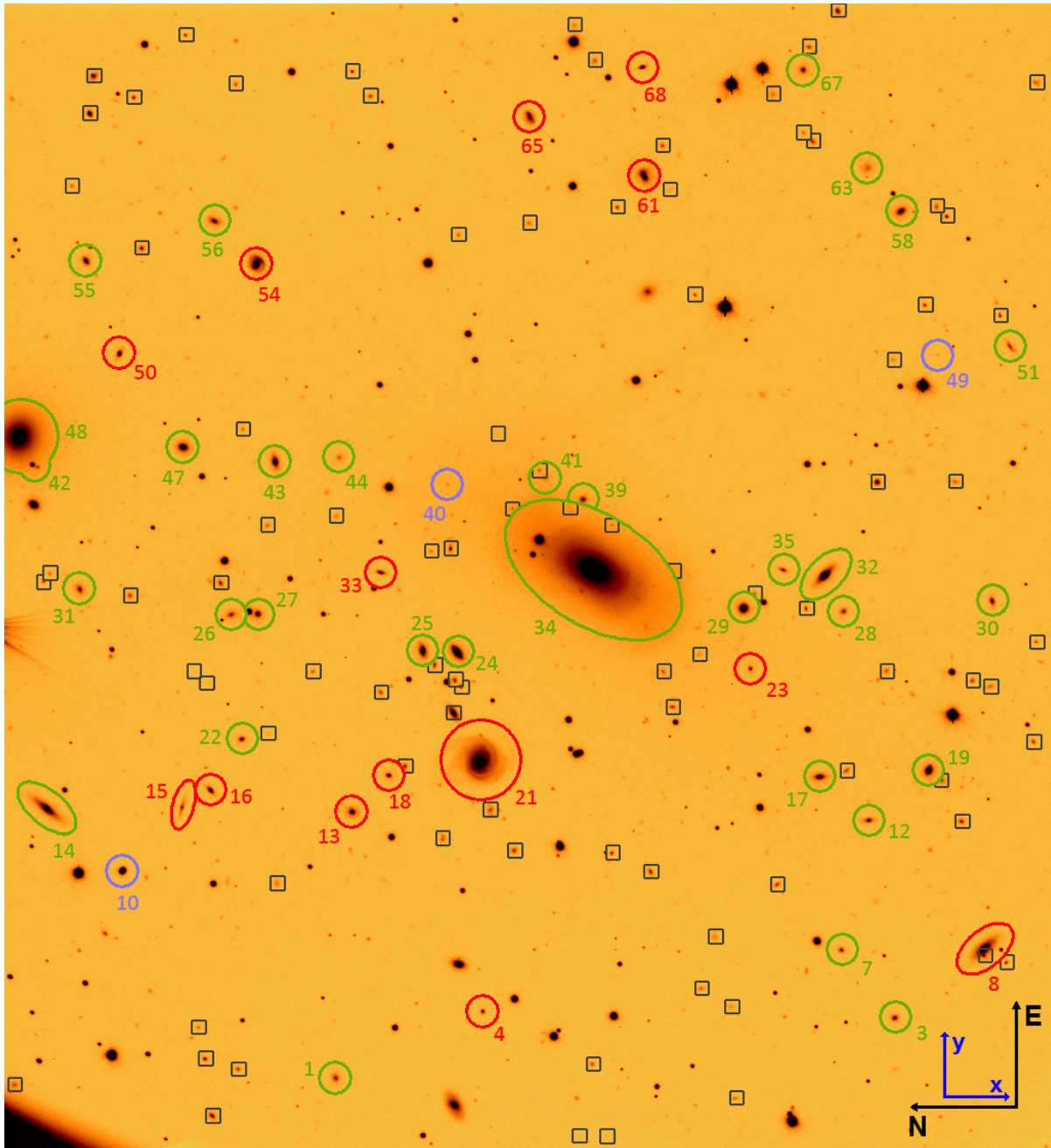


**Figure 4.10:** Spectroscopic targets – quadrant 3. Numbers as given in Table 4.6.

*Color coding*

group members: ○ nonmembers: ○ no consistent velocity within xcsao: ○  
 assigned slits but no extracted spectra: ○ SDSS galaxies down to  $i' = 21^{\text{mag}}$ : □

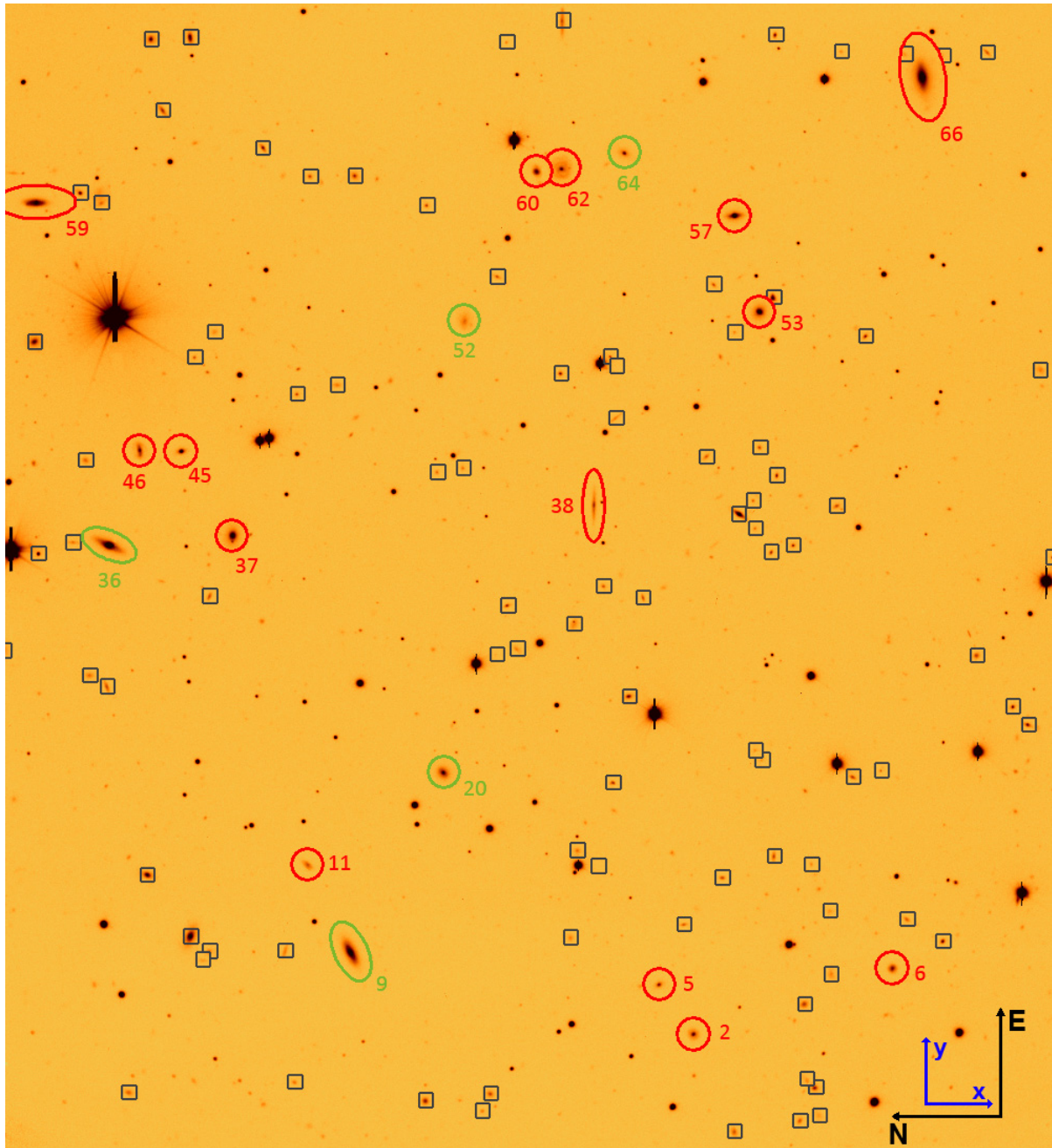


**Figure 4.11:** Spectroscopic targets – quadrant 4. Numbers as given in Table 4.6.

*Color coding*

group members: ○ nonmembers: ○ no consistent velocity within xcsao: ○  
 assigned slits but no extracted spectra: ○ SDSS galaxies down to  $i' = 21^{\text{mag}}$ : □

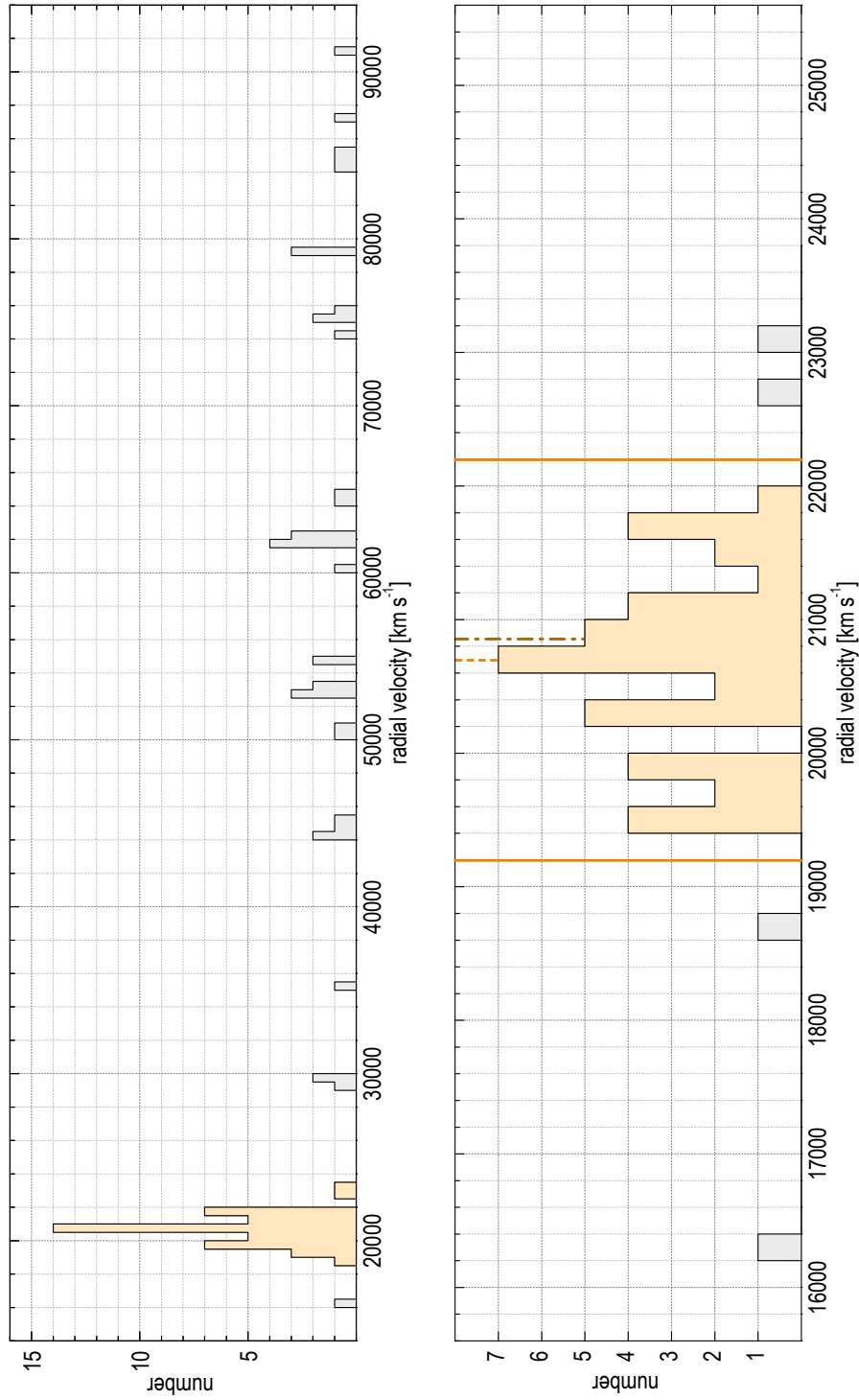


**Figure 4.12:** Distribution of radial velocities for all objects in Table 4.6. Upper panel: total measured velocity range covering 80 000 km s<sup>-1</sup> with a bin size of 500 km s<sup>-1</sup>. Lower panel: cutout around the central elliptical covering 10 000 km s<sup>-1</sup> with a bin size of 200 km s<sup>-1</sup>. The dashed line shows the median of the orange distribution while the dash-dotted line presents the velocity of the central elliptical. Solid lines indicate the  $\Delta v = 1500$  km s<sup>-1</sup> group membership threshold.

## 8 Completeness

Due to the technical design of the VIMOS instrument with large gaps between the four quadrants present, a choice had to be made on how to position the detector on the sky when applying for observing time. To cover the inner regions of the group as top priority, the central elliptical was positioned on quadrant 3. Therefore, the spatial coverage of the outer parts of the group is strongly incomplete. Another source for incompleteness are the observations themselves. Since the HR blue grism only permits one slit along the dispersion direction, objects with nearly identical right ascension cannot be observed simultaneously. In addition, not all objects with assigned slits were extracted by the recipe due to their faintness. Table 4.7 gives number statistics of galaxies within group radii of 300 kpc, 500 kpc, and 1 Mpc while Fig. 4.13 shows the spatial coverage of the system by VIMOS. The table shows that the fraction of galaxies with measured redshifts is always above 90% with respect to all observed targets. Not surprisingly, the fraction of redshifts from the literature increases towards larger radii. It is also evident that out of all of the galaxies with redshifts, at least half of them are member galaxies.

**Table 4.7:** Number of galaxies within group radii of 300 kpc, 500 kpc, and 1 Mpc. Percentages of the individual subsamples are also listed.

	300 kpc		500 kpc		1 Mpc	
SDSS galaxies $i' < 20^{\text{mag}}$ <sup>a</sup>	63		160		444	
observed <sup>b</sup>	43	68%	51	32%	80	18%
measured redshifts <sup>c</sup>	41	95%	49	96%	74	93%
redshifts from literature <sup>d</sup>	2	5%	14	22%	31	30%
redshifts in total <sup>e</sup>	43	68%	63	39%	105	24%
members <sup>f</sup>	29	67%	40	63%	54	51%

<sup>a</sup> Numbers go down to  $i' = 20^{\text{mag}}$  since this was the limit for spectroscopic target selection. In the CMDs of Fig. 4.14, galaxies are shown down to  $21^{\text{mag}}$  just as the black squares in Figs. 4.8 to 4.11.

<sup>b</sup> Fractions with respect to SDSS galaxies  $i' < 20^{\text{mag}}$ .

<sup>c</sup> Fractions with respect to observed galaxies.

<sup>d</sup> Fractions with respect to total redshifts.

<sup>e</sup> Fractions with respect to SDSS galaxies  $i' < 20^{\text{mag}}$ .

<sup>f</sup> Fractions with respect to total redshifts.

Like in any spectroscopic survey, the incompleteness of redshift measurements is strongly magnitude dependent since fainter galaxies are much more difficult to observe than brighter ones. Therefore a limiting magnitude is expected below which the spectral S/N doesn't allow radial velocity measurements anymore. The faintest galaxy with a reliable redshift in the investigated sample has a magnitude of  $i' = 19.78^{\text{mag}}$ .

Figure 4.14 illustrates the completeness of the sample with respect to SDSS magnitudes. Again, radii of 300 kpc, 500 kpc, and 1 Mpc are considered. Panels a) to c) show colour-magnitude diagrams of SDSS galaxies  $i' < 21^{\text{mag}}$ . The magnitude limit of the MOS target selection is clearly visible around  $i' = 20^{\text{mag}}$ . Objects with untypical magnitudes and colours lying outside the main distribution have been checked in SDSS. Most of these objects could be identified as stars

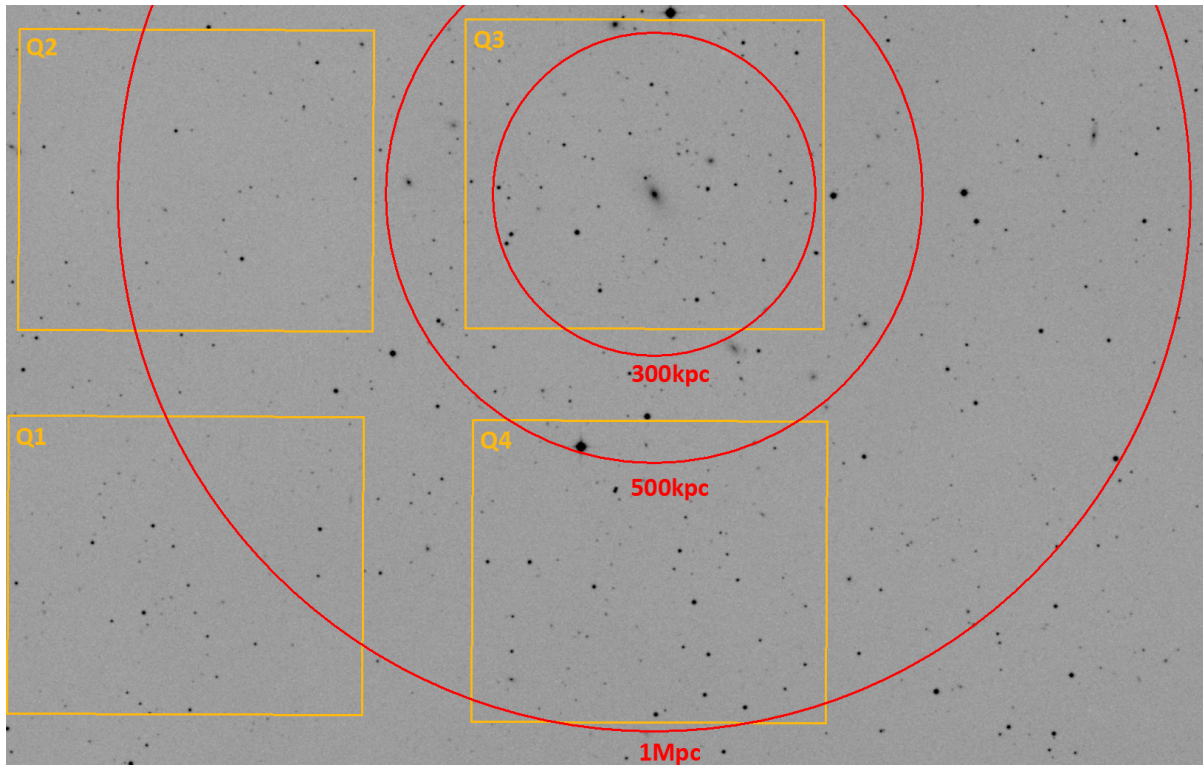


**Figure 4.13:** Spatial coverage of RX J1548.9+0851. The VIMOS detector is highlighted in orange while red circles show radii of 300 kpc, 500 kpc, and 1 Mpc around the central elliptical. The level of incompleteness increases strongly with radius.

misclassified as galaxies by SDSS and were removed from the plot. To complement the list of measured radial velocities, the SDSS and NED were checked for galaxies with spectra that have not been observed with VIMOS. Dark- and light-green dots show group members while red and orange dots indicate background galaxies (see color-coding in the caption of Figure 4.14.)

The group members form an unambiguous red sequence from the brightest galaxy into the dwarf regime while background galaxies are more diffusely distributed. To quantify the red sequence, a straight line was fit to member galaxies. This line was slightly shifted to the red to serve as a red sequence upper limit and is indicated as dashed line in the CMDs of Fig. 4.14. The equation of the line is  $g' - i' = -0.05317 \cdot i' + 2.36$ . In total, only 2 members are located above this upper limit while all other spectroscopically studied galaxies are background objects. Interestingly, these 2 galaxies (39 and 42) are found in the immediate vicinity of the two brightest ellipticals in the group (see Fig. 4.10). Panels d) to f) of Fig. 4.14 show the galaxy number distribution of the corresponding colour-magnitude diagrams in bins of  $1^{\text{mag}}$ . White histograms show all galaxies, orange ones only those with redshifts, and green ones present member galaxies. Thus, the orange shaded area gives the amount of spectroscopically confirmed background galaxies. Panels g) to i) show the fraction of galaxies with redshifts relative to all galaxies (black line) and relative to galaxies below the red sequence (brown line). Around  $i' = 17^{\text{mag}}$ , the incompleteness starts to rise continuously towards fainter magnitudes.

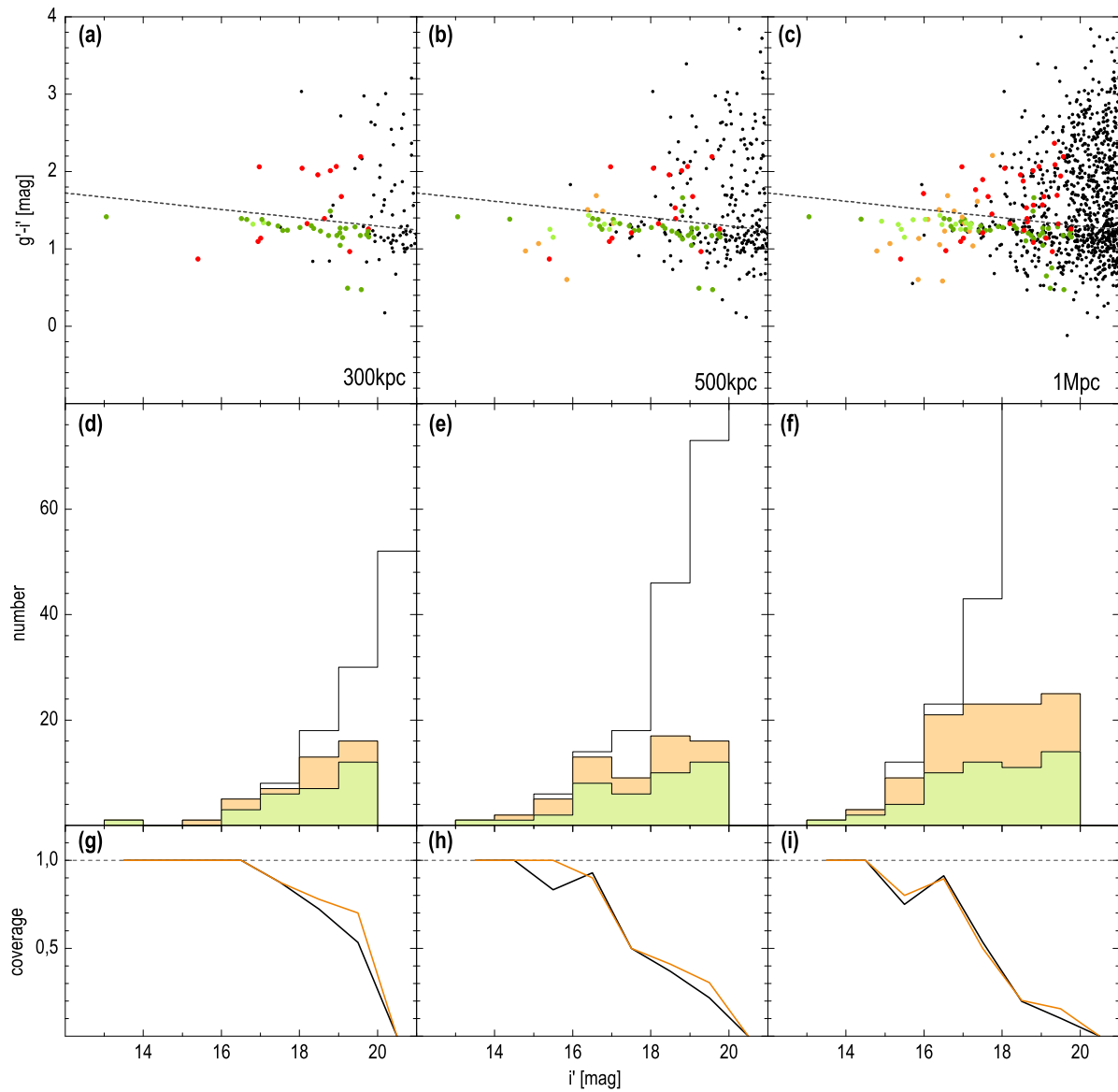


**Figure 4.14:** Magnitude dependent incompleteness. Panels **a)** to **c)**: colour-magnitude diagrams for radii of 300 kpc, 500 kpc, and 1 Mpc. *Color coding:* ● VIMOS non-members, ● SDSS and NED non-members, ● VIMOS members, ● SDSS members, · SDSS galaxies  $i' < 21^{\text{mag}}$ . Objects misclassified as galaxies have been removed. Dashed lines show the adopted upper limit  $g' - i' = -0.05317 \cdot i' + 2.36$  to the red sequence. Panels **d)** to **f)**: Number of galaxies in bins of  $1^{\text{mag}}$ . White histograms refer to all galaxies in the corresponding CMDs, orange ones represent galaxies with redshifts, and green ones are member galaxies. Panels **g)** to **i)**: fraction of galaxies with redshifts relative to all galaxies (black line) and relative to galaxies below the red sequence (brown line). Corresponding numbers are presented in Table 4.7.

## 1 Photometric redshifts

Since the studied system is fully covered in the SDSS, it is obvious to consider archive data as an additional source of information for group member classification if spectroscopic measurements are not available for all galaxies. The SDSS stores 3 estimates of photometric redshift for each entry in the `PhotObjAll` table. Since 105 redshifts are available within 1Mpc, these values can be used to evaluate the accuracy of the photometric redshift models of the SDSS, as is shown in Fig. 4.15. There is a clear correlation between photometric redshifts and the exact values. Nevertheless, a large spread in photometric redshifts is present around the system redshift  $cz_{\text{median}} = 21462 \text{ km s}^{-1}$ . The dashed line indicates unity while the brown line is a linear least squares fit excluding the outliers around the system redshift. Both lines do not necessarily need to be identical since, although unlikely, a systematic difference between the SDSS photometric redshift models and true redshifts could be present.

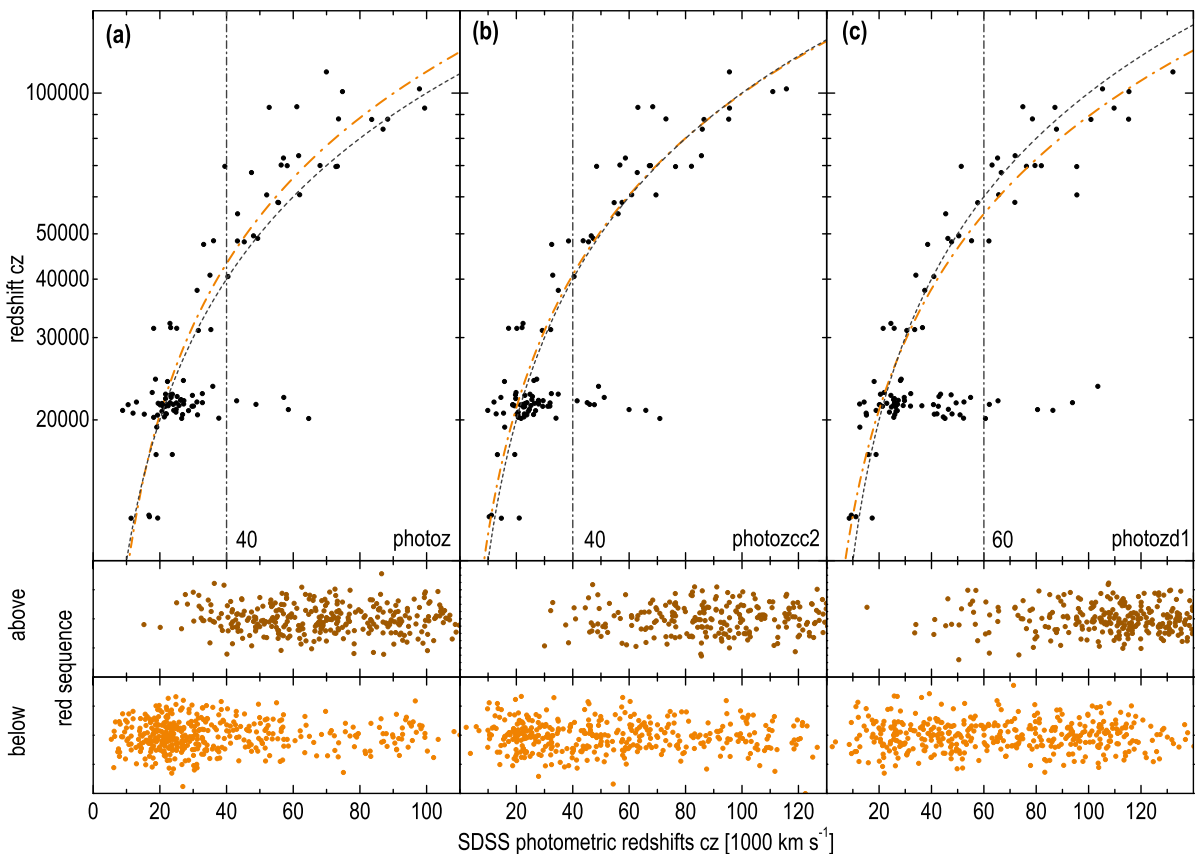


**Figure 4.15:** Accuracy of SDSS photometric redshifts.

Since all redshifts above the red sequence upper limit have revealed background galaxies with the exception of only two particular objects, photometric redshifts of the remaining satellites above the limit are also expected to be dominated by background galaxies. Assuming thresholds of  $cz_{\text{photoz}} = 40000 \text{ km s}^{-1}$ ,  $cz_{\text{photozcc2}} = 40000 \text{ km s}^{-1}$ , and  $cz_{\text{photozd1}} = 60000 \text{ km s}^{-1}$  based on the distribution of galaxies in Fig. 4.15, 94% of all galaxies above the upper limit can be



considered as background galaxies in any of the three models<sup>17</sup>. In contrast, below the red sequence only 33 to 61% are background objects, confirming the clear segregation of galaxies into members and non-members at the red sequence limit. Following these considerations, only objects fulfilling  $cz_{\text{photoz}} < 40000 \text{ km s}^{-1}$ ,  $cz_{\text{photozcc2}} < 40000 \text{ km s}^{-1}$ , and  $cz_{\text{photozd1}} < 60000 \text{ km s}^{-1}$  were classified as additional group members while all other galaxies have been excluded for the further analysis of the RX J1548.9+0851 luminosity function. Figure 4.16 shows the updated CMDs and histograms. Because of the increasing photometric redshift uncertainties at fainter magnitudes, likely violating the group member criterion in at least one of the three photometric redshift models, nearly no members are present at  $i' > 20$ . As expected, the additional members also align clearly with the existing red sequence. No pronounced dip is visible at  $M_{i'} = -18 + 5 \log h$ .

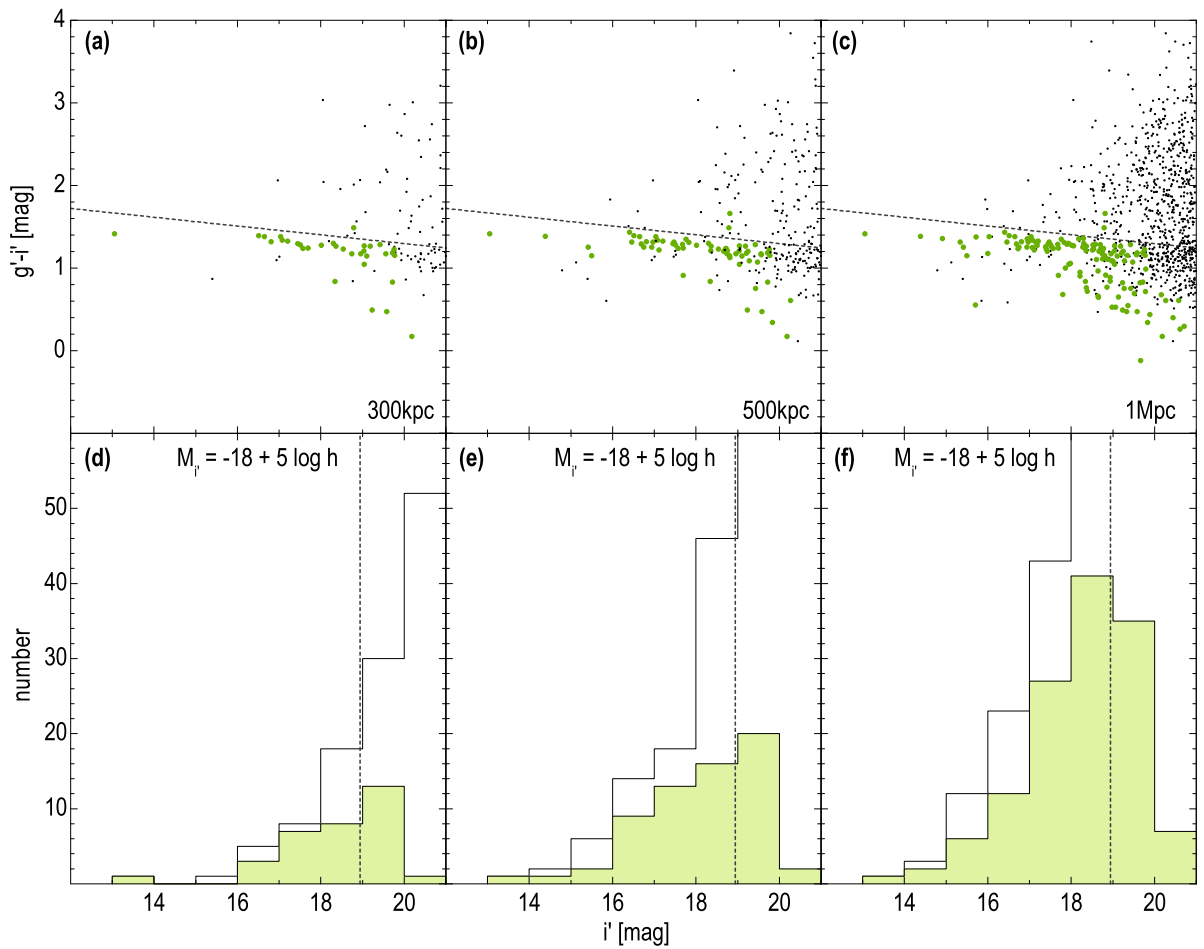


**Figure 4.16:** Same as Fig. 4.14, but taking into account the photometric redshift thresholds of Fig. 4.15. Green are spectroscopically and photometrically determined members while background galaxies are highlighted in orange. Vertical lines indicate absolute magnitudes of  $M_{i'} = -18 + 5 \log h$ .

<sup>17</sup> Assuming lower photometric redshift thresholds ( $cz_{\text{photoz}} = 30000 \text{ km s}^{-1}$ ,  $cz_{\text{photozcc2}} = 40000 \text{ km s}^{-1}$ , and  $cz_{\text{photozd1}} = 40000 \text{ km s}^{-1}$ ), this value rises to 99% for all models, increasing the chance of photometric redshift uncertainty, however.

## 9 The luminosity function

It is well-known that the global distribution of galaxies in luminosity is well-fit by a Schechter (1976) function

$$\Phi(L)dL = \left(\frac{\Phi^*}{L^*}\right) \left(\frac{L}{L^*}\right)^\alpha \exp\left(-\frac{L}{L^*}\right) dL \quad (4.2)$$

where  $\Phi(L)dL$  gives the number density of galaxies in the luminosity interval  $[L, L + dL]$ . Considering that the interval  $dL$  corresponds to an accordant interval  $dM$  in magnitudes, i.e.  $\Phi(L)dL = \Phi(M)dM$ , and following the relation  $dL/L = -0.4 \ln 10 dM$ , equation 4.2 can be rewritten in magnitudes as

$$\Phi(M)dM = (0.4 \ln 10) \Phi^* \cdot 10^{0.4(\alpha+1)(M^*-M)} \exp\left(-10^{0.4(M^*-M)}\right) dM \quad (4.3)$$

The Schechter function has three free parameters,  $\Phi^*$ ,  $L^*$  or  $M^*$ , and  $\alpha$ . The slope of the function at the faint end is determined by  $\alpha$  while  $L^*$  and  $M^*$  indicate a characteristic luminosity (magnitude) above which the number of galaxies falls steeply.  $\Phi^*$  is the number of galaxies per  $\text{Mpc}^3$  per luminosity (magnitude) bin at the characteristic luminosity (magnitude). A luminosity function (LF) with  $\alpha = -1$  is flat at the faint end. The total luminosity is calculated by integrating over all luminosity bins  $dL$

$$l_{\text{tot}} = \int_0^\infty L \Phi(L) dL = \Phi^* L^* \Gamma(2 + \alpha) \quad (4.4)$$

where  $\Gamma(x) = \int_0^\infty y^{(x-1)} e^{-y} dy$  is the gamma function. Equation 4.4 is finite for  $\alpha \geq -2$ . Figure 4.17 shows the galaxy luminosity distribution of RX J1548.9+0851 members in the SDSS  $g'$ ,  $r'$ , and  $i'$  bands and the corresponding Schechter fits. At fainter magnitudes members are dominated by photometrically determined ones, liable to photometric redshift uncertainties. Thus, one has to be careful when interpreting the resulting shapes of the LFs. Averaging the values from all three passbands yields an  $\alpha$  of  $-1.4 \pm 0.1$ , indicating a steep LF.

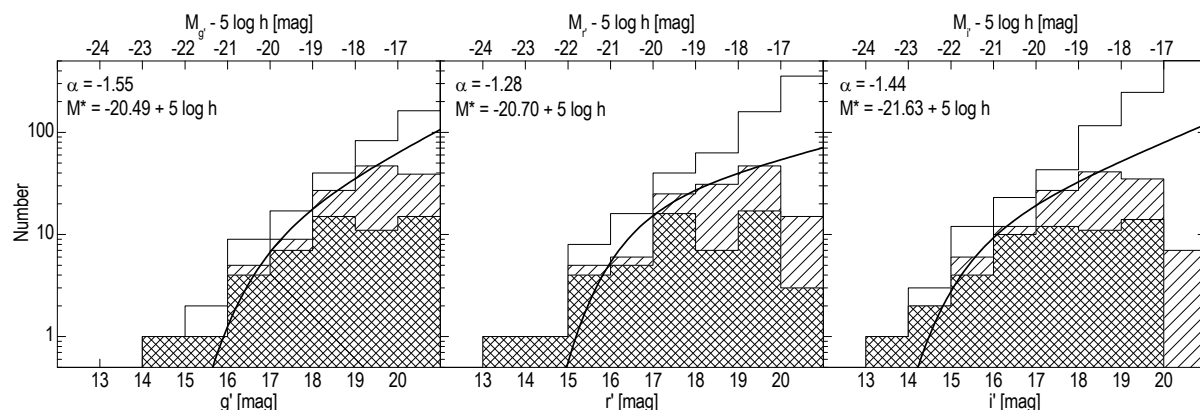


**Figure 4.17:** The galaxy luminosity function of RX J1548.9+0851 member galaxies. Open histograms refer to all SDSS galaxies within 1 Mpc, hatched ones to photometrically and spectroscopically classified members. The solid line is a Schechter fit to all member galaxies excluding the central elliptical.

## 10 Surface Photometry

Since pre-imaging is mandatory for all VIMOS MOS observations, imaging data are a useful by-product when applying for MOS spectroscopy. Thus, the data package sent to the PI not only consists of the requested MOS spectra but also pipeline-reduced science images SREI in the Bessel  $R$  band. In order to study the photometric properties of the spectroscopically confirmed group members of RX J1548.9+0851, these processed frames have also been analysed. Similar to the spectroscopic pipeline, raw imaging data are reduced by the predefined recipe *vmimobsstare*. The pipeline does bias subtraction, overscan removal, flat-fielding and cosmic ray removal. Images in the UBVRI filters are photometrically calibrated. The photometric zeropoints  $Z_P$  as well as extinction coefficients  $k$ , airmass  $X$  and an estimate of the sky background flux are stored in the image header of each individual quadrant.

### 1 Photometric flux calibration

These header entries were used to transform instrumental magnitudes  $m_{\text{instr}}$  to the standard magnitude system. Since zeropoints given by the *vmimobsstare* recipe are related to fluxes in ADU/sec, the reduced science frames were first divided by their exposure time. Then, magnitudes were derived by the photometric equation

$$m = m_{\text{instr}} + Z_P = -2.5 \log [\text{ADU}/\text{sec}] - k \cdot X + Z_P$$

The resulting magnitudes were checked for reliability by comparing magnitudes of some bright stars in each quadrant with SDSS  $r'$  band model magnitudes. The comparison revealed only small differences in the order of a few tenths of magnitudes which can be attributed to the filter differences of the Bessel  $R$  and SDSS  $r$  bands.

Since surface brightnesses of the group members are investigated, magnitudes  $\text{pixel}^{-2}$  had to be converted to magnitudes  $\text{arcsec}^{-2}$  by means of the relation

$$\mu \left[ \frac{\text{mag}}{\text{arcsec}^2} \right] = \mu \left[ \frac{\text{mag}}{\text{pixel}^2} \right] + 5 \log [s]$$

where  $s$  is the spatial scale of the CCD chip in  $\text{arcsec pixel}^{-1}$ . For the VIMOS CCDs this value corresponds to  $0.205 \text{ arcsec pixel}^{-1}$  resulting in a correction constant of  $\sim 3.44 \text{ mag}$ . Since magnitudes are relative units, the surface brightness errors remain constant in this transformation.

### 2 The central elliptical

In the analysis of surface brightness profiles of RX J1548.9+0851 member galaxies, special emphasis was placed on the central elliptical. Due to the galaxy's large spatial extent with respect to other group members, the diffuse light distribution of the galaxy is strongly contaminated by other objects. Therefore care was taken in masking all these sources properly to avoid systematic deviations in the surface brightness profile. Considering morphology, the galaxy is of special interest since shells are revealed unambiguously along the major axis. To enhance the appearance of these features, the image was smoothed by means of a median box filter<sup>18</sup>.

<sup>18</sup>The IRAF task `median` in the `images.imfilter` package with a box size of 100 pixel was used.

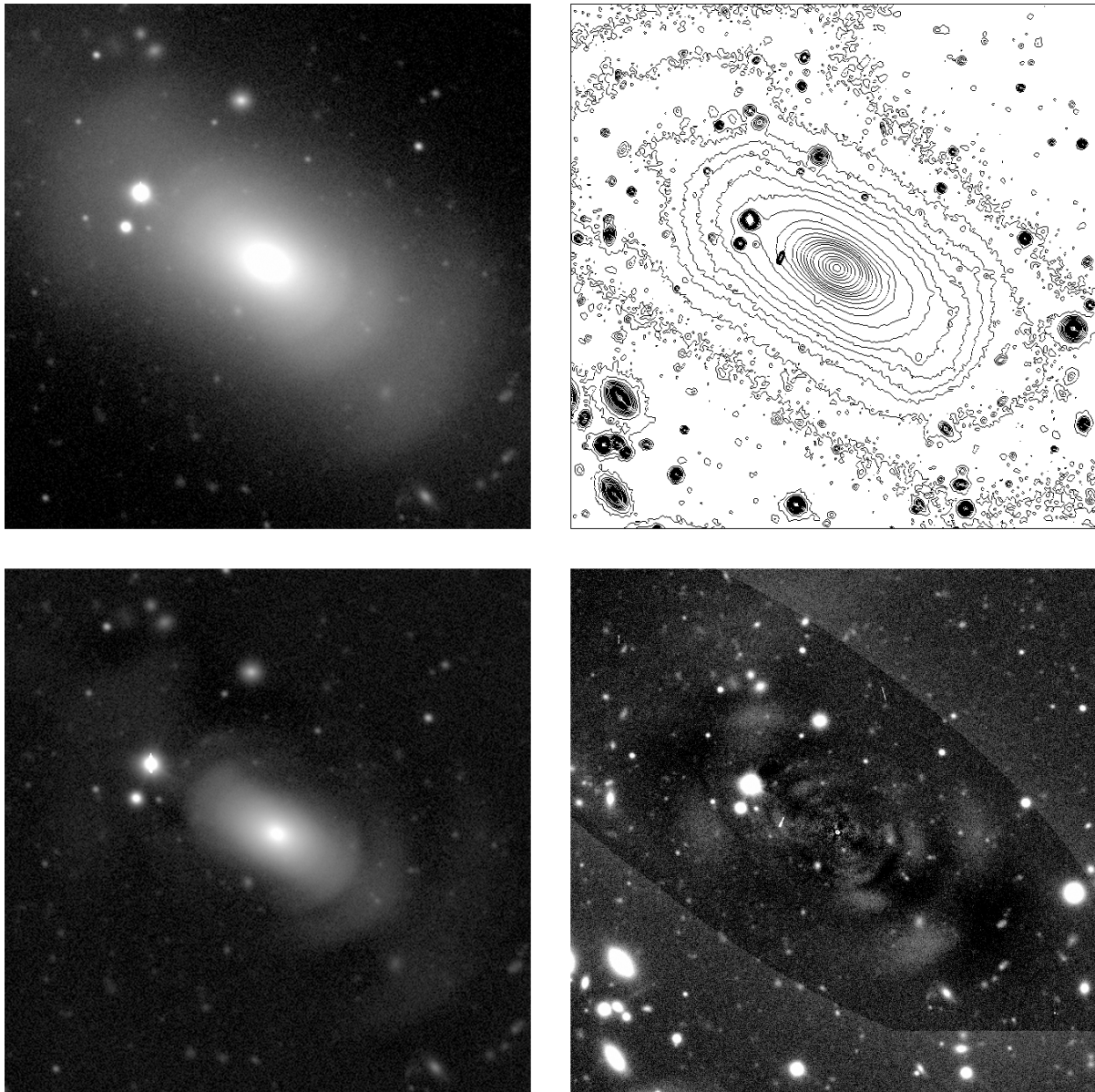


**Figure 4.18:** Morphology of the central elliptical. Upper left: *R* band image, upper right: isophote map, lower left: *R* band image after subtraction of the median box filter, lower right: residuals to the IRAF `ellipse` model. Shells are clearly visible in the lower panels and show strong symmetry along the major axis. The isophote map highlights the boxy structure in the outer regions of the galaxy. The residuals illustrate the large contamination of foreground sources which have been masked within the `ellipse` task. The field of view is  $\sim 1.5$  arcmin on a side in the left panels and  $\sim 2.2$  arcmin in the right ones.

Subtracting the smoothed frame from the original one reveals the shell structure in much more detail. Similarly, the galaxy model of the IRAF `ellipse` task was also subtracted from the original frame for the same purpose. Figure 4.18 shows the pipeline reduced SREI image, an isophote map, as well as the results of both unsharp masking techniques. The shell structure is evident in the system and shows high symmetry along the major axis. Figure 4.19 shows the surface brightness profile of the central elliptical in  $\text{mag arcsec}^{-2}$  against  $r^{1/4}$ . The linear brown line is the best-fit deVaucouleurs  $r^{1/4}$  law. Residuals indicate only minor deviations from the model in the order of  $0.1^{\text{mag}}$ . The coefficient  $a_4$  shows positive values at  $r^{1/4} > 2.9 \text{ arcsec}^{1/4}$ , indicative of boxy isophotes as expected from the  $R$  band image.

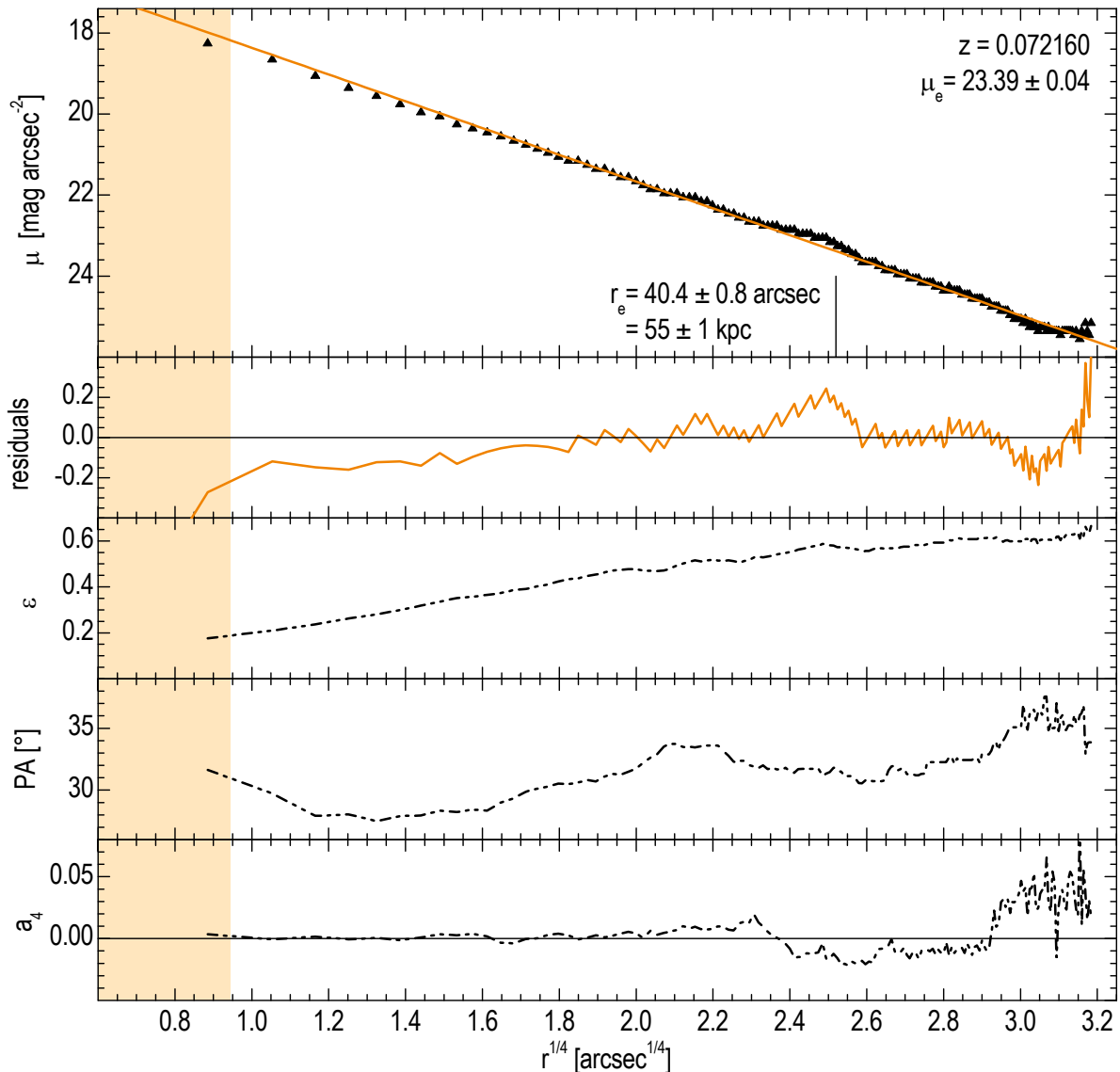


**Figure 4.19:** Surface brightness profile of the central elliptical plotted against  $r^{1/4}$ . The straight line is the deVaucouleurs fit to the data. The vertical line indicates the effective radius. The lower panel shows the residuals to the fit.

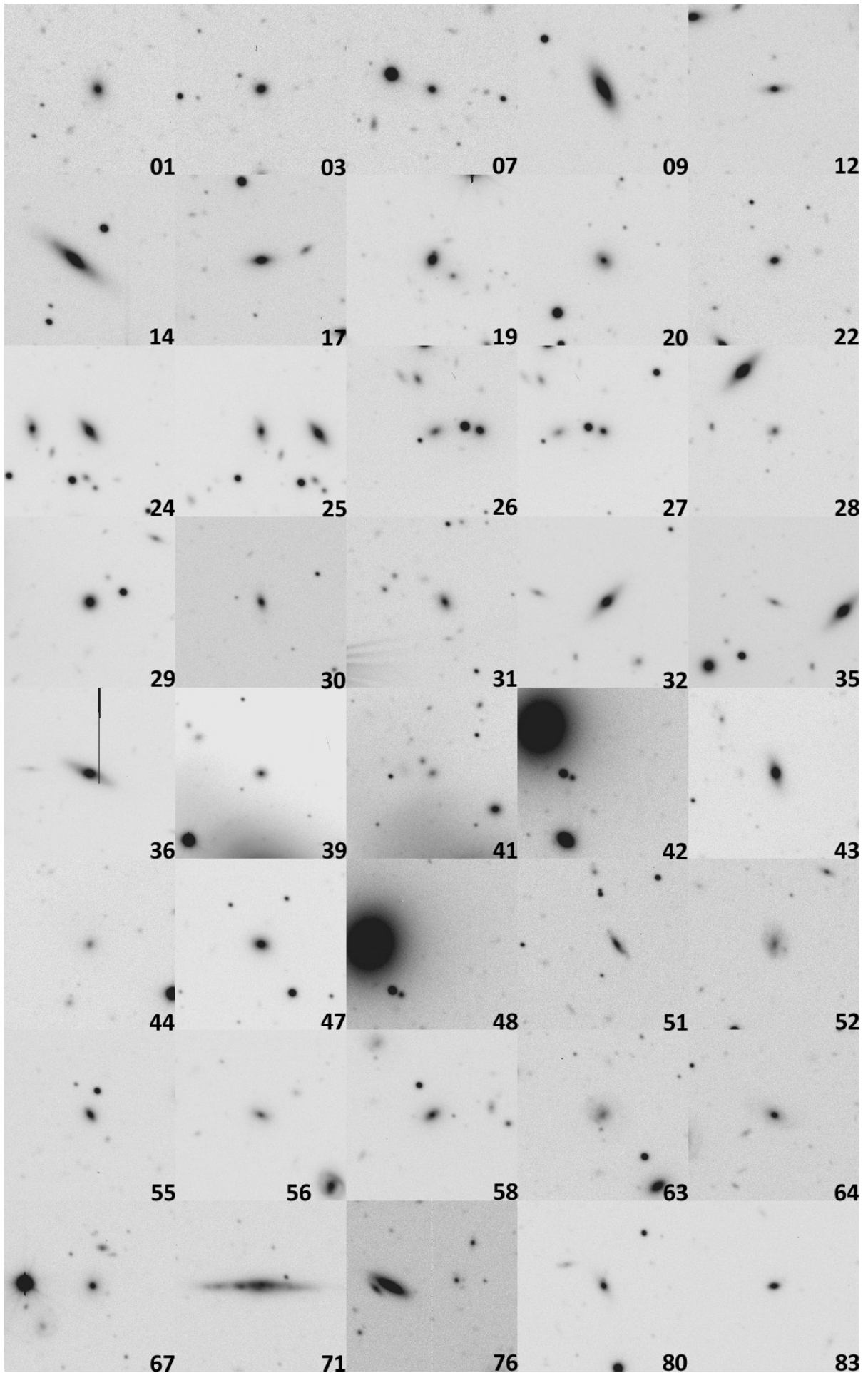


**Figure 4.20:** *R* band images of the faint galaxy population.

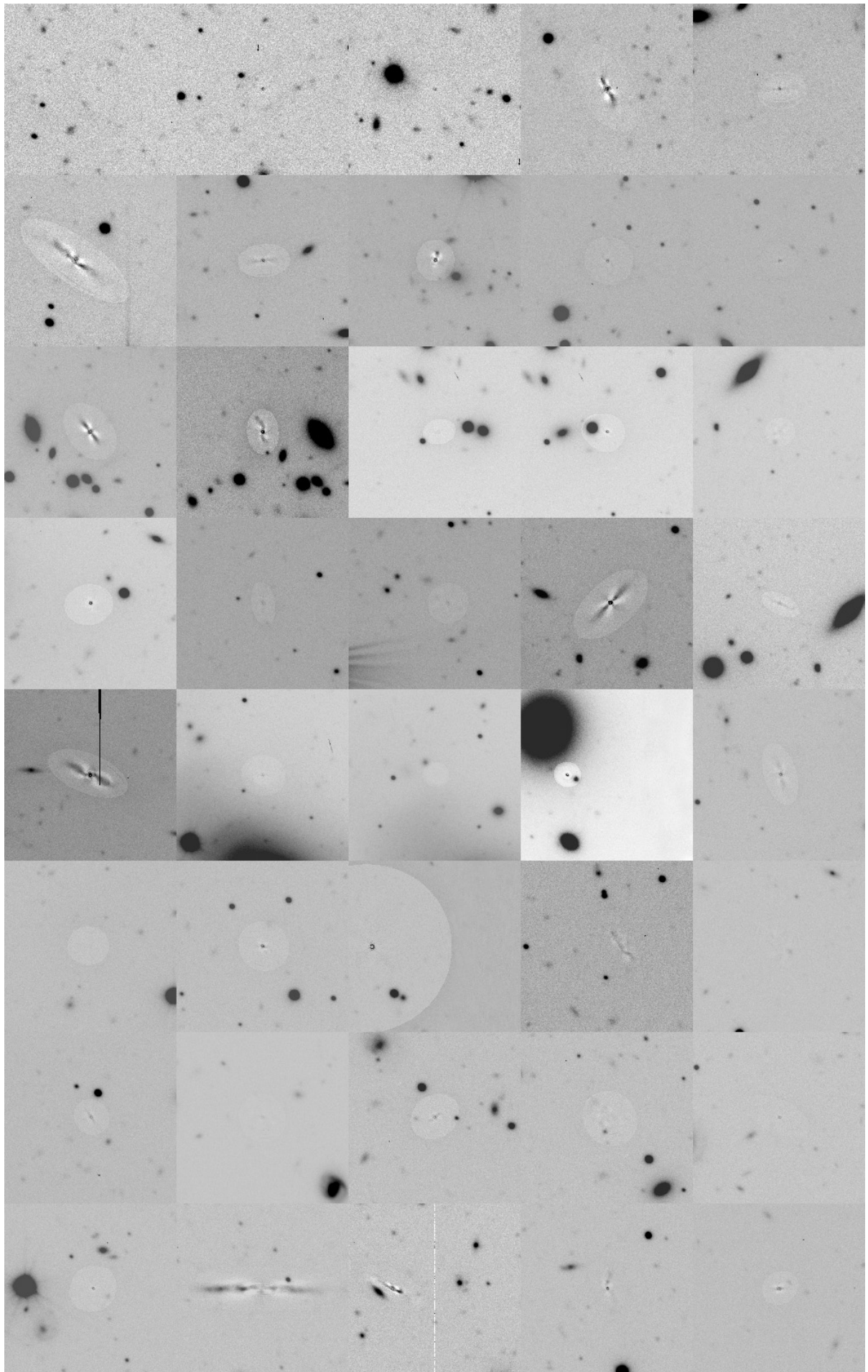


**Figure 4.21:** Residuals after subtraction of the IRAF ellipse model.

## 11 SSP equivalent ages and metallicities of group members

The ULySS full spectrum fitting technique as highlighted in chapter 3 was applied to all spectroscopically confirmed group members. Table 4.8 and Figs. 4.22–4.30 (see Sect. 3.7 for details) summarize the fit parameters and the resulting SSP ages and metallicities.

**Table 4.8:** ULySS SSP equivalent ages and metallicities of RX J1548.9+0851 group members.

object	LMIN–LMAX <sup>a</sup>	SNR <sup>b</sup>	age <sub>SSP</sub> [Gyr]	[Fe/H] <sub>SSP</sub>	$\sigma$ [km s <sup>-1</sup> ] <sup>c</sup>
01.....	4400–5850 Å	10	4.0 ± 1.3	-0.27 ± 0.10	14
03.....	4350–5850 Å	11	8.5 ± 3.6	-0.32 ± 0.10	46
07.....	4350–5850 Å	10	6.4 ± 3.8	-0.32 ± 0.14	43
09.....	4300–5850 Å	23	3.6 ± 0.7	-0.07 ± 0.05	108
12.....	4100–5850 Å	12	1.6 ± 0.3	-0.46 ± 0.10	27
14.....	4050–5850 Å	17	2.8 ± 0.3	0.07 ± 0.06	90
17.....	4050–5850 Å	16	6.1 ± 1.1	-0.15 ± 0.05	56
19.....	4200–5850 Å	41	15.6 ± 3.1	-0.29 ± 0.03	208
20.....	4200–5850 Å	13	4.7 ± 1.5	-0.26 ± 0.07	47
22.....	4150–5850 Å	15	10.4 ± 3.0	-0.62 ± 0.06	43
24.....	3800–5850 Å	34	9.9 ± 0.7	-0.15 ± 0.03	169
25.....	3920–5850 Å	24	7.0 ± 0.9	-0.15 ± 0.04	94
26.....	3800–5850 Å	10	2.2 ± 0.2	0.05 ± 0.05	46
27.....	3700–5850 Å	17	10.7 ± 1.3	-0.19 ± 0.04	83
28.....	3700–5850 Å	10	6.2 ± 2.4	-0.40 ± 0.11	46
29.....	3800–5850 Å	36	12.2 ± 0.7	-0.17 ± 0.02	166
30.....	3700–5850 Å	16	3.8 ± 0.6	-0.17 ± 0.05	49
31.....	3850–5850 Å	15	4.4 ± 0.5	-0.31 ± 0.04	56
32.....	3800–5850 Å	38	10.6 ± 0.7	-0.08 ± 0.03	182
34.....	3800–5850 Å	61	13.5 ± 0.7	0.00 ± 0.01	309
35.....	3800–5850 Å	10	4.5 ± 1.0	-0.36 ± 0.07	27
36.....	3700–5850 Å	22	7.2 ± 0.9	-0.09 ± 0.04	119
39.....	3700–5850 Å	16	5.2 ± 0.7	-0.16 ± 0.04	52
41.....	3700–5850 Å	6	2.3 ± 0.6	-0.10 ± 0.15	85
42.....	3800–5800 Å	24	10.3 ± 1.0	-0.07 ± 0.03	118
43.....	3800–5750 Å	26	5.4 ± 0.5	-0.05 ± 0.03	94
44.....	3800–5700 Å	5	1.6 ± 0.5	-0.17 ± 0.22	48
47.....	3700–5750 Å	24	8.6 ± 0.8	-0.14 ± 0.03	101
48.....	3800–5750 Å	67	11.4 ± 0.6	-0.001 ± 0.003	321
51.....	3700–5700 Å	8	–	–	–
52.....	3700–5750 Å	5	3.9 ± 3.0	-0.25 ± 0.34	–
55.....	3700–5600 Å	18	5.9 ± 0.7	-0.29 ± 0.04	64
56.....	3700–5550 Å	12	3.1 ± 0.3	0.14 ± 0.05	42
58.....	3800–5500 Å	11	5.2 ± 1.0	-0.14 ± 0.06	49
63.....	3700–5500 Å	5	–	–	–
64.....	3700–5550 Å	15	0.7 ± 0.1	-0.59 ± 0.12	–
67.....	3700–5400 Å	18	4.6 ± 0.6	-0.27 ± 0.05	53
71.....	4200–5750 Å	8	0.8 ± 0.2	-0.31 ± 0.15	14
76.....	4050–5850 Å	14	5.7 ± 1.6	-0.59 ± 0.08	42
80.....	3700–5750 Å	22	4.3 ± 0.9	-0.33 ± 0.04	74
83.....	3700–5650 Å	22	2.36 ± 0.05	-0.13 ± 0.04	62

<sup>a</sup> and <sup>b</sup> Same as in Tables 3.6 and 3.7.

<sup>c</sup> Corrected for instrumental and model dispersions following equations 3.7. The instrumental dispersion was estimated through the widths of the strongest sky lines in the SSRM files and amounts to  $\sigma_{\text{instr}} = 51 \text{ km s}^{-1}$ .



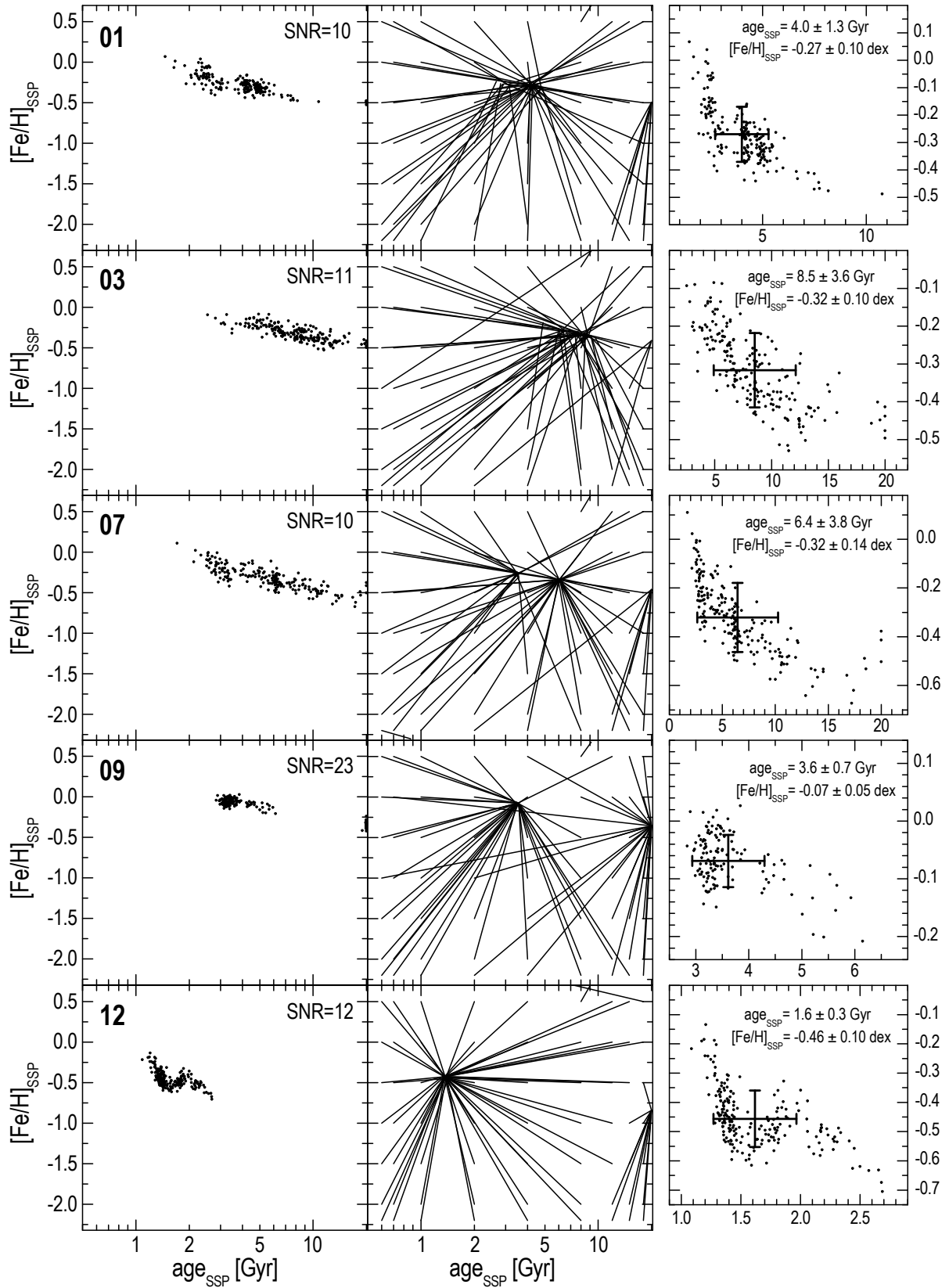


Figure 4.22: ULYSS fit results of RX J1548.9+0851 group members.

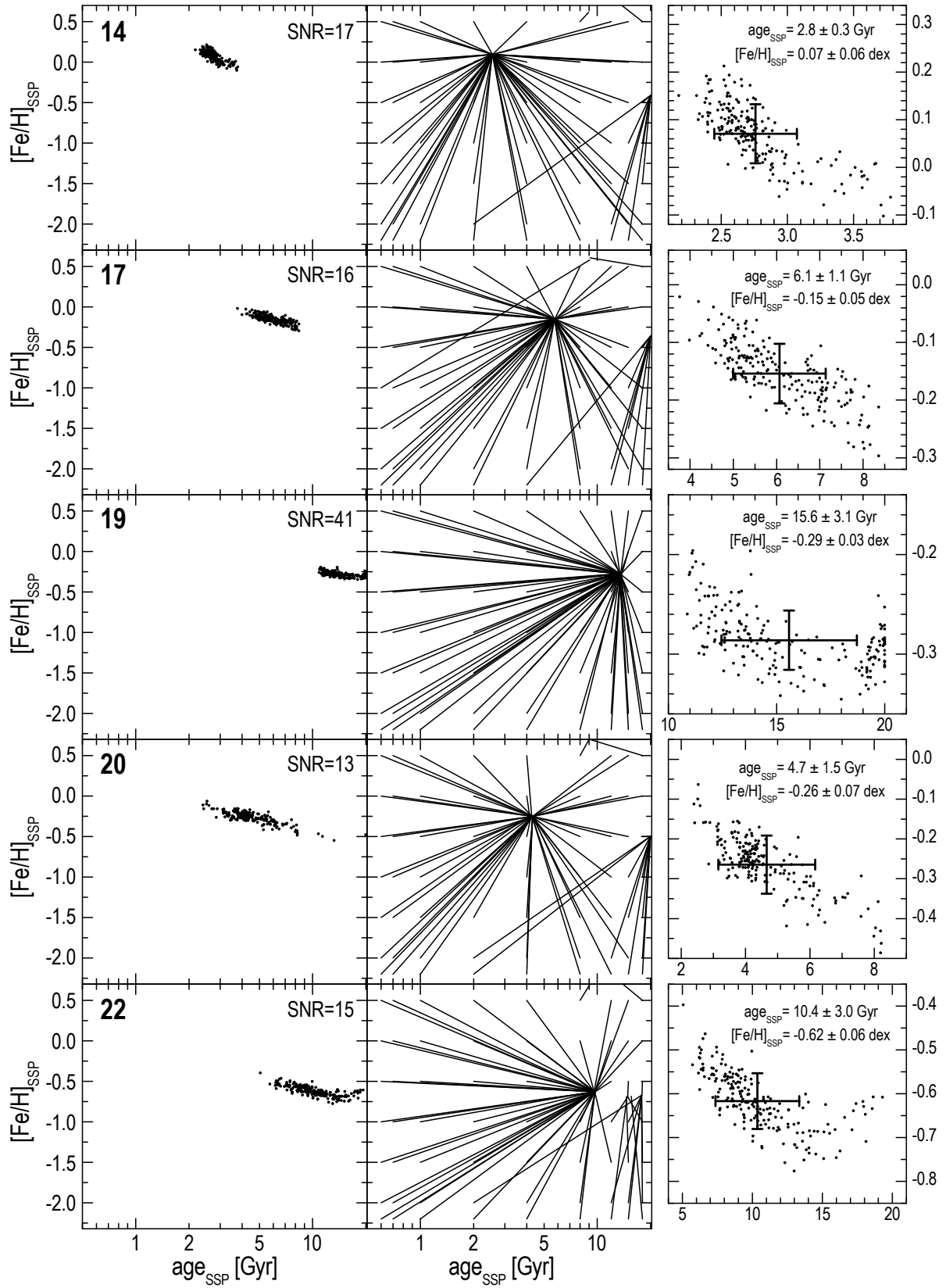


Figure 4.23: Same as Fig. 4.22.

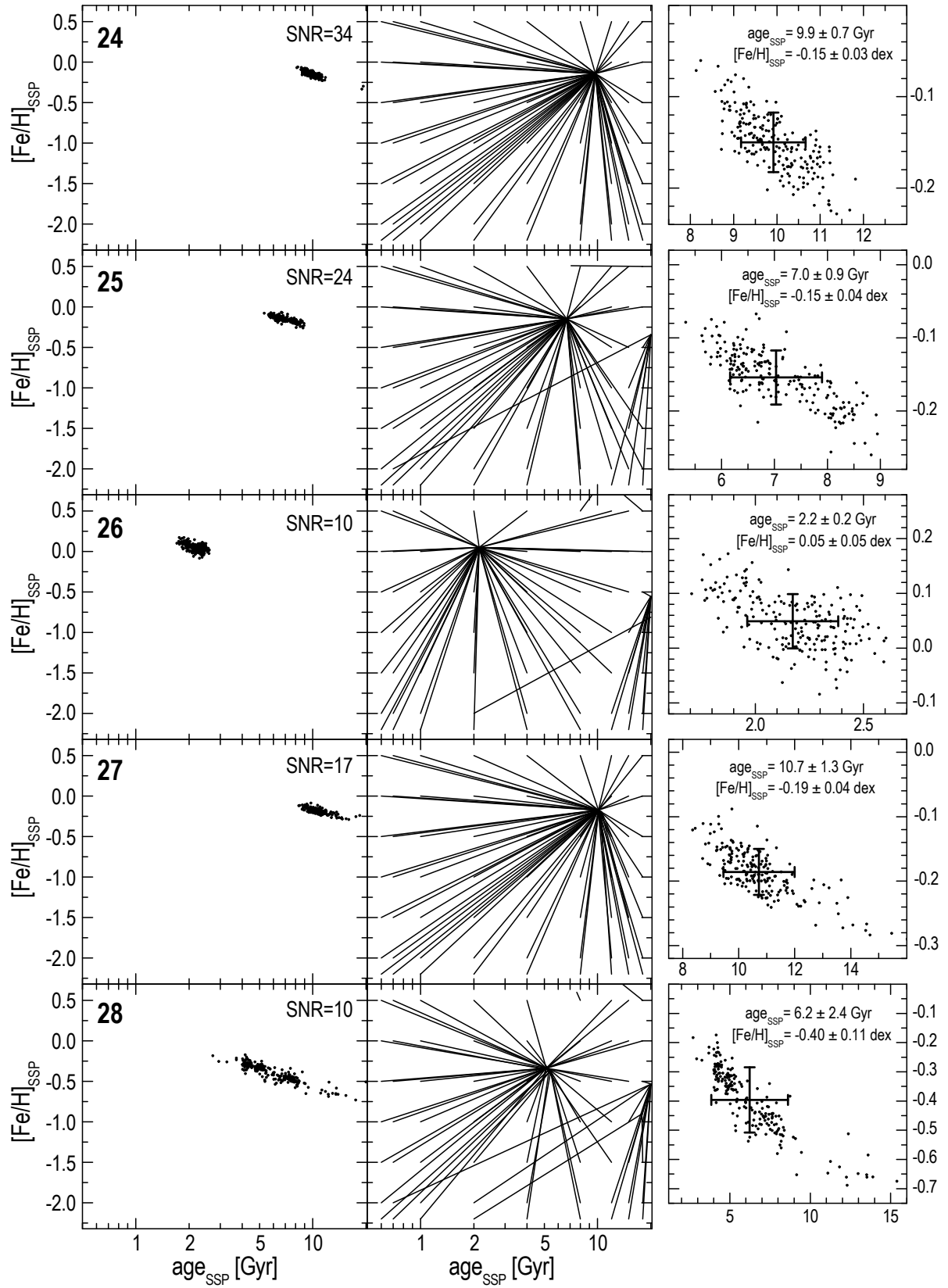


Figure 4.24: Same as Fig. 4.22.

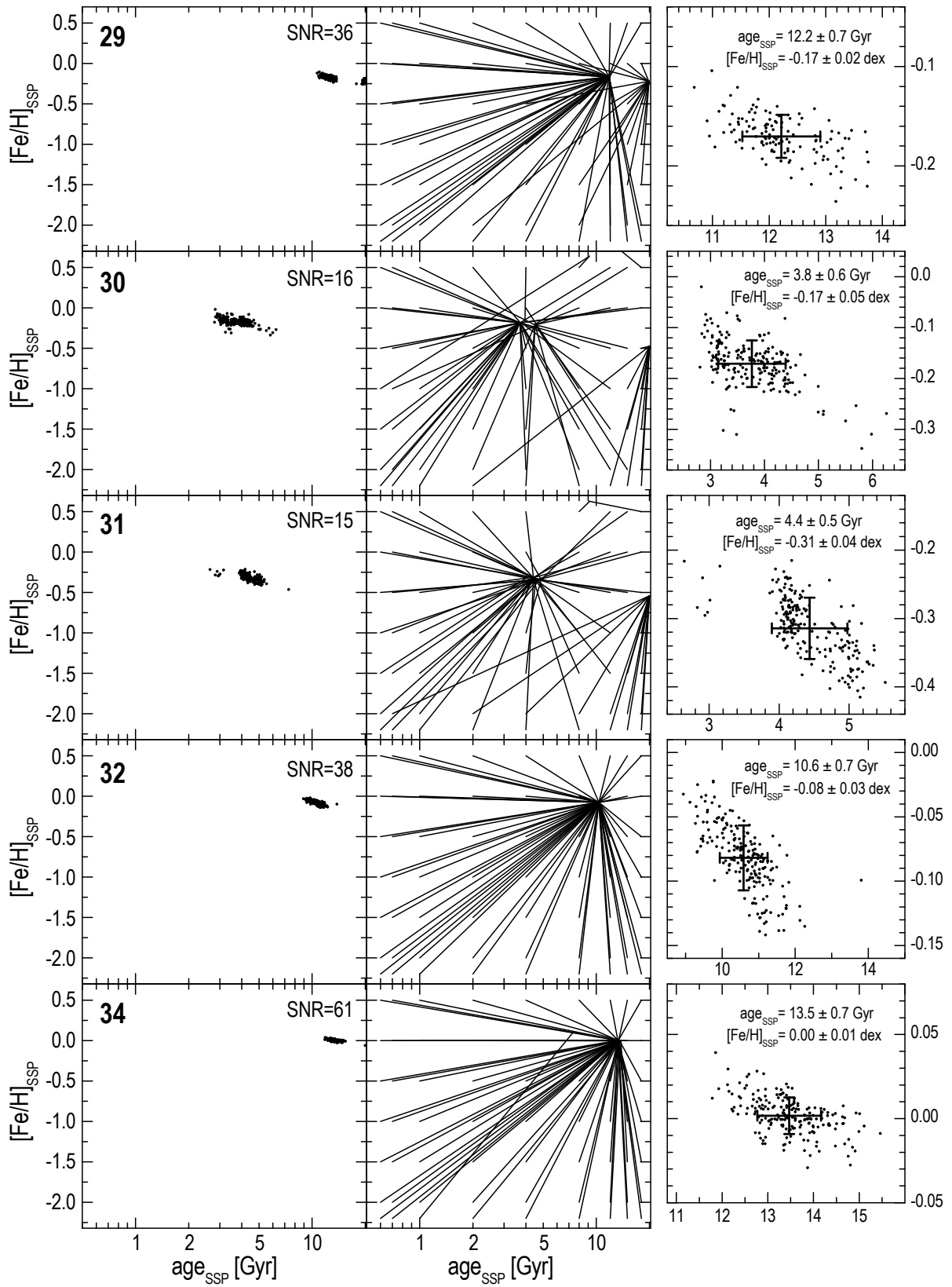


Figure 4.25: Same as Fig. 4.22.

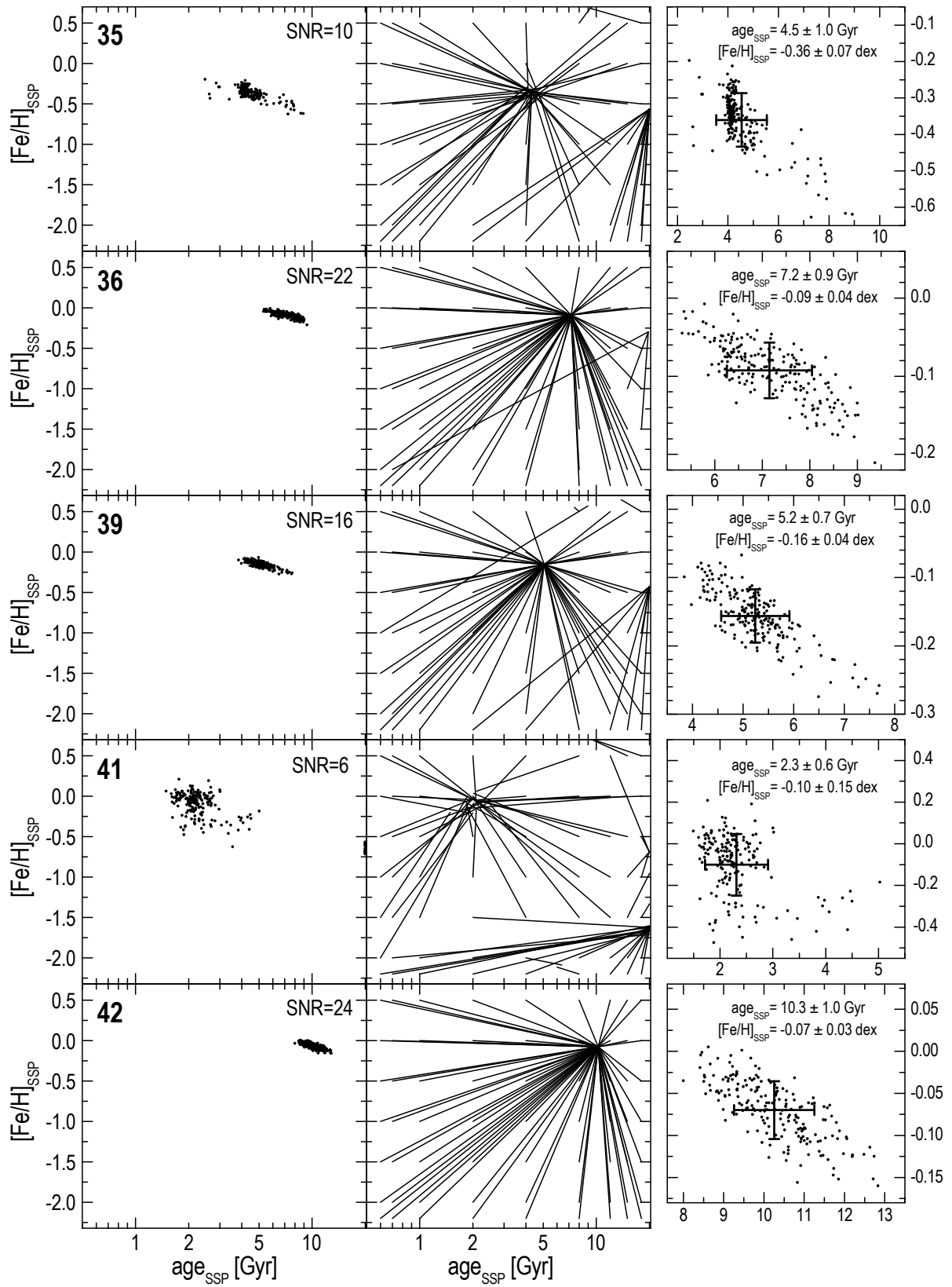


Figure 4.26: Same as Fig. 4.22.

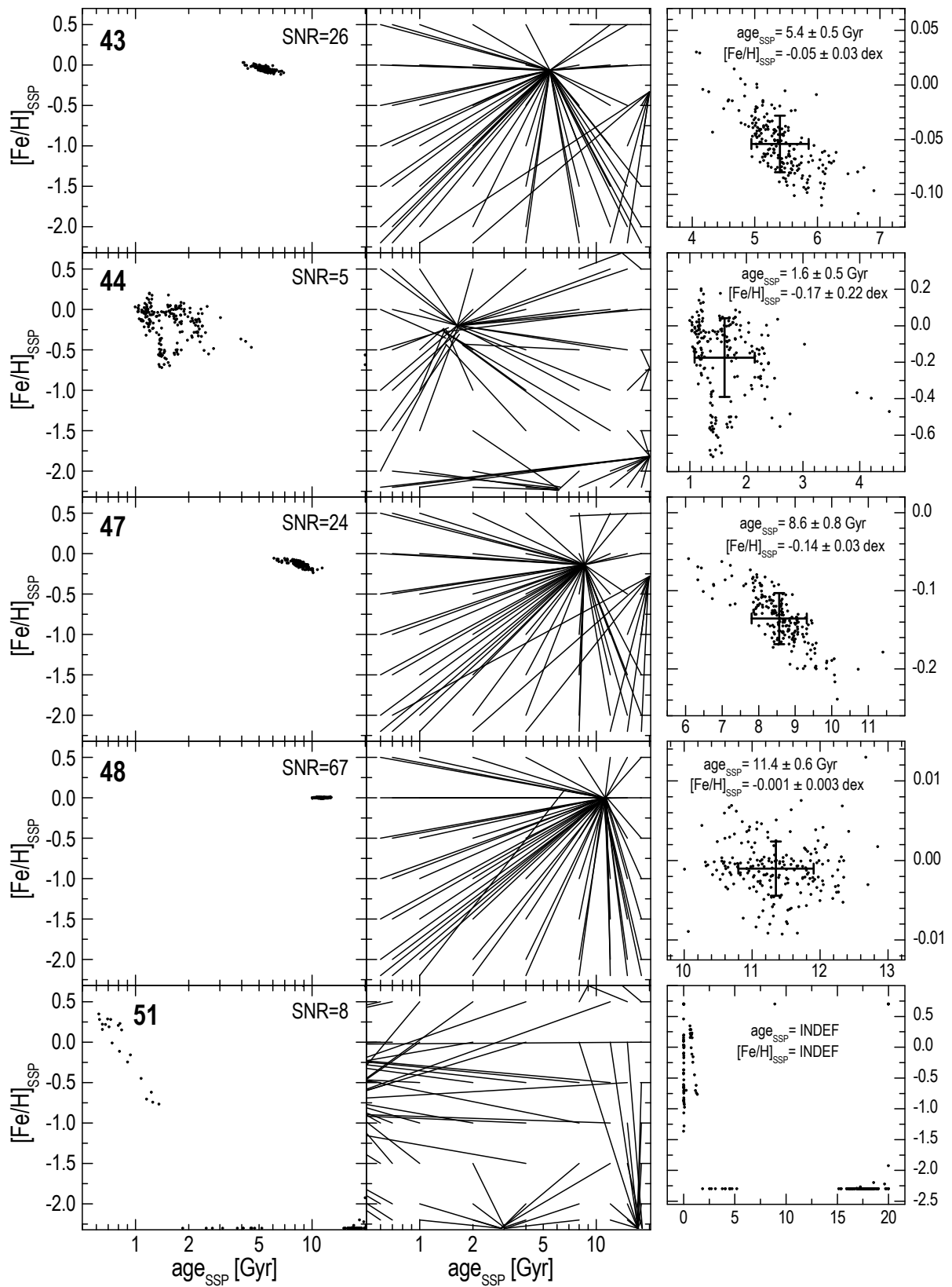


Figure 4.27: Same as Fig. 4.22.

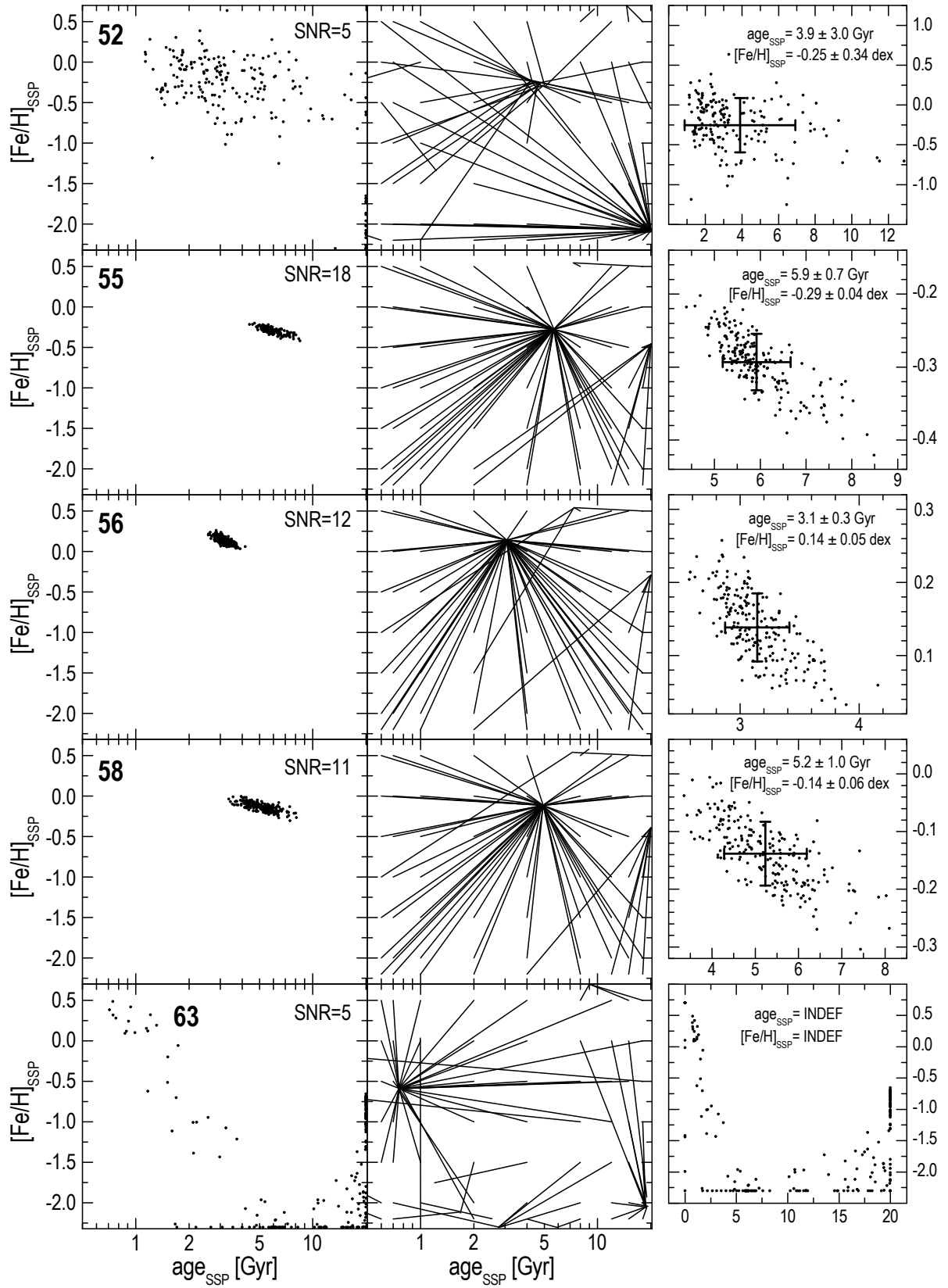


Figure 4.28: Same as Fig. 4.22.

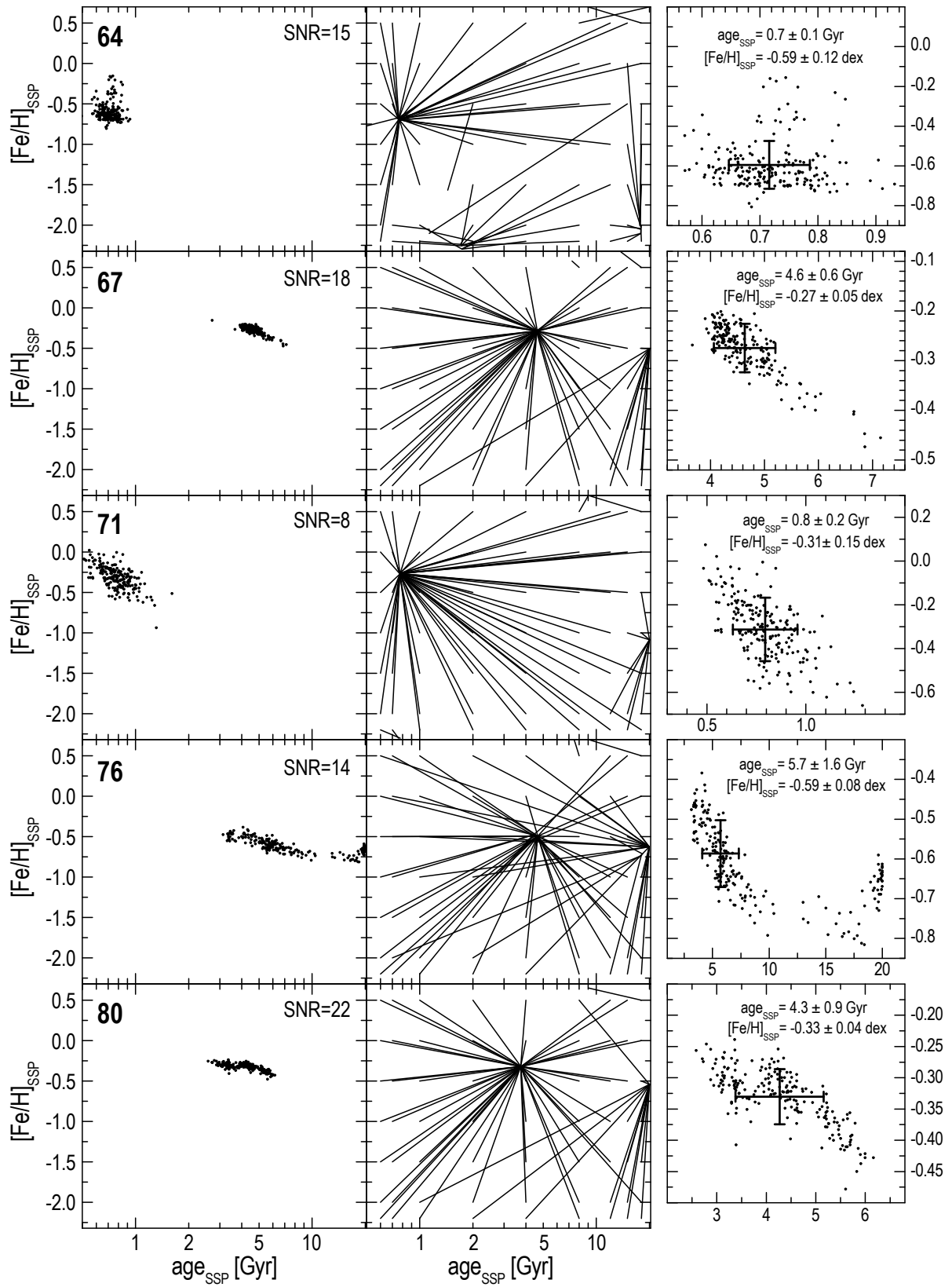
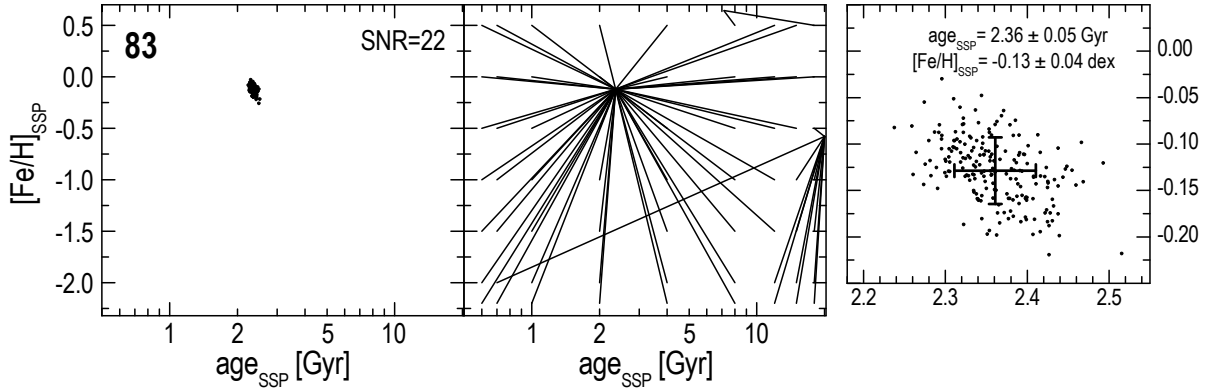


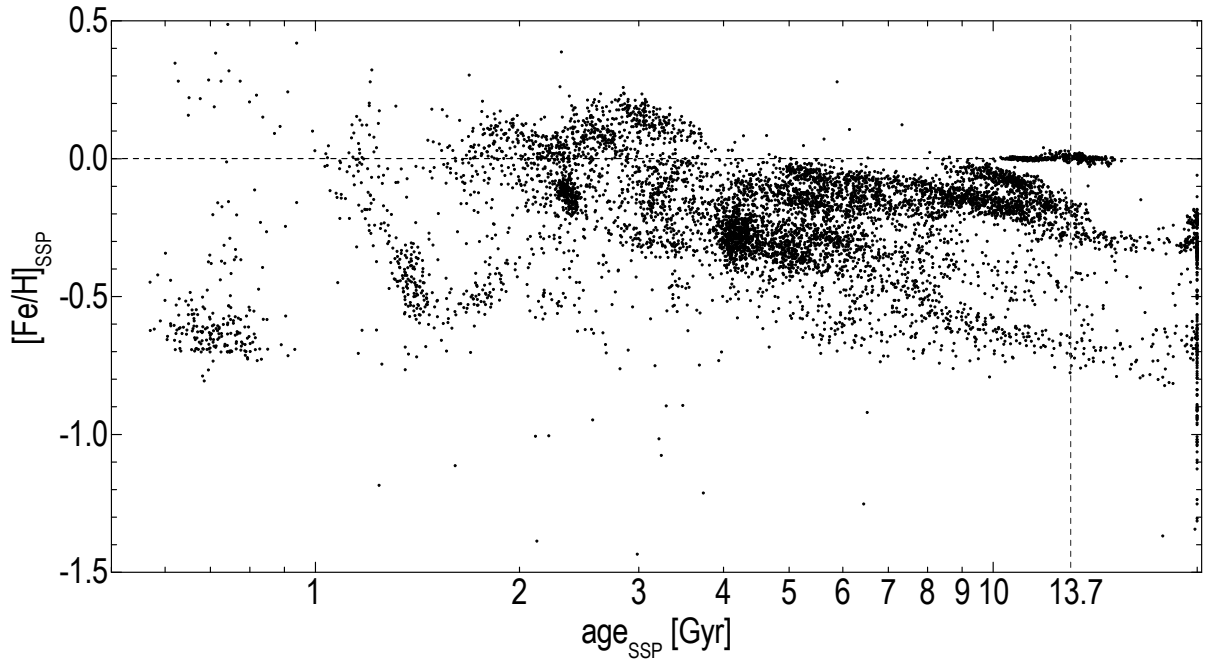
Figure 4.29: Same as Fig. 4.22.





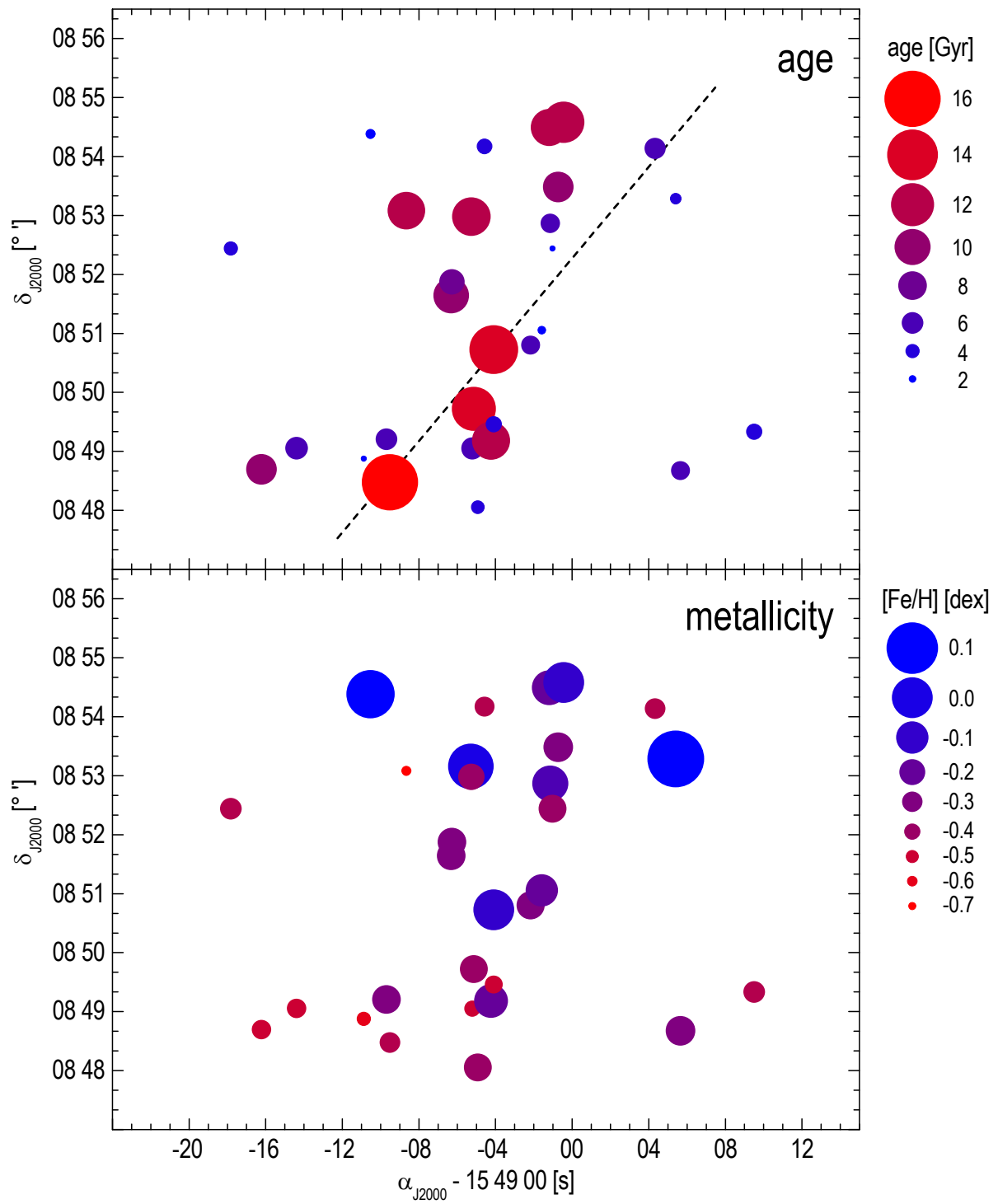
**Figure 4.30:** Same as Fig. 4.22.

Figure 4.31 summarizes all SSP ages and metallicities in the age-metallicity plane. The horizontal line indicates solar metallicity while the vertical one represents the age of the Universe. Similar to the results illustrated in Fig. 3.26, galaxies spread much more in age than in metallicity. Outliers populating the model age limit at 19.99 Gyr are also clearly seen.



**Figure 4.31:** Distribution of RX J1548.9+0851 group members in the age-metallicity plane.

To investigate the correlation between the measured SSP ages and metallicities with the spatial distribution of members, Fig. 4.32 shows age and metallicity maps of the inner  $\sim 300$  kpc region of RX J1548.9+0851. There is a clear segregation in age for the investigated faint galaxy population. While younger objects are diffusely distributed and found mostly in the outskirts of the system, the oldest objects form a clear elongated structure aligned with the orientation of the major axis of the central elliptical, indicated as a dashed line. The metallicity map also reveals an anisotropic distribution with the most metal rich objects found systematically on one side of the system.



**Figure 4.32:** Age and metallicity maps of RX J1548.9+0851 group members. The dashed line indicates the orientation of the central elliptical major axis.

## 12 Group dynamics and mass-to-light ratio

Besides the determination of group memberships, radial velocities offer the possibility to study the dynamics of a galaxy group or cluster. Once group members have been defined, these galaxies, especially the fainter ones can be considered as test particles in the overall group potential and can thus be used to estimate the dynamical mass of the system. This is accomplished by measuring the group velocity dispersion  $\sigma$ , which scales with the group virial mass according to equation 1.1. To evaluate the dynamical properties of RX J1548.9+0851, the luminosity weighted dynamical formulae presented in Firth et al. (2006) have been applied here.

Figure 4.33 a relates the SSP ages of RX J1548.9+0851 group members with measured radial velocities while Fig. 4.33 b shows the corresponding galaxy velocity distribution. Based on the age segregation found in Fig. 4.32, galaxies are separated into *old* and *young* objects at the arbitrary age of 8 Gyr. Figures 4.33 c and d show the spatial distribution of the old and young subpopulations. The two brightest ellipticals, hereafter BG1 and BG2, are the oldest objects in the sample (with the exception of one faint galaxy, exhibiting a huge error bar in age, however) and build up the centers of two subsamples in the velocity distribution of old galaxies.

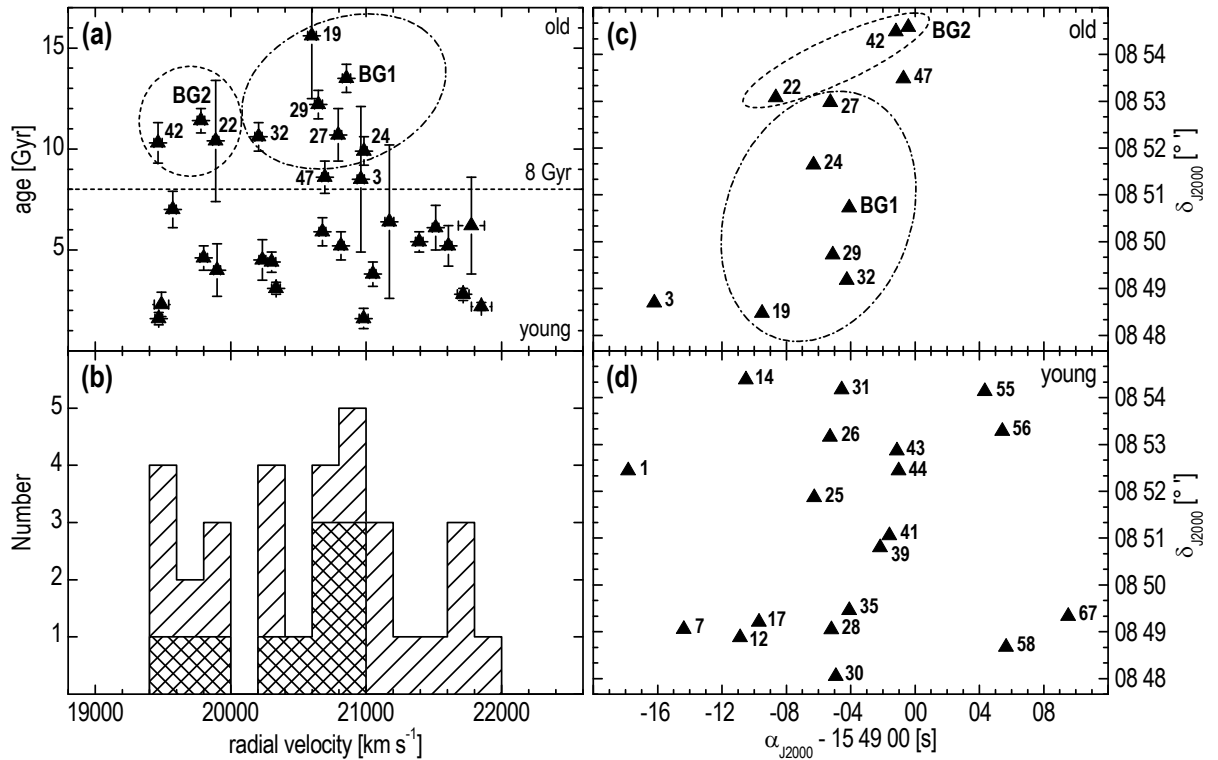


**Figure 4.33:** Galaxy velocity distribution of RX J1548.9+0851 member galaxies correlated with the measured SSP ages and the spatial galaxy distribution. (a): Age–velocity plane. Galaxies are separated into old and young objects. Ellipses divide old galaxies into subsamples around BG1 and BG2. (b): Galaxy velocity distribution. Old galaxies are indicated as cross-hatched histograms. (c) and (d): Spatial distribution of old and young objects. Ellipses correspond to those in panel (a). See text for details.

While the oldest galaxies around BG1 form the core of the overall velocity distribution, old galaxies around BG2 are found at systematically lower velocities. In contrast, young objects show a smooth distribution over all velocities and exhibit a much larger dispersion. Dashed ellipses in panels (a) and (c) contain the same objects, indicating that the subpopulations around BG1 and BG2 in radial velocity space are also more or less spatially correlated.

The results of the luminosity-weighted dynamical calculations as utilized in Firth et al. (2006) are presented in Table 4.9 for the sample shown in Figs. 4.32 and 4.33, i.e. the inner  $\sim 300$  kpc of the system. All velocities are given in  $\text{km s}^{-1}$ , radii in kpc, masses in  $10^{14}M_{\odot}$ , and the crossing times in Gyr. The second brightest elliptical BG2 obviously violates the fossil criterion and shows a radial velocity that is systematically too low compared to BG1, contrary to the expectations for a virialized halo. Therefore the dynamical properties of RX J1548.9+0851 have been calculated by either including or excluding BG2 to compare the different results. Moreover, the calculations have been carried out for both all members and the old subpopulation only, since a much smaller velocity dispersion is expected for this subsample.

Because of its brightness, BG2 severely alters the luminosity-weighted dynamical properties of RX J1548.9+0851. Already the mean radial velocity of the system differs by  $\sim 200 \text{ km s}^{-1}$  when omitting BG2. As expected from Fig. 4.33 b the group line-of-sight velocity dispersion shows a much smaller value in the absence of BG2. The two galaxies around BG2 in the velocity distribution contribute only little to this difference because of their faintness. Restricting to the old population also leads to smaller velocity dispersions, not as severe as the change by including or excluding BG2, however.

To evaluate the virial mass of the inner region of RX J1548.9+0851, the harmonic mean and virial radii have been calculated. The computation of the harmonic mean radius  $R_H$  involves the determination of the distances  $|r_i - r_j|$  of all  $N(N - 1)/2$  galaxy pairs within the sample. For the projected mass, the projected radial distances  $r_{\perp i}$  from the central elliptical have been applied. Characteristic system crossing times were estimated by dividing the virial radii by the velocity dispersions estimated with equation 4.4. Finally, the mean values of both mass estimates are shown with the corresponding standard deviations considered as errors.

The results show that the restriction of the sample to the old population does not change the group velocity dispersion as severely as the exclusion of BG2. This is evident since BG2 dominates the luminosity of all other faint and young galaxies by far, which as a consequence do not contribute significantly to the resulting dispersion. As expected, focusing on all members leads to the largest velocity dispersion ( $499 \text{ km s}^{-1}$ ) while restricting to the old population only leads to a slightly smaller value ( $440 \text{ km s}^{-1}$ ). Omitting BG2 leads to much smaller values for both the whole ( $329 \text{ km s}^{-1}$ ) and old ( $268 \text{ km s}^{-1}$ ) galaxy population. These data are also reflected in the derived mass estimates, showing the same trend with decreasing mass. In all estimates, projected masses are systematically higher than virial masses. The crossing times below 1 Gyr for the inner region of RX J1548.9+0851 suggest that members should have had enough time to virialize within the group potential.

**Table 4.9:** Luminosity weighted dynamics of RX J1548.9+0851.

(1)	(2)	(3)	(4)	(5)	(6)
Mean radial velocity	$\bar{v} = \frac{\sum_i w_i v_i}{\sum_i w_i}$	20633	20607	20821	20812
Velocity dispersion	$\sigma = \left[ \frac{\sum_i w_i (\Delta v_i)^2}{\sum_i w_i} \right]^{\frac{1}{2}}$	499	440	329	268
Harmonic radius	$R_H = \left[ \frac{\sum_i \sum_{j < i} (w_i w_j) / (r_i - r_j)}{\sum_i \sum_{j < i} (w_i w_j)} \right]^{\frac{1}{2}}$	194	200	147	126
Virial radius	$r_V = \frac{\pi R_H}{2}$	305	314	230	199
Crossing time	$t_c = \frac{\langle r \rangle}{\langle v \rangle}$	0.60	0.70	0.69	0.72
Virial mass	$M_V = \frac{3}{G} \sigma^2 r_V$	0.53	0.42	0.17	0.10
Projected mass	$M_p = \frac{32}{\pi G} \frac{\sum_i w_i (\Delta v_i)^2 r_{\perp i}}{\sum_i w_i}$	1.47	1.11	0.54	0.13
Mean mass value		$1.0 \pm 0.7$	$0.8 \pm 0.5$	$0.4 \pm 0.3$	$0.12 \pm 0.02$

**Notes:** Velocities are given in  $\text{km s}^{-1}$ , radii in kpc, masses in  $10^{14} M_{\odot}$ , and the crossing time in Gyr.

(1): Description.

(2): Dynamical formulae.

(3): Calculations for all members within  $\simeq 300 \text{kpc}$  ( $N = 32$ ).

(4): Restricting to the old ( $> 8 \text{Gyr}$ ) population as defined in Fig. 4.33 ( $N = 11$ ).

(5): Calculations for all members within  $\simeq 300 \text{kpc}$ , excluding BG2 ( $N = 31$ ).

(6): Restricting to the old ( $> 8 \text{Gyr}$ ) population as defined in Fig. 4.33, excluding BG2 ( $N = 10$ ).

To estimate mass-to-light ratios of RX J1548.9+0851 in the SDSS  $g'$ ,  $r'$ , and  $i'$  bands, total group luminosities have been estimated. For that purpose, the best-fit Schechter luminosity functions as shown in Fig. 4.17 have been integrated over all luminosity bins following equation 4.4. In addition, the luminosity of the central elliptical was added to this integrated luminosity since it was excluded in the Schechter fits. Since the Schechter function was fit to magnitudes instead of luminosities, absolute magnitudes of the sun in the  $g'$ ,  $r'$  and  $i'$  bands had to be considered, to determine the mass-to-light ratios in solar units. In this work, the values calculated by C. Willmer;  $M_{g'\odot} = 5.14$ ,  $M_{r'\odot} = 4.65$  and  $M_{i'\odot} = 4.54$ , based on the solar spectrum, have been applied<sup>19</sup>. Concerning group masses, the mean values of Table 4.9 have been applied. Table 4.10 summarizes the estimated mass-to-light ratios of RX J1548.9+0851 in the SDSS  $g'$ ,  $r'$ , and  $i'$  bands.

**Table 4.10:** Mass-to-light ratios of RX J1548.9+0851 in the SDSS  $g'$ ,  $r'$ , and  $i'$  bands.

	<i>Schechter fit parameters</i>			<i>Derivation of group luminosities and mass-to-light ratios</i>			
	$g'$	$r'$	$i'$	$g'$	$r'$	$i'$	
$\alpha$ .....	-1.55	-1.28	-1.44	$M_{\odot}$ [mag] .....	5.14	4.65	4.54
$M^*$ [mag] ...	-20.49	-20.70	-21.63	$L^*$ [ $L_{\odot}$ ] .....	$1.79 \cdot 10^{10}$	$1.37 \cdot 10^{10}$	$2.93 \cdot 10^{10}$
$\Phi^*$ .....	13.78	23.54	12.96	$M_{\text{BG1}}$ [mag] .....	-22.75	-23.50	-23.89
				$L_{\text{BG1}}$ [ $L_{\odot}$ ] .....	$1.43 \cdot 10^{11}$	$1.82 \cdot 10^{11}$	$2.36 \cdot 10^{11}$
				$L_{\text{tot}}$ [ $L_{\odot}$ ] .....	$6.25 \cdot 10^{11}$	$5.90 \cdot 10^{11}$	$8.41 \cdot 10^{11}$
				$L_{\text{BG1}}/L_{\text{tot}}$ .....	$\sim 23\%$	$\sim 31\%$	$\sim 28\%$
				$M/L$ [ $M_{\odot}/L_{\odot}$ ] ..	$90 \pm 60$	$100 \pm 70$	$70 \pm 50$

**Notes:**  $\Phi^*$  gives the number of galaxies in each magnitude bin instead of the number density.

Table 4.10 also highlights the luminosity fraction of the central elliptical compared to the overall group luminosity budget. The central elliptical amounts to  $\sim 30\%$  of the total group luminosity. Mendes de Oliveira et al. (2009) stated a corresponding value of  $\sim 80\%$  for the fossil RX J1340.6+4018. The lower fraction in RX J1548.9+0851 is most likely due to the presence of BG2, exhibiting only a slightly fainter  $\Delta m_{1,2} \sim 1.3^{\text{mag}}$  luminosity. The resulting mass-to-light ratios are not exceptional and show values around  $M/L \sim 100 M_{\odot}/L_{\odot}$ .

<sup>19</sup><http://mips.as.arizona.edu/~cnaw/sun.html>

# Chapter 5

## Discussion

In order to study the optical properties of fossil galaxy groups, the present work utilised both archive data from the SDSS as well as new observational data obtained with the William Herschel Telescope on La Palma and the Very Large Telescope in Chile. The corresponding data analysis techniques have been presented in sections 2, 3 and 4. The final chapter of this thesis summarizes and interprets the observational results presented in the previous sections in order to compare the new findings with the existing results on fossils in the literature.

### 1 New fossil candidates in the SDSS

Based on the observational selection criteria for fossils as defined by Jones et al. (2003), the SDSS was queried for new fossil candidates. Therefore an appropriate SQL code considering all fossil selection criteria, i.e. the dominance of the central elliptical in luminosity with respect to any surrounding galaxies ( $\Delta m_{1,2} \geq 2.0^{\text{mag}}$ ) within half the virial radius and the presence of an extended X-ray source, was developed. A similar study was carried out by Santos et al. (2007), focusing however on a slightly different SQL code. In contrast to focusing on a constant value of  $0.5h_{70}^{-1}$  Mpc for half the virial radius at all redshifts, the description of Evrard et al. (1996) (see equation 2.2) as used by Jones et al. (2003) was applied here. Santos et al. (2007) also considered photometric redshifts of the surrounding faint galaxies to differentiate possible group members from background galaxies. Since photometric redshifts can deviate from spectroscopic ones (see Fig. 4.15), this procedure hasn't been included in the present approach.

The performed query re-identifies 12 systems from the work of Santos et al. (2007) corresponding to  $\sim 35\%$  of their sample proving the functionality of the algorithm utilised in the present study. However, many objects could not be reidentified since the procedure used here excludes all systems involving galaxies within half the virial radius violating the  $2^{\text{mag}}$  criterion, regardless if they are background galaxies or not, thus eliminating possible fossil candidates that would pass the  $2^{\text{mag}}$  criterion if group memberships were known. This indicates that there might be

much more fossil candidates in the present query when accounting also for group memberships via photometric redshifts. In fact, 14 systems from Santos et al. (2007) host 1 galaxy violating the  $2^{\text{mag}}$  criterion in this work. Thus, compared to the work of Santos et al. (2007), the present query yields more fossil candidates considering the systematically lower estimate for half the virial radii but is more restrictive in the  $2^{\text{mag}}$  criterion since no distinction between group members or background galaxies is made.

The query identified 34 fossil candidates fulfilling the implemented criteria. Since the actual X-ray temperatures are not known for these systems, thus possibly underestimating the true extent of the virial radius, these 34 aggregates are considered as fossil candidates rather than fossil groups. Nonetheless they serve as ideal targets for studying groups dominated by a single massive elliptical. Figure 5.1 shows the central ellipticals from both Santos et al. (2007) and the present work. The diagram is similar to Fig. 2.4, however plotting the galaxy redshift instead of colour. All six ellipticals selected for follow-up observations at the WHT and VLT are marked with arrows. Galaxy 6 has been observed with both telescopes, the WHT data focusing on the central elliptical and the VLT data on the faint galaxy population. Compared to all other targets, NGC 1132 is the brightest by far, also clearly seen in the line-strength profiles when comparing Figs. 3.18–3.23.

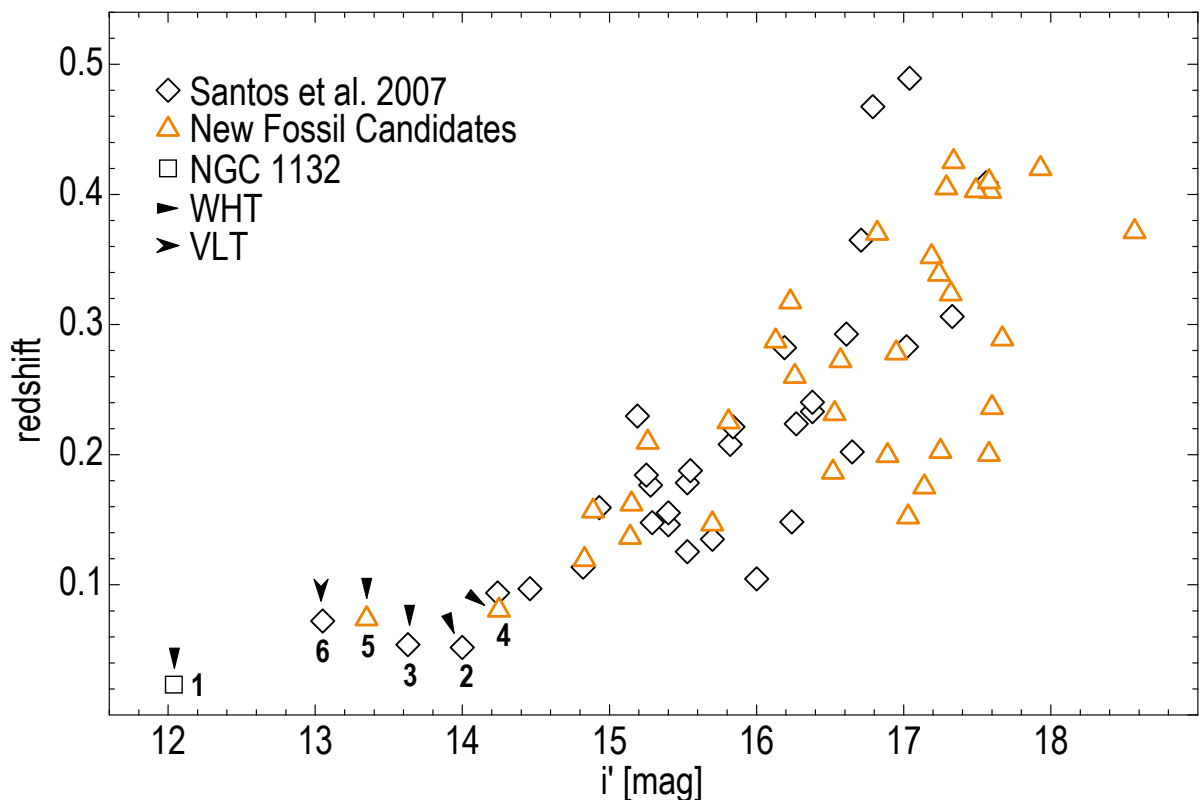


**Figure 5.1:** Same as Fig. 2.4 but plotting redshift instead of colour. Again, diamonds show the objects published by Santos et al. (2007) while triangles present the aggregates found in this work. The square indicates NGC 1132. Arrows point to the objects that have been observed with the WHT and the VLT. Numbers refer to the ID of Table 3.3 (see Chapter 3).



## 2 Characteristics of the central ellipticals observed at the WHT

The galaxies selected for follow-up observations at the WHT and VLT mark the bright end of the galaxy distribution in Fig. 5.1 and were thus the ideal candidates to choose from that sample. In addition, the prototypical fossil NGC 1132 was added to these fossil candidates to complement the SDSS target list. The WHT ellipticals exhibit redshifts of  $0.023133 < z < 0.080528$  corresponding to luminosity distances of 101 – 366 Mpc and angular size distances of 96 – 313 Mpc. These data correspond to an age of the universe at redshift  $z$  of 13.1 back to 12.4 Gyr. According to Fig. 1.8 a, the Millennium simulation predicts that fossils at these redshifts should have assembled at least 95% of their total dark matter mass.

As presented in Chapter 1, the structural parameters of early-type galaxies are not randomly distributed in the parameter space, but follow certain relations helping to constrain theories on elliptical galaxy formation. With the spectroscopic results obtained from the observations carried-out at the WHT and the corresponding photometric data presented in Chapter 2, the location of the six investigated ellipticals with respect to these relations can be determined. Focusing on photometric SDSS data, the relations from Bernardi et al. (2003a,b,c) have been considered as reference. Figures 5.2 and 5.3 show the colour-magnitude and colour-sigma relations for early-type galaxies from Bernardi et al. (2003c). To achieve a proper comparison between the observed ellipticals at the WHT and these relations, SDSS colours were first dereddened by means of the corresponding extinction data  $A_X$  stored in the SDSS database:  $(g' - r')_0 = (g' - r') - E_{g'-r'}$  where  $E_{g'-r'} = A_{g'} - A_{r'}$ . Absolute magnitudes were calculated following equation 2.3 with  $K$ -corrections estimated from the relation shown in Fig. 2.2 a. Velocity dispersions are the  $\sigma_{\text{phys}}$  data from Chapter 3.

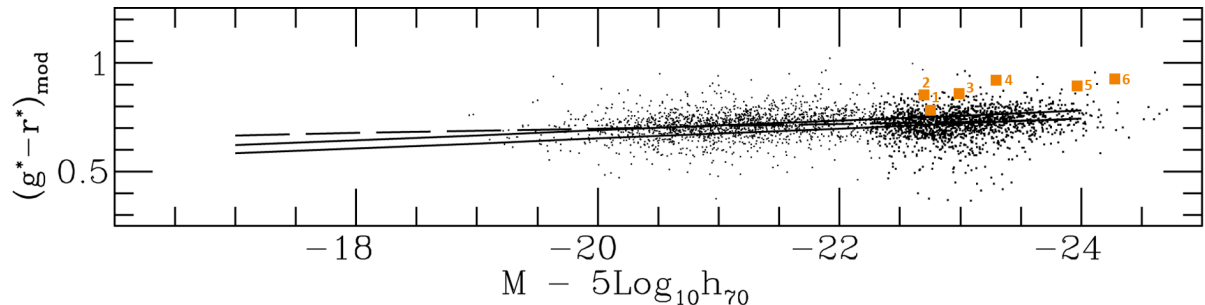


**Figure 5.2:** The WHT ellipticals in the colour-magnitude relation from Bernardi et al. (2003c).

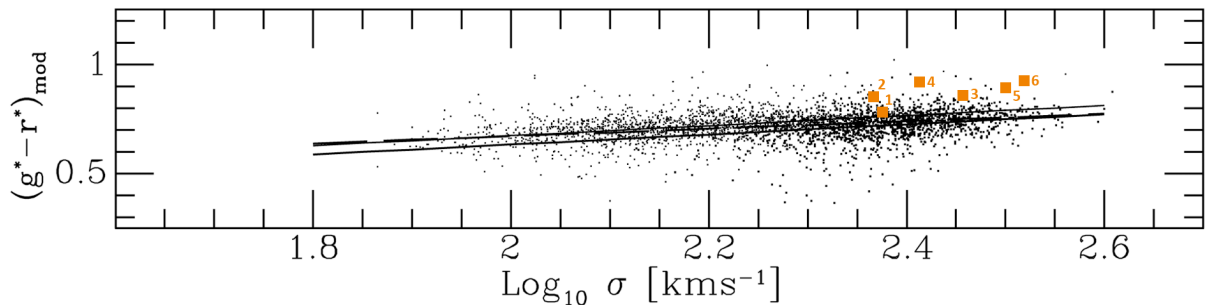


**Figure 5.3:** The WHT ellipticals in the colour-sigma relation from Bernardi et al. (2003c).

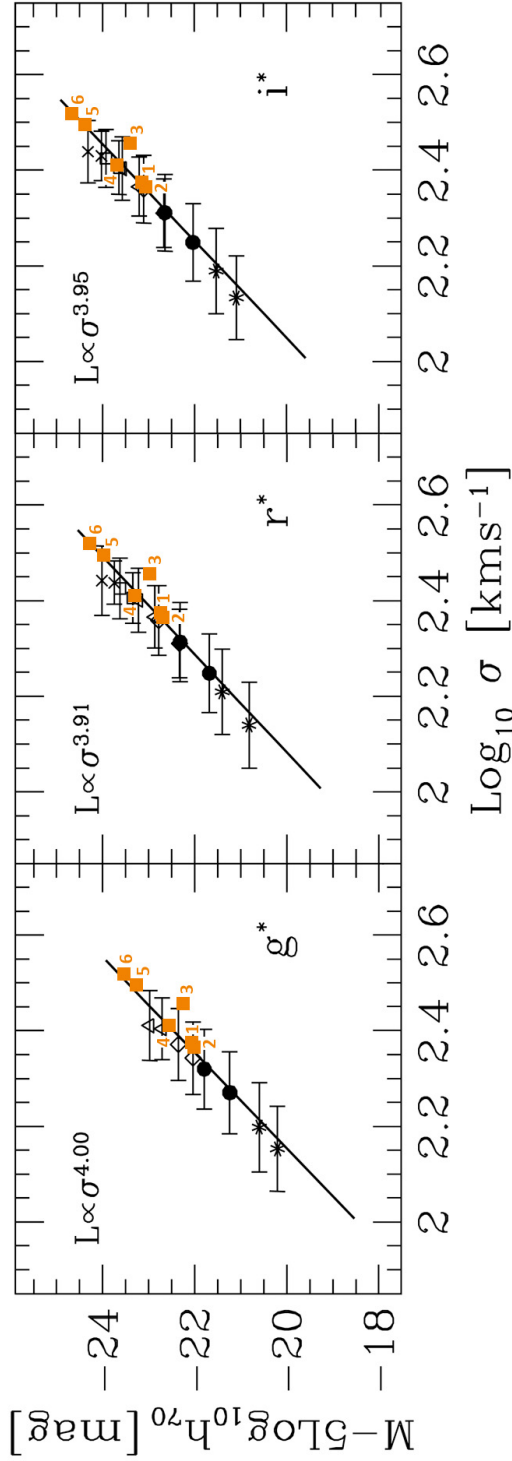


**Figure 5.4:** The WHT ellipticals on the Faber-Jackson relation of early-type galaxies. Diagrams adapted from Bernardi et al. (2003a).

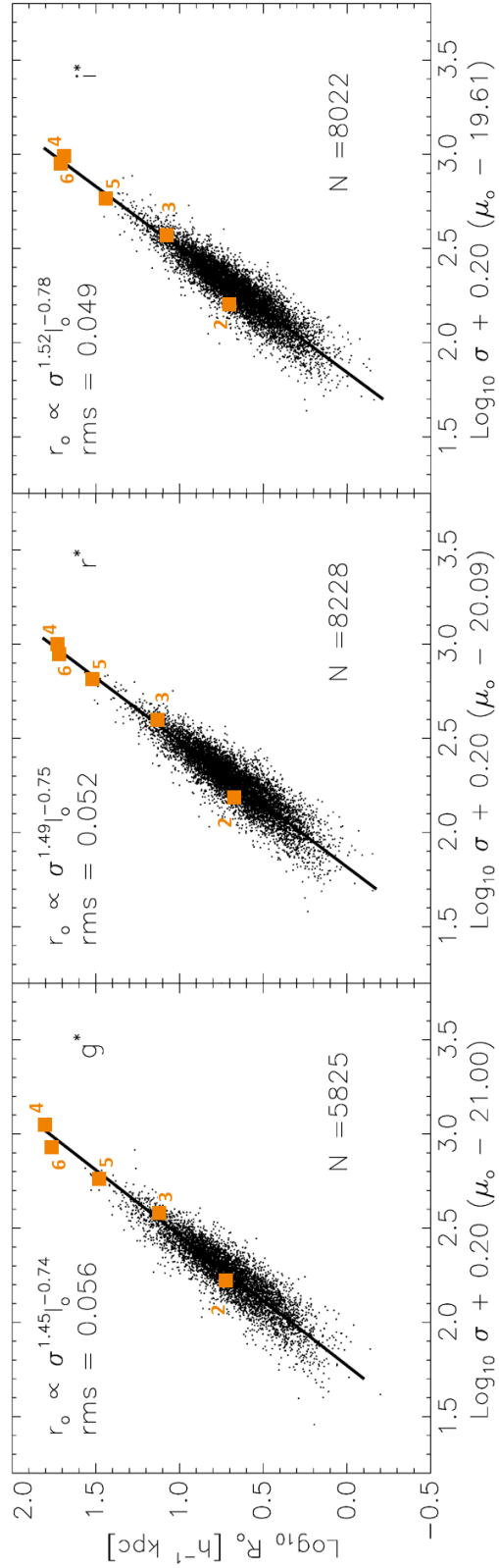


**Figure 5.5:** The WHT ellipticals on the fundamental plane of early-type galaxies. Diagrams adapted from Bernardi et al. (2003b).

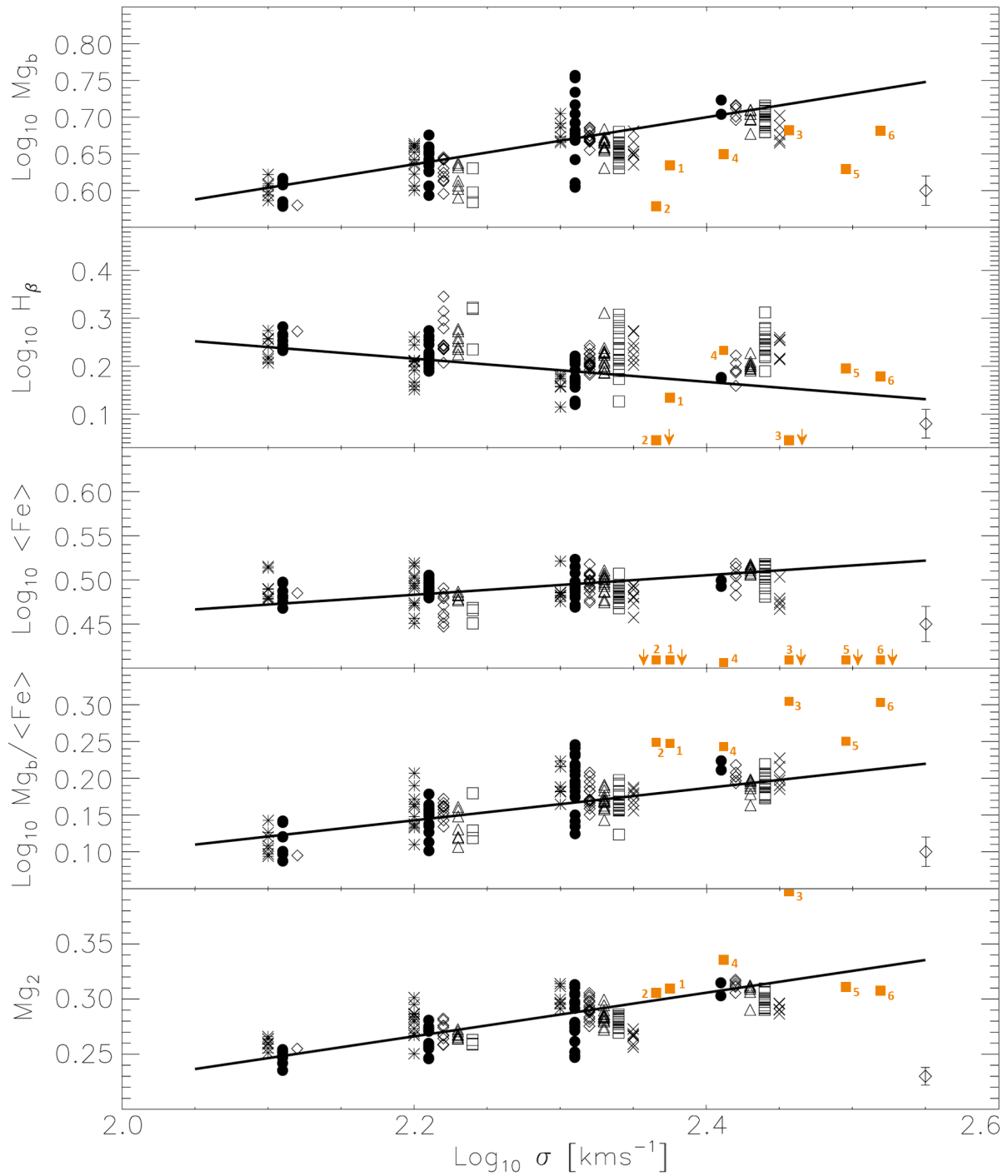


**Figure 5.6:** Relations between index strengths and velocity dispersion. The systematically too low values of the  $H\beta$  indices for galaxies 2 and 3 can be explained by the presence of emission lines in the spectra of these galaxies. Diagrams adapted from Bernardi et al. (2003c).

In both diagrams, all observed ellipticals lie slightly but systematically above the published relations, however following a similar slope, i.e. becoming redder with increasing luminosity and velocity dispersion. The diagrams involve SDSS model magnitudes as found in the SDSS sky server. The comparatively red colours of the WHT ellipticals suggest that these galaxies are dominated throughout by an old stellar population and did not experience recent star formation which would result in bluer observed colours. The ellipticals are also found at the right end of the relation confirming that these galaxies are indeed very luminous and massive as expected for the merger remnant of a poor group of galaxies.

Figures 5.4 and 5.5 show the Faber-Jackson relation and the fundamental plane of early-type galaxies as studied by Bernardi et al. (2003a,b). To properly determine the location of the observed ellipticals with respect to the latter relation, the effective radius  $r_e$  (denoted as  $r_0$  in Fig. 5.5) and the average surface brightness within the effective radius  $\langle\mu_e\rangle$  (denoted as  $\mu_0$  in Fig. 5.5) had to be computed. The effective radii in the SDSS  $g'$ ,  $r'$ , and  $i'$  bands were derived from the performed deVaucouleurs fits. Average surface brightnesses  $\langle\mu_e\rangle$  have been defined as  $\langle\mu_e\rangle = -2.5 \log((L/2)/R_e^2)$  by Bernardi et al. (2003b) where  $L$  is the luminosity of the galaxy. The corresponding values for the observed ellipticals were computed accordingly from the obtained IRAF `ellipse` data. As can be seen from the diagrams, all ellipticals observed at the WHT fall on the published relations suggesting that they are not exceptional with respect to other ellipticals. Bernardi et al. (2003b) have claimed that the fundamental plane derived from their work is tilted compared to the one expected by the virial theorem implying also a tilted fundamental plane for the observed ellipticals.

Figure 5.6 shows the relations between the most prominent absorption line strengths in ellipticals ( $Mgb$ ,  $\langle Fe \rangle = 1/2 (Fe5270 + Fe5335)$ ,  $H\beta$ ,  $Mg_2$ ) and velocity dispersion. The best match between the published relations and the index data from the WHT ellipticals is found for  $Mg_2$  and  $H\beta$ .  $\langle Fe \rangle$  and  $Mgb$  on the other hand are systematically below and above the corresponding relations, however following a similar trend with velocity dispersion.

The spatial variation of ages and metallicities along the spectrograph slit have been presented in chapter 3 for all observed ellipticals. To get a better overview on the slopes of these age and metallicity gradients, Fig. 5.7 shows the averaged age and metallicity data from both sides of the galaxy centre. The vertical dashed lines indicate the seeing dominated central galaxy regions while the dotted lines are linear least squares fits to the measured data. The linear fits reveal negative metallicity gradients for all observed ellipticals while ages show either positive or negative slopes. Since radii are shown on a logarithmic scale, the linear fits correspond to power-law gradients.

The negative gradients support the classical monolithic formation scenario for ellipticals where the galaxies form in a dissipative collapse (Larson 1974). Following the simulations of Mihos & Hernquist (1994) such power-law gradients cannot be reproduced by the merger of pure stellar disks unless the effects of a metal-rich starburst. Such an inside-out formation is also supported by the negative abundance gradients seen clearly in Figs. 3.18-3.23. Age gradients are found with both positive and negative slopes implying either a young burst of star formation confined to the inner galaxy regions, producing a steep positive gradient (Reda et al. 2007) or the merger of a gas-rich satellite (Kobayashi 2004) resulting in a negative age gradient.

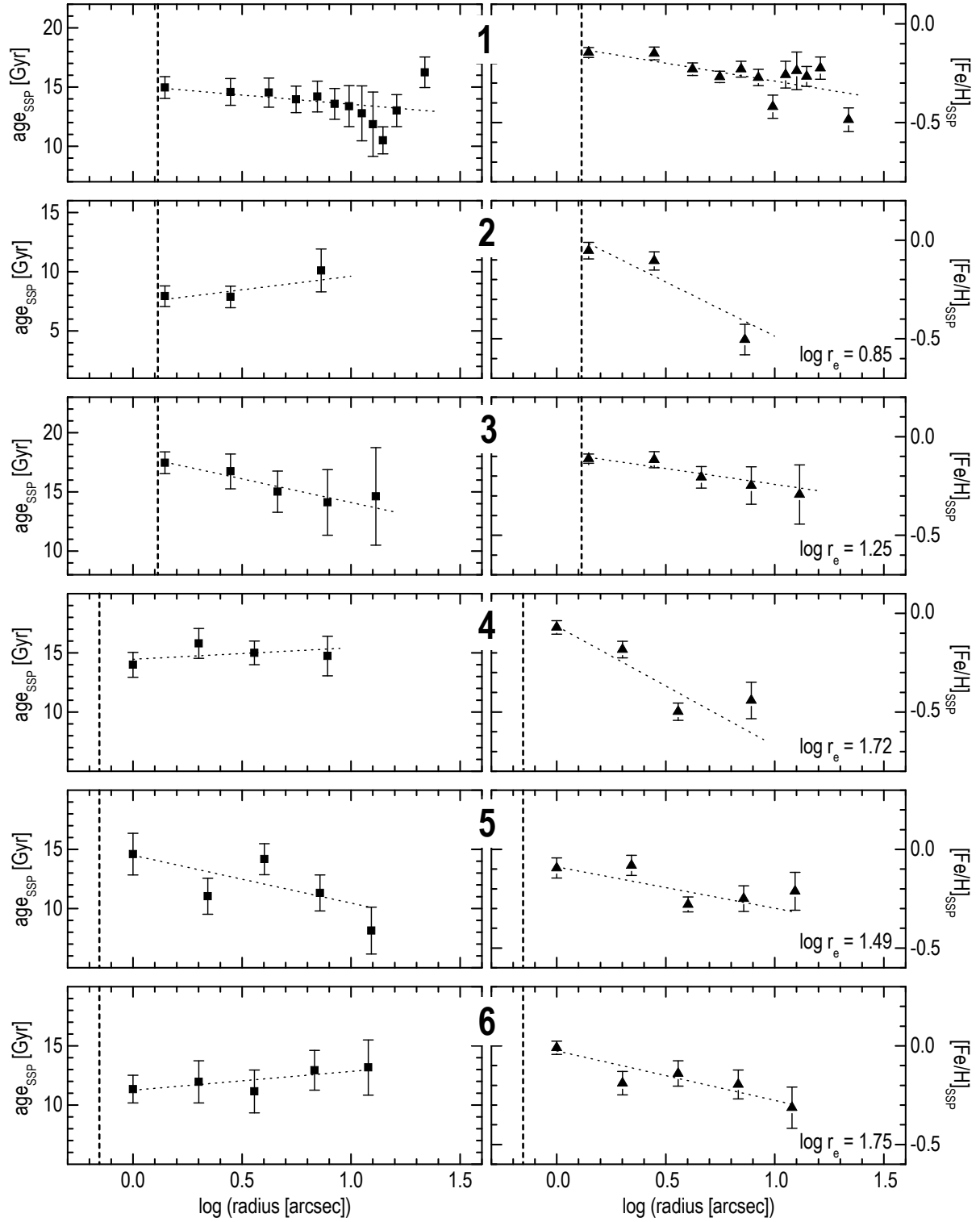


**Figure 5.7:** Age and metallicity gradients of the WHT ellipticals. Left panels refer to age, right ones present metallicity. Vertical lines indicate the seeing dominated regions. Dotted lines are linear least squares fits. All observed ellipticals exhibit negative metallicity gradients.

The SSP fitting results for the galaxies as a whole revealed that the studied ellipticals are made up of an old stellar population with an average age of  $13 \pm 2$  Gyr as expected for these morphological types. Only RX J0752.7+4557 (galaxy 2) shows a systematically lower age of  $8 \pm 1$  Gyr. This is not surprising however, since this galaxy exhibits prominent emission lines indicative of ongoing star formation. The presence of the very old stellar populations in the studied ellipticals confirms a scenario where these systems didn't experience any recent major merger triggering star formation that would lead to an overall younger stellar population. The measured ages are also consistent with those derived from the SSP model grids of Schiavon (2007) based on the  $H\beta$ , Fe5270, and Fe5335 indices. Only ages for galaxies 2 and 3 show a severe mismatch, predicting a much older age than the corresponding ULySS fit. This is easily explained by the presence of an emission component in the  $H\beta$  index for these galaxies misleading to the incorrect ages. Metallicities derived from the SSP fitting technique amount to  $-0.16 \pm 0.03$  dex on the average while the corresponding values from the analysis of Lick indices show lower values around -0.4 dex. In any case, the ULySS fit results are much more reliable compared to the single feature age and metallicity predictions.

As useful by-product of the SSP full spectrum fitting technique, the kinematic data along the spectrograph slit have been studied. Figure 3.33 shows radial velocity curves as well as velocity dispersion profiles of the WHT ellipticals. NGC 1132 (galaxy 1) as the brightest of the investigated objects shows the typical kinematic profiles as one would expect, a symmetric flat radial velocity curve and a central enhancement of the line-of-sight velocity dispersion. The fainter objects in the sample follow these trends more or less. No counter-rotating cores, indicative of a recent merger are visible in the profiles. Only galaxy 6 shows an abrupt change in the shape of the radial velocity curve near the center (around 5 arcsec, see Fig. 3.33) which might be the indication of recent dynamical interaction with a smaller satellite.

The performed surface photometry shows that all studied ellipticals can be modelled by a deVaucouleurs  $r^{1/4}$  profile. Only RX J1152.6+0328 (galaxy 4) exhibits slight deviations from a pure deVaucouleurs law which could be interpreted by an additional disk component. No light excess is found in the outer regions of the surface brightness profiles as seen in massive cD galaxies in the centres of galaxy clusters. Concerning the harmonic content of the ellipse fits, the isophote analysis didn't reveal any exceptional boxy or disky systems.

### 3 The galaxy population of the fossil candidate RX J1548.9+0851

In addition to the spectroscopic study of central ellipticals in fossil group candidates presented in Chapter 3, the faint galaxy population surrounding the central dominating galaxy has also been investigated for the fossil candidate RX J1548.9+0851 (galaxy 6) with VIMOS. At a redshift of  $z = 0.072146$ , the system lies at a luminosity distance of  $D_L = 326$  Mpc and an angular diameter distance of  $D_A = 283$  Mpc corresponding to a spatial scale of  $1.374$  kpc arcsec $^{-1}$ . At this redshift the age of the universe amounts to  $\sim 12.5$  Gyr. The system was selected from the Santos et al. (2007) sample of fossil candidates.

The optical appearance of the RX J1548.9+0851 system is dominated by two elliptical galaxies with a magnitude difference of  $\Delta m_{1,2} = 1.34$  in the  $r'$  band and a spectroscopic redshift difference of  $\Delta z \sim 0.004$  in the SDSS DR5. At a projected distance of 326 kpc this magnitude

difference clearly violates the  $2^{\text{mag}}$  criterion. However, the system is listed in the fossil sample of Santos et al. (2007) who use a constant value of  $0.5h_{70}^{-1}$  Mpc to estimate half the virial radius. This is still plausible though since these authors consider all galaxies surrounding an elliptical and fulfilling  $\Delta z > 0.002$  in the SDSS DR5 as nonmember galaxies. However, following the distribution of galaxies in radial velocity space as seen in Fig. 4.12, there is no reason to classify the galaxy as background object in this work. The Evrard et al. (1996) estimate of half the virial radius as used here yields a projected distance of 331 kpc which would classify RX J1548.9+0851 as non-fossil. In any case the group is of special interest since it is lacking any other bright galaxies that would be expected in a poor group environment.

Figure 4.12 shows the distribution of radial velocities for all galaxies in the studied VIMOS field-of-view. The diagram reveals that the RX J1548.9+0851 system is clearly defined in radial velocity space and hence represents a real gravitationally bound system instead of a chance superposition along the line-of sight. No significant excess of background galaxies is found at higher redshifts. In the whole VIMOS field-of-view 41 group members have been identified. Including galaxies with adequate redshifts from the literature, this value rises up to 54 member galaxies within 1 Mpc of the central elliptical. Out of all galaxies with measured redshifts from this work and the literature, at least half of them are member galaxies (see Table 4.7).

The physical existence of the RX J1548.9+0851 system is also evident in the corresponding colour-magnitude diagram (see Fig. 4.14). Spectroscopically confirmed group member galaxies form a clear red sequence as expected for groups and clusters of galaxies. This red sequence is even more pronounced when accounting also for photometric redshift data as additional group membership criterion (see Fig. 4.16). In fact, it is so well-defined that a straight line was set as red sequence upper limit. Only 2 group members have been found above this upper limit while all other spectroscopically studied galaxies above the adopted line are background objects. Interestingly, these 2 galaxies (39 and 42) are found in the immediate vicinity of the two brightest ellipticals in the group (see Fig. 4.14). This is in agreement with the work of Eigenthaler & Zeilinger (2010) who found a similar object in the vicinity of the massive central elliptical of the NGC 5846 group in the Local supercluster, also representing the reddest faint galaxy of that system. The fact that such objects are systematically redder than other member galaxies at the same brightness and found close to the most massive ellipticals in a group suggests that they might have been tidally stripped by these host ellipticals, leaving behind a dominating old, red stellar population.

Considering morphology, the central elliptical of the RX J1548.9+0851 system is of special interest. Symmetric shells are revealed unambiguously along the major axis of the galaxy. To enhance the appearance of these features, an unsharp masking technique was applied to the VIMOS pre-image. The presence of these strongly symmetric shells indicates the presence of a recent minor merger. In fact, Ebrova et al. (2010) have simulated shell galaxies with the conclusion that a significantly smaller secondary galaxy interacting with the dark matter halo of the primary elliptical can reproduce such observed regular shell systems. In their simulation, a satellite falling radially towards the center of the primary galaxy is assumed to be instantly ripped apart when approaching the center of the primary. Its stars subsequently oscillate in the potential of the primary elliptical and produce arc-like structures at the orbit turning points as observed. Thus, being the most massive object in the RX J1548.9+0851 system and

exhibiting the observed fine structure, it is very likely that a recent minor merger has occurred in this system. This would be in agreement with the evolution scenario for fossils where these aggregates have assembled most of their mass at early epochs and grow typically by minor mergers afterwards (Dariush et al. 2007). As already highlighted in the previous section, the surface brightness profile of the elliptical (galaxy 6 of the WHT sample) is well-fit by a pure deVaucouleurs  $r^{1/4}$  law without any indication of a light excess in the outer galaxy regions as seen in cD galaxies.

The luminosity function of the RX J1548.9+0851 system has been studied in the SDSS  $g'$ ,  $r'$ , and  $i'$  bands within 1 Mpc of the central elliptical. The slopes of the fitted Schechter functions at the faint end of the galaxy luminosity distribution amount to  $\alpha_{g'} = -1.55$ ,  $\alpha_{r'} = -1.28$ , and  $\alpha_{i'} = -1.44$  yielding an average value of  $\alpha = -1.4 \pm 0.1$  and representing a steep luminosity function at the faint end. Mendes de Oliveira et al. (2009) have claimed that a scenario seems to be emerging where massive fossil groups tend to have steep luminosity functions. The derived slope for the RX J1548.9+0851 system would support such a scenario. At fainter magnitudes member galaxies are dominated by photometrically determined ones however, liable to photometric redshift uncertainties. Thus, one has to be careful when interpreting the resulting shape of the fitted luminosity function. The observed slope is comparable to those of the fossil RX J1340.6+4018 ( $\alpha = -1.6 \pm 0.2$ ), the Virgo ( $\alpha = -1.28 \pm 0.06$ ) and Coma ( $\alpha = -1.47 \pm 0.09$ ) clusters and the 2dF and RASS-SDSS clusters ( $\alpha \simeq 1.3$ ). No pronounced dip around  $M = -18 + 5 \log h$  has been found in the present study.

Similarly to the analysis of stellar populations in the six ellipticals observed at the WHT, the VIMOS spectra of RX J1548.9+0851 member galaxies have been fit with SSP models to determine SSP equivalent ages and metallicities of the group galaxy population. The distribution of SSP ages within the system shows a clear spatial segregation. While galaxies exhibiting an old ( $> 8$  Gyr) stellar population are confined to an elongated, central distribution, galaxies with young ( $< 8$  Gyr) stars are more diffusely distributed and predominantly found in the outer regions of the system. Interestingly, the distribution of old galaxies is also correlated with the orientation of the major axis of the central elliptical.

This is in agreement with the simulations of Sales et al. (2007) who found that red satellites are clearly much more concentrated towards a massive central galaxy than blue ones (see Fig. 1.9 a). They argue that this is presumably due to the gas loss of satellites once they are accreted. The earlier a satellite was accreted, the older, i.e. redder, its stellar population will be. This suggests that the distribution of old stellar population galaxies in the RX J1548.9+0851 system was formed first, likely representing a virialized substructure whereas galaxies with younger stellar populations are not in dynamical equilibrium within the group potential. A further hint supporting this idea is the fact that the simulation of Sales et al. (2007) also revealed a systematic anisotropy in the spatial distribution of satellites (see Fig. 1.9 b) showing an anti-Holmberg effect, i.e. being aligned along the plane perpendicular to the angular momentum axis of the halo. Assuming that the major axis of a primary galaxy is aligned with the major axis of the dark matter halo, an alignment of satellites with the major axis of the central galaxy would thus be expected, exactly what is observed in the RX J1548.9+0851 system.



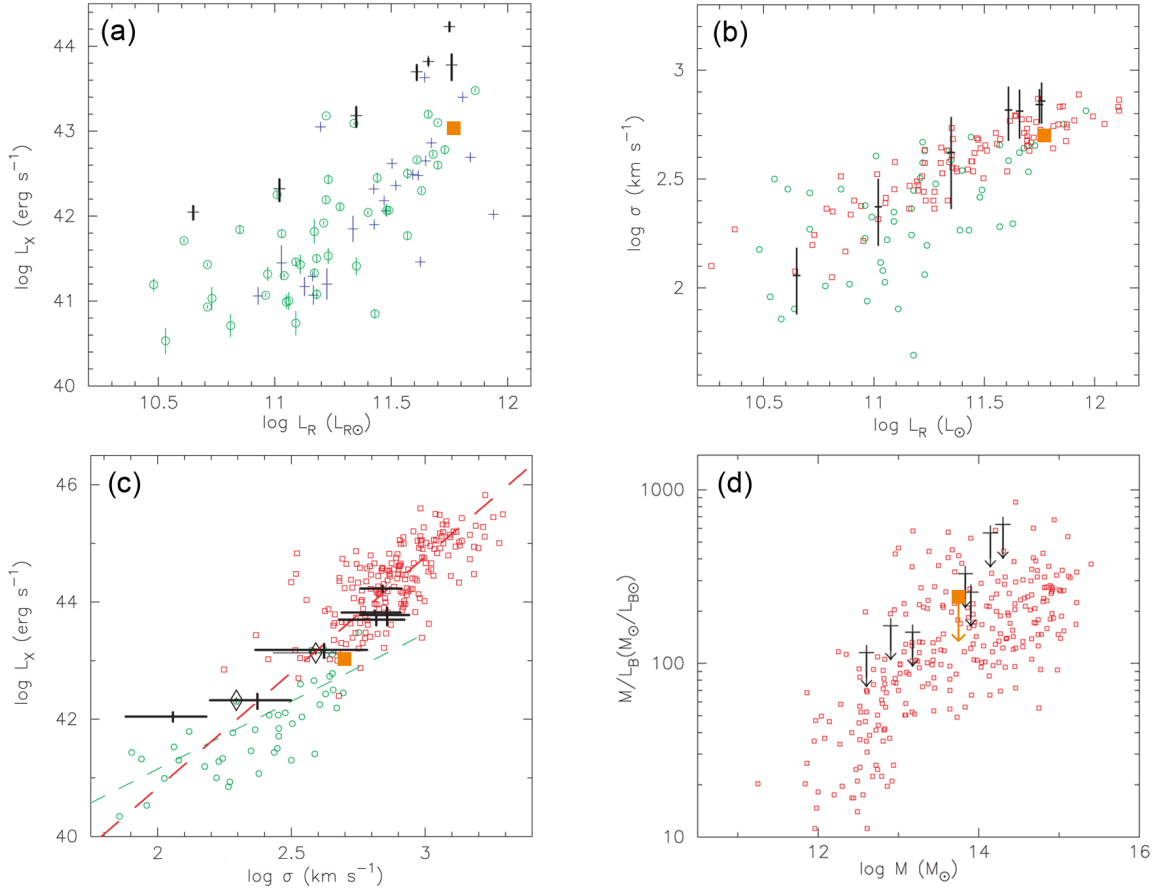


**Figure 5.8:** The RX J1548.9+0851 system in the group–cluster scaling relations from Khosroshahi et al. (2007). Green circles are GEMS groups from Osmond & Ponman (2004). Red squares in panel c) are clusters from Wu et al. (1999) while red squares in panels b) and d) present groups and clusters from Girardi et al. (2002). Black crosses are the fossils studied by Khosroshahi et al. (2007) while the brown square indicates the studied aggregate.

The measured SSP ages are not only correlated with the location of the satellites within the system, but also with the observed radial velocity distribution. The sample of old galaxies is made up of two subpopulations in radial velocity space around the two brightest ellipticals BG1 and BG2 which are also the oldest objects in the system. While old galaxies around BG1 form the core of the overall velocity distribution, old galaxies around BG2 are found at systematically lower velocities. In contrast, young objects show a smooth distribution over all velocities and exhibit a much larger dispersion. This supports the already highlighted scenario in which the sample of old galaxies in the RX J1548.9+0851 system formed first, leaving enough time for these galaxies to virialize around the most massive subhaloes BG1 and BG2, building up the cores of these two radial velocity distributions. Galaxies with younger stellar populations on the other hand have not yet found an equilibrium configuration in the overall group potential.

This is in agreement with the work of Mendes de Oliveira et al. (2006) on the fossil cluster RX J1552.2+2013. The authors have shown that the velocity dispersion of the system is much lower when excluding emission-line galaxies (i.e. galaxies hosting younger stellar populations)

from the sample, predominantly occupying the edges of the galaxy velocity distribution. This is expected since emission-line galaxies are believed to have just recently been accreted by the cluster and thus present not yet a virialized galaxy subsample, exactly what is observed in RX J1548.9+0851 studied in the present work.

Radial velocities have also been used to determine the luminosity-weighted dynamical properties of the inner ( $\sim 300$  kpc) region of the RX J1548.9+0851 system. For that purpose the dynamical formulae from Firth et al. (2006) have been applied. Dynamical properties have been calculated by either including or excluding the second brightest elliptical and for the old subpopulation alone. Because of its brightness, including or excluding BG2 severely alters the luminosity-weighted dynamical properties of RX J1548.9+0851. Considering all members yields the largest velocity dispersion ( $499 \text{ km s}^{-1}$ ) while restricting to the old population only leads to a slightly smaller value ( $440 \text{ km s}^{-1}$ ). Omitting BG2 leads to much smaller values for both the whole ( $329 \text{ km s}^{-1}$ ) and old ( $268 \text{ km s}^{-1}$ ) galaxy populations. These data are also reflected in the derived masses with values ranging from  $1 - 5.3 \cdot 10^{13} M_{\odot}$  for the virial mass estimator and  $1.3 - 14.7 \cdot 10^{13} M_{\odot}$  for the projected mass. In all estimates, projected masses are systematically higher than virial masses. Crossing times below 1 Gyr for the inner region of RX J1548.9+0851 suggest that members should have had enough time to virialize within the group potential.

Mass-to-light ratios have been estimated for the RX J1548.9+0851 system in the SDSS  $g'$ ,  $r'$ , and  $i'$  bands by considering the average mass estimates in all three passbands and integrating the best-fit Schechter function over all luminosity bins including the luminosity of the central elliptical. The luminosity fraction of the central elliptical compared to the overall group luminosity budget amounts to  $\sim 30\%$  which is significantly lower than what has been observed for the fossil RX J1340.6+4018 ( $\sim 80\%$ ), most likely due to the presence of BG2. Mass-to-light ratios are not exceptional and show values around  $M/L \sim 100 M_{\odot}/L_{\odot}$ .

Figure 5.8 compares the derived group parameters with the scaling relations for groups and clusters as published in Khosroshahi et al. (2007). Total group luminosities  $L_R$  were estimated with the adequate  $r'$  band data from the integrated Schechter function while X-ray luminosities  $L_X$  were derived from ROSAT count rates as highlighted in Chapter 2. The velocity dispersion estimated from all member galaxies ( $499 \text{ km s}^{-1}$ ) is shown. Concerning the mass of the group, the average of all estimates was considered. To convert the derived mass-to-light-ratio in the  $r'$  band to the corresponding value in  $B$ , the same approach as discussed in Khosroshahi et al. (2007) was utilized. A uniform colour of  $(B - R) = 1.5$  (assuming all satellites to be early-types) was adopted for the whole galaxy population yielding an upper limit in the resulting  $B$ -band mass-to-light ratio. Similarly, a lower limit was estimated by assuming all satellites to be late-types ( $(B - R) = 0.8$ ).

In all diagrams, the RX J1548.9+0851 system is found within the distributions of ordinary groups and clusters showing no exceptional deviations from the published relations. Compared to the fossils studied by Khosroshahi et al. (2007) (black crosses), RX J1548.9+0851 is not as X-ray overluminous with respect to its optical luminosity. However, X-ray luminosities have been derived from low-signal ROSAT count rates which aren't the best quality data to accurately estimate the overall X-ray luminosity of the system. In the remaining panels, RX J1548.9+0851

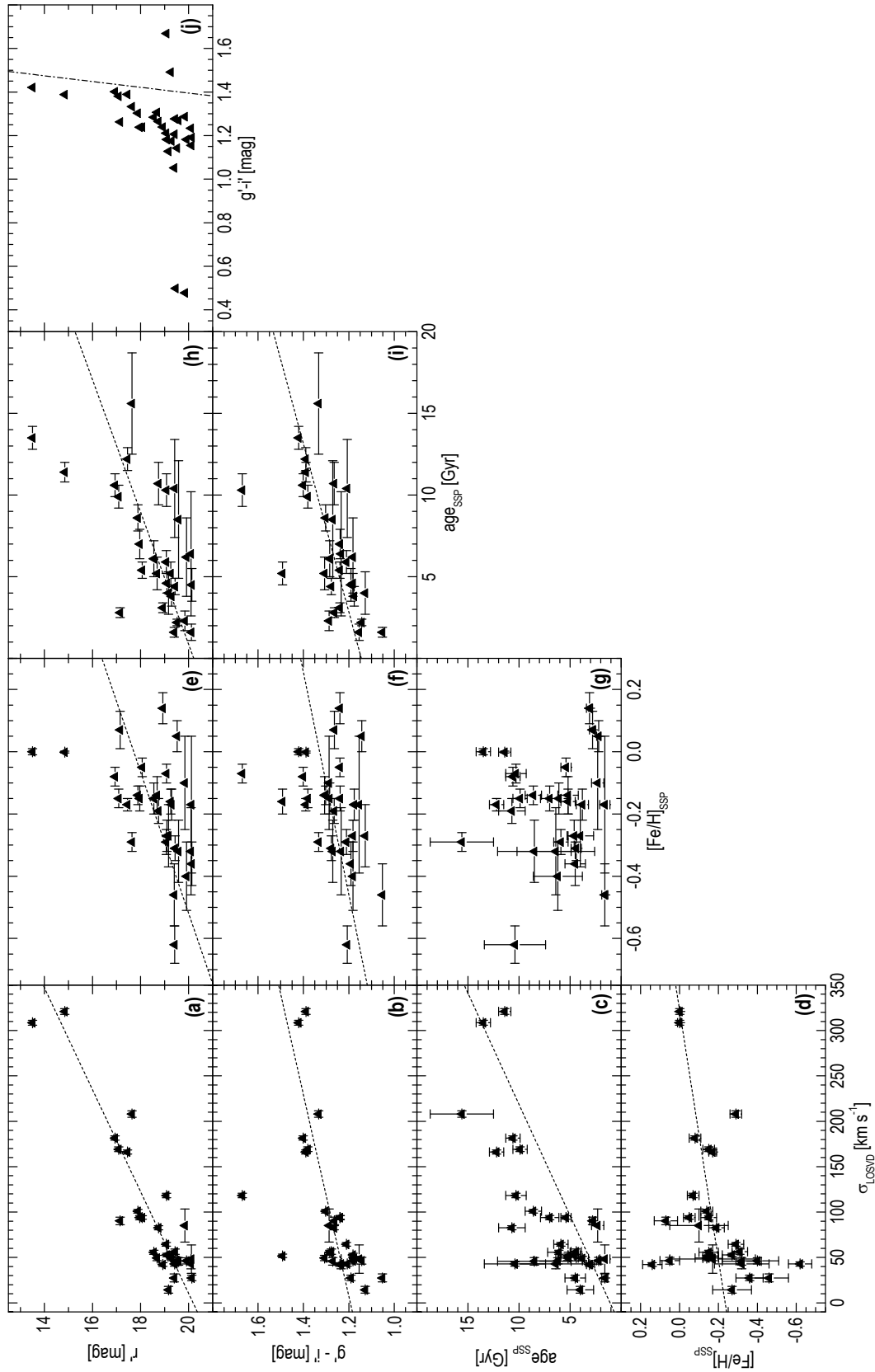


Figure 5.9: Scaling relations for RX J1548.9+0851 group members.

matches the distribution of the Khosroshahi et al. (2007) fossils, showing only a slightly smaller velocity dispersion for given  $R$  band luminosity. The mass-to-light ratio fits nicely in the sequence of published fossils at the upper envelope of the overall group and cluster distribution. Despite the comparatively low X-ray luminosity, RX J1548.9+0851 follows the existing scaling relations for fossils indicating a similar formation scenario.

Figure 5.9 shows scaling relations between brightness, colour, velocity dispersion, age, and metallicity for the investigated RX J1548.9+0851 group members. Dashed lines present linear least squares fits to the data. Panels **a)–d)** relate the galaxy velocity dispersion with the remaining galaxy parameters. The panels clearly show that with increasing velocity dispersion, galaxies tend to be brighter, redder, older, and more metal rich. Panels **e)** and **f)** indicate a slight increase of galaxy brightness and colour with metallicity. No trend is observed when correlating SSP ages with SSP metallicities. Panels **h)** and **i)** show a clear trend between brightness, colour, and age. Especially colour shows a comparatively tight relation with age, only members 39 and 42 in the vicinity of the two brightest ellipticals being systematically redder. Panel **j)** is another view of the system’s red sequence, indicated by the dash-dotted line. Again, only galaxies 39 and 42 lie unambiguously above the red sequence. The presented scaling relations for the galaxy population of the RX J1548.9+0851 system clearly highlight the fact that more massive galaxies (higher velocity dispersion) are redder, brighter, older and more metal rich compared to less massive ones, implying also the observed relations without velocity dispersion (mass). This is plausible since more-massive galaxies, ellipticals, exhibit higher luminosities when assuming a constant mass-to-light ratio, can retain more metals due to their deeper potential wells, and are passively evolving with a dominating old stellar population absent of any young stars dominating the galaxy light in the blue.

## 4 Summary, conclusions and outlook

Utilizing both archival and newly obtained data from the Sloan Digital Sky Survey, the William Herschel Telescope, and the Very Large Telescope, the optical properties of fossil galaxy groups have been studied in the frame of this PhD thesis. New fossil candidates have been identified in the SDSS completing the sample of existing fossil aggregates. Long-slit spectra for a collection of six central ellipticals in fossils (fossil candidates) have been analyzed to investigate the stellar populations of these systems while multi-object spectroscopy was used to study the faint galaxy population of one fossil aggregate. The obtained results have shown that the studied central ellipticals are indeed very old objects, as expected for fossils. However, the performed observations are not able to construct a clear-cut formation scenario for these aggregates. While negative metallicity gradients in the spectra of the studied central ellipticals are consistent with a monolithic formation scenario, the optical appearance of the central elliptical in the RX J1548.9+0851 system supports the scenario described by Dariush et al. (2007), where fossils are formed early by the merger of  $L^*$  galaxies and grow only by minor mergers afterwards.

The low number statistics of a handful of fossils studied in detail in the literature and the scarce sample of unambiguously identified fossils in general make the proper understanding of these systems a difficult task. A clearer picture on the formation and evolution of these aggregates will only emerge when a systematic study on the whole sample of existing fossils will be carried out in long-slit and especially multi-object spectroscopy.

# Appendix **A**

## Publications

On the next pages the conference proceeding Eigenthaler & Zeilinger (2009), published in the frame of the Joint European National Astronomy Meeting (JENAM) 2008 in Vienna, is presented. Two upcoming papers, involving the results from the William Herschel Telescope and the Very Large Telescope presented in this thesis, are in preparation.

## The properties of fossil groups of galaxies

P. Eigenthaler\* and W.W. Zeilinger

Institut für Astronomie, Universität Wien, Türkenschanzstraße 17, A-1180 Wien, Austria

Received 2009 Aug 4, accepted 2009 Sep 14

Published online 2009 Oct 20

**Key words** galaxies: dwarf – galaxies: elliptical and lenticular, cD – galaxies: evolution – galaxies: interactions

Numerical simulations as well as optical and X-ray observations over the last few years have shown that poor groups of galaxies can evolve to what is called a fossil group. Dynamical friction as the driving process leads to the coalescence of individual galaxies in ordinary poor groups leaving behind nothing more than a central, massive elliptical galaxy supposed to contain the merger history of the whole group. Due to merging timescales for less-massive galaxies and gas cooling timescales of the X-ray intragroup medium exceeding a Hubble time, a surrounding faint-galaxy population having survived this galactic cannibalism as well as an extended X-ray halo similar to that found in ordinary groups, is expected. Recent studies suggest that fossil groups are very abundant and could be the progenitors of brightest cluster galaxies (BCGs) in the centers of rich galaxy clusters. However, only a few objects are known to the literature. This article aims to summarize the results of observational fossil group research over the last few years and presents ongoing work by the authors. Complementary to previous research, the SDSS and RASS surveys have been cross-correlated to identify new fossil structures yielding 34 newly detected fossil group candidates. Observations with ISIS at the 4.2 m William Herschel Telescope on La Palma have been carried out to study the stellar populations of the central ellipticals of 6 fossil groups. In addition multi-object spectroscopy with VLTs VIMOS has been performed to study the shape of the OLF of one fossil system.

© 2009 WILEY-VCH Verlag GmbH & Co. KGaA, Weinheim

### 1 Introduction

Redshift surveys have shown that galaxies in the nearby universe are not randomly distributed in space but rather found in aggregates, so called galaxy groups (Geller & Huchra 1983; Tully 1987). Basically galaxy groups can be divided into three major classes that differ mainly in their optical and physical characteristics: poor groups, compact groups, and fossil groups.

Poor or loose groups with a space density of  $\sim 10^{-5} \text{ Mpc}^{-3}$  (Nolthenius & White 1987) resemble simple multiplets of galaxies, represent the most common class and are simply referred to as galaxy groups. They are comprised of approximately 50 members, including numerous dwarf galaxies and take up typical diameters of  $\sim 1.5 \text{ Mpc}$ . Compact groups with a space density of  $\sim 1\text{--}2 \times 10^{-6} \text{ Mpc}^{-3}$  (Hickson 1982) are less abundant and typically made up of only 4 to 5 bright galaxies strongly interacting with each other due to their mutual gravitational attraction causing tidal forces to form tails around closely interacting members. Since today, about 1000 compact groups have been classified (Hickson 1997). Fossil groups are characterised through a dominating central bright elliptical galaxy comparable to cD galaxies in clusters surrounded by a diffuse and extended X-ray halo together with a significant fainter galaxy population. Recent studies have estimated space densities of fossil systems in the local universe to be  $\sim 1\text{--}4 \times 10^{-6} \text{ Mpc}^{-3}$ , comparable to HCGs. Besides the fact

that the vast majority of galaxies in the universe appear to be located in groups, these systems play also a key role in our understanding of galaxy evolution. Since the masses of groups are comparatively small ( $\sim 10^{13} \text{ M}_{\odot}$ ) with respect to the richer clusters ( $\sim 10^{14} \text{ M}_{\odot}$ ), the virial theorem implies lower values for the group velocity dispersions favoring galaxy interactions leading to the coalescence of individual galaxies, galaxy merging.

Numerical simulations have shown that this cannibalism can proceed as long as a single, massive elliptical galaxy remains as final product of multiple merging events (Barnes 1989) on a timescale of a few gigayears. The physical origin behind the merging of galaxies is explained by dynamical friction of the group member galaxies with the group dark-matter halo and acts not for all types of galaxies similarly effective. According to the description of dynamical friction by Chandrasekhar (1943), the friction force is strongly mass dependent leading to longer merging timescales (see Binney & Tremaine 1987, p. 429) for less massive galaxies which therefore should have survived this galactic cannibalism up to now. Moreover, the hot X-ray gas, as found in  $\sim 50\%$  of all known galaxy groups (not correlated with individual group members but rather diffusely distributed following the global gravitational group potential (Mulchaey 2000)) is also expected to be observed in this state of hierarchical galaxy evolution since gas temperatures and electron densities of a typical intragroup medium with  $T \sim 10^7 \text{ K}$  and  $n_e \sim 10^{-3} \text{ cm}^{-3}$  suggest gas cooling timescales  $\tau_{\text{cool}} \propto n_e^{-1} T_g^{1/2}$  exceeding the age of the universe. Thus, one

\* Corresponding author: eigenthaler@astro.univie.ac.at

claims that *fossil groups* represented by a central bright, massive elliptical galaxy surrounded by a diffuse and extended X-ray halo and a fainter galaxy population are the remnants of what was initially a poor group of galaxies that has been transformed to this old, *fossil* stage of galaxy evolution in low density environments with compact groups acting as likely way station in this evolution. If this scenario is correct then the relative space densities of these three different types of systems give information on their transformation rates. Moreover, Jones et al. (2003) assume that fossil systems constitute of probably 8–20% of all systems with comparable X-ray luminosity ( $\geq 10^{42}$  erg s $^{-1}$ ), thus acting also very likely as the site of formation of brightest cluster galaxies (BCGs) before the infall into clusters. Similar optical luminosities of the central ellipticals in fossil groups compared to that of BCGs support this idea. Therefore fossils play a crucial role in our understanding of galaxy evolution in low-density environments and the physical connection between groups and clusters respectively.

The definition of a fossil system as proposed by Jones et al. (2003) was the first real attempt to attribute exact observational characteristics to this class. According to their influential paper a fossil system is a spatially extended X-ray source with an X-ray luminosity from diffuse, hot gas of  $L_{X,\text{bol}} \geq 10^{42} h_{50}^{-2}$  erg s $^{-1}$ . The optical counterpart is a bound system of galaxies with  $\Delta m_{1,2} \geq 2.0$  mag, where  $\Delta m_{1,2}$  is the absolute total magnitude difference in the Johnson *R* band between the two brightest galaxies in the system within half the projected virial radius. No upper limit is given for the X-ray luminosity or temperature. The ideas behind this classification scheme are simple. The lower limit in X-ray luminosity excludes normal bright elliptical galaxies exhibiting a hot coronal gas component. The magnitude gap of  $\Delta m_{1,2} \geq 2.0$  mag for the two brightest galaxies of the group ensures that one single elliptical galaxy dominates the system. Studies of luminosity functions of galaxy groups have shown that this threshold acts as a good criterion to distinguish between poor groups and fossil aggregates since observations have shown that such a high magnitude gap is extremely unlikely to occur in ordinary groups or clusters (Beers et al. 1995).

The first fossil group identified, RX J1340.6+4018, was published in *Nature* (Ponman et al. 1994). Since then, few other objects have been assigned to this class resulting in a catalogue of 15 fossil systems summarized by Mendes de Oliveira et al. (2006).

However, not all listed objects represent what is typically referred to as fossil group since more massive systems with velocity dispersions in the range of 600 km s $^{-1}$ , thus more appropriate to galaxy clusters, are also present (Cypriano et al. 2006; Mendes de Oliveira et al. 2006). More recently, Santos et al. (2007) have cross-correlated optical and X-ray data from the Sloan Digital Sky Survey (SDSS) (Adelman-McCarthy et al. 2008) and the ROSAT All Sky Survey (RASS) (Voges et al. 1999) respectively to identify new fossil group candidates. Their findings comprise a list

**Table 1** Fossil galaxy groups as summarized by Mendes de Oliveira et al. (2006). RX denotations refer to ROSAT X-ray sources.

Name	$\alpha_{2000}$	$\delta_{2000}$	$z$	$L_{X,\text{bol}}^a$
NGC 1132	02 52 51.8	-01 16 29	0.023	1.9
RX J0454.8-1806	04 54 52.2	-18 06 56	0.031	1.9
ESO 306-G 017	05 40 06.7	-40 50 11	0.036	129
RX J1119.7+2126	11 19 43.7	+21 26 50	0.061	1.7
RX J1159.8+5531	11 59 51.4	+55 32 01	0.081	22
CL 1205+44	12 05 53.7	+44 29 46	0.59	180
RX J1256.0+2556	12 56 03.4	+25 56 48	0.232	61.
RX J1331.5+1108	13 31 30.2	+11 08 04	0.081	5.9
RX J1340.6+4018	13 40 33.4	+40 17 48	0.171	25
RX J1416.4+2315	14 16 26.9	+23 15 32	0.137	220.
RX J1552.2+2013	15 52 12.5	+20 13 32	0.136	63
NGC 6034	16 03 32.1	+17 11 55	0.034	0.75
NGC 6482	17 51 48.8	+23 04 19	0.013	2.17
RX J2114.3-6800	21 14 20.4	-68 00 56	0.130	20
RX J2247.4+0337	22 47 29.1	+03 37 13	0.199	41

<sup>a</sup> Bolometric X-ray luminosity taken in  $10^{42} h_{50}^{-2}$  erg s $^{-1}$ .

of 34 candidates, ranging up to  $z = 0.489$ . The majority of all known 49 systems ( $\sim 86\%$ ) resides in the northern celestial hemisphere whereas only 7 objects ( $\sim 14\%$ ) have been identified in the southern one. The nearest fossil group was identified with the elliptical NGC 6482 at a redshift of  $z = 0.013$  (Khosroshahi et al. 2004) while the most distant fossil aggregate was found at  $z = 0.59$  combining HST, Chandra and XMM-Newton data (Ulmer et al. 2005, see Fig. 1).

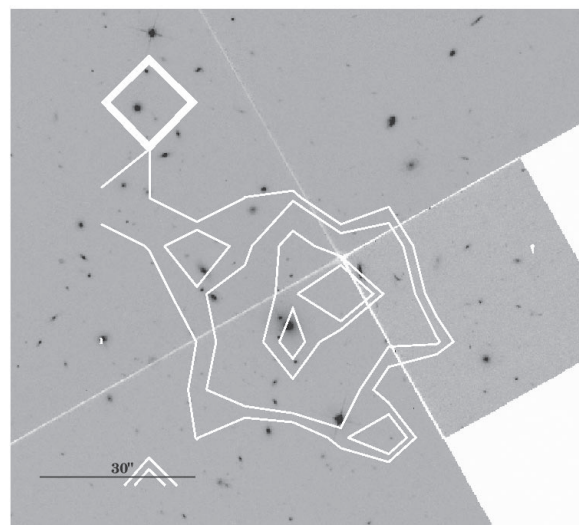


**Fig. 1** F702W HST image of Cl1205+44, the most distant fossil group known. Chandra contours in the range 0.5–8 keV indicate the diffuse and extended X-ray gas component. North is up, East is to the left. Taken from Ulmer et al. (2005).

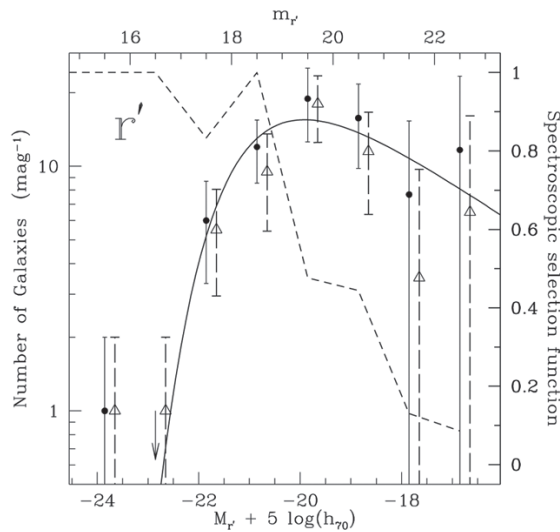


**Fig. 2** Luminosity function of the fossil cluster RX J1552.2+2013 in the SDSS  $r'$  band. Solid circles show the completeness-corrected number of spectroscopically confirmed members while triangles show photometrically determined members estimated through number counts and statistical background subtraction. The dotted line represents a selection function of the spectroscopic sample while the continuous line shows the best Schechter fit to the spectroscopic sample excluding the brightest galaxy. A clear dip in the LF can be found around  $M_{r'} = -18$ . Taken from Mendes de Oliveira et al. (2006).

## 2 The properties of fossil groups

Since the catalogue of known fossil aggregates is only made up of a few objects, an analysis of the optical or X-ray properties of fossil groups has only been carried out for a few systems leaving the formation process of this special class of objects still unclear. This section highlights some of the results that have been obtained over the last few years.

### 2.1 The luminosity function of fossil galaxy groups

The optical luminosity function (OLF) of fossil groups exhibits a lack of bright galaxies (by definition since fossil systems are characterised as low-density environments with no bright galaxies besides the central elliptical). Thus, the bright end of the OLF of these systems is unusual compared to what is normally observed in poor groups, with too few  $L^*$  galaxies present. Few effort has been made so far to study the shape of the OLF at fainter magnitudes. Existing studies focusing on the fainter part of the OLF of fossil galaxy groups have only investigated three fossil systems. Surprisingly, all these aggregates are rather classified as fossil clusters than groups due to their relatively large velocity dispersions ( $623 \text{ km s}^{-1}$ ,  $584 \text{ km s}^{-1}$ , and  $565 \text{ km s}^{-1}$ ) (Cypriano et al. 2006; Mendes de Oliveira et al. 2006; Mendes de Oliveira et al. 2009). Interestingly, be-

sides the expected magnitude gap around  $L^*$  galaxies, a dip in the OLF of RX J1552.2+2013 at the transition to dwarf galaxies at  $M_{r'} = -18$  has been found (see Fig. 2). Such dips in the OLFs have been observed in several systems, mostly dense, dynamically well-evolved aggregates such as X-ray emitting cD clusters (Valotto et al. 2004) or compact groups of galaxies (Hunsberger et al. 1996), suggesting that there may be more than one mechanism driving the depletion of galaxies in these different environments. Assuming the merger scenario hypothesis from hierarchical galaxy evolution models, the lack of  $L^*$  galaxies is explained by dynamical friction, resulting in a deceleration of the orbital velocity of a galaxy which loses its kinetic energy to the surrounding dark matter particles, and subsequent merging. The same physical processes cannot be efficient enough to reproduce the comparatively small number of low-mass galaxies around  $M_R = -18$ . One explanation for these missing galaxies could be a succession of tidal encounters (Gnedin 2003). If this scenario is correct, one would not expect such a dip in the luminosity functions for less rich galaxy aggregates than the observed fossil cluster, since the galaxy density and thus the tidal stripping efficiency is much lower in these systems. However, RX J1416.4+2315 and RXJ1340.6+4018 do not show any evidence of a dip in the OLF around  $M_R = -18$ , suggesting that the scenario of fossil group formation is far more complicated than expected. More studies focusing on multi-object spectroscopy of the faint-galaxy population in fossil groups or fossil systems in general is therefore needed.

### 2.2 Masses and mass-to-light ratios of fossil groups

The symmetric and regular X-ray emission together with the lack of  $L^*$  galaxies and the large early-type fraction observed in fossil groups suggest that these systems are old, evolved systems. Thus, from a dynamical point of view, fossil groups should present relaxed, virialized galaxy aggregates. The dynamical properties of the faint-galaxy population of fossil systems studied so far show that the radial velocity distributions exhibit far too high velocity dispersions to be considered as remnants of what was initially a poor group of galaxies and are fairly well fit by a Gaussian velocity distribution, indicating relaxed systems. It is feasible to estimate the masses of fossil groups from the gas density and temperature profiles of the extended X-ray gas component assuming the gas distribution to be spherically symmetric and in hydrostatic equilibrium. Then the total gravitational mass is given by

$$M_{\text{grav}}(< r) = -\frac{kT(r)r}{G\mu m_p} \left[ \frac{d \ln \rho(r)}{d \ln r} + \frac{d \ln T(r)}{d \ln r} \right], \quad (1)$$

where  $\mu$  is the mean molecular weight and  $m_p$  the proton mass. X-ray studies confirm the high masses derived from the dynamical state of these systems, showing that the intragroup medium of a number of fossil groups is similar to those of galaxy clusters with temperatures exceeding even 4 keV for some aggregates. These results are inconsistent



with the idea that fossil groups are the remains of galactic cannibalism in ordinary groups. Complementary, Yoshioka et al. (2004) has shown that the  $M/L$  ratios of four fossil groups reach up to  $M/L_B = 1100 M_\odot/L_\odot$  being at least one order of magnitude higher than the typical  $M/L$  ratios for groups and clusters of comparable mass supporting the idea that it is unlikely that these systems are the remnants of regular groups and clusters. Other recent studies derive much lower values of  $M/L$ , however (e.g. Sun et al. 2004), showing that a general formation scenario for fossil systems is far from understood and further observations in both optical and X-rays are needed to get reliable mass estimates for a higher number of fossil aggregates and to see if all fossil structures resemble cluster-like systems rather than groups.

### 2.3 Surface brightness profiles of the central ellipticals

The shape of the surface brightness profiles of ellipticals are known to depend on the formation histories of these systems and can thus act as indicators for different imaginable evolution tracks. More precisely, dissipationless merger simulations from Naab & Burkert (2003) have shown that unequal-mass mergers lead to fast rotating, discy ellipticals, while equal mass mergers produce slowly rotating, pressure supported systems. Major mergers between bulge dominated systems result in boxy ellipticals, independent of the mass ratio while merger remnants that subsequently accrete gas are always discy. More recently, it has been shown that the mergers of spiral galaxies alone cannot reproduce the kinematic and photometric properties of very massive ellipticals (Naab, Khochfar & Burkert 2006) nor can they reproduce the observed correlation between isophotal shapes and the luminosity of ellipticals. Khoshroshahi et al. (2006) have investigated the profile shapes of the central ellipticals in seven fossil systems with the conclusion that the isophote shapes of ellipticals in fossil groups are different compared to the brightest central galaxies in non-fossil systems, especially rich clusters. Luminous elliptical galaxies in non-fossil systems do not present discy isophotes (Kormendy & Bender 1996). In contrast, the brightest ellipticals in fossil groups show discy and boxy isophotes in similar proportions. If the central ellipticals in groups have indeed formed via the merging of all other major galaxies, then some of these merging events would have been gas rich, since groups are known to consist of a large spiral fraction. The discy characteristics of central ellipticals in fossil groups would then be consistent with numerical simulations, that discy isophotes result from gas-rich mergers. The difference in the observed isophote shapes of fossil group central galaxies and the brightest cluster galaxies does not rule out the possible evolutionary link of infalling pre-processed merged ellipticals from groups in clusters, however. This could still be the case if these ellipticals have undergone later gas-free mergers within the cluster environment. Moreover, about 40% of the brightest cluster galaxies exhibit at least one secondary nucleus, strongly supporting the idea of late mergers within the cluster environment. Further investigation of the

isophote shape characteristics of central ellipticals in fossil groups will help to confirm or question the existing results and will shed more light on the evolution of fossil group central ellipticals and possible connection to the brightest cluster galaxies.

### 2.4 Scaling relations in fossil groups

The first study of the scaling properties of fossil groups compared to ordinary groups and clusters was carried out by Khoshroshahi et al. (2007). Based upon Chandra X-ray observations as well as optical imaging and spectroscopy this study comprised the information of seven fossil groups showing regular, symmetric X-ray emission, indicating no recent mergers. Scaling relations focusing on the total gravitational mass, X-ray temperature, X-ray luminosity, group velocity dispersion and the optical luminosity were studied. For a given optical luminosity of the whole group, fossil systems turn out to be more X-ray luminous than non-fossil groups. Focusing on the  $L_X-T_X$  relation, fossils cannot be distinguished from ordinary groups or clusters, however. Fossils also show that for a given group velocity dispersion, X-ray luminosity and temperature are higher compared to non-fossil systems. The  $M_X-T_X$  relation suggests that fossils are hotter, for a given total gravitational mass, consistent with an early formation epoch.

## 3 The search for new fossil group candidates

Complementary to the previous work on fossil groups as highlighted in Sect. 2, the attempt to identify new fossil structures was made by the authors. This undertaking seems reasonable since the space densities of fossil groups determined so far suggest that these systems are as abundant as Hickson compact groups while the actual catalogue comprises only a negligible fraction compared to HCGs. The  $\Lambda$ CDM concordance model ( $\Omega_m = 0.3$ ,  $\Omega_\Lambda = 0.7$ ,  $H_0 = 70 \text{ km s}^{-1} \text{ Mpc}^{-1}$ ) was used throughout this work. Luminosity distances  $D_L$  and angular diameter distances  $D_A$  have been calculated via the ‘Cosmology Calculator’ (Wright 2006). In order to identify new fossil group candidates, the Sloan Digital Sky Survey and Rosat All Sky Survey have been cross-correlated to shortlist candidates of interest that meet the classification criteria as proposed by Jones et al. (2003). The query was defined via Structured Query Language (SQL). A similar approach has been carried out by Santos et al. (2007) focusing on different selection criteria, however. The query presented here focuses on intrinsically bright  $M_{r'} \leq -21 + 5 \log h$ ,  $\text{red } g' - r' > 0.8$  galaxies relating to ellipticals. The lower limit in absolute magnitude was ensured by calculating the corresponding apparent magnitudes via luminosity distances  $D_L$  derived from the SDSS spectroscopic redshifts of the central ellipticals,

$$m < M + 25 + 5 \log \left[ \frac{D_L}{h^{-1} \text{ Mpc}} \right] + A + K(z), \quad (2)$$

accounting for galactic extinction  $A$  and  $K$  correction too. Only galaxies with an entry in the SDSS ROSAT table were considered for the further shortlisting of fossil group candidates. The associated X-ray component had to be extended with a ROSAT extent parameter of at least one arcsecond. This value does not reflect the true extent of the X-ray source but gives the excess over the ROSAT point-spread function. Furthermore the distance of the ROSAT source had to be less than 100 kpc from the central elliptical accounting also for the ROSAT position error. The SQL code is given in Appendix A. The resulting sample was finally shortlisted via the 2 mag criterion forcing all systems to have no galaxies with  $\Delta m_{1,2} \geq 2.0$  mag in the SDSS  $r'$  band within one-half virial radius. In contrast to the work of Santos et al. (2007) who use a constant value of  $0.5h^{-1}$  Mpc for half the virial radius, the description of Evrard et al. (1996),

$$r_{\text{vir}} = 1.945 \left( \frac{T}{10 \text{ keV}} \right)^{1/2} (1+z)^{-3/2} h^{-1} \text{ Mpc}, \quad (3)$$

as used by Jones et al. (2003) was applied here assuming a lower limit of the X-ray temperature of fossil groups of 0.7 keV. The 2 mag criterion was accounted for via an SDSS SQL function (see Appendix A). The remaining objects were checked for morphology. Five galaxies were identified as spirals while three objects have been found in the vicinity of bright stars. These systems have been excluded from the sample leaving a final list of 34 previously nondetected fossil group candidates. The query also re-identified objects listed in the Santos et al. (2007) sample. However, many objects could not be re-identified since the procedure used here excludes all galaxies within half the virial radius not taking into account possible background galaxies, thus eliminating possible fossil group candidates that would pass the 2 mag criterion if group memberships were known. This indicates that there might be far more fossil candidates in our query when accounting also for group memberships via photometric redshifts. Table 3 gives coordinates as well as SDSS and ROSAT identifications of the new fossil group candidates. Table 4 presents the most important properties of the fossil group central ellipticals as well as the associated ROSAT X-ray component. Figure 5 shows a colour-magnitude diagram of the newly found fossil group central ellipticals as well as the Santos et al. (2007) sample. The symbol size indicates the prominence of the associated X-ray source, visualizing the ROSAT extent/ $\Delta$  ratio as presented in Table 4. Arrows point to galaxies that have been observed with the William Herschel Telescope (WHT) and the Very Large Telescope (VLT). In order to get a glimpse on the optical luminosity function (OLF) of the newly detected fossil group candidates, SDSS photometric and spectroscopic redshifts, when available, have been used to estimate group memberships and construct an OLF for all systems. Some of the OLFs confirm the lack of faint galaxies as previously observed by Mendes de Oliveira et al. (2006) while most of the systems don't show a dip in the OLF at fainter magnitudes. Figure 4 presents the photometrically selected OLF of RX

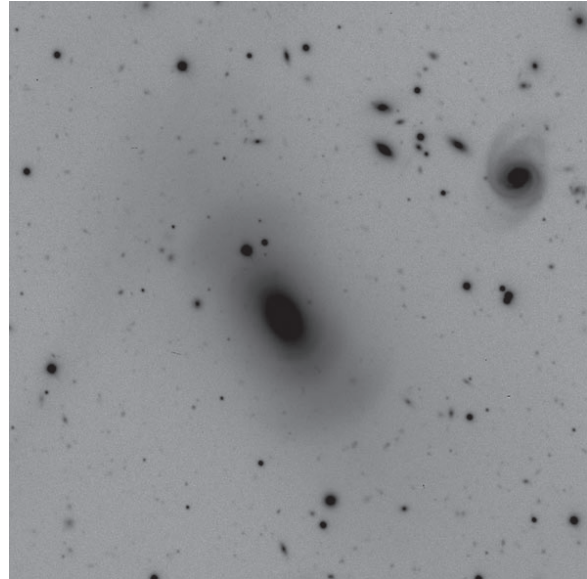


**Fig. 3** VIMOS PRE-IMG of the fossil group candidate RX J1548.9+0851 from the Santos et al. (2007) sample. The bright spiral shows a redshift difference of  $\Delta z \sim 0.008$  to the central elliptical and doesn't violate the 2 mag criterion. Shells can be clearly seen around the elliptical which suggest multiple past merging events that would confirm the status of RX J1548.9+0851 as a fossil group. North is up, east is to the left. The field of view is  $\sim 2$  arcmin on a side.

J1520.9+4840 from the new list of fossil aggregates. A clear dip in the OLF is visible around  $M_i' = -18$ . It has to be kept in mind, however, that this result is based upon photometric redshifts which exhibit far larger errors than spectroscopic measurements necessitating the use of multi-object spectroscopy of the faint galaxy population to confirm the lack of faint galaxies in fossil galaxy groups.

## 4 Observations

Table 2 summarizes the observations at the WHT and VLT that have been carried out to complement the existing data on fossil groups. Long-slit spectra have been obtained with the ISIS spectrograph at the WHT to measure Lick-IDS indices (Worthey et al. 1994) of the central ellipticals from both the new sample as well as fossil groups from the literature. These measurements will yield radial profiles of ages and metallicities of the central elliptical stellar populations that are supposed to contain the merger history of the whole group. It is then feasible to study how uniform the process of coalescence occurred in these systems and if fossil group central ellipticals are indeed the progenitors of brightest cluster galaxies (BCGs) or show similar stellar populations as found in non BCGs. In addition, VIMOS observations in service mode have been carried out at VLT UT3 Melipal to study the OLF of one fossil aggregate. Spec-

trosopic targets have been selected via SDSS magnitudes to determine the OLF down to  $i' \sim 20$  corresponding to  $M_{i'} \sim -17$ . This magnitude limit ensures to identify a dip in the OLF around  $M_{i'} \sim -18$  if present. Figure 3 shows the VIMOS pre-image of the central elliptical of the fossil group candidate RX J1548.9+0851. The image reveals shells around the central elliptical that would confirm the idea of the system being the remainder of multiple merging events. The acquired data from the WHT and the VLT will shed more light on the formation process of fossil groups of galaxies complementing the few optical studies that have been carried out so far.

*Acknowledgements.* Paul Eigenthaler is supported by the University of Vienna in the frame of the Initiative Kolleg (IK) 'The Cosmic Matter Circuit' I033-N.

## References

- Adelman-McCarthy, J., et al.: 2008, ApJS 175 , 297  
 Barnes, J.E.: 1989, Nature 338 , 123  
 Beers, T. et al.: 1995, AJ 109 , 874  
 Binney, J., Tremaine, S.: 1987, *Galactic Dynamics*, Princeton University Press, Princeton  
 Chandrasekhar, S.: 1943, ApJ 97 , 255  
 Cypriano, E.S., et al.: 2006, AJ 132 , 514  
 Evrard, A.E., et al.: 1996, ApJ 469 , 494  
 Gnedin, O.Y.: 2003, ApJ 589 , 752  
 Geller, M.J., Huchra, J.P.: 1983, ApJS 52 , 61  
 Hickson, P.: 1982, ApJ 255 , 382  
 Hickson, P.: 1997, ARA&A 35 , 357  
 Hunsberger, S.D., et al.: 1996, ApJ 462 , 50  
 Jones, L.R., et al.: 2003, MNRAS 343 , 627  
 Kalberla, P., et al.: 2005, A&A 440 , 775  
 Khosroshahi, H.G., et al.: 2004, MNRAS 349 , 1240  
 Khosroshahi, H.G., et al.: 2006, MNRAS 372 , 68  
 Khosroshahi, H.G., et al.: 2007, MNRAS 377 , 595  
 Kormendy, J., Bender, R.: 1996, ApJ 464 , 119  
 Mendes de Oliveira, C., et al.: 2006, AJ 131 , 158  
 Mendes de Oliveira, C., et al.: 2009, AJ 138 , 502  
 Mukai, K.: 1993, Legacy 3 , 21  
 Mulchaey, J.S.: 2000, ARA&A 38 , 289  
 Naab, T., Burkert, A.: 2003, ApJ 597 , 893  
 Naab, T., Khochfar, S., Burkert, A.: 2006, ApJ 636 , 81  
 Nolthenius, R., White, S.: 1987, MNRAS 225 , 505  
 Ponman, T.J., et al.: 1994, Nature 369 , 462  
 Santos, W.A., et al.: 2007, AJ 134 , 1551  
 Sun, M., et al.: 2004, ApJ 612 , 805  
 Tully, R.B.: 1987, ApJ 321 , 280  
 Ulmer, M.P., et al.: 2005, ApJ 624 , 124  
 Valotto, C.A., et al.: 2004, ApJ 603 , 67  
 Vikhlinin, A., et al.: 1999, ApJ 520 , 1  
 Voges, W., et al.: 1999, A&A 349 , 389  
 Worthey, G., et al.: 1994, ApJS 94 , 687  
 Wright, E.L.: 2006, PASP 118 , 1711  
 Yoshioka, T., et al.: 2004, AdSpR 34 , 2525

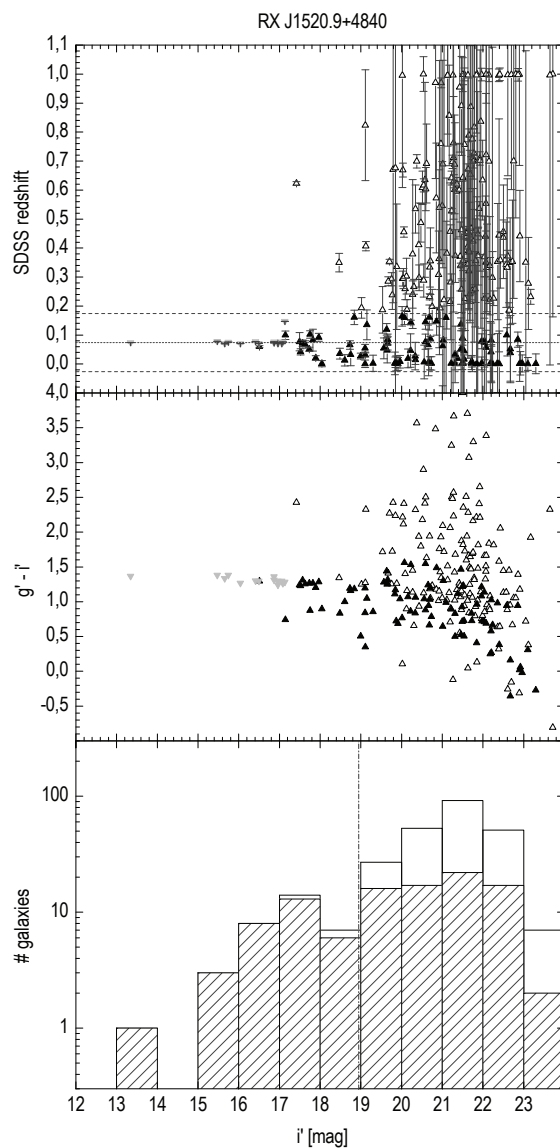


**Fig. 4** Photometrically determined optical luminosity function of the fossil group candidate RX J1520.9+4840 from the new sample. All objects in the SDSS classified as galaxies within one-half virial radius are plotted. *Upper panel*: open and black triangles represent SDSS photometric redshifts while gray triangles indicate SDSS spectroscopic redshifts. The dotted line indicates the spectroscopic redshift  $z$  of the central elliptical, while dashed lines at  $z \pm \Delta z$  ( $\Delta z = 0.1$ ; SDSS photometric redshift uncertainty) indicate borders for group membership. *Middle panel*: colour-Magnitude Diagram of the investigated galaxy population. Galaxies exhibiting adequate photometric redshifts for group membership follow a red sequence as observed in ordinary groups. *Lower panel*: photometrically-determined luminosity function. Blank histograms show all galaxies while dashed ones indicate objects within  $z \pm \Delta z$ . The dash dotted line corresponds to  $M_{i'} = -18$ . A dip in the photometrically selected OLF around  $M_{i'} = -18$  is clearly visible.

**Table 2** Fossil systems observed with the WHT and the VLT.

Galaxy	$\alpha_{2000}$	$\delta_{2000}$	Exposure [s]	Resolution [ $\text{\AA}$ pix $^{-1}$ ]		Date
William Herschel Telescope <sup>a</sup>						
				Blue	Red	
RX J0752.7+4557	07 52 44.2	+45 56 57.4	3×3000	0.86	0.26	20.12.2008
RX J0844.9+4258	08 44 56.6	+42 58 35.7	3×3000	0.86	0.26	20.12.2008
NGC 1132	02 52 51.8	−01 16 28.8	4×2700	0.86	0.26	20.12.2008
RX J1548.9+0851	15 48 55.9	+08 50 44.4	3×2600	0.86	0.93	28.04.2009
RX J1520.9+4840	15 20 52.3	+48 39 38.6	3×2600	0.86	0.93	28.04.2009
RX J1152.6+0328	11 52 37.6	+03 28 21.8	3×2700	0.86	0.93	28.04.2009
Very Large Telescope <sup>b</sup>						
RX J1548.9+0851	15 48 55.9	+08 50 44.4	4500	0.51		26.05.2009

<sup>a</sup> Observations carried out in Visitor Mode.<sup>b</sup> Observations carried out in Service Mode. The date refers to the completion of the last Observing Block (OB) for the given target.**Table 3** Fossil group candidates: ROSAT and SDSS identifications.

ID Number	ROSAT Name	SDSS $\alpha_{2000}$ <sup>a</sup>	SDSS $\delta_{2000}$ <sup>a</sup>	SDSS Objid
(1)	(2)	(3)	(4)	(5)
01.....	RXJ0159.8−0850	01 59 49.3	−08 49 58.8	587727884161581256
02.....	RXJ0725.7+3741	07 25 41.3	+37 40 27.7	587737826206482926
03.....	RXJ0730.3+3728	07 30 20.4	+37 27 40.8	587725775602450780
04.....	RXJ0801.0+3603	08 00 56.8	+36 03 23.6	587728905564258619
05.....	RXJ0825.9+0415	08 25 57.8	+04 14 48.3	587732702851170810
06.....	RXJ0826.9+3108	08 26 57.6	+31 08 04.9	587732469849325635
07.....	RXJ0909.9+3106	09 09 53.3	+31 06 03.2	588016878295318532
08.....	RXJ1005.8+1058	10 05 50.7	+10 58 11.7	587734949665243313
09.....	RXJ1006.1+0710	10 06 08.3	+07 10 29.5	587732579379904650
10.....	RXJ1030.5+1416	10 30 34.8	+14 15 41.8	587735349637349534
11.....	RXJ1041.8+5303	10 41 47.6	+53 03 41.4	587733081343656013
12.....	RXJ1055.1+4246	10 55 06.6	+42 45 24.4	588017626148634721
13.....	RXJ1056.1+0252	10 56 06.6	+02 52 13.5	587726033315299465
14.....	RXJ1107.4+1245	11 07 24.2	+12 44 20.0	588017567629509093
15.....	RXJ1115.9+0130	11 15 51.9	+01 29 55.1	587728307491897590
16.....	RXJ1128.6+3530	11 28 34.4	+35 30 14.0	587739305286238362
17.....	RXJ1152.6+0328	11 52 37.6	+03 28 21.8	587726033858330762
18.....	RXJ1211.1+3520	12 11 08.3	+35 19 58.8	587739304216232052
19.....	RXJ1327.1+0212	13 27 01.0	+02 12 19.5	587726015078465728
20.....	RXJ1349.9+4217	13 49 51.1	+42 16 47.8	588017604154687567
21.....	RXJ1352.0+6105	13 51 58.3	+61 04 19.0	588011219135889619
22.....	RXJ1353.4+4424	13 53 20.3	+44 24 19.8	588298662507184284
23.....	RXJ1402.8+3431	14 02 46.6	+34 31 08.0	587739131880603717
24.....	RXJ1431.3−0054	14 31 21.2	−00 53 44.3	588848898855469518
25.....	RXJ1450.2+4134	14 50 08.3	+41 33 59.8	588017116130246662
26.....	RXJ1453.6+0359	14 53 38.5	+03 59 33.4	587726101487747355
27.....	RXJ1501.3+5455	15 01 18.0	+54 55 18.3	588011101565354082
28.....	RXJ1520.9+4840	15 20 52.3	+48 39 38.6	587735666921898155
29.....	RXJ1539.8+4143	15 39 51.4	+41 43 25.4	587733397568356378
30.....	RXJ1540.4+3622	15 40 23.0	+36 21 56.6	587736751928770630
31.....	RXJ1624.7+3727	16 24 43.4	+37 26 42.4	587735666392105305
32.....	RXJ1653.1+3909	16 53 07.8	+39 08 53.1	588007005270966692
33.....	RXJ1717.1+2931	17 17 06.9	+29 31 21.1	587729408084935169
34.....	RXJ2139.5−0722	21 39 28.5	−07 21 46.6	587726878878728621

<sup>a</sup> Right ascension is given in hours, minutes, and seconds and declination is given in degrees, arcminutes, and arcseconds.

**Table 4** Fossil group candidates: properties of the central elliptical and the associated X-ray component.

ID Number (1)	Central Elliptical Galaxy					ROSAT X-Ray Properties			
	Redshift <sup>a</sup> (2)	$i'$ <sup>a</sup> [mag] (3)	$g' - i'$ <sup>a</sup> [mag] (4)	$M_{i'}$ <sup>a</sup> [mag] (5)	$\frac{1}{2}r_{\text{vir}}$ <sup>b</sup> [arcmin] (6)	$\Delta$ <sup>c</sup> [arcsec] (7)	Extent <sup>c</sup> [arcsec] (8)	extent/ $\Delta$ <sup>c</sup> (9)	$L_X$ (0.5–2 keV) <sup>d</sup> [erg s <sup>-1</sup> ] (10)
01	0.405	17.29	2.00	-24.37	0.680	12.8	44	3.44	8.42E+44
02	0.425	17.34	2.58	-24.56	0.647	42.8	56	1.31	1.84E+44
03	0.200	17.58	1.69	-22.04	1.411	21.8	40	1.83	6.29E+43
04	0.287	16.13	2.23	-24.30	0.970	35.5	47	1.33	3.85E+44
05	0.225	15.81	2.01	-24.31	1.249	21.4	21	0.98	1.51E+44
06	0.209	15.26	1.92	-24.43	1.346	52.1	76	1.46	1.25E+44
07	0.272	16.57	1.20	-23.65	1.026	9.2	22	2.39	6.65E+44
08	0.162	15.15	1.68	-24.10	1.755	7.4	85	11.45	4.58E+43
09	0.202	17.25	1.35	-22.39	1.394	48.9	22	0.45	1.89E+43
10	0.317	16.23	2.31	-24.49	0.875	26.1	61	2.34	2.07E+44
11	0.187	16.52	1.71	-22.59	1.517	28.2	13	0.46	1.97E+43
12	0.371	18.57	1.48	-23.05	0.744	7.2	17	2.36	1.00E+44
13	0.236	17.60	1.28	-22.27	1.189	6.1	19	3.12	1.03E+45
14	0.420	17.93	2.46	-23.12	0.655	15.8	9	0.57	1.19E+44
15	0.352	17.19	2.03	-24.26	0.786	22.5	57	2.54	7.30E+44
16	0.402	17.59	2.52	-23.59	0.685	15.6	12	0.77	3.02E+44
17	0.081	14.25	1.38	-23.06	3.600	27.4	71	2.59	1.08E+43
18	0.136	15.14	1.58	-23.52	2.097	35.8	52	1.45	4.11E+43
19	0.260	16.26	2.16	-24.11	1.075	40.5	58	1.43	2.30E+44
20	0.289	17.67	1.92	-22.77	0.964	8.2	19	2.30	1.08E+44
21	0.323	17.32	2.34	-23.47	0.858	23.2	6	0.26	3.61E+43
22	0.152	17.03	1.37	-21.48	1.873	24.1	9	0.37	1.23E+43
23	0.175	17.14	1.31	-22.61	1.619	6.7	10	1.49	1.28E+43
24	0.403	17.49	2.70	-23.80	0.684	43.1	52	1.21	2.27E+44
25	0.157	14.89	1.65	-24.02	1.818	35.9	54	1.50	2.24E+43
26	0.370	16.82	2.35	-24.24	0.746	36.1	42	1.16	2.33E+44
27	0.339	17.24	1.83	-23.63	0.818	7.3	15	2.05	1.54E+44
28	0.074	13.35	1.37	-24.12	3.933	31.4	71	2.26	4.35E+43
29	0.119	14.83	1.55	-23.96	2.404	10.3	12	1.17	7.06E+42
30	0.231	16.53	1.76	-23.35	1.213	27.7	11	0.40	2.63E+43
31	0.199	16.89	1.79	-23.99	1.417	12.1	13	1.08	2.97E+43
32	0.147	15.70	1.64	-23.14	1.945	33.0	19	0.58	1.40E+44
33	0.278	16.95	1.68	-22.12	1.003	4.2	30	7.08	6.92E+44
34	0.410	17.58	2.50	-23.88	0.672	26.3	20	0.76	1.53E+44

<sup>a</sup> Redshifts and magnitudes are taken from the SDSS DR 6.

<sup>b</sup> Half the virial radius given in arcminutes. The virial radius was estimated via  $r_{\text{vir}} = 1.945 \left(\frac{T}{10 \text{ keV}}\right)^{1/2} (1+z)^{-3/2} h^{-1} \text{ Mpc}$  as used in Jones et al. (2003). For the X-ray temperature a lower limit of 0.7 keV was assumed.

<sup>c</sup> ROSAT  $\Delta$  and extent parameters.  $\Delta$  gives the distance of the X-ray source to the central elliptical. Extent gives the excess of the detected X-ray source over the ROSAT PSF. The ratio extent/ $\Delta$  indicates the prominence of the X-ray source with larger values indicating more extended sources close to the central elliptical.

<sup>d</sup> ROSAT X-ray luminosities. ROSAT countrates have been converted to X-ray fluxes via the tool PIMMS (Mukai, 1993) assuming a Raymond-Smith model with 2 keV and a metallicity of  $Z = 0.4 Z_{\odot}$ . H I column densities of the Leiden/Argentine/Bonn (LAB) Survey of Galactic H I (Kalberla et al. 2005) were taken into account to determine extinction-free fluxes.

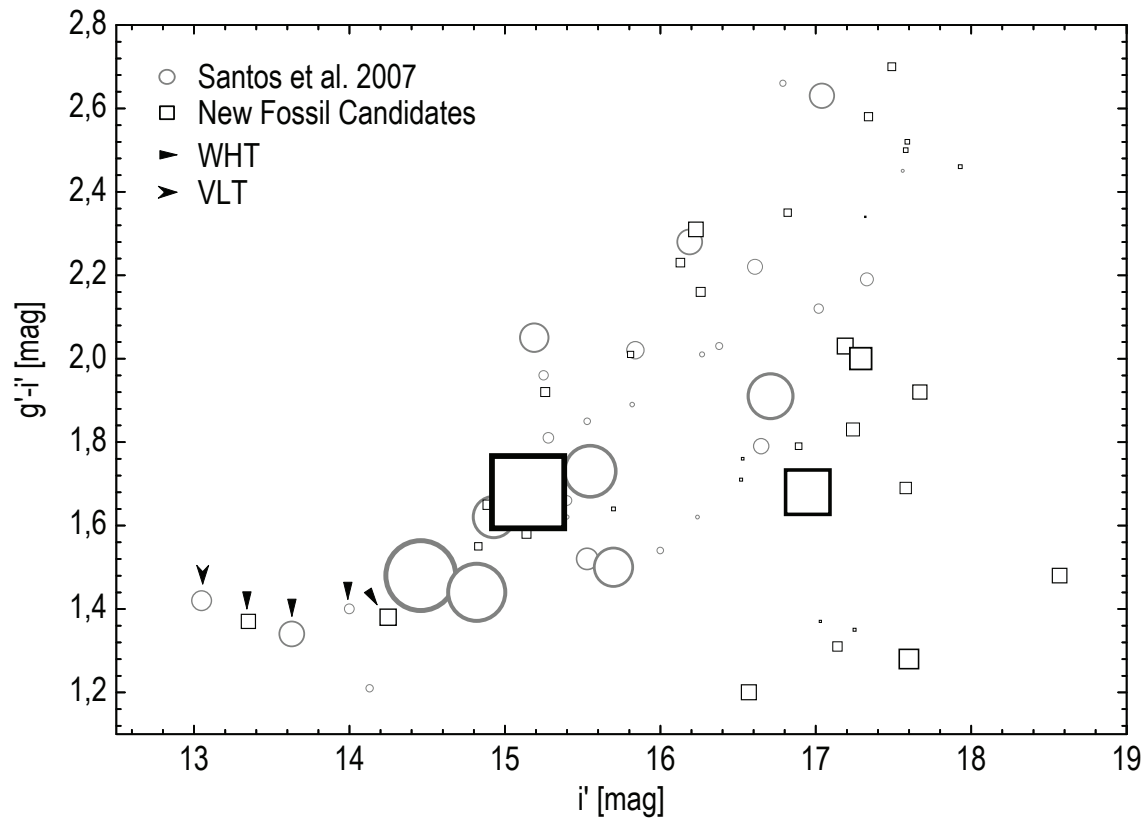


**Fig. 5** Colour-magnitude diagram for the central elliptical galaxies of fossil structures identified in the SDSS. Circles show the list of Santos et al. (2007) while squares represent new structures identified by the authors. The arrows point to objects that have been observed with the WHT and the VLT by the authors. The size of the symbols indicates the extent/ $\Delta$  ratio as presented in Table 4.

## A SQL Query

SQL query used within SDSS DR6 to select the fossil group candidates listed in Table 3.

```
SELECT p.objid, s.z, p.ra, p.dec, p.r, p.g-p.r, r.delta, r.cps, r.cpserr, r.extent
FROM specobj s, photoobj p, rosat r
WHERE s.bestobjid= p.objid
```

Selection of objects that have been spectroscopically classified as galaxies with  $z \leq 0.5$  and show an entry in the SDSS ROSAT table.

```
AND s.specclass = 2
AND p.objid= r.objid
AND s.z BETWEEN 0.0 AND 0.50
```

Selection of bright ( $M_r' \leq -21 + 5 \log h$ ), red ( $g' - r' > 0.8$ ) galaxies via the relation:  $m < M + 25 + 5 \log (D_L[\text{Mpc}] \cdot h) + A + K(z)$ <sup>1</sup>

```
AND p.r <
-21.0
+ 25 + 5*LOG10 ((-0.15958 + 4290.00033 *s.z + 3255.86186 *s.z*s.z - 1009.42877 *s.z*s.z*s.z) *0.7)
- 0.00554 + 1.31479 *s.z - 1.08771 *s.z*s.z + 5.09347 *s.z*s.z*s.z
+ p.extinction_r
AND p.g - p.r > 0.8
```

Selecting galaxies with an extended X-ray source within 100kpc taking into account the ROSAT position error.<sup>2</sup>

```
AND r.extent >= 1
AND r.delta <= 100/(0.00717 + 20.42378 *s.z - 21.97056 *s.z*s.z + 11.06756 *s.z*s.z*s.z) + r.poserr
```

Identifying non-fossil systems. All objects within half the virial radius that are photometrically classified as galaxies and less than 2 mag fainter than the central elliptical are counted.<sup>3</sup>

```
SELECT count(*)-1
FROM photoObj p, dbo.fGetNearbyObjEq(ra, dec, radius) n
WHERE p.objID = n.objID
AND p.type = 3
AND p.r - m1 < 2.0
```

<sup>1</sup>  $D_L$  and  $K(z)$  were implemented via third order polynomials that were fit to the  $D_L$  and  $K(z)$  data derived from the 'Cosmology Calculator' and SDSS for redshifts up to  $z = 0.5$ . The `kcrr_r` entry in the SDSS photoz table was not directly used in the query since these values are based upon photometric redshifts which can strongly deviate from spectroscopic redshifts and would lead to wrong results. Therefore  $K(z)$  was determined based upon galaxies with  $g' - r' > 0.8$  that show hardly any difference in photometric and spectroscopic redshifts.

<sup>2</sup> The polynomial gives the angular scale as a function of redshift based upon angular diameter distances  $D_A$ .

<sup>3</sup> This query has been performed for all galaxies shortlisted via the previous criteria. `ra`, `dec` give the coordinates of the central galaxy in decimal degrees while `radius` presents half the virial radius in arcminutes. `m1` stands for the  $r'$  band magnitude of the central galaxy.





# Appendix B

## Night conditions

Appendix B summarizes the night conditions of the observing runs at the William Herschel Telescope and the Very Large Telescope.

Figures B.1 and B.2 show the night conditions for both observing blocks carried out at the VLT. Both diagrams present amongst others temperature, humidity and seeing during the observing night. The actual observing blocks are highlighted in red. Time refers to UT. Grey shaded areas indicate the beginning and end of the corresponding night. The data were taken from the ESO archive.

Figures B.3 and B.4 show the corresponding parameters for both nights at the WHT. Temperature and humidity are shown for both inside and outside the telescope dome. In particular, the inside temperature is the mirror temperature of the telescope. An interesting fact in the graphs of the 20<sup>th</sup> of December 2008 is the sharp drop off in humidity short after twilight. Fortunately this drop off occurred at the very beginning of the night allowing for the scheduled observations to be carried out.

Figures B.5 show the change in altitude and airmass for all objects observed at the WHT in the course of the two scheduled nights from sunset to sunrise. End and beginning of twilight are indicated as vertical dashed lines. The curved dashed line presents the moon's altitude. Targets are numbered in the order of observation during each night. The legends on the right relate the numbers to the ID of Table 3.3. The graphs were created with the ING `staralt` tool<sup>1</sup> and used to arrange the individual observing time slots for all targets.

---

<sup>1</sup><http://catserver.ing.iac.es/staralt/>

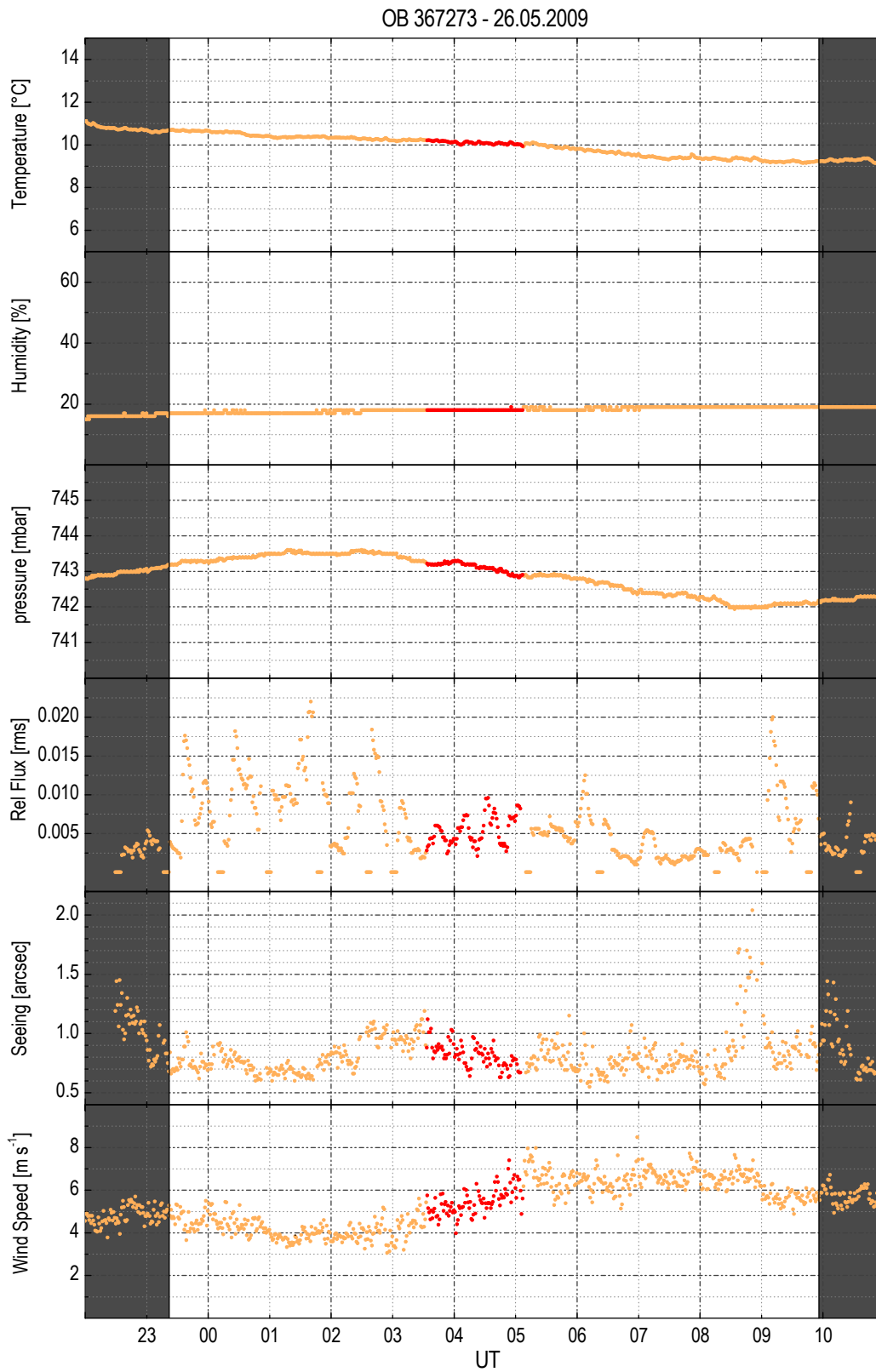


**Figure B.1:** Night conditions for OB367273. The red region indicates the observing block.

OB 367282 - 24.04.2009

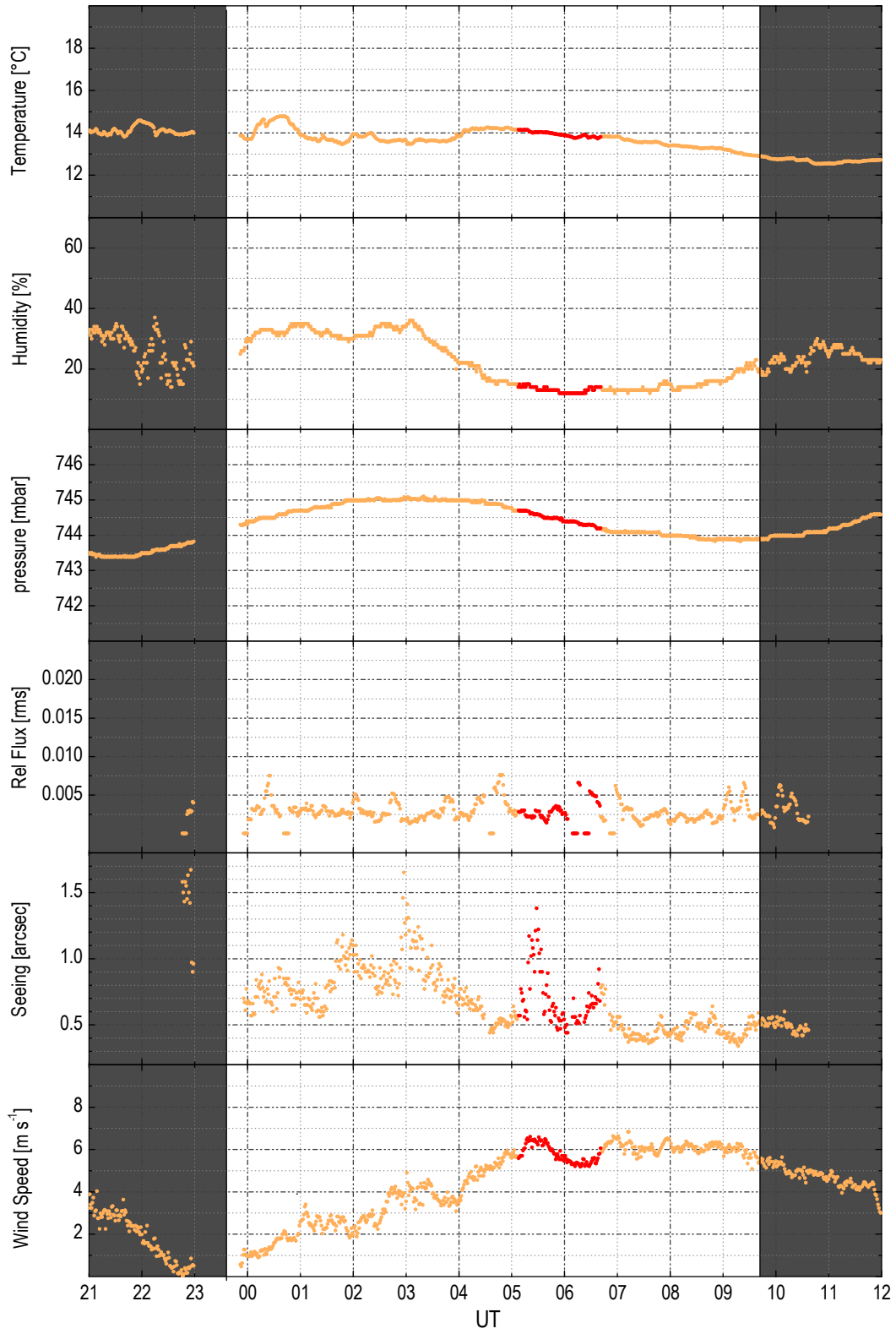


**Figure B.2:** Night conditions for OB367282. The red region indicates the observing block.

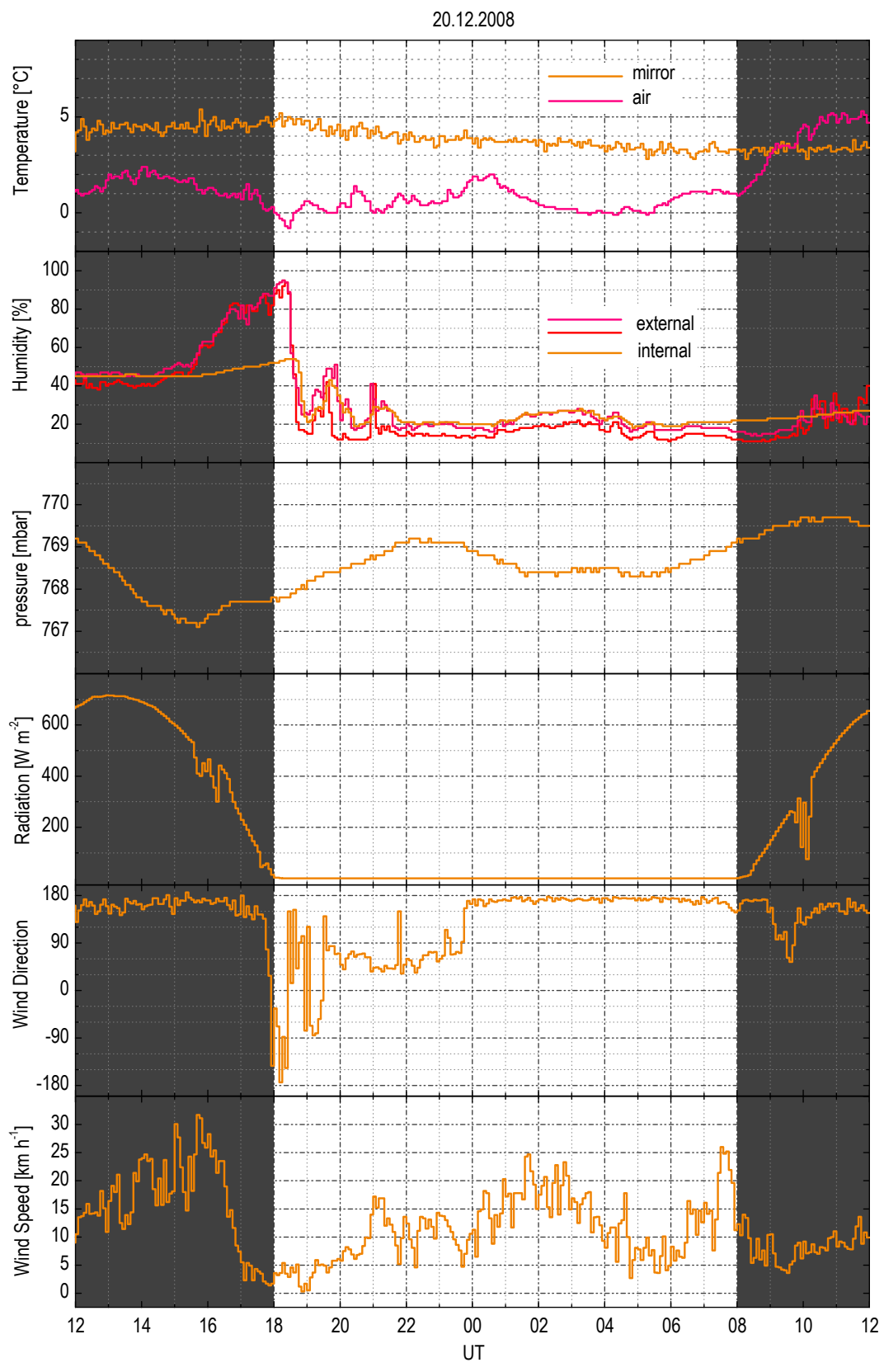


**Figure B.3:** Night conditions at the WHT for the 20<sup>th</sup> of December 2008.

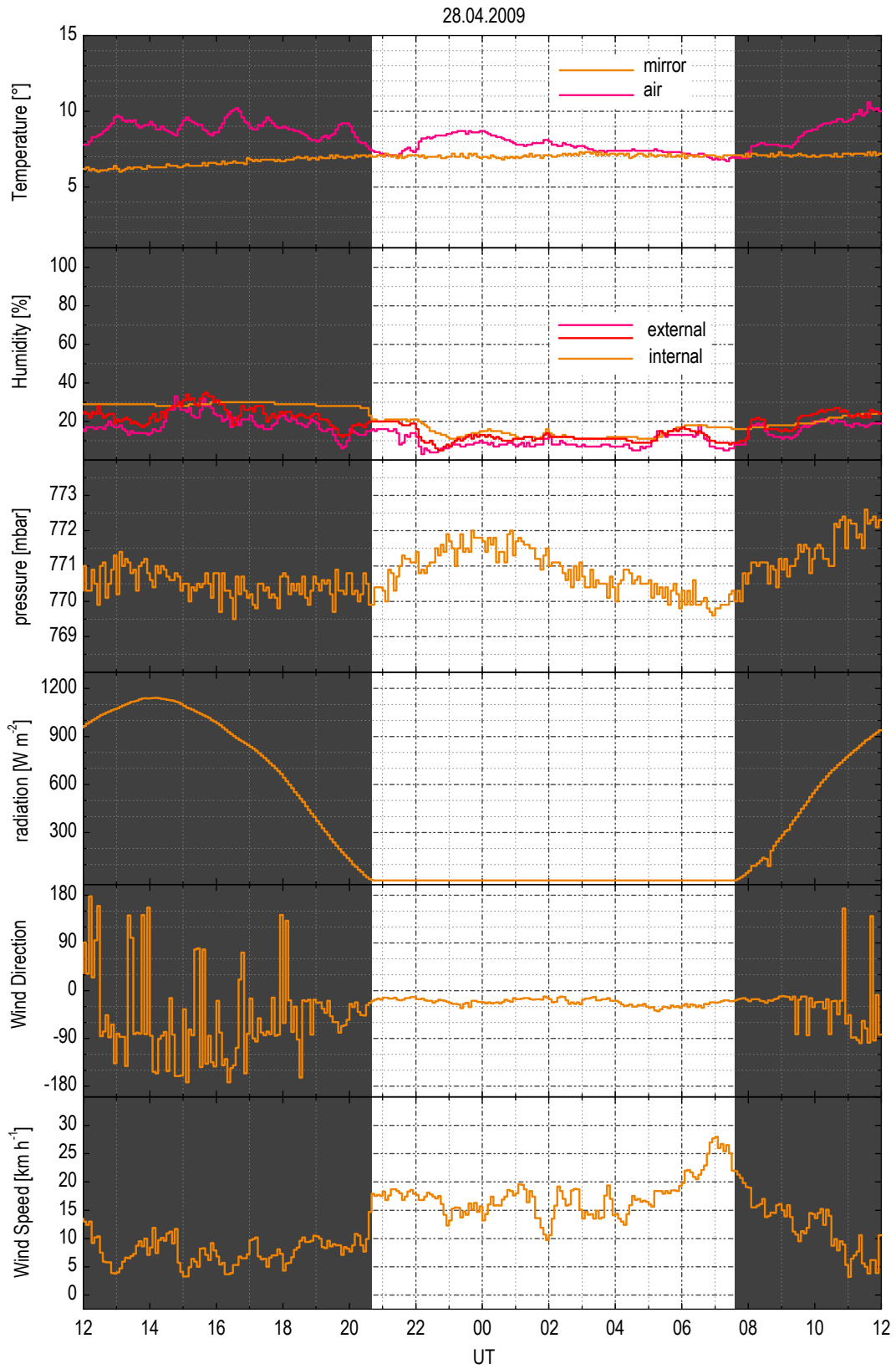


**Figure B.4:** Night conditions at the WHT for the 28<sup>th</sup> of April 2009.

## Appendix B. Night conditions

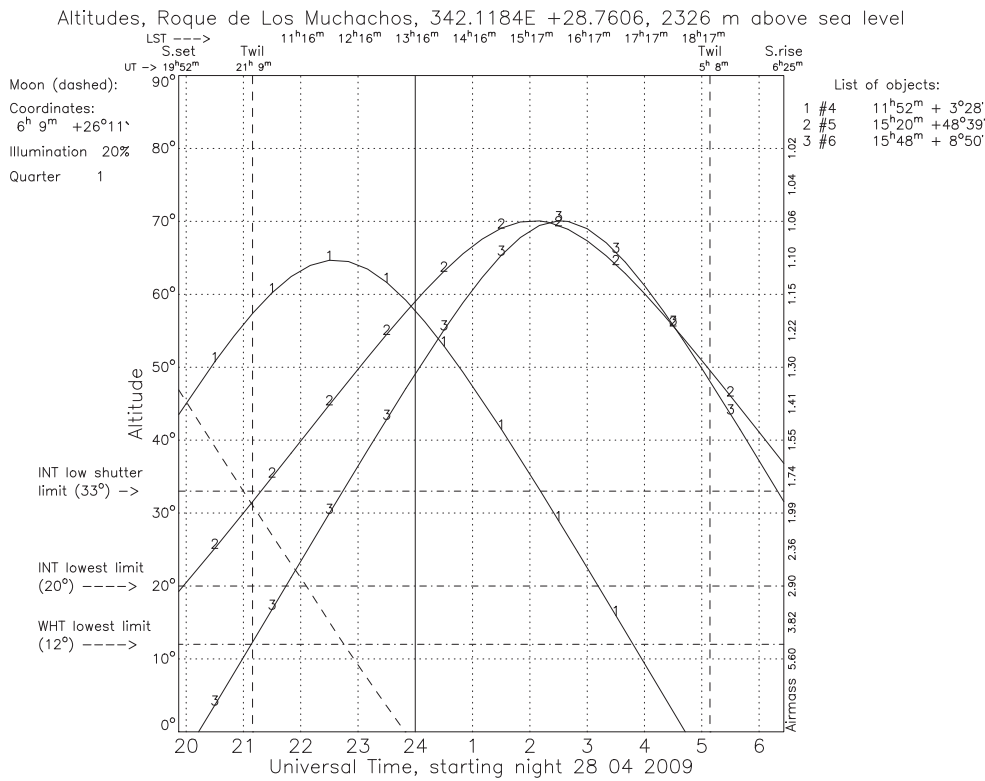
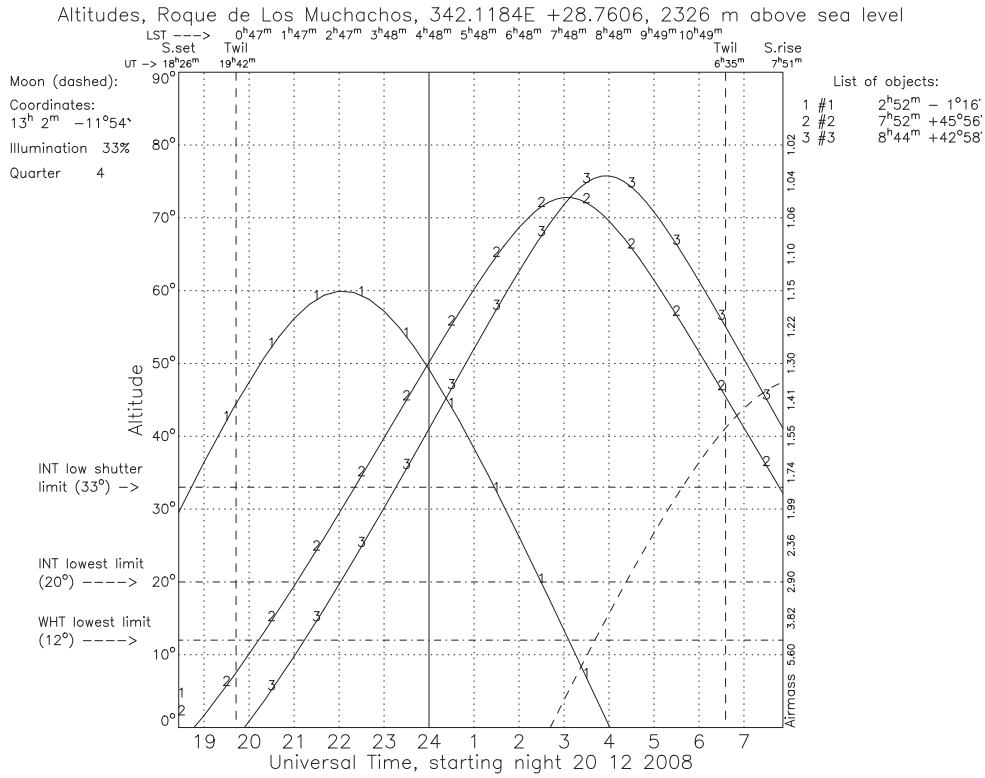


**Figure B.5:** Object visibility for all targets observed with the WHT. Upper panel: night from 20.12.2008. Lower panel: night from 28.04.2009. Object altitudes and corresponding airmasses are shown. The object lists on the right refer to Table 3.3. The dashed line indicates the moon.

## References

- Adelman-McCarthy, J. et al. 2008, *ApJS*, **175**, 297
- Angeletti, L., Giannone, P. 2003, *A&A*, **403**, 449
- Annibali, F. et al. 2007, *A&A*, **463**, 455
- Barnes, J. E. 1989, *Nature*, **338**, 123
- Baum, W. A. 1959, *PASP*, **71**, 106
- Bender, R., Döbereiner, S., Möllenhoff, C. 1988, *A&AS*, **74**, 385
- Bernardi, M. et al. 2003, *AJ*, **125**, 1849
- Bernardi, M. et al. 2003, *AJ*, **125**, 1866
- Bernardi, M. et al. 2003, *AJ*, **125**, 1882
- Binney, J., Tremaine, S. 1987, *Galactic Dynamics*, Princeton University Press
- Biviano, A. et al. 1997, *A&A*, **321**, 84
- Bower, R. G., Lucey, J. R., Ellis, R. S. 1992, *MNRAS*, **254**, 601
- Burstein, D. et al. 1984, *ApJ*, **287**, 586
- Cardiel, N. 2007, in *Highlights of Spanish Astrophysics IV*
- Chandrasekhar, S. 1943, *ApJ*, **97**, 255
- Chiappini, C. et al. 2002, *ASPC*, **253**, 321
- Csabai, I. et al. 2003, *AJ*, **125**, 580
- Cypriano, E. S. et al. 2006, *AJ*, **132**, 514
- Dariush, A. et al. 2007, *MNRAS*, **382**, 433
- Davies, R. L. et al. 1993, *MNRAS*, **262**, 650
- Di Matteo, P. et al. 2009, *A&A*, **499**, 427
- Djorgovski, S., Davis, M. 1987, *ApJ*, **313**, 59
- D'Onghia, E. et al. 2005, *ApJ*, **630**, 109
- Dressler, A. 1980, *ApJ*, **236**, 351
- Dressler, A. et al. 1987, *ApJ*, **313**, 42

## References

---

- Ebrova, I. et al. 2010, ASPC, **423**, 236
- Eigenthaler, P., Zeilinger, W. W. 2009, AN, **330**, 978
- Eigenthaler, P., Zeilinger, W. W. 2010, A&A, **511**, A12
- Ellis, S. C., O’Sullivan, E. 2006, MNRAS, **367**, 627
- Evrard, A. E. et al. 1996, ApJ, **469**, 494
- Faber, S. M., Jackson, R. E. 1976, ApJ, **204**, 668
- Ferreras, I., Silk, J. 2002, MNRAS, **336**, 1181
- Firth, P. et al. 2006, MNRAS, **372**, 1856
- Geller, M. J., Huchra, J. P. 1983, ApJS, **52**, 61
- Girardi, M. et al. 2002, ApJ, **569**, 720
- Gorgas, J. et al. 1993, ApJS, **86**, 153
- Gnedin, O. Y. 2003, ApJ, **589**, 752
- Hartley, W. G. et al. 2008, MNRAS, **386**, 2015
- Hickson, P. 1982, ApJ, **255**, 382
- Hopkins, P. F. et al. 2005, ApJ, **618**, 1
- Horne, K. 1986, PASP, **98**, 609
- Hunsberger, S. D. et al. 1996, ApJ, **462**, 50
- Jacoby, G. H., Hunter, D. A., Christian, C. A. 1984, ApJS, **56**, 257
- Jedrzejewski, R. I. 1987, MNRAS, **226**, 747
- Jones, L. R. et al. 2003, MNRAS, **343**, 627
- Kalberla, P. et al. 2005, A&A, **440**, 775
- Khosroshahi, H. G. et al. 2004, MNRAS, **349**, 1240
- Khosroshahi, H. G. et al. 2006a, MNRAS, **369**, 1211
- Khosroshahi, H. G. et al. 2006b, MNRAS, **372**, 68
- Khosroshahi, H. G. et al. 2007, MNRAS, **377**, 595
- Kobayashi, C. 2004, MNRAS, **347**, 740
- Kodama, T., Bower, R. G., Bell, E. F. 1999, MNRAS, **306**, 561
- Koleva, M. et al. 2009, A&A, **501**, 1269
- Kormendy, J. 1977, ApJ, **218**, 333
- Kormendy, J. 1985, ApJ, **295**, 73
- Kormendy, J., Djorgovski, S. 1989, ARA&A, **27**, 235
- Kurtz, M. J., Mink, D. J. 1998, PASP, **110**, 934
- Larson, R. B. 1974, MNRAS, **166**, 585
- Le Borgne, D. et al. 2004, A&A, **425**, 881
- McConnachie, A. W. et al. 2009, MNRAS, **395**, 255
- Mendes de Oliveira, C. et al. 2006, AJ, **131**, 158
- Mendes de Oliveira, C. et al. 2009, AJ, **138**, 502
- Mihos, J. C., Hernquist, L. 1994, ApJ, **427**, 112



---

Mukai, K. 1993, *Legacy*, **3**, 21  
Mulchaey, J. S. 2000, *ARA&A*, **38**, 289  
Naab, T., Burkert, A. 2003, *ApJ*, **597**, 893  
Naab, T., Khochfar, S., Burkert, A. 2006, *ApJ*, **636**, 81  
Navarro, J. F., Frenk, C. S., White, S. D. M. 1995, *MNRAS*, **275**, 720  
Nolthenius, R., White, S. 1987, *MNRAS*, **225**, 505  
Ogando, R. L. C. et al. 2005, *ApJ*, **632**, 61  
Osmond, J. P. F., Ponman, T. J. 2004, *MNRAS*, **350**, 1511  
Ponman, T. J. et al. 1994, *Nature*, **369**, 462  
Prugniel, P., Soubiran, C. 2001, *A&A*, **369**, 1048  
Prugniel, P. et al. 2007, *astro.ph*, 3658  
Ramella, M., Diaferio, A., Geller, M. J., Huchra, J. P. 1994, *AJ*, **107**, 1623  
Reda, F. M. et al. 2007, *MNRAS*, **377**, 1772  
Rood, H. J., Struble, M. F. 1994, *PASP*, **106**, 413  
Sales, L. V. et al. 2007, *MNRAS*, **382**, 1901  
Sandage, A. 1961, *The Hubble Atlas of Galaxies*, Carnegie Institution  
Sandage, A., Visvanathan, N. 1978, *ApJ*, **223**, 707  
Sandage, A., Visvanathan, N. 1978, *ApJ*, **225**, 742  
Sanderson, A. J. R. et al. 2003, *MNRAS*, **340**, 989  
Santos, W.A. et al. 2007, *AJ*, **134**, 1551  
Sarazin, C. L. 1986, *RvMP*, **58**, 1  
Schechter, P. 1976, *ApJ*, **203**, 297  
Schiavon, R. P. 2007, *ApJS*, **171**, 146  
Schirmer, M. et al. 2010, *A&A*, **514**, 60  
Sodré, L. Jr. et al. 1989, *AJ*, **97**, 1279  
Springel, V. et al. 2005, *Nature*, **435**, 629  
Stetson, P. B. 1989, *HiA*, **8**, 635  
Sun, M. et al. 2004, *ApJ*, **612**, 805  
Tonry, J., Davis, M. 1979, *AJ*, **84**, 1511  
Toomre, A., Toomre, J. 1972, *ApJ*, **178**, 623  
Trager, S. C. 1997, *Ph.D. thesis*, Univ. California, Santa Cruz  
Tully, R. B. 1987, *ApJ*, **321**, 280  
Tully, R. B., Fisher, J. R. 1988, *Nearby Galaxies Catalog*, Cambridge University Press  
Ulmer, M. P. et al. 2005, *ApJ*, **624**, 124  
Valotto, C. A. et al. 2004, *ApJ*, **603**, 67  
Vikhlinin, A. et al. 1999, *ApJ*, **520**, 1  
Voges, W. et al. 1999, *A&A*, **349**, 389  
Wang, Y. et al. 2008, *ApJ*, **687**, 919

## References

---

- White, S. D. M. 1980, MNRAS, **191**, 1  
Worthey, G. et al. 1994, ApJS, **94**, 687  
Worthey, G., Ottaviani, D. L. 1997, ApJS, **111**, 377  
Worthey, G. 1999, ASPC, **192**, 283  
Wright, E. L. 2006, PASP, **118**, 1711  
Wu, X., Xue, Y., Fang, L. 1999, ApJ, **524**, 22  
Yoshioka, T. et al. 2004, AdSpR, **34**, 2525

# List of Figures

1.1	Poor, compact and fossil groups of galaxies . . . . .	2
1.2	Numerical simulation of a compact galaxy group . . . . .	4
1.3	Scaling relations in fossil groups . . . . .	7
1.4	Isophotal shapes of fossil group central ellipticals . . . . .	9
1.5	Luminosity function of the fossil cluster RX J1552.2+2013 . . . . .	10
1.6	Dynamics and mass-to-light ratios of fossils . . . . .	11
1.7	Fossils in the Millennium and Millennium gas simulations . . . . .	12
1.8	The mass build up of fossil dark matter haloes as a function of redshift . . . . .	13
1.9	Satellite galaxies in the Millennium simulation . . . . .	14
1.10	The fundamental plane of ellipticals and its projections . . . . .	15
1.11	The colour-magnitude, colour- $\sigma$ and Mg <sub>2</sub> - $\sigma$ relations . . . . .	16
1.12	The age-metallicity degeneracy . . . . .	17
1.13	SSP model grids of Lick/IDS indices . . . . .	17
1.14	Metallicity gradients in ellipticals . . . . .	18
2.1	Bimodality of galaxy colors in the SDSS . . . . .	24
2.2	Cosmological distances, scales and $K$ corrections . . . . .	25
2.3	Fossil candidates . . . . .	32
2.4	Colour-magnitude diagram of the fossil group central ellipticals . . . . .	34
2.5	The faint galaxy populations of the WHT and VLT targets . . . . .	36
2.6	Surface photometry of RX J0752.7+4557 . . . . .	38
2.7	Surface photometry of RX J0844.9+4258 . . . . .	39
2.8	Surface photometry of RX J1152.6+0328 . . . . .	40
2.9	Surface photometry of RX J1520.9+4840 . . . . .	41
2.10	Surface photometry of RX J1548.9+0851 . . . . .	42
3.1	William Herschel Telescope and ISIS . . . . .	44
3.2	Observing semesters at the WHT . . . . .	45
3.3	WHT control room . . . . .	48
3.4	Timetables for both WHT nights . . . . .	51
3.5	ISIS TV camera preview . . . . .	51
3.6	Orientations of the spectrograph slit . . . . .	52
3.7	Blue arm long-slit spectra . . . . .	56
3.8	Red arm long-slit spectra . . . . .	57
3.9	NGC 1132 – Lick/IDS index passbands . . . . .	59
3.10	RX J0752.7+4557 – Lick/IDS index passbands . . . . .	59

3.11	RX J0844.9+4258 – Lick/IDS index passbands . . . . .	60
3.12	RX J1152.6+0328 – Lick/IDS index passbands . . . . .	60
3.13	RX J1520.9+4840 – Lick/IDS index passbands . . . . .	61
3.14	RX J1548.9+0851 – Lick/IDS index passbands . . . . .	61
3.15	Comparison between measured and original indices for the observed Lick standards	63
3.16	Index strengths as a function of velocity dispersion . . . . .	65
3.17	NGC 1132 – index gradients . . . . .	66
3.18	NGC 1132 line strength gradients . . . . .	67
3.19	RX J0752.7+4557 line strength gradients . . . . .	68
3.20	RX J0844.9+4258 line strength gradients . . . . .	69
3.21	RX J1152.6+0328 line strength gradients . . . . .	70
3.22	RX J1520.9+4840 line strength gradients . . . . .	71
3.23	RX J1548.9+0851 line strength gradients . . . . .	72
3.24	ULySS multiplicative polynomial . . . . .	74
3.25	ULySS 1-D fit results . . . . .	76
3.26	The WHT ellipticals in the age-metallicity plane . . . . .	77
3.27	SSP age and metallicity profiles of NGC 1132 . . . . .	78
3.28	SSP age and metallicity profiles of RX J0752.7+4557 . . . . .	79
3.29	SSP age and metallicity profiles of RX J0844.9+4258 . . . . .	80
3.30	SSP age and metallicity profiles of RX J1152.6+0328 . . . . .	81
3.31	SSP age and metallicity profiles of RX J1520.9+4840 . . . . .	82
3.32	SSP age and metallicity profiles of RX J1548.9+0851 . . . . .	83
3.33	Kinematics of the WHT ellipticals . . . . .	87
4.1	VIMOS multi-object spectrograph . . . . .	90
4.2	VIMOS field of view . . . . .	91
4.3	ESO observing periods . . . . .	91
4.4	The guidecam tool . . . . .	93
4.5	VIMOS catalog . . . . .	95
4.6	VIMOS mask preparation . . . . .	96
4.7	Cross-correlation with <code>xcsao</code> . . . . .	103
4.8	Spectroscopic targets – quadrant 1 . . . . .	106
4.9	Spectroscopic targets – quadrant 2 . . . . .	107
4.10	Spectroscopic targets – quadrant 3 . . . . .	108
4.11	Spectroscopic targets – quadrant 4 . . . . .	109
4.12	Radial velocity distribution . . . . .	110
4.13	Spatial coverage of RX J1548.9+0851 . . . . .	112
4.14	Magnitude dependent incompleteness . . . . .	113
4.15	Accuracy of SDSS photometric redshifts . . . . .	114
4.16	Photometrically and spectroscopically determined members . . . . .	115
4.17	Schechter luminosity function of RX J1548.9+0851 member galaxies . . . . .	116
4.18	Morphology of the central elliptical . . . . .	118
4.19	Surface brightness profile of the central elliptical . . . . .	119
4.20	Morphology of the faint galaxy population . . . . .	120
4.21	Fine structure of the faint galaxy population . . . . .	121
4.22	ULySS fit results of group members – 1 . . . . .	123

---

4.23	ULySS fit results of group members – 2 . . . . .	124
4.24	ULySS fit results of group members – 3 . . . . .	125
4.25	ULySS fit results of group members – 4 . . . . .	126
4.26	ULySS fit results of group members – 5 . . . . .	127
4.27	ULySS fit results of group members – 6 . . . . .	128
4.28	ULySS fit results of group members – 7 . . . . .	129
4.29	ULySS fit results of group members – 8 . . . . .	130
4.30	ULySS fit results of group members – 9 . . . . .	131
4.31	Distribution of group members in the age-metallicity plane . . . . .	131
4.32	Age and metallicity maps . . . . .	132
4.33	Group dynamics . . . . .	133
5.1	Redshifts and colours of fossil candidates selected from the SDSS . . . . .	138
5.2	The WHT ellipticals in the colour-magnitude relation . . . . .	139
5.3	The WHT ellipticals in the colour-sigma relation . . . . .	139
5.4	The WHT ellipticals on the Faber-Jackson relation . . . . .	140
5.5	The WHT ellipticals on the fundamental plane . . . . .	140
5.6	Relations between index strengths and velocity dispersion . . . . .	141
5.7	Age and metallicity gradients of the WHT ellipticals . . . . .	143
5.8	RX J1548.9+0851 in group–cluster scaling relations . . . . .	147
5.9	Scaling relations of RX J1548.9+0851 group members . . . . .	149
B.1	Night conditions for OB367273 . . . . .	164
B.2	Night conditions for OB367282 . . . . .	165
B.3	WHT night conditions – 20 <sup>th</sup> December 2008 . . . . .	166
B.4	WHT night conditions – 28 <sup>th</sup> April 2009 . . . . .	167
B.5	Object visibility for all targets observed with the WHT . . . . .	168



# List of Tables

1.1	Fossils in the literature . . . . .	5
2.1	SDSS tables queried in the present work . . . . .	22
2.2	Fossil candidates – ROSAT and SDSS identifications . . . . .	29
2.3	Fossil candidates – optical and X-ray properties . . . . .	30
3.1	Allocated nights at the WHT . . . . .	46
3.2	Standard stars observed at the WHT . . . . .	47
3.3	Elliptical galaxies observed with ISIS . . . . .	50
3.4	Observing log of spectroscopic observations . . . . .	50
3.5	Lick/IDS indices . . . . .	58
3.6	ULySS 1-D fit results of the WHT ellipticals . . . . .	75
3.7	2-D ULySS fit results of the WHT ellipticals . . . . .	84
4.1	Accepted ESO runs . . . . .	92
4.2	Masks prepared with the VMPS tool . . . . .	96
4.3	Night conditions of spectroscopic OBs . . . . .	97
4.4	VIMOS MOS science products . . . . .	99
4.5	Stellar cross correlation templates . . . . .	101
4.6	Radial velocities of the candidate faint galaxy population . . . . .	104
4.7	Number of galaxies within group radii of 300kpc, 500kpc, and 1Mpc . . . . .	111
4.8	SSP equivalent ages and metallicities of group members . . . . .	122
4.9	Luminosity weighted group dynamics . . . . .	135
4.10	Mass-to-light ratios . . . . .	136





Mag. Paul Eigenthaler

Department of Astronomy  
University of Vienna

Türkenschanzstraße 17  
A-1180 Vienna / Austria  
phone: +43 1 4277 53834  
fax: + 43 1 4277 9518

email: paul.eigenthaler@univie.ac.at



# Curriculum Vitæ

## Personal Data

Name	Mag. Paul Eigenthaler
Date of birth	07.12.1980
Place of birth	St.Pölten
Citizenship	Austria

## Academic Career

01.01.2008 - 31.12.2010	* Assistant within the Graduate School (Initiativkolleg) <i>The Cosmic Matter Circuit</i> at the University of Vienna
2008 - 2009	* Member of the Search Committee <i>Galaxy Formation in the Early Universe</i> for a full professorship at the Institute of Astronomy in Vienna
WS 2006/07	* Starting Doctoral Studies of Natural Sciences at the University of Vienna Dissertation Field: Extragalactic Astronomy
17.10.2006	* Diploma Examination with Distinction
October 2004	* Starting Diploma Thesis <i>The Dwarf Galaxy Population of the NGC 5846 Group</i>
WS 2000/01	* Starting Studies of Astronomy at the University of Vienna

## Awards

2006	* Diplomarbeitspreis of the <b>Österreichische Gesellschaft für Astronomie und Astrophysik (ÖGAA)</b> 2006
------	--

## Grants

01.01.2007 - 31.12.2007	* Forschungsstipendium of the University of Vienna (Project: F133-N)
-------------------------	--

---

## Observing Runs

---

- 2009 ESO Period 83   ★ Very Large Telescope (VLT), Short Programme (Service Mode), PI  
2009 April 28       ★ William Herschel Telescope (WHT), 1 Night (Visitor Mode), CoI  
2008 December 20   ★ William Herschel Telescope (WHT), 1 Night (Visitor Mode), CoI

---

## Research Stays

---

- 2009 June 7 - 20   ★ Centre de Recherche Astronomique de Lyon, Observatoire de Lyon

---

## Conferences

---

- 2010 September 6 - 10       ★ JENAM 2010, Lisbon (Poster)  
2010 June 14 - 18         ★ A Universe of dwarf galaxies, Lyon (Poster)  
2009 September 21 - 25     ★ AG fall meeting, Potsdam (Talk)  
2009 September 2 - 4       ★ ÖGA<sup>2</sup> annual meeting, Innsbruck (Talk)  
2008 September 8 - 12     ★ JENAM (EAS and ÖGA<sup>2</sup> annual meeting & AG fall meeting),  
Vienna (Talk)  
2007 September 24 - 28     ★ AG fall meeting, Würzburg (Poster)  
2007 April 12 - 14         ★ ÖGA<sup>2</sup> annual meeting, Vienna (Talk)  
2006 April 21 - 22         ★ ÖGA<sup>2</sup> annual meeting, Innsbruck (Talk)  
2005 September 26 - October 1   ★ AG fall meeting, Cologne (Poster)

---

## Publications

---

### *Refereed publications*

- ★ **Eigenthaler, P.**; Zeilinger, W. W.  
*Revisiting the low-luminosity galaxy population of the NGC 5846 group with SDSS*  
2010, A&A **511** A12

### *Conference Proceedings*

- ★ **Eigenthaler, P.**; Zeilinger, W. W.  
*The properties of fossil groups of galaxies*  
2009, AN **330** 978
- ★ **Eigenthaler, P.**; Zeilinger, W. W.  
*The Search for Fossil Groups of Galaxies*  
2007, AN **328** 699
- ★ **Eigenthaler, P.**; Zeilinger, W. W.  
*Dwarf galaxies in the NGC 5846 Group*  
2005, AN **326** 490